

Spin-Orbit Coupled Fermi Gases Under Adiabatic Rotation

by

Enis Doko

A Dissertation Submitted to the
Graduate School of Sciences and Engineering
in Partial Fulfillment of the Requirements for
the Degree of
Doctor of Philosophy
in
Physics



August 9, 2016

Spin-Orbit Coupled Fermi Gases Under Adiabatic Rotation

Koç University

Graduate School of Sciences and Engineering

This is to certify that I have examined this copy of a doctoral dissertation by

Enis Doko

and have found that it is complete and satisfactory in all respects,
and that any and all revisions required by the final
examining committee have been made.

Committee Members:

Assoc. Prof. Dr. Menderes Işkın (Advisor)

Prof. Dr. Özgür Müstecaplıoğlu

Assoc. Prof. Dr. Levent Subaşı

Assoc. Prof. Dr. Özgür Oktel

Assoc. Prof. Dr. Kaan Güven

Date: _____

Dedem Cabir ile Ninem Hatiye'nin aziz hatıralarına. Ve annem Melekzat'a.

ABSTRACT

In this thesis we analyze the interplay of adiabatic rotation and Rashba spin-orbit coupling (SOC) throughout the BCS-BEC evolution of a harmonically trapped Fermi gas in two dimensions under the assumption that vortices are not excited. We first study the non-interacting Fermi gas by taking the trapping potential into account via both semi-classical and exact quantum-mechanical approaches. We show that for high enough spin-orbit coupling strength or rotation, the gas forms a characteristic ring shaped annulus. We demonstrate that formation of such an intriguing annulus requires presence of both the spin-orbit coupling and rotation. We compute the critical rotation frequency for emergence of this density profile and we predict that it survive at experimentally accessible finite temperatures.

Then, by taking the interactions into account via the BCS mean-field approximation, we study the pair-breaking mechanism that is induced by rotation, i.e., the Coriolis effect. We calculate the critical rotation frequencies for the onset of pair breaking in the superfluid phase and the destruction of superfluidity as a function of interaction or SOC strength. Comparing full quantum mechanical Bogoliubov-de Gennes calculations with local density approximation results, we show that the interplay between spin-orbit coupling and rotation allows the possibility of creating either an isolated annulus of rigidly rotating normal particles that is disconnected from the central core of non-rotating superfluid pairs or an intermediate mediator phase where the superfluid pairs and normal particles coexist as a partially rotating gapless superfluid.

We present extensive phase diagrams and find that a gapless superfluid phase may occupy a considerable region in the trap profile.

We also study all the limits in great detail providing analytic and semi-analytic

results when possible. We note that the effect of adiabatic rotation on a two dimensional interacting Fermi gas without SOC is not studied previously either. We provide an analytical expression for the critical rotation for the onset of pair breaking in the no SOC case.

ÖZETÇE

Bu tezde adiyabatik dönme ile Rashba spin-momentum bağının (SMB) harmonik tuzaklanmış iki boyutlu Fermi gaz sistemlerinde BCS-BEY geçişi boyunca ortak etkileri girdaplar uyarılmadığı varsayımı altında incelenmiştir. Öncelikle etkileşimsiz Fermi gazı, tuzak potansiyeli hem yarı-klasik hem de kesin kuantum mekaniksel yaklaşımlar altında ele alınarak incelenmiştir. Yeterince yüksek şiddetli SMB ya da yüksek dönme hızlarında gaz yoğunluğu karakteristik bir halka şeklini alır. Bu ilginç halka şekline sahip sistemin oluşması için hem spin-momentum bağının hem de dönmenin mevcut olması gerektiği gösterilmiştir. Bu yoğunluk profilinin oluşması için gereken kritik dönme frekansı hesaplanmış ve bu profilin deneysel olarak ulaşılabilir sıcaklıklara kadar varlığını sürdürebileceği öngörülmüştür.

Daha sonra, BCS orta-alan yaklaşımı ile parçacık etkileşimleri göz önünde bulundurularak, dönmenin, diğer bir deyişle Coriolis etkilerinin, üstün-akışkan durumda oluşan Cooper çiftlerini kırma mekanizması incelenecektir. Çift kırılmasının başladığı ve üstün-akışkanlığın tamamen yok olduğu kritik dönme frekansları SMB'nin şiddeti ya da etkileşimin bir fonksiyonu olarak hesaplanmıştır. Yerel yoğunluk yaklaşımı sonuçları ile tam kuantum mekaniksel Bogoliubov-de Gennes hesapları karşılaştırılıp, dönme ile SMB'nin ortak ve zıt etkilerinin, merkezdeki dönmeyen üstün-akışkan çiftlerden boşluk ya da kısmi olarak dönen üstün-akışkan çiftlerle normal parçacıkların bir arada olduğu bir ara faz, enerji aralıksız üstün-akışkan, ile ayrılmış rijit şekilde dönen normal parçacıklar halkası ihtimallerine izin verdiği gösterilmiştir.

Kapsamlı faz diyagramları sunulmuş, enerji aralıksız üstün-akışkanın tuzak profilinde kayda değer bir bölgeyi kaplayabileceği gösterilmiştir.

Bütün limitler detaylıca incelenerek mümkün olan durumlarda analitik ve yarı-analitik sonuçlar verilmiştir. SMB'siz iki boyutlu etkileşimli Fermi gaz sistemleri de

daha 6nceden ok az incelenmiřtir. SMB'siz durumda ift kırılmasının bařladıđı kritik rotasyon ile ilgili analitik ifade bulunmuřtur.

ACKNOWLEDGMENTS

I still remember the day, my mother Melekzat thought me the basics of arithmetics (probably when I was four years old). I could read numbers and make arithmetical operations before I learned the alphabet. I admire my mother as my first math teacher, a person who made me love the numbers. She raised and looked after me by herself without any support, I can never pay my dept to her. On the other hand my grandmother Hatiye was my first physics teacher. My early understanding of the universe was based on her explanations, which most of the time were scientific. She was the first person to explain the effects of the Coriolis force on liquids due to Earth's rotation (although she did not know the name). Effects of the Coriolis force on Cooper pairs is one of the main themes in this thesis. She always insisted that I need to study and become a very educated man, rather than quit education after high school like most of the Turks used to do in my hometown. Without her support I will not have completed my PhD. I am also grateful to my grandfather Cabir for his endless love and support. He was practically my father; he did everything to ensure that I would have proper education. I also thank my brother Cabir for his support throughout my education. My girlfriend Jale Akdemir deserves special thanks for her love, support and understanding. Their love and support were essential for me.

There is a saying that "physics is very difficult if you have brilliant people around you, but impossible if you are alone". I was lucky enough to work with such brilliant physicists. I am extremely grateful to my advisor Dr. Menderes Işkın , for his constant support in the past six years. He never gave up on me and I really appreciate his efforts to educate me. I am also very grateful to Dr. Levent Subaşı whom I collaborated with since the beginning of my PhD. He taught me the fine details of the computational physics, he was always there ready to help me with the problems I encountered. I

can not pay my debt to both Dr. Işkın and Dr. Subaşı for their contributions to my scientific career. I also thank to Selahattin Kalafat, my room mate, my home mate and collaborator. He was not only my first friend in the university but also the first person who explained to me the BCS-BEC crossover. I learned a lot from him. Last, but not the least I thank Dr. Onur Umucalılar with whom we had useful discussions.

I am also extremely grateful to all my committee members Dr. Özgür Müstecaplıođlu, Dr. Özgür Oktel and Dr. Kaan Güven for their useful comments and contributions.

I thank my home mates Enes Özel, Ahad Khaleghi, Adnan Hassan and Ahsan Jalal for their companionship.

Lastly, I acknowledge the financial support from TUBITAK, The Scientific and Technological Research Council of Turkey, via TUBITAK-2215 Ph.D. Fellowship and Koç University.

TABLE OF CONTENTS

List of Figures	xiv
Nomenclature	xxx
Chapter 1: Introduction	1
Chapter 2: Fundamentals of Ultracold Fermi Gases	8
2.1 What is an Ultracold Quantum Gas?	8
2.2 Quantum Statistics	13
2.3 Trapping and Cooling Atoms	16
2.4 Density of States	21
2.5 Second Quantization	24
2.6 Non-Interacting Fermi Gas in 3D	27
2.7 Non-Interacting Fermi Gas in 2D	33
2.8 2D Harmonic Oscillator	36
Chapter 3: Interacting Fermi Gas and Superfluidity	42
3.1 Scattering in 3D	42
3.2 Pseudo-potential	47
3.3 Tuning the Interaction Strength: Fano-Feshbach Resonance	49
3.4 Scattering in 2D	51
3.5 Two Body Bound States in 2D and 3D	55
3.6 The Cooper Problem	58
3.7 BCS-BEC Crossover in 3D	61
3.8 BCS-BEC Crossover in 2D	71

3.9	BCS-BEC Crossover in a 2D Harmonic Trap	75
3.10	Superfluidity	81
Chapter 4: Trapped 2D Fermi Gas with Spin-Orbit Coupling		88
4.1	Physical Origin of Spin-Orbit Coupling	88
4.2	Artificial Gauge Fields, Berry Phase and the Adiabatic Principle . . .	93
4.3	Synthetic Spin Orbit Coupling in Cold Atomic Gases	96
4.4	Single Particle Properties with Rashba Spin-Orbit Coupling in 2D . .	99
4.5	Non-Interacting Homogeneous Fermi Gas with Rashba Spin-Orbit Coupling in 2D	102
4.6	Trapped non-interacting Fermi gas with Rashba spin-orbit coupling in 2D	103
4.7	Trapped Interacting Fermi Gas with Rashba Spin-Orbit Coupling in 2D	110
Chapter 5: Rotating 2D Fermi Gas		117
5.1	Motion in Rotating Frame of Reference	117
5.2	Rotating Non-interacting 2D Fermi Gas: Local Density Approximation	121
5.3	Rotating Non-interacting 2D Fermi Gas: Exact Quantum Mechanical Approach	124
5.4	Rotating Superfluids: Hess-Fairbank Effect and Vortices	129
5.5	2D Interacting Fermi Gas Under Adiabatic Rotation	132
Chapter 6: Rotating Rashba Coupled 2D Fermi Gas		142
6.1	Rotating Non-Interacting 2D Fermi Gas with Rashba SOC: Local Den- sity Approximation	142
6.2	Rotating Non-Interacting 2D Fermi Gas with Rashba SOC: Exact Quan- tum Mechanical Approach	153
6.3	Rashba Coupled 2D Interacting Fermi Gas Under Adiabatic Rotation: Local Density Approximation	158

6.4	Phase Diagram and Trap Profiles	161
6.5	Rashba Coupled 2D Interacting Fermi Gas Under Adiabatic Rotation: Bogoliubov de-Gennes Approach	172
Chapter 7:	Conclusion and outlook	177
	Bibliography	181

LIST OF FIGURES

1.1	Bosons vs. fermions at zero temperature. Bosons and fermions behave similarly at high temperatures, where in each quantum state there is very small probability of occupancy, and particle statistics shows the behavior of distinguishable particles. When temperature is lowered degenerate bosons and fermions behave differently. Bosons condense to the lowest energy state, and form the Bose-Einstein condensate. Fermions due to Pauli exclusion principle can not occupy the same quantum state, rather they occupy the lowest states with one Fermion per quantum state forming a Fermi sea.	3
1.2	The BCS-BEC crossover. In cold atoms by tuning the interactions via Feshbach resonance it is possible to smoothly cross from BCS limit of Cooper pairs overlapping in space to BEC limit of tightly bound molecules.	5
2.1	Length scales of a thermal quantum gas. The de-Broglie wavelength λ_T should be greater or comparable to inter-particle spacing d_n for an ultracold gas. Both d_n and λ_T are much greater than the effective range of the interaction R_e . See text for details.	9
2.2	Sketch of typical interaction between two neutral atoms as modeled with Lennard-Jones type potential $(C_1/r^{12} - C_2/r^6)$. We clearly see that at long distances van der Waals attraction takes over the repulsive potential due to Fermi exclusion. At even larger distance which we defined as R_e interaction is very weak and can be safely ignored. . .	11

2.3 Sketch of mechanisms involved in laser cooling. (a) Assume laser is tuned in frequency ν_1 below the resonant frequency ν_0 of the atom, i.e. $\nu_1 < \nu_0$ as a result atom does not absorb the photon. (b) If the atom is moving away from the laser, due to Doppler shift light is red-shifted, and again atom does not absorb any photon. (c) If the atom is moving towards the laser, this time frequency is blue-shifted, it can now match the resonant frequency, thus atom absorbs the photon. (d) Since atom absorbs photon moving in opposite direction of its motion, due to the conservation of momentum it receives a momentum kick in that direction and its velocity decreases. (e) Absorbed photon will be emitted in random direction and if averaged over many absorption/emission cycles net momentum transfer due to emission will be zero. As a result in average only absorption will effect the velocity of the atoms. Atoms will lose velocity and as a result the gas will cool. 18

2.4 Schematic diagram of evaporative cooling. Trap potential is lowered so that atoms with high kinetic energy can escape the trap. Selective removal of hot atoms causes the remaining atoms to cool due to collisional equilibrium. 21

2.5 Sketch of density of states of homogenous gas for different dimensions. The behavior of density of states strongly depends on the dimensionality of the system. Note that density of states increases at low energies with decreased dimensionality. 23

2.6	(a) Energy dependence of average occupation of a state j for different temperatures. Temperatures are scaled with $T_0 = \mu/k_B$. Note that at low T , the curve has form of a step function such that all the states below μ are occupied and states above μ are vacant. At high temperatures, curves take the shape of Boltzmann distribution with considerable occupation probability of states with energy higher than μ . (b) Temperature dependence of average occupation of a state j for $\epsilon_j > \mu$. As $T \rightarrow 0$ all the states above μ become vacant, while at high temperatures the average occupation tends to go toward 0.5.	29
2.7	(a) Density distribution of 3D harmonically trapped two species non-interacting Fermi gas under LDA. Central density is given as $n(0) = k_F^{3/2}/(3\pi^2)$. (b) Density distribution of 2D harmonically trapped two species non-interacting Fermi gas under LDA. Central density is given as $n(0) = k_F^2/(2\pi)$. For both density profiles $R_F = \sqrt{2E_F/(M\omega^2)}$. We should note that the relation between E_F and particle number N depends on dimensionality and is provided in the text.	31
2.8	Illustration of a stack of pancake-shaped traps, created by interference of two coherent laser beams. Particles are confined to stay at a single pancake and we have effectively 2D system.	36
2.9	Density profile computed via exact quantum mechanical calculations compared with semi-classical LDA result for different particle numbers: (a) $N = 100$, (b) $N = 500$, (c) $N = 1000$, (d) $N = 5000$. In low particle numbers such as $N = 100$ LDA fails to capture the Friedel oscillations at the center of the trap and low density tail of the gas. For considerable particle numbers such as $N = 5000$, Friedel oscillations become invisible and low energy tail becomes very small compared to the system size. Thus in the thermodynamic limit LDA and exact QM calculations become indistinguishable.	41

3.1	Solution of the scattering problem for short ranged (R_e range) potential at large distances $ \mathbf{r} \gg R_e$ is superposition of (a) a plane wave and (b) a spherical wave.	43
3.2	Scattering of a particle from a potential $U(r)$ with finite range R_e . The particle can see the potential only if $d < R_e$, which places a constraint on the angular momentum of the particle ($L = pd$) $L < pR_e$. Therefore only particles with angular momentum less than pR_e will be affected from the potential. In quantum mechanics angular momentum states are discrete, if momentum is sufficiently small like in cold atoms, than only particles at lowest s-wave state can see the potential.	45
3.3	Schematic diagram showing two-channel model of Feshbach resonance. Closed channel supports bound state with energy E_b . As explained in the text relative distance between these two channels can be tuned via external magnetic field.	51
3.4	The Cooper problem. Two particles with opposite spin and momenta interact on the top of Fermi sea. The Fermi sea reduces the dimensionality of the system from 3D to 2D by blocking the low energy states . Since arbitrarily weak attractive interaction in 2D leads formation of bound pairs, these two particles form a Cooper pair.	58
3.5	(a) Chemical potential μ and (b) order parameter Δ as a function scattering length $1/k_F a_s$ obtained from the self-consistent solution of the gap and number equations. Analytical expressions derived for the BCS and BEC limits are indicated with dashed lines, they agree very well with the numerical results. The transition from the BCS to the BEC side is smooth.	68

3.6	Momentum distribution n_k for different interactions strengths across the BCS-BEC crossover. In the BCS limit we observe a Fermi distribution broadened with width Δ , which clearly indicates fermionic character. On the other hand in the BEC limit we have occupation numbers much smaller than one, indicating absence of fermionic behavior.	68
3.7	Schematic diagram of quasi-particle excitation spectrum on BCS ($\mu > 0$) and BEC ($\mu \leq 0$) sides. There is always a finite gap in the spectrum. Spectrum's behavior changes at $\mu = 0$, which can be identified as transition point from BCS to BEC side.	71
3.8	(a) Chemical potential μ and (b) order parameter versus Δ as a function of binding energy E_b obtained from self-consistent solution of the gap and number equations in two dimensions. They are analytic and given in the text.	73
3.9	(a) Mean-field density profile under local density approximation of 2D Fermi gas for any E_b . The density profile is not effected by interaction.(b) Mean-field order parameter profile under local density approximation of a 2D Fermi gas for representatve E_b values. Interaction enhances the pairing and the order parameter, and the system is superfluid as a whole at $T = 0$	77
3.10	The trap profiles for a representative $E_b = 0.5E_F$. (a) $n(r)$ for $N = 100$, (b) $\Delta(r)$ for $N = 100$, (c) $n(r)$ for $N = 500$, (d) $\Delta(r)$ for $N = 500$. Even for $N = 100$ LDA is in very good agreement with BdG calculations. Interactions destroy the Friedel oscillations, therefore we have perfect agreement at the center of the trap. LDA fails at the low density region at the edge of the gas as expected. Note that by comparing $N = 100$ and $N = 500$, as the particle number increases the region at which LDA fails becomes small compared to the system size.	82

4.1 (a) Free electron moving in the presence of electric field due to ions. If we move to the rest frame of the electron, it will see apparent motion of the ions which will create magnetic field acting on the electron. This effective magnetic field which is proportional to the electron's velocity can couple with the magnetic moment of the electron, which is proportional to its spin. As a result of this spin of electron is coupled with its momentum. (b) In its rest frame electron will feel an effective magnetic field due to the apparent motion of the proton. This magnetic field which is proportional to the velocity of the electron in the proton's rest frame will couple to the electron's magnetic moment leading to coupling between its momentum and spin. 89

4.2 Schematic representation of the NIST scheme. (a) Two counter propagating Raman lasers couple together (b) a selected pair of atomic states labelled by $|\uparrow\rangle$ and $|\downarrow\rangle$ that represent the pseudo-spin of the atom. These lasers are arranged in a two-photon Raman configuration that uses an off-resonant intermediate state shown with black line in the figure and link atomic motion to the atoms pseudo-spin. $\Omega/2$ is strength of Raman coupling and δ is the two photon detuning. 98

4.3	Illustration of the splitting of the spin degeneracy due to Rashba SOC. All the plots are shown for $k_x = 0$ without loss of generality since system has a symmetry of simultaneous rotation of spin and momentum at $k_x - k_y$ plane. (a) Dispersion relation of free Fermi gas, it is simple parabola. Both time reversal symmetry and inversion symmetry are present $\varepsilon_{-\mathbf{k}\uparrow} = \varepsilon_{\mathbf{k}\uparrow}$. We have spin degeneracy. (b) Dispersion relation of Fermi gas in the presence of Zeeman field. Zeeman field lifts the spin degeneracy and time reversal symmetry is broken. But inversion symmetry is still present. (c) Rashba SOC behaves like momentum dependent Zeeman field. Spin degeneracy is lifted (except at $\mathbf{k} = 0$) but time reversal symmetry is still present. Unlike standard Zeeman field, SOC breaks the inversion symmetry. (d) The positive and negative helicity bands of Rashba SOC.	101
4.4	Density profile of the trapped Rashba coupled non-interacting Fermi gas.(a) Non-interacting density profile with changing SOC strength α . Central density monotonically increases and the gas shrinks. (b) Density at representative SOC values. We can clearly see that at the center of the trap we have a parabolic density profile, while at the edge where we have just negative helicity particles the density profile is non-parabolic.	106
4.5	Distribution of + and - helicity particles in the trap for changing SOC strength α . For SOC strength $\alpha < \alpha_c = \sqrt[4]{6}E_F/k_F$ at the center of the trap we have both + and - helicity particles characterized by a parabolic density distribution and at the edge just - helicity particles characterized by a non-parabolic density distribution. Beyond α_c all the particles in the system are negative helicity particles.	107

4.6	Density profile computed via the exact quantum mechanical calculations compared with the semi-classical LDA results for different particle numbers and SOC strengths: (a) $N = 100$, $\alpha = 1E_F/k_F < \alpha_c$ (b) $N = 100$, $\alpha = 3E_F/k_F > \alpha_c$ (c) $N = 5000$, $\alpha = 1E_F/k_F < \alpha_c$ (d) $N = 5000$, $\alpha = 3E_F/k_F > \alpha_c$. In low particle numbers such as $N = 100$ LDA fails to capture the Friedel oscillations and low density tail of the gas. For considerable particle numbers such as $N = 5000$, Friedel oscillations become invisible and the low density tail becomes very small compared to the system size. Thus at high particle limit LDA and exact QM calculations become practically indistinguishable for any SOC strength.	109
4.7	Schematic diagram of the quasi-particle excitation spectrum of the negative helicity particles for different μ values. The momentum values of the minima are $k_1 = M \left(\alpha - \sqrt{\alpha^2 + 2\mu} \right)$, $k_2 = M\alpha$ and $k_3 = M \left(\alpha + \sqrt{\alpha^2 + 2\mu} \right)$. SOC pushes the excitation minima to the higher momentum states and they remain so even in the extreme BEC limit.	112
4.8	The trap profile of Rashba coupled interacting Fermi gas. In all the figures $E_b = 0.5E_F$. (a)The order parameter profile with changing SOC strength α . For small SOC $\alpha < 1E_F/k_F$, order parameter profile does not change, for higher values order parameter increases. (b) The density profile with changing SOC strength α . For small SOC $\alpha < 1E_F/k_F$, density profile does not change, on the other hand for higher SOC values central density increases and the gas shrinks. (c) Order parameter at representative SOC values. (d) Density at representative SOC values.	114

4.9	Trap profile for Rashba coupled Fermi gas for changing E_b . In all the curves $\alpha = 1.5E_F/k_F$.(a) Density profile for different E_b values. Note that as E_b increases density expands, and eventually it becomes identical with the $\alpha = 0$ profile. (b) Order parameter profile for different E_b values.	115
-----	--	-----

4.10	The trap profiles for representative $E_b = 0.5E_F$ and $\alpha = 2E_F/k_F$. (a) $n(r)$ for $N = 100$, (b) $\Delta(r)$ for $N = 100$, (c) $n(r)$ for $N = 500$, (d) $\Delta(r)$ for $N = 500$. Even for $N = 100$ LDA is in very good agreement with the BdG calculations. Interactions destroy the Friedel oscillations, therefore we have a perfect agreement at the center of the trap. LDA fails at the low density region at the edge of the trap as expected. Note that by comparing $N = 100$ and $N = 500$, as the particle number increases the region at which LDA fails becomes small compared to the system size.	116
------	---	-----

5.1	The density profile of the rotating non-interacting Fermi gas.(a) Density profile with changing rotation frequency Ω . The central density monotonically decreases and gas expands due to the centrifugal effects. (b) Density at representative Ω values. Density retains its parabolic shape under LDA.	124
-----	---	-----

- 5.2 Density profile computed via the exact quantum mechanical calculations compared to the semi-classical LDA results for representative $\Omega = 0.75\omega$ and different particle numbers: (a) $N = 100$, (b) $N = 500$, (c) $N = 1000$, (d) $N = 2500$. In low particle numbers such as $N = 100$ LDA fails to capture Friedel oscillations at the center of the trap and low density tail of the gas. For considerable particle numbers such as $N = 2500$, Friedel oscillations become invisible and low density tail becomes very small compared to the system size. Thus at high particle limit LDA and exact QM calculations become indistinguishable both for all Ω except the fast rotation limit $\Omega \rightarrow \omega$. See text for details. 126
- 5.3 Schematic representation of the energy levels for (a) $\Omega = 0$, (b) $0 < \Omega < \omega$, (c) $\Omega \rightarrow \omega$. Numbers denote the angular momentum quantum number l . We can clearly see the emergence of Landau level structure with energy gap 2ω in $\Omega \rightarrow \omega$ limit. 127
- 5.4 Schematic representation of the possible responses of the superfluid to the rotation. (a) Hess-Fairbank effect. At low rotations $\Omega < \Omega_1 = 1/(2MR^2)$, superfluid is irrotational and "expels" the angular momentum. (b) Vortex. At higher rotational frequencies $\Omega > \Omega_1$ superfluid can carry angular momentum with the help of singularities known as the vortex. (c) Vortex lattice. Angular momentum carried via vortices is quantized and at even higher rotation frequencies hexagonal vortex array with same circulation emerges. (d) Superfluid-Normal phase separation. If rotation is introduced adiabatically so that vortices does not emerge, Coriolis force may break the Cooper pairs at the edge of the trap, creating gappless superfluid which can rotate non-rigidly and normal fluid which rotates rigidly, surrounding the non-rotating superfluid core respectively. 134

5.5	Schematic diagrams showing the excitation spectrum $E_{\mathbf{k}}(r)$ with $\Omega \neq 0$ for (a) a gapped superfluid at $r = 0$, (b) a gapless superfluid at $r > 0$. The regions with negative quasi-particle energy result in the pair breaking effect.	136
5.6	Critical rotation frequency for the onset of pair breaking as a function of binding energy E_b . Since rotation frequency is limited by the trap frequency, $\Omega \leq \omega$, it follows that pair breaking cannot occur in the trapped gas for $E_b > 2E_F$	138
5.7	Trap profile of an adiabatically rotating interacting Fermi gas with $\Omega > \Omega_c$. We present density, order parameter and mass current density for representative (a) $E_b = 0.1E_F$ ($\Omega_c = 0.2236\omega$), $\Omega = 0.3\omega$ and (b) $E_b = 0.5E_F$ ($\Omega_c = 0.5\omega$), $\Omega = 0.6\omega$. gSF region is very small but still visible between the SF and N phase.	139
5.8	The trap profiles for representative $E_b = 0.5E_F$ and $\Omega = 0.7\omega$. (a) $n(r)$ for $N = 100$, (b) $\Delta(r)$ for $N = 100$, (c) $n(r)$ for $N = 500$, (d) $\Delta(r)$ for $N = 500$. LDA provides reasonable approximation to BdG calculations. Rotation breaks the Cooper pairs and leads to the emergence of a normal phase. As a result of this Friedel oscillations are resurrected at the edge of the trap. This results in a considerable amount of difference between LDA and BdG in the outer regions of the trap for low particle numbers such as $N = 100$. We should note that the sharp decrease in $\Delta(r)$ is not present in BdG where $\Delta(r)$ decreases continuously.	141
6.1	Illustration of negative helicity Fermi surfaces: $(\Omega/\omega, \alpha k_F/E_F) = (0, 0.5)$ in (a), $(0, 2)$ in (b), $(0.8, 0)$ in (c), $(0.35, 1)$ in (d), $(0.35, 1.47)$ in (e), $(0.35, 1.49)$ in (f), respectively. See text for discussion.	144

6.2	Local energy density of states in the trap for increasing values of Ω and α . Within LDA for a gas without SOC (a) ($\Omega = 0, \alpha = 0$) and (b) ($\Omega = 0.4\omega, \alpha = 0$) LDOS displays standard constant behavior for the energy DOS in 2D except the outward extension due to rotation. SOC enhances LDOS for lowest energies as in (c) ($\Omega = 0, \alpha = 3E_F/k_F$). For the most general case (d) ($\Omega = 0.8\omega, \alpha = 3E_F/k_F$), rotation pushes the minimum of LDOS away from the center and removes the divergence for $r \neq 0$ as discussed in the main text in detail.	145
6.3	Non-interacting density profiles in the trap with changing SOC strength α for (a) $\Omega = 0.15\omega$ and (b) $\Omega = 0.5\omega$. The density at representative SOC values from (a) and (b) are plotted in (c) and (d), respectively. The rotating gas takes up a ring-shaped form as α is increased. . . .	149
6.4	Non-interacting density profiles in the trap with changing Ω for (a) $\alpha = 1k_F/E_F$ and (b) $\alpha = 4k_F/E_F$. The density at representative Ω values from (a) and (b) are plotted in (c) and (d), respectively. The SOC gas takes up a ring-shaped form as Ω is increased.	150
6.5	The critical rotation frequency Ω_c^0 for the depletion of the center as a function of SOC strength α , at which the disk shaped density of the non-interacting gas transforms into a ring. An annulus forms at $\Omega < \omega$ for any finite α . The $\alpha \rightarrow 0$ limit of Ω_c^0 gives the trap frequency ω indicating the necessity of SOC for this effect.	150
6.6	Finite temperature non-interacting density profiles for $\Omega > 0$ and $\alpha > 0$. Increasing either Ω or α from (a) ($\Omega = 0.5\omega, \alpha = 1E_F/k_F$), the disk profile transform into a ring for (b) ($\Omega = 0.8\omega, \alpha = 1E_F/k_F$) and (c) ($\Omega = 0.5\omega, \alpha = 3E_F/k_F$), where the depletion of the central density is visible for low T . Increasing either Ω or α further, the effect persists for higher temperatures as in (d) ($\Omega = 0.8\omega, \alpha = 3E_F/k_F$).	152

- 6.7 The polarization in angular direction for $\alpha > 0$ and $\Omega > 0$, increases monotonically starting from zero at the center and becoming unity at the edge. When the gas takes up a ring shape, it becomes almost fully polarized. 152
- 6.8 Exact solutions for the (a)-(c) number density, and (d)-(f) mass-current density are compared with those of semi-classical LDA approach, where $\Omega/\omega = 0.5$ in (a) and (d), 0.68 in (b) and (e), and 0.7 in (c) and (f). We also set $N = 800$ and $\alpha = 1.33E_F/k_F$ in all figures. The overall results are in excellent agreement with each other up to minor deviations due to finite-size effects. 157
- 6.9 Energy levels as a function of angular momentum for a rapidly-rotating Fermi gas with Rashba coupling in the Landau regime when $\Omega = 0.99\omega$. Here, $\alpha = 0$ limit is shown in purple dots for the first three Landau levels as a reference. (a) $\alpha = 0.2\sqrt{\omega/M}$: Rashba coupling splits each of the Landau levels into two helicity branches with a widening energy gap in between as a function of angular momentum. (b) $\alpha = 0.4\sqrt{\omega/M}$: the helicity branches display avoided level crossings. (c) $\alpha = 0.8\sqrt{\omega/M}$: all of the negative-helicity branches not only occupy lowest energies but they also develop minimum at finite angular momentum. All of these couplings are in the perturbative $\alpha \ll 2a_0\omega$ regime. 159

6.10 Radial-density profiles at $T = 0$ in the Landau regime when $\Omega = 0.99\omega$. The (purple) dotted, (green) dashed and solid (blue) lines correspond, respectively, to higher Rashba couplings where $\alpha = 0, 0.2, 0.4\sqrt{\omega/M}$ in (a) with $N = 750$ in the lowest-Landau level, $\alpha = 0, 0.2, 0.4\sqrt{\omega/M}$ in (b) with $N = 900$ in the first two Landau levels, and $\alpha = 0, 0.4, 0.8\sqrt{\omega/M}$ in (c) with $N = 1600$ in the first three Landau levels. These intriguing profiles directly reflect the corresponding energy-level structures shown in Fig. 6.9, where the higher the angular momentum of the single-particle state the further away its localization distance from the trap center. 159

6.11 Typical profiles showing (a) a partially-rotating gSF region, and (b) a vacuum separating the non-rotating SF pairs from the rigidly-rotating N particles. Here, $E_b = 0.1E_F, \alpha = 0.8E_F/k_F$ and $\Omega = 0.3\omega$ in (a), and $E_b = 1E_F, \alpha = 7E_F/k_F$ and $\Omega = 0.5\omega$ in (b), where $n_0 = k_F^2/(2\pi)$ and $J_0 = Mn_0\omega R_F$ 162

6.12 (a) In the absence of rotation the whole gas is superfluid (SF). (b) High enough rotation can through pair breaking induce an intermediate gSF phase separating SF from the normal (N) gas. (c) N phase can appear disconnected from the SF as a ring for higher rotation in the presence of spin-orbit coupling. 163

6.13	<p>The critical rotation frequency for pair breaking and the appearance of a normal phase for (a) different interaction strengths characterized by binding energy E_b as function of SOC strength α and (b) fixed values of α as a function of E_b. The “x” indicate the point beyond which the normal phase emerges disconnected from the superfluid separated by vacuum as the relevant curve is crossed. The details of the structures of the curves are discussed in the text. The phase profiles in the trap along the horizontal (blue) arrows in (a) are shown in Fig. 6.16 as a function of α and the phase profiles along the vertical (red) arrows in (a) are shown in Fig. 6.17 as a function of Ω in horizontal and vertical panels, respectively. Similarly the phase profiles along the horizontal lines in (b) are shown in Fig. 6.18.</p>	164
6.14	<p>Schematic diagrams showing the excitation spectrum of negative helicity particles $E_{\mathbf{k}-}(r)$ with $\Omega \neq 0$ and $\alpha \neq 0$ for (a) a gapped superfluid at $r = 0$, (b) a gapless superfluid at $r > 0$. The regions with negative quasi-particle energy result in the pair breaking effect. Finite α shifts excitation minimum to higher momenta, which can make pair breaking easier.</p>	165
6.15	<p>The rotation frequency Ω_s for complete destruction of the superfluid phase for (a) various interaction strengths characterized by the binding energy E_b as function of SOC strength α and (b) fixed α values as a function of E_b. The horizontal part at $\Omega = \omega$ of each curve indicates the persistence of the superfluid for all rotation frequencies up to a threshold value of α for the corresponding E_b or vice versa. The complete disappearance of SF in 2D requires the simultaneous presence of SOC and rotation and is accompanied by the depletion of the central density. The trap profiles along the dashed arrows are as given in Fig. 6.13.</p>	166

6.16	Radial phase profile in the trap with changing SOC: SF-Superfluid (dark blue), N-Normal phase (green) and V-Vacuum (white). (a) $E_b = 3E_F$ $\Omega = 0.8\omega$, (b) $E_b = 2E_F$ $\Omega = 0.68\omega$, (c) $E_b = 1E_F$ $\Omega = 0.5\omega$. The three panels show the different possibilities of the appearance of the normal phase as a function of the SOC strength α	167
6.17	Radial phase profile in the trap with changing Ω : SF-Superfluid (dark blue), gSF-gapless superfluid (light blue), N-Normal phase (green) and V-Vacuum (white). (a) $E_b = 0.1E_F$, $\alpha = 0.6E_F/k_F$, (b) $E_b = 0.1E_F$, $\alpha = 7E_F/k_F$. The two panels show the different possibilities of the appearance of the normal phase as a function of the rotation frequency Ω	168
6.18	Radial phase profile in the trap with changing interaction: SF-Superfluid (dark blue), gSF-gapless superfluid (light blue), N-Normal phase (green) and V-Vacuum (white). (a) $\alpha = 0.5E_F/k_F$, $\Omega = 0.7\omega$, (b) $\alpha = 2E_F/k_F$, $\Omega = 0.7\omega$, (c) $\alpha = 4E_F/k_F$, $\Omega = 0.6\omega$. The three panels show the different possibilities of the appearance of the SF phase as a function of the interaction strength E_b	169
6.19	(a) Radial phase profile in the trap as a function of SOC for weak interaction $E_b = 0.1E_F$ and rotation $\Omega = 0.3\omega$: SF-Superfluid (dark blue), gSF-gapless superfluid (light blue), N-Normal phase (green) and V-Vacuum (white). The interplay of SOC and rotation effects may allow for an increased gSF region. (b) Sample gSF trap profile along the dashed (red) arrow in (a) showing the order parameter and current comparing LDA (dot-dashed) and BdG (solid lines) with $N = 500$ results for $\alpha = 0.8E_F/k_F$	172
6.20	The trap profiles for representative $E_b = 2E_F$, $\alpha = 2E_F/k_F$ and $\Omega = 0.7\omega$ for $N = 100$. (a) $\Delta(r)$, (b) $n(r)$. LDA is in very good agreement with BdG calculations even for $N = 100$. Cut-off used in BdG calculation is $E_c \sim 60E_F$	176

NOMENCLATURE

1D	One Dimensional
2D	Two Dimensional
3D	Three Dimensional
BCS	Bardeen-Cooper-Schrieffer
BEC	Bose-Einstein Condensate
DOS	Density of States
ERD	Equal Rashba-Dresselhaus
gSF	Gapless Superfluid
LDA	Local Density Approximation
LDOS	Local Density of States
N	Normal Gas
NIST	National Institute of Standards and Technology
QM	Quantum Mechanical
SF	Superfluid
SOC	Spin-Orbit Coupling

Chapter 1

INTRODUCTION

Ultracold atoms are atoms which are maintained in ultra cold temperatures, very close to absolute zero, typically on the order of hundred nanokelvins. They are very important because they can be used as a quantum simulators of condensed-matter systems which are complicated and therefore difficult to understand theoretically. Let us take high temperature superconductivity as an example. Electrons in a metal have very complicated behavior, they interact with each other, with the lattice vibrations, with the impurities, they may be constrained to move in quasi-2D planes etc. It is clear that such a complicated system can not be solved exactly to deduce its properties analytically. Therefore theorists need to develop simplified model Hamiltonians which can capture the physics of the high temperature superconductivity and do further approximations to solve these model Hamiltonians. In building these models we have to decide which aspects of the complicated system we are going to avoid and which ones we will include in our model? This is a very difficult question. Suppose we developed a model and solve it using relevant approximations and the solution does not describe the features of the system which we want to explain. Should we assume that model is faulty and search for some additional features? Which aspects of the model we should retain and which ones we should change? Or should we assume that the approximations are invalid and stick to our model searching for different approximation schemes? These questions may seem to be unanswerable at first glance, but this is the place where ultra-cold atoms come into the scene. Their high purity as well as their controllable system parameters, such as inter-particle interaction strength, dimensionality, geometry, the spin-imbalance etc. make them promising candidate to

create an idealized system whose Hamiltonian is exactly known [Bloch et al., 2008]. Therefore using cold atoms we can create our models in reality and check directly whether they capture the desired properties of real systems. For example using cold atoms we can realize Hubbard model [Greiner et al., 2002], which is one of the main tools used to understand high-temperature super-conductivity, and check its explanatory power. Since cold atoms can be used to create, and experimentally probe these ideal Hamiltonians, as well as tune their parameters they also provide test ground for validity regime of the approximation schemes. The complications such as lattice (created using lasers), impurity etc., can be added back to the system, making it possible to study all the physical components of the condensed matter individually. With this extraordinary ability of ultracold atoms we seem to have come very close to realize the dream of Richard Feynman, a quantum simulator which can simulate very complicated many body systems [Feynman, 1982, Feynman, 1986].

The first success of ultracold atoms community which lead to the rapid expansion of the field was the first creation of a Bose-Einstein condensate (BEC) in 1995 [Anderson et al., 1995]. BEC was first predicted by Satyendra Bose and Albert Einstein in 1924 [Bose, 1924, Einstein, 1925]. BEC is a state of matter composed of a gas of bosons cooled to low temperatures, where a macroscopic fraction of them occupy the lowest energy state, effectively creating a macro quantum system. After four years from the creation of BEC, the first degenerate Fermi gas was created [DeMarco, 1999]. Due to Pauli exclusion principle, two fermions can not occupy the same quantum state, therefore fermions do not undergo BEC and there is no phase transition for non-interacting Fermi gas when it is cooled. Rather at zero temperature all fermions are forced to occupy all the lowest energy states, one fermion per state. In Fig. 1.1 we sketch the zero temperature behavior of bosons and fermions. In Ch. 2, we define ultracold quantum gas and review the basic tools of statistical quantum mechanics which we will use to analyze ultracold Fermi gases. We analyze both uniform and trapped non-interacting Fermi gases in two and three dimensions. We discuss the experimental techniques used in cooling and trapping the atoms.

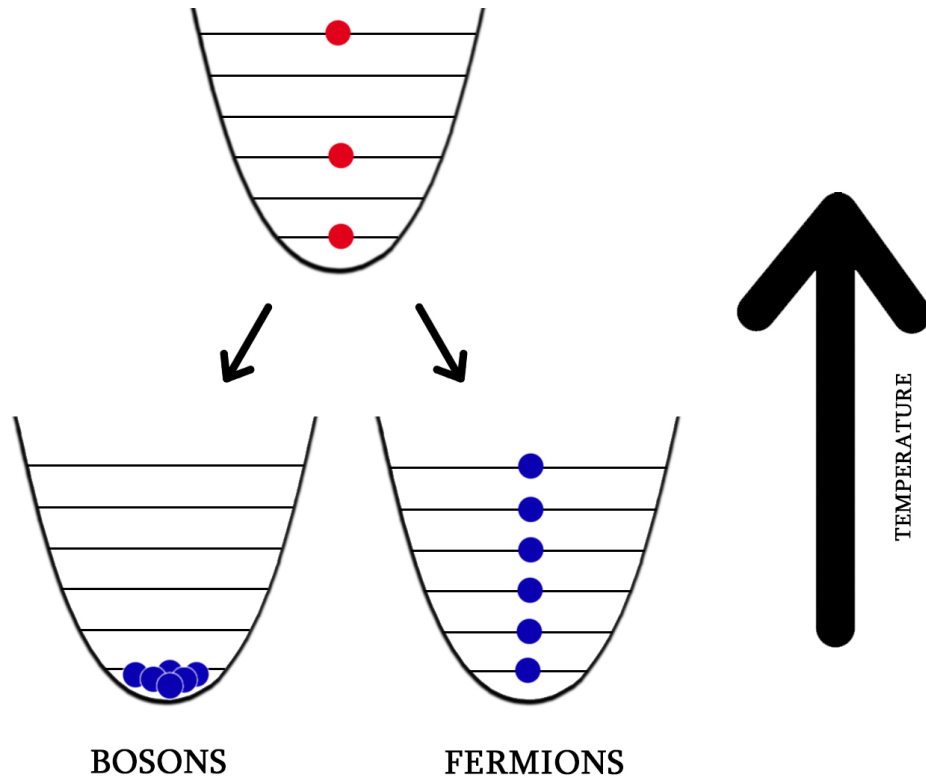


Figure 1.1: Bosons vs. fermions at zero temperature. Bosons and fermions behave similarly at high temperatures, where in each quantum state there is very small probability of occupancy, and particle statistics shows the behavior of distinguishable particles. When temperature is lowered degenerate bosons and fermions behave differently. Bosons condense to the lowest energy state, and form the Bose-Einstein condensate. Fermions due to Pauli exclusion principle can not occupy the same quantum state, rather they occupy the lowest states with one Fermion per quantum state forming a Fermi sea.

One may think that Fermi gases are not very interesting since they do not undergo phase transition. However if there is a strong attraction between the Fermions it is possible to create bound molecules, which are bosonic and therefore can undergo BEC. On the other hand if atoms interact weakly they form pairs analogous to Cooper pairs of electrons in superconductors. This is known as a Bardeen-Cooper-Schrieffer (BCS) state. BCS theory was developed in 1957 to explain superconductivity via formation, of Cooper pair of electrons, which are formed due to effective attractive interaction resulting from phonon-electron coupling [Bardeen et al., 1957]. In 1998, it was demonstrated that it is possible to arbitrarily tune the two-particle interaction via Feshbach mechanism [Inouye et al., 1998]. This lead to experimental realization of BEC of molecules formed from two fermionic atoms [Greiner et al., 2003, Jochim et al., 2003, Zwierlein et al., 2003]. Later, BCS state was realized and by tuning the interaction, the system is made to smoothly evolve from BCS to BEC state [Regal et al., 2004]. This was the first experimental realization of BCS-BEC crossover(see Fig. 1.1) predicted first by Eagles [Eagles, 1969] and Leggett [Leggett, 1980]. Analogous to superconductivity, attractively interacting Fermi gas at low temperatures undergoes phase transition to the superfluid state. Superfluidity is a state of matter which behaves like a fluid with zero viscosity. In Ch. 3 we discuss the scattering and interaction in ultracold Fermi gases in both 2D and 3D. We review the BCS-BEC crossover problem in different dimensions and provide its extension for trapped Fermi gases both using semi-classical local density approximation and quantum mechanical Bogoliubov de Gennes approach. We conclude the chapter with definition of superfluidity.

BCS-BEC crossover is just one example of the many realized/realizable many body phenomena using ultracold atoms. Since cold atoms are charge neutral particles one may think that many exotic phenomena which involve interaction with electric or magnetic fields, such as integer and fractional quantum Hall effects, quantum spin Hall effect, and a topological insulators, cannot be simulated by cold atoms. However, while it is true that cold atoms can not experience gauge fields, such as magnetic field, nevertheless it is possible to simulate the gauge fields artificially.

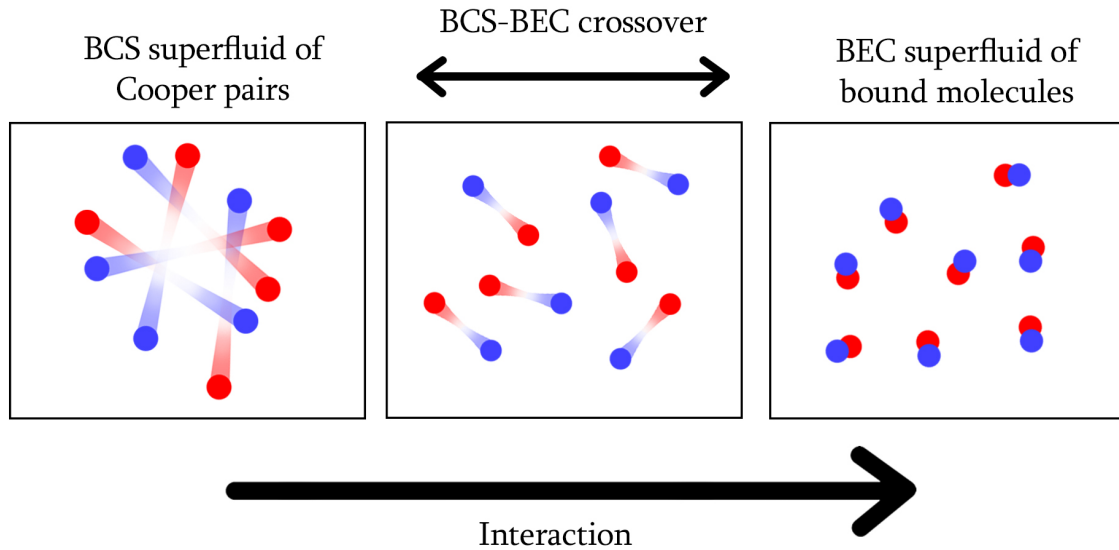


Figure 1.2: The BCS-BEC crossover. In cold atoms by tuning the interactions via Feshbach resonance it is possible to smoothly cross from BCS limit of Cooper pairs overlapping in space to BEC limit of tightly bound molecules.

One way to achieve this is to rotate the gas rapidly, and use the analogy between the magnetic component of the Lorentz force and the Coriolis force [Fetter, 2009]. Rapid rotation mimics the constant magnetic field and may lead to formation of Landau levels and integer quantum Hall phenomenon [Ho and Ciobanu, 2000], or it may lead to quantized vortices [Abo-Shaer et al., 2001, Zwierlein et al., 2005] which are analogous to Abrikosov vortices in superconductors as a result of applied magnetic field [Abrikosov, 1957]. Observation of quantized vortices in ultracold atoms is the smoking gun proof of superfluidity.

Another method to create artificial gauge fields, which can create more complicated fields than constant magnetic field is to use position dependent atom laser beam interaction to create a Berry connection. Using this approach in 2009, Spielman's group created the first synthetic field in bosonic cold atoms [Lin et al., 2009b]. It was a uniform vector potential, therefore corresponded to zero magnetic field. Same

year they realized first synthetic magnetic field in cold atoms [Lin et al., 2009a]. After two years first synthetic electric field was also artificiality created [Lin et al., 2011a]. In 2011 this series of experiments of Spielman's group culminated with the creation of first artificial spin-orbit coupling in bosonic atoms [Lin et al., 2011b]. Spin-orbit coupling (SOC) is the interaction between particle's spin and momentum. In cold atoms, the role of spin is played by the hyperfine state of the atom. Spin-orbit coupling has become one of the key themes in modern condensed-matter and atomic physics, playing a central role for systems such as topological insulators and superconductors [Hasan and Kane, 2010, Qi and Zhang, 2011], quantum spin-Hall systems [Sinova et al., 2015] and spintronics applications [Žutić and Das Sarma, 2004]. In 2012 two groups realized spin-orbit coupling in fermionic atoms [Wang et al., 2012, Cheuk et al., 2012]. These all were one dimensional couplings, coupling only certain direction in momentum space. In 2016 first 2D SOC was realized in fermionic atoms [Huang et al., 2016], extending the stage to investigate more interesting SOC types such as Rashba SOC which is isotropic in momentum space. Experimental realization of SOC stimulated numerous theoretical studies on Fermi gases with SOC both in 3D [Vysanakere et al., 2011], [Jiang et al., 2011], [Yu and Zhai, 2011], [Gong et al., 2012], [Iskin and Subasi, 2011], [Yi and Guo, 2011], [Seo et al., 2012], [Zhou and Zhang, 2012], [Liao et al., 2012] as well as in 2D [He and Huang, 2012], [Gong et al., 2012], [Yang and Wan, 2012], [Takei et al., 2012], [Ambrosetti et al., 2014], [Zhang and Yi, 2013], [Doko et al., 2012], [Cao et al., 2014]. These works have revealed a plethora of intriguing phenomena, including topological superfluids, Majorana modes, spin textures, skyrmions, etc.

In Ch. 4 we discuss the origin of spin-orbit coupling as well as physical systems in which it occurs naturally. Then we discuss the basic principles used to engineer spin-orbit coupling in neutral atomic gases. Next we review single particle properties of the Rashba SOC. We discuss non-interacting Fermi gas under SOC and the mean-field BCS theory for 2D gas with SOC. In Ch. 5 we review the motion in rotating frame and explain the analogy between the Coriolis force and the magnetic compo-

ment of the Lorentz force. We discuss the effect of the rotation on non-interacting Fermi gas, including the fast rotation limit where the Landau level structure becomes evident. We then analyze the effect of rotation on interacting Fermi gas, i.e. on the superfluid state. We consider the alternative responses of the superfluid to rotation: Quenching of the moment of inertia for slow rotation, vortex formation for fast rotation and pair-breaking due to Coriolis force which leads to emergence of normal gas together with gapless superfluid at the edge of the system for adiabatic rotation. In Ch. 6 we study the combined effect of SOC and rotation on trapped 2D Fermi gas. We investigate the trap profiles when both SOC and rotation is applied to non-interacting and interacting Fermi gas, respectively. In both cases we investigate the possible phases of the system with emphasis on the formation of a ring shaped normal component. We provide numerical calculations of the critical rotation frequency for the onset of pair breaking and complete destruction of the superfluidity as well as present extensive phase diagrams demonstrating all the possible phase profiles. We conclude with a discussion of our results in Ch. 7.

Chapter 2

FUNDAMENTALS OF ULTRACOLD FERMI GASES

2.1 What is an Ultracold Quantum Gas?

We can think of a gas as N number of atoms moving around in some volume V . There are three characteristic length scales of the gas which determine its properties (see Fig. 2.1). The first important length scale is the average inter-particle distance d_n , which is determined by the density of the gas $n = N/V$ as

$$d_n = n^{-1/3}. \quad (2.1)$$

This relation can be obtained by dividing the volume V , to small cubic regions with volume d_n^3 , such that every region has single atom. Then obviously d_n is the average distance between the atoms and total number of particles can be written as $N = V/d_n^3$, which yields the above relation.

The second important length scale is determined by the temperature T and is known as the thermal de Broglie wavelength of the atoms λ_T . The thermal de-Broglie wavelength is given as (in this thesis we take $\hbar = 1$):

$$\lambda_T = \sqrt{\frac{2\pi}{MTk_B}} \quad (2.2)$$

where M denotes the mass of an atom and k_B is the Boltzman's constant. The de-Broglie wavelength can be thought as the length scale associated with thermal kinetic energy of the atoms. We can rewrite above equation as a equality between the thermal energy to kinetic energy up to a factor of π , i.e. $\pi k_B T = k^2/(2M)$, where we related the momentum to the wavelength λ via the de-Broglie relation $k = 1/(2\pi\lambda)$.

In classical physics each atom's motion is described by its position \mathbf{r}_i and momentum \mathbf{k}_i , where $i \in \{1, 2, \dots, N\}$ is the index for an atom. In any realistic gas,

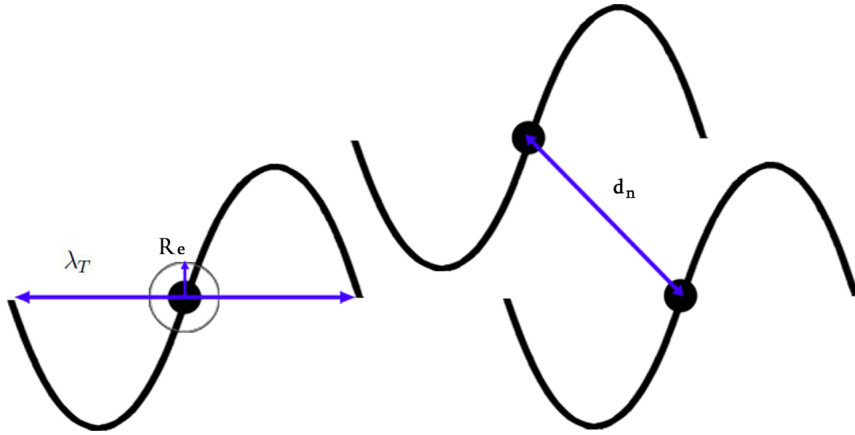


Figure 2.1: Length scales of a thermal quantum gas. The de-Broglie wavelength λ_T should be greater or comparable to inter-particle spacing d_n for an ultracold gas. Both d_n and λ_T are much greater than the effective range of the interaction R_e . See text for details.

atoms interact with each other via an inter-atomic potential $U(\mathbf{r}_i - \mathbf{r}_j)$. For charge neutral atoms, which we consider in this thesis, this interaction is isotropic, i.e. the potential has central symmetry. A central symmetric potential is a potential which does not depend on the orientation of the atoms, but only on their relative distance $r_{ij} = |\mathbf{r}_i - \mathbf{r}_j|$, hence inter-atomic potential can be written as $U(r_{ij})$. Besides being isotropic, the interaction potential of the neutral atoms is short-ranged. By short-ranged we mean that there is some distance R_e beyond which the effect of the interaction is negligible. R_e is known as the range of the potential or the radius of interaction and it is the third important length scale which characterizes the gas [Ueda, 2010]. In order to estimate R_e and justify the claim that inter-atomic potential has central symmetry let us analyze the origin and behavior of inter-atomic interaction. When the inter-particle distance between the atoms is on the order of the radius of the atom, they will feel a strong repulsive interaction due to the Pauli principle which forbids electron clouds to overlap with each other. This force is usually modeled as hard core sphere potential with atomic radius or as a Leonard-Jones potential term with

$U(r_{ij}) = C_1/r_{ij}^{12}$, where $C_1 > 0$ is constant. This potential has obviously central symmetry and is short ranged, with range on the order of the atomic radius. At greater distances the force between the atoms is attractive. This force is known as the van der Waals force whose origin is mutual polarization of the atoms. A neutral atom in position \mathbf{r}_i gains an instantaneous dipole moment \mathbf{P}_1 , which points in a random direction and therefore in average is zero ($\langle \mathbf{P}_1 \rangle = 0$). This dipole moment will induce another dipole moment \mathbf{P}_2 in another atom at \mathbf{r}_2 , which will be $\mathbf{P}_2 = \alpha_p \mathbf{E} \propto -\alpha_p \mathbf{P}_1 / r_{12}^3$, where \mathbf{E} is electric field and α_p is atomic polarizability. The two dipole moments will interact via $U(r_{12}) \propto \mathbf{P}_1 \mathbf{P}_2 / r_{12}^3 \propto -\alpha_p \mathbf{P}_1^2 / r_{12}^6$. We should note that $\langle \mathbf{P}_1^2 \rangle \neq 0$, therefore there is effective attractive force between the atoms with potential $-C_2 / r_{12}^6$, where $C_2 > 0$ is constant. This potential has central symmetry and is short ranged. The range can be estimated from the fact that we are interested in low temperature behavior of the gas, where the total energy is almost zero. As a result of this the effective range can be estimated by taking the momentum $k = 1/R_e$ and reduced mass $M/2$ we have $1/(MR_e^2) - C_2/R_e^6 \Rightarrow R_e = (C_2 M)^{1/4}$. Sketch of typical interaction potential is given in Fig. 2.2.

Given these three characteristic length scales, d_n , λ_T and R_e , we are ready to define the dilute ultracold quantum gas. A gas is called dilute if the interaction radius is much smaller than the inter-particle distance:

$$d_n \gg R_e \Rightarrow nR_e^3 \ll 1 \quad (2.3)$$

On the other hand if $d_n \leq R_e$, than the motion of the atoms is not free anymore and we usually have either solid or liquid. In dilute gases since inter-particle distance is much greater than radius of the interaction, the probability of finding three particles inside this radius is much smaller than the probability of finding two particles inside that distance. Therefore interaction of the gas is governed by binary interactions, i.e. interaction between two particles. Absence of three body collisions is very important for the stability of the gas. We will study gas at very low temperatures at which normally matter is at solid phase. At such low temperatures gas is meta-stable and

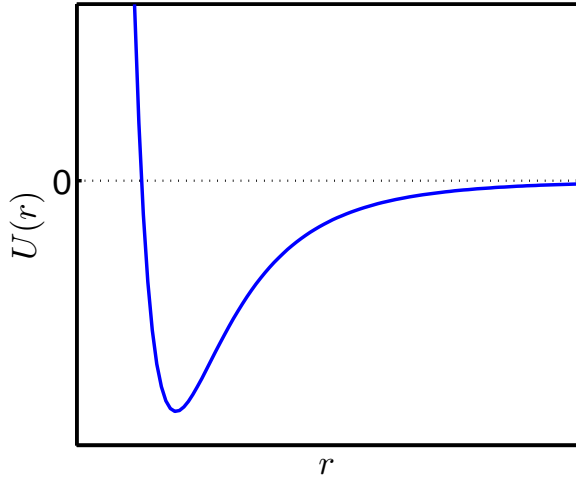


Figure 2.2: Sketch of typical interaction between two neutral atoms as modeled with Lennard-Jones type potential ($C_1/r^{12} - C_2/r^6$). We clearly see that at long distances van der Waals attraction takes over the repulsive potential due to Fermi exclusion. At even larger distance which we defined as R_e interaction is very weak and can be safely ignored.

can live long enough thanks to the low probability of three body collisions. Law of conservation of energy and momentum forbids formation of bound molecules in two body collisions, a third particle which will carry excess momentum must be present. Therefore dilute gas can remain gas even at very low temperatures long enough to be studied experimentally on the order of 1-10 seconds.

A gas is called ultracold if the thermal de Broglie wavelength is much bigger than the radius of the interaction:

$$\lambda_T \gg R_e \quad (2.4)$$

In ultracold gases s-wave collisions (collisions with zero angular momentum) are the dominant type of collisions as we will demonstrate in next section. The first ultracold dilute gas was produced by I.F.Silvera and J.T.M. Walraven in 1980, using spin-polarized Hydrogen [Silvera and Walraven, 1980].

A gas is called quantum gas if it obeys the quantum statistics when it becomes degenerate. This happens when the particle indistinguishability becomes important,

and therefore thermal de Broglie wavelength is on the order of the interparticle distance:

$$\lambda_T \geq d_n \Rightarrow n\lambda_T^3 \geq 1. \quad (2.5)$$

Above $n\lambda_T^3$ is known as phase-space density and it determines the character of the gas. If it is very small compared to unity, the gas is classical and can be understood via Boltzman statistics. On the other hand when it approaches unity, than the quantum statistics becomes important. The temperature T for which phase space density approaches unity $n\lambda_T^3 \sim 1$ is known as degeneracy temperature T_d . Degeneracy temperature is given as:

$$T_d \sim \frac{2\pi n^{2/3}}{k_B M} \quad (2.6)$$

From this expression we see that there are two ways to arrive at the quantum degeneracy, either density can be increased, or temperature can be decreased.

In any real experiment gas has to be confined. If the gas is confined in a vessel such that its density is constant, it is called homogeneous gas. Usually vessel's surface will greatly effect the properties of the gas, rendering theoretical analysis difficult. Fortunately this can be overcome in the experiments, where gas can be trapped in wall-free environment using some external potential $V(\mathbf{r})$. This potential in experiments is usually created using laser beams. This kind of gas trapped in potential is known as an inhomogeneous gas. Since experiments are done using an inhomogeneous gas, in this thesis we will be mostly interested in the inhomogeneous gas. Usually this trapping potential can be approximated with a harmonic potential. The presence of the trap introduces us another characteristic length scale known as the characteristic length of the harmonic oscillator which we will denote with a_0 and define as

$$a_0 = \sqrt{\frac{1}{M\omega}}. \quad (2.7)$$

Here ω is the frequency of the trap, such that $V(\mathbf{r}) = (\omega/2)(r/a_0)^2$ and we assume that the trap is isotropic. In experiments, a_0 is much larger than the other characteristic lengths in the problem. In such systems we can use the so called local

density approximation, where in some small sub region in the trap we can assume that system is homogeneous and use the results derived for a homogeneous system. We will frequently make use of this local density approximation. To demonstrate the validity of this approximation let us take the density of the gas at point \mathbf{r}_1 and \mathbf{r}_2 to be $n(\mathbf{r}_1)$ and $n(\mathbf{r}_2)$ respectively. Then the density difference can be expressed as $n(\mathbf{r}_1) - n(\mathbf{r}_2) \approx n(\mathbf{r}_1) - n(\mathbf{r}_1)[1 - O(|\mathbf{r}_2 - \mathbf{r}_1|/a_0)]$, where $O(x)$ means on the order of x . Note that as long as the two points \mathbf{r}_1 and \mathbf{r}_2 are close with respect to a_0 so that $a_0 \gg |\mathbf{r}_2 - \mathbf{r}_1|$ and the density between these two points is approximately constant, it can be described by the physics of homogeneous system.

First ultra-cold quantum gas was created on 5 June 1995 by JILA group of Eric Cornell and Carl Wieman using Rubidium-87 atoms which were cooled to 170 nK [Anderson et al., 1995]. About one month later Rice university group of Randall Hulet realized ultra-cold quantum gas using Lithium atoms (but published their results after two years) [Bradley et al., 1997]. Few months latter, MIT group of Wolfgang Ketterle also created ultra-cold quantum gas using Sodium-23 [Davis et al., 1995]. All three experiments used bosonic atoms. Ketterle, Cornell and Wieman were awarded with the Nobel prize in physics in 2001 for their achievements.

Before concluding this section, let us provide some rough numbers for the length scales given above. We will provide the estimates based in terms of the Bohr radius $a_B \approx 0.53 \times 10^{-10}m$. The smallest length scale R_e ranges between $50a_B - 200a_B$. The ranges for λ_T and d_n are $10^4a_B - 4 \times 10^4a_B$ and $800a_B - 3000a_B$ respectively, hence they are much larger than R_e and roughly at the same order. The largest length scale is a_0 which takes value between $3 \times 10^3a_B - 3 \times 10^5a_B$. These numerical values are taken from [Boettcher et al., 2012].

2.2 Quantum Statistics

One special characteristic of quantum mechanics is the indistinguishability of identical particles. If we interchange coordinates of two identical particles, the system should remain unchanged. Physically this means that many-body wave function Ψ of the

system can change only by some global phase factor λ when these two particles are interchanged:

$$\Psi(\dots, \chi_i, \dots, \chi_j, \dots) = \lambda \Psi(\dots, \chi_j, \dots, \chi_i, \dots) \quad (2.8)$$

Here $\chi_i = (\mathbf{r}_i, \sigma_i)$ denotes the position and spin of the i 'th particle respectively. Since two consecutive interchanges of the same coordinates will leave system identical, we have either $\lambda = 1$ (wavefunction is symmetric under exchange of particles) or $\lambda = -1$ (wavefunction is anti-symmetric under exchange of particles). Particles which have symmetric wave function under exchange of particles are called bosons and particles which have anti-symmetric wave function are called fermions. Fierz-Pauli Spin-Statistics theorem [Fierz, 1939, Pauli, 1940] states that particles with integer spin are bosons, whereas particles with half-integer spin are fermions. One very important consequence of Spin-Statistics theorem is that no two identical fermions can occupy the same quantum state. This is known as the Pauli exclusion principle and is responsible for the stability of matter. All the stable elementary particles such as electrons, protons, neutrons are fermions, while force carrier particles such as photons are bosons. Besides elementary particles, composite particles such as atoms can also be classified as bosons or fermions depending on the total number of fermions contained in them. If the total number of constituent fermionic particles is even the atom is a composite boson. On the other hand if the total number of constituent protons, electrons and neutrons is odd it is a composite fermion. Since in neutral atoms number protons is equal to number of electrons, atoms with odd neutrons are fermions and atoms with even number of neutrons are bosons.

In order to describe a large system with many particles and quantum states, the grand canonical ensemble can be used. In this ensemble, the system can exchange particles and energy with a large reservoir. The thermodynamic variables of the grand canonical ensemble are absolute temperature T and chemical potential μ , which is defined as change in total energy E when another particle is added to N particles at constant volume V and entropy S

$$\mu = \left(\frac{\partial E}{\partial N} \right)_{V,S}. \quad (2.9)$$

Using the grand canonical partition function, one can derive the distribution function for an average occupation of a single particle quantum state j with energy ϵ_j

$$\langle n_j \rangle = f(\epsilon_j) = \frac{1}{e^{\beta(\epsilon_j - \mu)} \pm 1} \quad (2.10)$$

where $\beta = 1/(k_B T)$. The sign in the denominator depends on the quantum statistics of the particles. If the particles are bosons than the minus sign is used and the distribution is known as the Bose-Einstein distribution, on the other hand if the particles are fermions than the plus sign is used and the distribution is known as the Fermi-Dirac distribution. In that case the function $f(\epsilon_j)$ is known as the Fermi function. When we have high temperatures such that phase-space density defined in previous section is very small compared to unity, than both distributions reduce to

$$f(\epsilon_j) = e^{-\beta(\epsilon_j - \mu)}, \quad (2.11)$$

which is known as the Boltzmann distribution. Hence, as discussed in the previous section the effects of quantum statistics become unimportant at high temperatures. Using the distribution function we can in principle calculate the mean energy E

$$E = \sum_j \epsilon_j f(\epsilon_j) \quad (2.12)$$

and the mean particle number N

$$N = \sum_j f(\epsilon_j). \quad (2.13)$$

The last equation can be used to determine chemical potential μ for given particle number N .

2.3 Trapping and Cooling Atoms

In this section we will outline basic procedures used in creating ultracold quantum gases and sketch the basics of cooling and trapping techniques of atoms. For more systematic treatment the reader can consult [Pethick and Smith, 2008] and [Jervis and Thywissen, 2014].

The most basic method used in cooling atoms is the so called laser cooling. We tend to think that lasers heat the system, but combined with proper physical principles they can be used in cooling an atomic gas (see Fig. 2.3). To understand how cooling can be achieved let us consider a two level atom with ground state $|g\rangle$ and excited state $|e\rangle$ with energies E_g and E_e , respectively. In order to excite the electron to excited state $\Delta E = E_e - E_g$ energy must be supplied. If the electron is hit by a photon with frequency $\nu_0 = \Delta E/h$, where h is the Planck's constant, than electron is excited to the excited state, while photon is absorbed by the atom. Due to conservation of momentum, atom will receive a kick in the direction of motion of the photon, gaining momentum equal to $h\nu_0/c$, where c denotes the speed of light. As the atom returns to the ground state, by spontaneous emission it emits photon and gets another momentum kick, which is in the opposite direction of the emitted photon. Since spontaneous emission is a random process, its direction will be arbitrary and if averaged over many absorption/emission cycles net momentum transfer due to emission will be zero. Hence the net momentum gain of the atom on average will be exclusively due to absorption. If we want to cool the atom, we must always transfer momentum in the opposite direction to atom's motion, so that it slows down and the gas cools. This can be achieved by tuning lasers to frequencies lower than the resonant frequency, $\nu_1 < \nu_0$. If an atom is moving towards the laser beam with some velocity v , than due to Doppler effect the frequency of the laser is blue shifted in the reference frame of the atom. The frequency ν_2 of the laser from the perspective of the atom can be calculated via the Doppler shift formula

$$\nu_2 = \nu_1 \sqrt{\frac{1 + (v/c)}{1 - (v/c)}} \approx \nu_1 \left(1 + \frac{v}{c}\right) \quad (2.14)$$

If we look at the problem from the laser's frame, than the absorption spectrum of the atom is red shifted and best absorption frequency now is $\nu'_0 = \nu_0(1 - v/c)$. If velocity has right value, which can be calculated as $v = c(\nu_0 - \nu_1)/\nu_0$, than the laser's frequency will match that of the atom's best absorption frequency. Therefore, the atom will receive a momentum kick in opposite direction of its motion and its new velocity v' will be lower. The new velocity can be shown via conservation laws to satisfy the following relation

$$v' = v - \frac{\Delta E}{Mc} \quad (2.15)$$

where M denotes the mass of the atom. On the other hand, if the atom is moving in the opposite direction of the laser beam, absorption spectrum of the atom will be blue-shifted and therefore will not absorb the photon. If we put six laser, one in each direction in 3D space, than no matter in which direction an atom is moving, it will slow down. Of course to slow particles in all velocities, the laser frequencies should be slowly tuned, so that all atoms will interact with the laser beams.

In order to hold the atoms, a trap from magnetic field can be created. These traps are known as magneto-optical traps. In order to understand the working principle of these traps let us assume that we have atoms having total angular momentum $F = 0$ in the ground state and $F = 1$ in their excited state. The excited state will be three-fold degenerate, due to three possible z -components $m_F = \{-1, 0, 1\}$ of the total angular momentum. These three states are degenerate at zero magnetic field, but when magnetic field is turned on it leads to the so called Zeeman splitting. Suppose we place these atoms in a non-uniform magnetic field whose value is lowest at the center and highest at the edges. Besides the sign of the magnetic field is opposite at the opposite edges. As a result of this configuration $|F = 1, m_F = 1\rangle$ state will have highest energy at one side (say right) and $|F = 1, m_F = -1\rangle$ at the other side (say

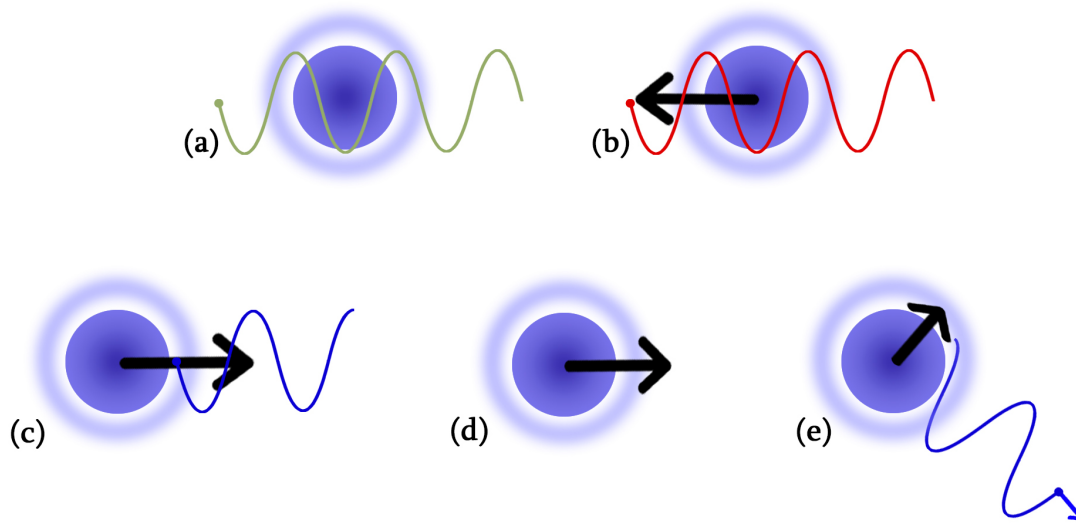


Figure 2.3: Sketch of mechanisms involved in laser cooling. (a) Assume laser is tuned in frequency ν_1 below the resonant frequency ν_0 of the atom, i.e. $\nu_1 < \nu_0$ as a result atom does not absorb the photon. (b) If the atom is moving away from the laser, due to Doppler shift light is red-shifted, and again atom does not absorb any photon. (c) If the atom is moving towards the laser, this time frequency is blue-shifted, it can now match the resonant frequency, thus atom absorbs the photon. (d) Since atom absorbs photon moving in opposite direction of its motion, due to the conservation of momentum it receives a momentum kick in that direction and its velocity decreases. (e) Absorbed photon will be emitted in random direction and if averaged over many absorption/emission cycles net momentum transfer due to emission will be zero. As a result in average only absorption will effect the velocity of the atoms. Atoms will lose velocity and as a result the gas will cool.

left). Suppose we have lasers in both sides, shining with same frequency ν ($\nu < \nu_0$ as described above so that they can cool the atom) but opposite circular polarizations (σ_+ and σ_-). The laser with σ_+ polarization is placed in left side, and the other one in the right side of the trap. σ_+ polarized light will interact with $|F = 0, m_F = 0\rangle$ state to excite it only to $|F = 1, m_F = 1\rangle$ state, while σ_- polarized light will interact with $|F = 0, m_F = 0\rangle$ state to excite it only to $|F = 1, m_F = -1\rangle$ state. Therefore due to the Doppler effect described above, atom moving in the left direction will absorb photon and transfer to $|F = 1, m_F = 1\rangle$ state. The atom not only will get momentum kick in opposite direction, but it will also feel restoring force towards the center of the trap because in left side of the set up energy of $|F = 1, m_F = 1\rangle$ state is highest due to the magnetic field. This analysis is also valid for particle moving in the right direction as well. If this setup is mounted in all the three spatial axis, than atoms will be trapped in the middle of the trap.

While laser cooling is a very effective way to cool the atoms, the temperatures which can be reached are limited. As we pointed above spontaneous emission of the photon is a random process and the momentum kicks average to zero, thus mean velocity of the particle due to emission is zero. But unfortunately the mean squared velocity of atoms due to spontaneous emission is not zero and as a result heat is supplied to the atom. At equilibrium, the heating and cooling rates become equal, setting limit on the temperature to which gas can be cooled known as Doppler limit of the temperature. Doppler limit of the temperature can be estimated via the following expression

$$T_{\text{Doppler}} = \frac{\gamma}{2k_B} \quad (2.16)$$

where γ is the the absorption line-width. Doppler limit of the temperature is on the order $100 \mu K$, which is several order of magnitudes higher than T_d of the atoms. Using another laser cooling technique called Sisyphus cooling, atoms can be cooled down to $10 \mu K$, but this is also far too "hot" to observe the effects of quantum statistics in such dilute system. Fortunately there is another technique called evaporative cooling,

which can cool atoms to temperature of 500 pK . First atoms are taken to some conservative trap such as a static magnetic trap, so that atoms will not heat due to spontaneous emission. Static magnetic traps are composed of magnetic field which has minimum at the center of the trap. In order to be trapped in this trap, atoms must have magnetic moment which points in opposite direction to the magnetic field. These states are known as weak field seeking states. These states, in order to minimize their energy move to low magnetic field, hence are trapped at the center where magnetic field is minimum. Once atoms are trapped in static magnetic field, then the depth of the trapping potential is lowered so that high energetic hot atoms can escape from the trap (See Fig. 2.4). This selective removal of hot atoms, causes the remaining atoms to cool due to collisional equilibrium. This kind of cooling is very familiar from our everyday life. For example, take a cup of tea, the most energetic molecules leave the cup via evaporation. Since average kinetic energy of the molecules leaving the cup is higher than the mean kinetic energy of the tea, effectively temperature of the tea falls. Evaporative cooling of atoms, essentially uses the same mechanism which cools our tea.

The success of evaporative cooling depends on gas reaching the collisional equilibrium. In such low temperatures atoms in ultracold gas can only collide if they approach head on, i.e. they have no relative angular momentum, in the so called s-wave collisions. But as we will show in next chapter, identical fermions do not undergo s-wave collisions due to Pauli exclusion principle. This lack of collisions, makes use of evaporative cooling for a gas composed of identical fermions impossible. Fortunately, fermionic atoms that are in different internal states can collide through s-wave collision and therefore can be cooled via evaporative cooling. First degenerate ultracold Fermi gas using this method of cooling was realized in 1999 by Jin and DeMarco at JILA [DeMarco, 1999]. We should note that even if we have two species Fermi gas, cooling fermions is still a challenge because when a gas becomes sufficiently degenerate collisions are blocked because the number of unoccupied quantum states available diminishes. Since this blocking again is a result of Pauli exclusion

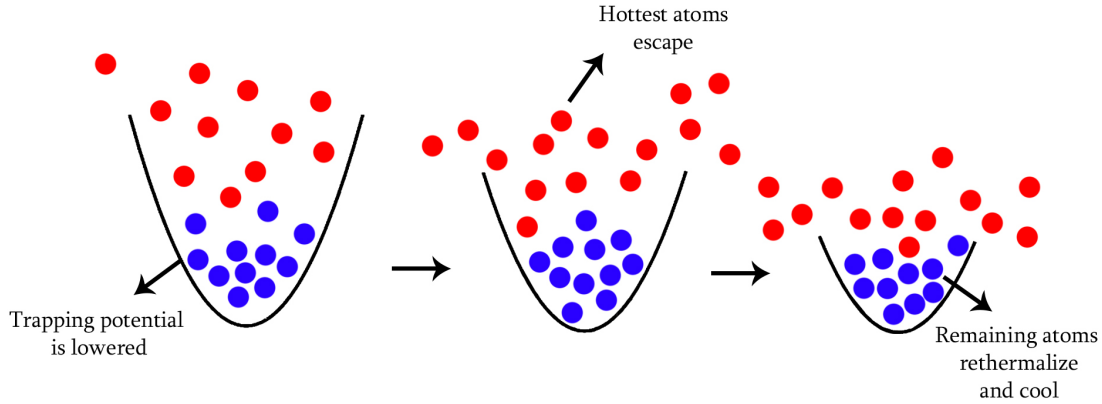


Figure 2.4: Schematic diagram of evaporative cooling. Trap potential is lowered so that atoms with high kinetic energy can escape the trap. Selective removal of hot atoms causes the remaining atoms to cool due to collisional equilibrium.

principle, it is termed as Pauli blocking. Alternatively one can cool fermions with a method known as a sympathetic cooling. In this method, mixture of different isotopes of same element, one bosonic and one fermionic are cooled together. Bosons are cooled via evaporative cooling in the usual way, while fermions cool by being in thermal contact with fermions. This is similar to cooling soda by putting ice in it, so that cold ice cools the soda. Degenerate Fermi gas cooled with sympathetic cooling was realized using a mixture of lithium-6 and lithium-7 in 2001 by Randall Hulet's group at Rice University [Truscott et al., 2001] and Christophe Salomon at the ENS in Paris [Schreck et al., 2001]. Using these techniques Fermi gases can be cooled to temperatures of 50 nK .

2.4 Density of States

As a result of Heisenberg's uncertainty principle phase space in quantum mechanics is quantized and we have single state in volume $(2\pi)^d$, where d denotes the

dimensionality of the space. The region of the momentum space for which magnitude of the momentum is less than k has volume $v_d k^d$ in d dimensions, where $v_d = \pi^{d/2}/\Gamma(d/2 + 1)$, $\Gamma(x)$ is the Gamma function, which for integer x satisfies following identities $\Gamma(x) = (x - 1)!$ and $\Gamma(1/2 + x) = \sqrt{\pi}(2x)!/(4^x x!)$. Using the dispersion relation for free particles $\epsilon = k^2/(2M)$, the total number of states $G(\epsilon)$ with energy less than ϵ can be written as

$$G(\epsilon) = \frac{V_d v_d k^d}{(2\pi)^d} = \frac{V_d v_d (2M\epsilon)^{d/2}}{(2\pi)^d} \quad (2.17)$$

Here V_d denotes the generalized volume of the system in real space in d dimensions. The density of states (DOS), denoted by $D(\epsilon)$, describes how the available quantum states are distributed and can be calculated from the total number of states as

$$D(\epsilon) = \frac{dG(\epsilon)}{d\epsilon} = \frac{dV_d v_d (2M)^{d/2} (\epsilon)^{d/2-1}}{2(2\pi)^d} \quad (2.18)$$

For the usual three dimensions $d = 3$, $V_d = V$ and DOS is given as

$$D(\epsilon) = \frac{VM^{3/2}\sqrt{\epsilon}}{\sqrt{2}\pi^2}. \quad (2.19)$$

It turns out that DOS is independent from energy in two dimensions, where generalized volume is the area $V_d = A$

$$D(\epsilon) = \frac{AM}{2\pi}. \quad (2.20)$$

Lastly DOS of one dimensional system is proportional to $1/\sqrt{\epsilon}$, diverging at $\epsilon = 0$. In Fig. 2.5 we sketch DOS for different dimensions. In general at low energies DOS increases with decreasing dimensionality as a function of energy.

One can also calculate DOS of d dimensional harmonically trapped system with frequencies ω_i by estimating $G(\epsilon)$ using the dispersion relation $\epsilon = \sum_i \omega_i (n_i + 1/2)$, where $n_i = 0, 1, 2, \dots$ denotes the energy levels. The final result is given as

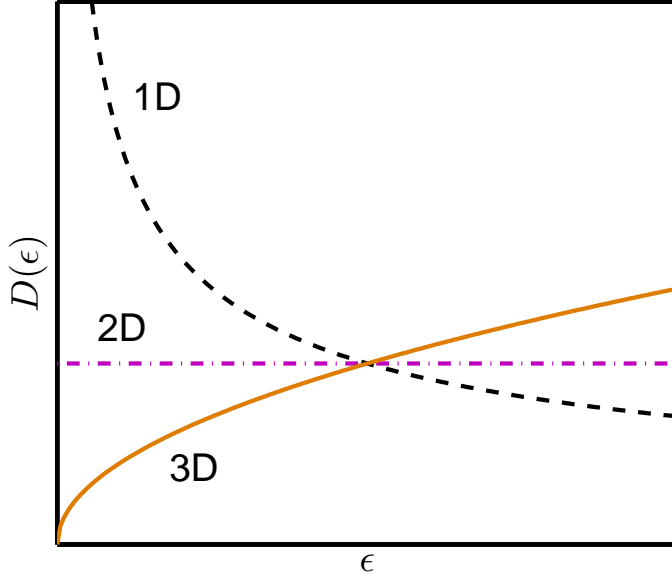


Figure 2.5: Sketch of density of states of homogenous gas for different dimensions. The behavior of density of states strongly depends on the dimensionality of the system. Note that density of states increases at low energies with decreased dimensionality.

$$D(\epsilon) = \frac{\epsilon^{d-1}}{(d-1)! \prod_i \omega_i}. \quad (2.21)$$

Using DOS we can replace the sums over the discrete energy states with an integral over energy. Hence the mean particle number and total energy can be expressed as

$$N = \int_0^\infty d\epsilon f(\epsilon) D(\epsilon), \quad (2.22)$$

$$E = \int_0^\infty d\epsilon \epsilon f(\epsilon) D(\epsilon). \quad (2.23)$$

We should note that in the thermodynamic limit, sums over \mathbf{k} may also be replaced with the integrals as $\sum_{\mathbf{k}} \rightarrow \frac{V_d}{(2\pi)^d} \int d^d k$. Also note that when sums are expressed as integrals the zero energy state could be ignored, since it is usually multiplied by zero due to vanishing DOS at that energy. This may cause a problem for bosons, where the lowest energy state can be occupied by macroscopic number of particles.

Before finishing this section, let us give a general definition for DOS, which can reproduce all the above results and can be used to calculate DOS for any given single particle spectrum E_j :

$$D(\epsilon) = \frac{1}{V_d} \sum_j \delta(\epsilon - E_j) \quad (2.24)$$

In next sections we will use this general relation to compute DOS of various dispersion relations.

2.5 Second Quantization

We saw in previous sections that individual positions of identical particles can not be determined, the only sensible information we can get about system is the number of particles in each quantum state. Since "first quantized" quantum mechanics is formulated in a way that position of the particle is specified, it is not suitable for representing many particles. To demonstrate this let us take two identical fermions, one in state $|1\rangle$ and one in state $|2\rangle$. Due to the indistinguishability of these particles, wave function describing them must be anti-symmetric. This gives us following wave function which includes two terms

$$\Psi(\chi_a, \chi_b) = [\phi_1(\chi_a)\phi_2(\chi_b) - \phi_2(\chi_a)\phi_1(\chi_b)]/\sqrt{2}. \quad (2.25)$$

Here $\phi_1(\chi)$ ($\phi_2(\chi)$) denotes the wave function of state $|1\rangle$ ($|2\rangle$). Above wave function may look like manageable, but in case of N identical fermions, in order to make wave function anti-symmetric we need to write a slater determinant of N single particle wave functions. This means that our N body wave function will have $N!$ terms, obviously such notation is impractical. Even for 10 particles we need 3628800 terms to write down their anti-symmetric wave-function. Therefore "first quantization" notation can not be used for many particle systems.

The solution to this problem is to use the so called "second quantization" notation, where we give up the impossible task of keeping track of the position of the individual

particles and only keep track of the number of particles in each single particle state. In this notation we work in Fock space and use occupation number states,

$$|n_1, n_2, \dots\rangle. \quad (2.26)$$

Here n_i denotes the number of particles in a single particle state i , and the total particle number is given by $N = \sum_i n_i$. For bosons n_i can take any integer value and for fermions it is either 1 or 0 due to Pauli exclusion principle. The state which contains no particle is known as vacuum state and is denoted by $|0\rangle$. Using single particle states one can prove that occupation number states also satisfy the orthogonality and closure properties

$$\langle n_1, n_2, \dots | n'_1, n'_2, \dots \rangle = \delta_{n_1, n'_1} \delta_{n_2, n'_2} \dots, \quad (2.27)$$

$$\sum_{n_1, n_2, \dots} |n_1, n_2, \dots\rangle \langle n_1, n_2, \dots| = \text{I} \quad (2.28)$$

where I is the identity operator. Next creation/annihilation operators $\hat{a}_i^\dagger/\hat{a}_i$ which create/destroy a particle in single particle state i can be introduced

$$\hat{a}_i^\dagger |\dots, n_i, \dots\rangle = \sqrt{n_i + 1} |\dots, n_i + 1, \dots\rangle, \quad (2.29)$$

$$\hat{a}_i |\dots, n_i, \dots\rangle = \sqrt{n_i} |\dots, n_i - 1, \dots\rangle. \quad (2.30)$$

In second quantization the symmetric/anti-symmetric nature of the many body wave function is carried by the creation/annihilation operators, which satisfy the following commutation (for bosons) or anti-commutation (for fermions) relations

$$[\hat{a}_i, \hat{a}_j]_{\mp} = \hat{a}_i \hat{a}_j \mp \hat{a}_j \hat{a}_i = [\hat{a}_i^\dagger, \hat{a}_j^\dagger]_{\mp} = 0, \quad (2.31)$$

$$[\hat{a}_i, \hat{a}_j^\dagger]_{\mp} = \delta_{i,j}. \quad (2.32)$$

Note that for fermions, Pauli exclusion principle directly follows from above anti-commutation relations $[\hat{a}_i^\dagger \hat{a}_i^\dagger]_+ = 2\hat{a}_i^\dagger \hat{a}_i^\dagger = 0$.

We can express any operator using these creation/annihilation operators. For example suppose that \hat{O} is single particle operator, i.e. operator which acts on single particle. This operator in second quantization notation can be expressed as

$$\hat{O} = \sum_{i,j} \langle i | \hat{O} | j \rangle \hat{a}_i^\dagger \hat{a}_j. \quad (2.33)$$

The most common single particle operators are total particle number operator $\hat{N} = \sum_i \hat{a}_i^\dagger \hat{a}_i$ and the Hamiltonian $\hat{H} = \sum_i \epsilon_i \hat{a}_i^\dagger \hat{a}_i$ where ϵ_i is the single particle energy of level i . Besides single particle operators we will need two particle operators to represent the binary interactions of ultracold atoms. For any two particle operator \hat{V} we have the following representation

$$\hat{V} = \sum_{i,j,i',j'} v_{ij i' j'} \hat{a}_i^\dagger \hat{a}_j^\dagger \hat{a}_{i'} \hat{a}_{j'} \quad (2.34)$$

where $v_{ij i' j'}$ can be expressed in terms of position wave functions $\phi_i(\mathbf{r})$ as

$$v_{ij i' j'} = \int d\mathbf{r} d\mathbf{r}' \phi_i^*(\mathbf{r}) \phi_j^*(\mathbf{r}') \hat{V} \phi_{i'}(\mathbf{r}) \phi_{j'}(\mathbf{r}'). \quad (2.35)$$

We can transform from one basis to another basis via

$$\hat{a}_\lambda^\dagger = \sum_i \langle i | \lambda \rangle \hat{a}_i^\dagger. \quad (2.36)$$

The creation/annihilation operators of real space basis $\hat{\psi}^\dagger(\mathbf{r})/\hat{\psi}(\mathbf{r})$ are one of the most important basis and are known as the field operators. Another important basis is the momentum basis whose the creation/annihilation operators are denoted as $\hat{a}_\mathbf{k}^\dagger/\hat{a}_\mathbf{k}$. Using the above relation both bases can be related as

$$\hat{\psi}^\dagger(\mathbf{r}) = \sum_{\mathbf{k}} \langle \mathbf{k} | \mathbf{r} \rangle \hat{a}_{\mathbf{k}}^\dagger = \frac{1}{\sqrt{V}} \sum_{\mathbf{k}} e^{-i\mathbf{r} \cdot \mathbf{k}} \hat{a}_{\mathbf{k}}^\dagger, \quad (2.37)$$

$$\hat{a}_{\mathbf{k}}^\dagger = \frac{1}{\sqrt{V}} \int d\mathbf{r} e^{i\mathbf{r} \cdot \mathbf{k}} \hat{\psi}^\dagger(\mathbf{r}) \quad (2.38)$$

Following identities are useful in proving above relations $\frac{1}{\sqrt{V}} \sum_{\mathbf{k}} e^{i(\mathbf{r}-\mathbf{r}') \cdot \mathbf{k}} = \delta(\mathbf{r}-\mathbf{r}')$ and $\frac{1}{\sqrt{V}} \int d\mathbf{r} e^{-i\mathbf{r} \cdot (\mathbf{k}-\mathbf{k}')} = (2\pi)^3 \delta(\mathbf{k}-\mathbf{k}')$. In this thesis we will usually use the second quantization notation, and use the transformations introduced in this section very frequently.

2.6 Non-Interacting Fermi Gas in 3D

In this section we analyze gas composed of non-interacting fermions in 3D. In this thesis we will study properties of Fermi gas composed of atoms from two different hyperfine states, labeled by psuedo-spin \uparrow and \downarrow . Whenever we refer to spin of a atom, we are actually referring to the hyperfine state of the atom.

Let us start our study with homogeneous non-interacting Fermi gas at temperature $T = 0$. Since, no two identical particles can occupy the same quantum state, each quantum state will be occupied by two fermions at most one with spin \uparrow and one with spin \downarrow . Thus all the low energy levels below certain energy will be occupied, while the energy levels above this energy will be empty. The highest occupied energy state is known as the Fermi energy E_F and is equal to the chemical potential of the system $\mu = E_F$ at $T = 0$. This fact that all the energy levels below E_F are occupied, while the energy levels with higher energy than E_F are vacant can also be seen from the Fermi-Dirac distribution function which turns to step function at zero temperature

$$\langle n_j \rangle = \lim_{\beta \rightarrow \infty} \frac{1}{e^{\beta(\epsilon_j - \mu)} + 1} = \Theta(E_F - \epsilon_j). \quad (2.39)$$

Here $\Theta(x)$ denotes the Heaviside step function which is a discontinuous function whose value is zero for negative argument and one for positive argument. In Fig. 2.6 we

show the behavior of Fermi function as function of energy for different temperature values. We can clearly see that at $T \approx 0$ all the states with energy below μ are occupied and while the states above μ are vacant.

The Fermi energy depends on the density of the gas. The expression relating the particle density and E_F can be calculated either using its definition $G(E_F) = 2N$ (here 2 denotes the spin degeneracy) or by integrating expression Eq. (2.22). This expression for 3D homogeneous Fermi gas gives

$$E_F = \frac{(3\pi^2 n)^{2/3}}{2M}. \quad (2.40)$$

Using the Fermi energy we can define Fermi temperature $T_F \equiv E_F/k_B$, whose value can be determined as

$$T_F \approx \frac{3.8n^{2/3}}{k_B M}. \quad (2.41)$$

This is temperature at which Fermi-Dirac distribution starts deviating significantly from Maxwell-Boltzmann distribution. Note that it has the same order of magnitude with the estimated degeneracy temperature given at Eq. (2.6). By integrating Eq. (2.23) we can also calculate the ground state energy, which can be much higher than the classically expected zero energy $E = 3k_B T/2 = 0$ at $T = 0$,

$$E = \frac{3E_F N}{10}. \quad (2.42)$$

When there is some finite temperature T , particles will start to occupy the states above the Fermi energy as can be seen from Fig. 2.6. The effect for small temperatures $T \ll E_F/k_B$ can be estimated via Sommerfeld expansion [Sommerfeld, 1928, Ashcroft and Mermin, 1976]. For example chemical potential for 3D Fermi gas can be estimated as $\mu = E_F \left[1 - \frac{\pi^2}{12} \left(\frac{k_B T}{E_F} \right)^2 \right]$, which indicates that energy required to add a new particle has decreased. This result can be explained with particles occupying higher energy states above E_F , hence leaving some lower energy states empty. Hence it takes less energy to add a new particle to the system.

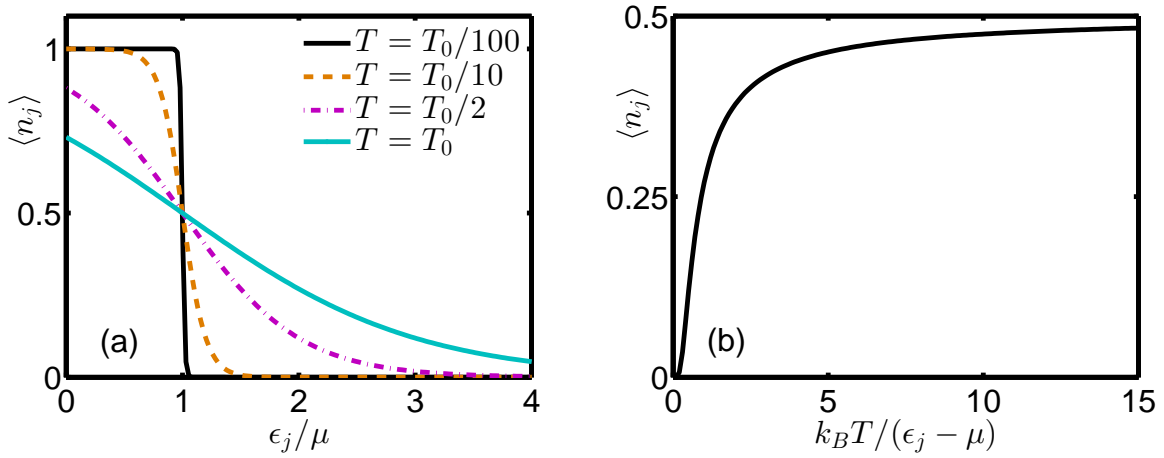


Figure 2.6: (a) Energy dependence of average occupation of a state j for different temperatures. Temperatures are scaled with $T_0 = \mu/k_B$. Note that at low T , the curve has form of a step function such that all the states below μ are occupied and states above μ are vacant. At high temperatures, curves take the shape of Boltzmann distribution with considerable occupation probability of states with energy higher than μ . (b) Temperature dependence of average occupation of a state j for $\epsilon_j > \mu$. As $T \rightarrow 0$ all the states above μ become vacant, while at high temperatures the average occupation tends to go toward 0.5.

For a gas trapped in three dimensional harmonic trap dispersion relation and DOS changes as we already discussed. If we assume that gas is trapped in isotropic harmonic trap, than dispersion relation simplifies to $\epsilon_n = \omega(n + 3/2)$. Here n is the quantum number which determines the single-particle energy, and each state is $(n + 1)(n + 2)/2$ fold degenerate. If we distribute N atoms to these energy states we get an equation which determines E_F of the system

$$\frac{N}{2} = \sum_{n=0}^{n_F} \frac{(n+1)(n+2)}{2} = \frac{(n_F+1)(n_F+2)(n_F+3)}{6} \quad (2.43)$$

where n_F is the quantum number of the Fermi energy, i.e $E_F = \omega(n_F + 3/2)$. If N is very large, i.e. we are close to the thermodynamic limit, than $n_F \gg 1$ and above expression reduces to $n_F = (3N)^{1/3}$. Then the Fermi energy takes the following form:

$$E_F = \omega(3N)^{1/3} \quad (2.44)$$

Note that we can get above expression by inserting DOS for 3D isotropic harmonic trap $D(\epsilon) = \epsilon^2/(2\omega^3)$ to Eq. (2.22) and taking $\mu = E_F$. We can also insert the DOS expression to Eq. (2.23), and calculate the internal energy of the gas:

$$E = \frac{E_F^4}{8\omega^3} = \frac{3NE_F}{8}. \quad (2.45)$$

The density distribution at the trap can be estimated using the semi-classical local density approximation (LDA). In this approximation we assume that gas can be treated as uniform in any point in the trap. As we discussed in previous section this approximation is valid when the characteristic length scale of the oscillator is very big compared to the other length-scales. Using this approximation we can define a local Fermi energy $E_F(\mathbf{r})$ and local Fermi momentum $k_F(\mathbf{r}) = \sqrt{2ME_F(\mathbf{r})}$ in any point \mathbf{r} in the trap. Then the number of atoms that can fill the momentum sphere with radius $k_F(\mathbf{r})$ can be easily determined

$$n(\mathbf{r}) = 2 \frac{1}{(2\pi)^3} \frac{4\pi k_F(\mathbf{r})}{3}. \quad (2.46)$$

From energy conservation we have $E_F(\mathbf{r}) = E_F - V(\mathbf{r})$. If we substitute this to above equation we get the density distribution in the trap

$$n(\mathbf{r}) = \frac{1}{3\pi^2} [2M(E_F - V(\mathbf{r}))]^{3/2}. \quad (2.47)$$

The point at which $V(\mathbf{r}) = E_F$ determines the edge of the gas and is known as the Thomas-Fermi radius. For an isotropic 3D harmonic trap, the Thomas-Fermi radius R_F is given as

$$R_F = \sqrt{\frac{2E_F}{M\omega}} = (24N)^{1/6} a_0. \quad (2.48)$$

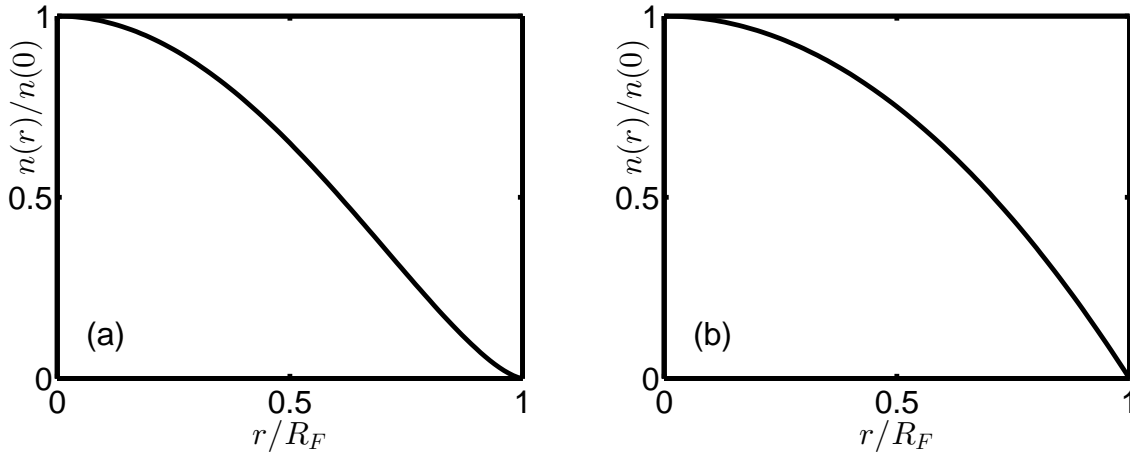


Figure 2.7: (a) Density distribution of 3D harmonically trapped two species non-interacting Fermi gas under LDA. Central density is given as $n(0) = k_F^{3/2}/(3\pi^2)$. (b) Density distribution of 2D harmonically trapped two species non-interacting Fermi gas under LDA. Central density is given as $n(0) = k_F^2/(2\pi)$. For both density profiles $R_F = \sqrt{2E_F/(M\omega^2)}$. We should note that the relation between E_F and particle number N depends on dimensionality and is provided in the text.

Here $a_0 = \sqrt{1/(M\omega)}$ is characteristic length of the harmonic oscillator. We can express the density distribution in terms of the Thomas-Fermi radius as

$$n(\mathbf{r}) = \frac{8N}{\pi^2 R_F^3} \left(1 - \frac{r^2}{R_F^2}\right)^{3/2}. \quad (2.49)$$

We show this density distribution in Fig. 2.7(a). The computed density profile is a result of Pauli exclusion principle's quantum kinetic pressure, thus is direct result of the quantum statistics. Similar to the homogeneous case, when temperature is turned on states above E_F starts to get occupied and therefore global chemical potential starts to drop. Using the Sommerfeld expansion we can again estimate the low temperature behavior of the chemical potential $\mu = E_F[1 - \frac{(\pi k_B T)^2}{3E_F^2}]$.

Before finishing this section let us further comment on the validity of LDA. As we commented above, LDA is valid for slowly varying potentials. Let us specify what we mean by slowly varying [Nicolai Nygaard, 2004]. Assume that we partition the potential to cells of dimension δ , such that in each cube δ^3 density can be taken as

approximately uniform and following condition is satisfied $\delta^3 n(\mathbf{r}) \gg 1$. If the strength of the potential is small compared to local Fermi energy, i.e. $|V(\mathbf{r})| \ll E_F(\mathbf{r})$, than only particles in the vicinity of the Fermi surface will "feel" the potential. As a result of this the spatial variation of potential over a cell can be neglected if $\delta|\nabla V(\mathbf{r})| \ll E_F(\mathbf{r})$. In that case the potential is approximately constant on the scale of oscillations of the single-particle wavefunctions. If we insert the expression for the $E_F(\mathbf{r})$, the condition takes the following form

$$\delta|\nabla V(\mathbf{r})| \ll \frac{[3\pi^2 n(\mathbf{r})]^{2/3}}{2M}. \quad (2.50)$$

Combining this condition with $\delta^3 n(\mathbf{r}) \gg 1$, we get the final expression for the validity of LDA

$$|\nabla V(\mathbf{r})| \ll \frac{(3\pi^2)^{2/3} n(\mathbf{r})}{2M}. \quad (2.51)$$

Note that LDA is many body version of WKB approximation, where we also assume that potential is slowly varying such that de-Broglie wavelength must be small compared to the distance at which the potential changes considerably. In fact above condition can be also derived by the validity condition of the WKB approximation, $dV/dr \ll k^3/(2\pi M)^2$. Similar to WKB approximation's failure at the classical turning points, LDA fails at the edge of the gas, where local Fermi energy becomes comparable with $V(\mathbf{r})$. The failure of the LDA at the edge of the gas can be also deduced from the fact that density vanishes at the edge of the gas, hence above condition obviously can not be satisfied there. In general LDA fails if the density is low, therefore LDA is not good approximation for the systems composed of small number of particles. On the other hand, as we move toward the thermodynamic limit, LDA becomes very powerful approximation providing very accurate results as we will demonstrate in the next sections.

2.7 Non-Interacting Fermi Gas in 2D

In this section we investigate the properties of ideal Fermi gas in two dimensions, since two dimensions will be our focus in this thesis. As we demonstrated DOS in two dimensions is independent of energy, as a result of this the properties of 2D Fermi gas can deviate from that of 3D Fermi gas.

We can obtain the Fermi energy of two dimensional non-interacting homogeneous Fermi gas analogously to the three dimensional case

$$E_F = \frac{\pi n}{M}. \quad (2.52)$$

From this expression we can deduce the Fermi temperature in 2D

$$T_F = \frac{\pi n}{k_B M}. \quad (2.53)$$

Integrating Eq. (2.23) gives us the total internal energy, which again significantly deviates from $E = 0$ at $T = 0$ predicted by equipartition theorem of classical statistical mechanics

$$E = \frac{NE_F}{4}. \quad (2.54)$$

Eq. (2.22) can be integrated even at finite temperatures. Hence the chemical potential of 2D homogenous Fermi gas can be determined analytically as $\mu = k_B T \ln[\exp(T_F/T) - 1]$. Note that at low temperatures $T \ll T_F$ the temperature dependent part of μ is exponential $\mu \approx E_F - k_B T \exp(-E_F/T)$, in contrast to 3D where it is proportional to T^2 .

Trapped 2D Fermi gas is also significantly different than its 3D counterpart. In 3D there are six degrees of freedom, but in 2D we have just four degrees of freedom. As a result the space gas occupies is smaller and gas is expected to expand faster as new particles are added. Dispersion relation for isotropic 2D harmonic trap, as we

will demonstrate in next section, is $\epsilon_n = \omega(n + 1)$, where n is the primary quantum number. Each n orbital is $n + 1$ fold degenerate. Similar to 3D case, we can determine E_F by distributing the N atoms to these energy states

$$\frac{N}{2} = \sum_{n=0}^{n_F} (n + 1) = \frac{(n_F + 1)(n_F + 2)}{2} \quad (2.55)$$

where n_F is the main quantum number of Fermi energy $E_F = \omega(n_F + 1)$. Than Fermi energy can be expressed as

$$E_F = \omega \left(\frac{\sqrt{4N + 1} - 1}{2} \right). \quad (2.56)$$

In thermodynamic limit where $N \gg 1$, the Fermi energy reduces to following simple expression

$$E_F = \omega\sqrt{N}. \quad (2.57)$$

The density of states of 2D isotropic harmonic trap is energy dependent, i.e. $D(\epsilon) = \epsilon/\omega^2$. Using this, the energy of zero temperature Fermi gas can be calculated as

$$E = \frac{NE_F}{3}. \quad (2.58)$$

The density distribution of the 2D non-interacting Fermi gas can be also estimated using LDA. Again we define local fermi energy $E_F(\mathbf{r}) = E_F - V(\mathbf{r})$ and use Eq. (2.52) to relate local fermi energy to local density, which gives as the density profile of the system

$$n(r) = \frac{M}{\pi} \left(E_F - \frac{M\omega^2 r^2}{2} \right). \quad (2.59)$$

By equating $n(r) = 0$ we get the Thomas-Fermi radius of the 2D Fermi gas

$$R_F = \sqrt{\frac{2E_F}{M\omega^2}} = (4N)^{1/4}a_0. \quad (2.60)$$

The gas grows with $N^{1/4}$ as new particles are added, which as expected is faster than 3D Fermi gas which grows with $N^{1/6}$. Using R_F , the density profile can be expressed as

$$n(r) = \frac{k_F^2}{2\pi} \left(1 - \frac{r^2}{R_F^2}\right). \quad (2.61)$$

The density profile is also different than 3D Fermi gas and has the shape of an inverted parabola. We plot density distribution in Fig. 2.7(b), where it can be compared with its 3D version. This parabolic shape can also be deduced from the local density of states (LDOS) which is LDA generalization of standard DOS, and can be calculated using

$$D(r, \epsilon) = \sum_{\mathbf{k}} \delta[\epsilon - \varepsilon(r, k)], \quad (2.62)$$

where $\varepsilon(r, k) = k^2/(2M) + M\omega^2 r^2/2$ is the local dispersion relation. If we change the above sum with an integral and perform the integration we get LDOS of 2D Fermi gas

$$D(r, \epsilon) = \frac{MA\Theta(\epsilon_r)}{\pi}, \quad (2.63)$$

where $\epsilon_r = \epsilon - M\omega^2 r^2/2$. The constant LDOS has a parabolic shape, which leads to the inverted parabola shape of the density.

Unlike the homogeneous case, finite temperature behavior of chemical potential of 2D trapped Fermi gas is similar to 3D Fermi gas' behavior $\mu = E_F[1 - \frac{\pi^2}{6}(\frac{k_B T}{E_F})^2]$.

Before finishing this section, let us note that 2D (or quasi-2D) Fermi gas has been created experimentally [Martinyanov et al., 2010, Dyke et al., 2011, Fröhlich et al., 2011,

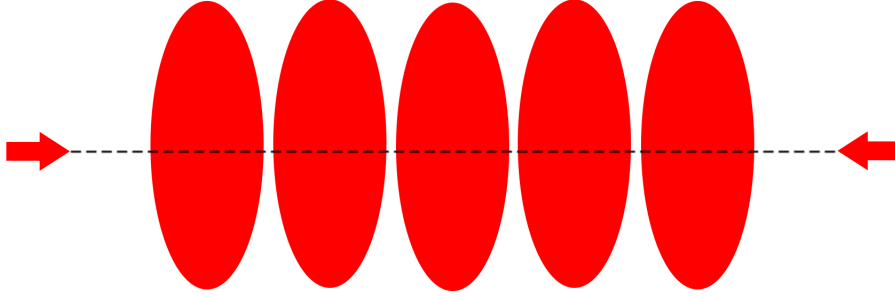


Figure 2.8: Illustration of a stack of pancake-shaped traps, created by interference of two coherent laser beams. Particles are confined to stay at a single pancake and we have effectively 2D system.

Feld et al., 2011, Sommer et al., 2012, Ries et al., 2015] and therefore it is not just a theoretical consideration. 2D or quasi-2D Fermi gas is achieved by trapping the Fermions in harmonic trap with very large aspect ratio. In other words confinement in the radial direction (x and y) is weak, where as there is strong confinement in the z direction. As result of this anisotropy only the ground state is populated in z direction. This can be achieved by using a standing wave created by the interference of two coherent laser beams, which create inference patterns where the inference maxima are round. Thus the interference of these laser beams create a stack of pancake-shaped traps (See Fig. 2.8). The particles are confined to stay at a single pancake and we have effectively 2D system. In other words motion in z direction is frozen, because kinetic energy of particles is smaller than the excitation energy in z direction ω_z .

2.8 2D Harmonic Oscillator

In this thesis we will frequently make use of the angular momentum basis of the 2D harmonic oscillator. Therefore it will be useful to review the 2D isotropic har-

monic oscillator problem in quantum mechanics [Cohen-Tannoudji et al., 1977]. The Hamiltonian of the 2D harmonic oscillator can be written as

$$H_0 = \frac{\hat{p}_x^2 + \hat{p}_y^2}{2m} + \frac{1}{2}m\omega^2(\hat{x}^2 + \hat{y}^2). \quad (2.64)$$

Here $\hat{p}_x = -i\partial/\partial x$ and $\hat{p}_y = -i\partial/\partial y$ denotes the usual momentum operators, \hat{x} and \hat{y} denote the position operators. Position and momentum operators are canonically conjugate and therefore satisfy following commutation relation $[\hat{x}, \hat{p}_x] = i$.

Note that above the Hamiltonian is invariant under rotations along the z -axis, which is a direct result of its isotropy. This implies that z projection of angular momentum operator

$$\hat{L}_z = \hat{x}\hat{p}_y - \hat{y}\hat{p}_x \quad (2.65)$$

must commute with the Hamiltonian. Therefore they must have simultaneous eigenstates. These eigenstates can be generated via the ladder operators associated with left and right circular quanta which are defined as:

$$\hat{b}_{R/L} = \frac{1}{2} \left[\frac{\hat{x} \pm i\hat{y}}{a_0} + ia_0(\hat{p}_x \pm i\hat{p}_y) \right] \quad (2.66)$$

with $a_0 = \sqrt{1/m\omega}$ being the harmonic oscillator length. These operators satisfy independent harmonic oscillator algebra

$$[\hat{b}_L, \hat{b}_L^\dagger] = 1 = [\hat{b}_R, \hat{b}_R^\dagger] \quad (2.67)$$

with all other commutators equal to zero. The associated number operators which count number of left/right quanta $\hat{n}_{L/R} = \hat{b}_{L/R}^\dagger \hat{b}_{L/R}$ can be used to uniquely label states with their eigenvalue $N_{L/R}$. With these new operators Hamiltonian can be expressed as:

$$H_0 = \omega(\hat{b}_L^\dagger \hat{b}_L + \hat{b}_R^\dagger \hat{b}_R + 1) = \omega(\hat{n}_L + \hat{n}_R + 1). \quad (2.68)$$

Similarly the angular momentum operator can be written as

$$\hat{L}_z = (\hat{b}_L^\dagger \hat{b}_L - \hat{b}_R^\dagger \hat{b}_R) = (\hat{n}_L - \hat{n}_R) \quad (2.69)$$

The simultaneous eigenstates of these two operators which form a complete set, can be denoted by $|n, l\rangle$. The integer quantum numbers n and l ($n \geq |l| \geq 0$) are related to eigenvalues of $n_{L/R}$ via $n = N_L + N_R$ and $l = N_L - N_R$ so that the energy and angular momentum eigenvalues can be written as $\epsilon_n = \omega(n+1)$ and $l_z = l$ respectively. From the relation between n , l and N_L , N_R integers we can deduce that for each energy quantum number n , there are $n+1$ states, each having unique angular momentum quantum number l taking value from the set $\{-n, -n+2, -n+4, \dots, n-2, n\}$. Thus if n is even, l must be even and if n is odd, l must be odd too.

The excited states can be generated from the harmonic oscillator ground state by applying the raising operators

$$|n, l\rangle = \frac{(\hat{b}_L^\dagger)^{N_L} (\hat{b}_R^\dagger)^{N_R}}{\sqrt{N_L! N_R!}} |0, 0\rangle. \quad (2.70)$$

The action of the ladder operators associated with left and right circular quanta on the states of harmonic oscillator can be deduced as

$$\begin{aligned} \hat{b}_L^\dagger |n, l\rangle &= \sqrt{\frac{n+l}{2} + 1} |n+1, l+1\rangle, & \hat{b}_R |n, l\rangle &= \sqrt{\frac{n-l}{2}} |n-1, l+1\rangle, \\ \hat{b}_L |n, l\rangle &= \sqrt{\frac{n+l}{2}} |n-1, l-1\rangle, & \hat{b}_R^\dagger |n, l\rangle &= \sqrt{\frac{n-l}{2} + 1} |n+1, l-1\rangle. \end{aligned} \quad (2.71)$$

The normalized orbital angular momentum wavefunctions can be written as

$$\langle r\theta | n, l \rangle \equiv R_n^{(l)}(r) e^{il\theta} = (-1)^{(n-|l|)/2} \sqrt{\frac{((n-|l|)/2)!}{\pi a_0^2 ((n+|l|)/2)!}} e^{il\theta} \left(\frac{r}{a_0}\right)^{|l|} e^{-r^2/2a_0^2} L_{(n-|l|)/2}^{|l|}(r^2/a_0^2), \quad (2.72)$$

The associated Laguerre polynomials $L_n^{|m|}(x)$ can be generated from the recursion relation

$$L_{n+1}^{|m|}(x) = \frac{1}{n+1} \left[(2n+1+|m|-x)L_n^{|m|}(x) - (n+|m|)L_{n-1}^{|m|}(x) \right] \quad (2.73)$$

for $n > 1$ using $L_0^{|m|}(x) = 1$ and $L_1^{|m|}(x) = 1 + |m| - x$.

Before concluding this section, let us calculate the exact density distribution of 2D Fermi gas trapped in isotropic harmonic trap and compare with the LDA result. Using field operators, density distribution is given as

$$n(\mathbf{r}) = \sum_{\sigma} \langle \hat{\psi}_{\sigma}^{\dagger}(\mathbf{r}) \hat{\psi}_{\sigma}(\mathbf{r}) \rangle. \quad (2.74)$$

Here $\sigma = \{\uparrow, \downarrow\} = \{1/2, -1/2\}$ denotes pseudo-spins of the atom. Using equation Eq. (2.72) and Eq. (2.36) field operators can be expressed as

$$\hat{\psi}_{\sigma}(\mathbf{r}) = \sum_{n,l} R_n^{|l|}(r) e^{il\theta} \hat{a}_{nl\sigma}, \quad (2.75)$$

where $\hat{a}_{nl\sigma}$ annihilates particle at state $|n, l\rangle$ with spin σ , while its dagger creates a particle at the same state with the same spin state. Substituting these to density equation above we get

$$n(\mathbf{r}) = \sum_{n,l,n',l,\sigma} R_n^{|l|}(r) R_{n'}^{|l'|}(r) e^{i(l-l')\theta} \langle \hat{a}_{nl\sigma}^{\dagger} \hat{a}_{n'l'\sigma} \rangle = 2 \sum_{n=1}^{n=n_F} \sum_{l=-n}^{l=n} [R_n^{|l|}(r)]^2. \quad (2.76)$$

Prime in above sum denotes the constraint on the sum to be performed by two steps, energy quantum number of Fermi energy can be related to total particle number with $n_F = (\sqrt{4N+1} - 3)/2$. In deriving the above equation we used the fact that, the average occupation of a single particle state is given with Fermi-Dirac distribution $\langle \hat{a}_{nl\sigma}^{\dagger} \hat{a}_{n'l'\sigma} \rangle = f(\epsilon_n) \delta_{n,n'} \delta_{l,l'}$, and the Fermi function reduces to the step function at zero temperature as given in Eq. (2.39).

In Fig. 2.9 we compare LDA result with exact quantum mechanical calculations outlined in this section for different particle numbers. We see that at low particle numbers such as $N = 100$ or $N = 500$ while LDA provides good approximation for overall density profile qualitatively, it fails to account for two features. First as we already mentioned above, LDA fails in regions where density is low and hence it always fails at the edge of the trap. Note that this failure is minuscule and disappears as the particle number increases, since the low density region becomes smaller compared to the system size as the particle number increases. Second there are oscillations at the center of the trap which are not present in LDA. These oscillations are known as Friedel oscillations in condensed matter physics [Friedel, 1958] and are direct consequence of the sharp cut-offs in the Fermi surface. The wavelength of the oscillations is on the order of $1/k_F$ and therefore oscillations become practically invisible as the particle number increases. This can be clearly seen in Fig. 2.9, where oscillations get smaller with increased particle number and become invisible to the eye on this scale for particle numbers higher than $N = 5000$. Thus while LDA misses Friedel oscillations and fails to estimate the density at the edge of the gas accurately, but at high particle number it becomes practically indistinguishable from exact results. Thus LDA is a very powerful and accurate approximation to exact density profile of the system.

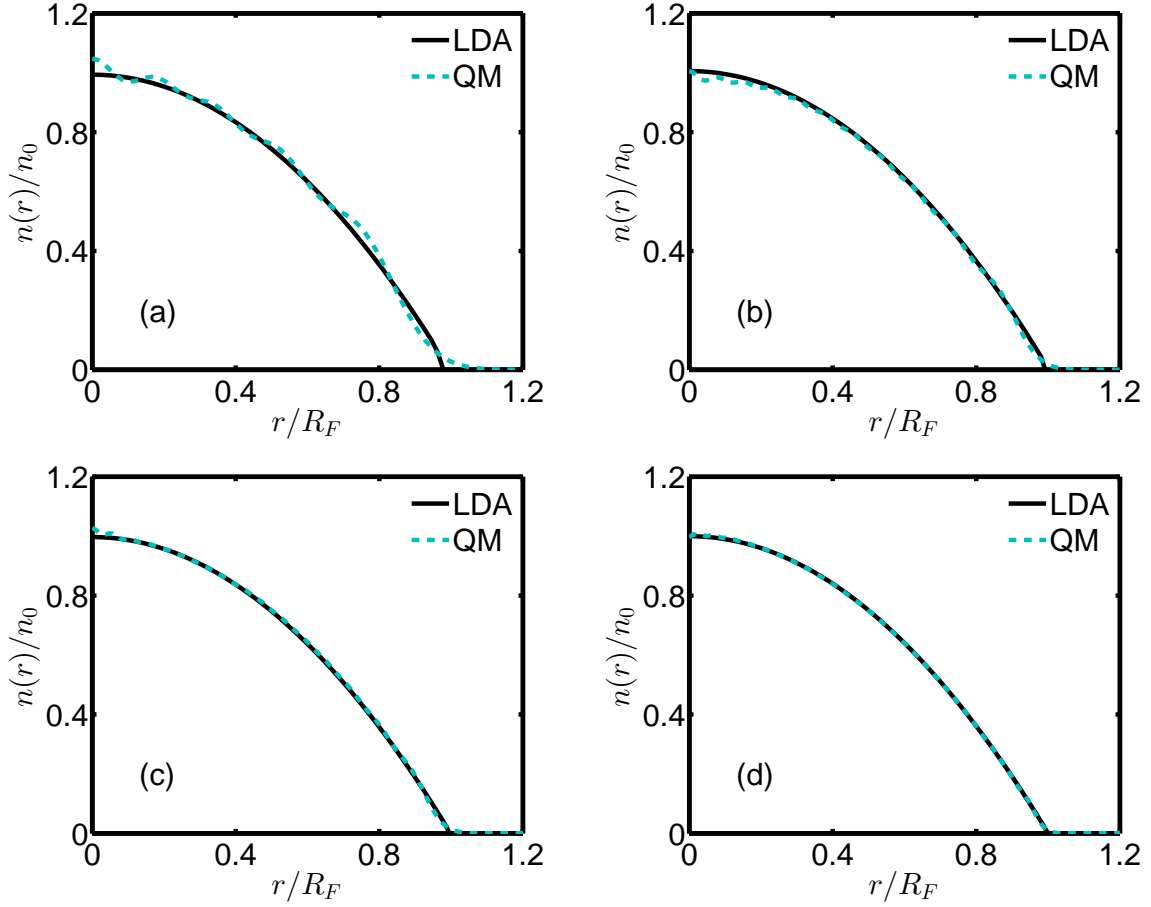


Figure 2.9: Density profile computed via exact quantum mechanical calculations compared with semi-classical LDA result for different particle numbers: (a) $N = 100$, (b) $N = 500$, (c) $N = 1000$, (d) $N = 5000$. In low particle numbers such as $N = 100$ LDA fails to capture the Friedel oscillations at the center of the trap and low density tail of the gas. For considerable particle numbers such as $N = 5000$, Friedel oscillations become invisible and low energy tail becomes very small compared to the system size. Thus in the thermodynamic limit LDA and exact QM calculations become indistinguishable.

Chapter 3

INTERACTING FERMI GAS AND SUPERFLUIDITY

3.1 Scattering in 3D

In this section we study the collisional properties of ultracold atoms. For a pedagogical and detailed analysis the reader is advised to look at [Dalibard, 1999]. We start with the assumption that we have $U(\mathbf{r}) = U(r)$ a spherically symmetric central potential, which as we discussed in previous chapter is perfectly valid approach for cold atoms. Besides we will assume that scattering is elastic. For now let us also assume that the particles are distinguishable, later we will comment on the effect of indistinguishability. Two body scattering problem with spherical potential is best described in the center of mass frame, because only the relative motion is relevant for the problem. This leads to reduction from six degrees of freedom two body problem to three degrees of freedom and thus to a single body scattering problem, with reduced mass $M_r = M/2$, assuming both atoms have the same mass M . We describe the motion in terms of relative position $\mathbf{r} = \mathbf{r}_1 - \mathbf{r}_2$. The system obeys following Schrödinger equation

$$\left[-\frac{\nabla^2}{2M_r} + U(\mathbf{r}) \right] \psi_{\mathbf{k}}(\mathbf{r}) = \epsilon_k \psi_{\mathbf{k}}(\mathbf{r}) \quad (3.1)$$

where $\epsilon_k = k^2/(2M_r)$ is the kinetic energy. We are interested in scattering from a short ranged potential with an effective range R_e , therefore at large distance $|\mathbf{r}| \gg R_e$, the potential can be ignored $U(r) \rightarrow 0$. In this region the collision state can be expressed as a superposition of incoming plane wave, and scattered spherical wave (see Fig. 3.1)

$$\psi_{\mathbf{k}}(\mathbf{r}) = e^{i\mathbf{k}\mathbf{r}} + f(k, \theta) \frac{e^{ikr}}{r} \quad (3.2)$$

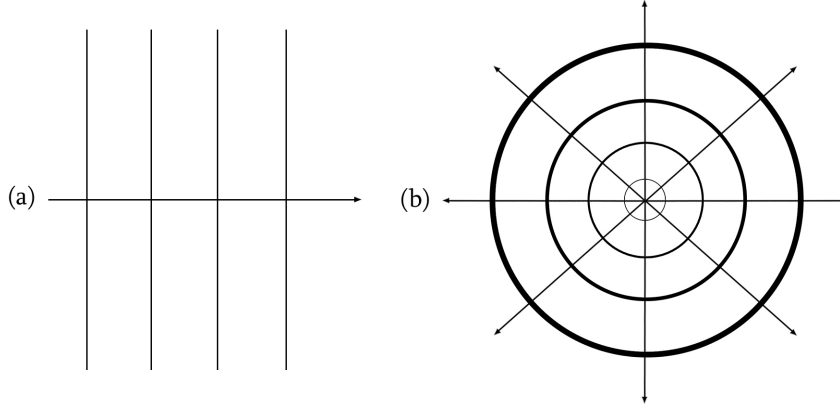


Figure 3.1: Solution of the scattering problem for short ranged (R_e range) potential at large distances $|\mathbf{r}| \gg R_e$ is superposition of (a) a plane wave and (b) a spherical wave.

where the angle between the incident and the scattered wave is θ . $f(k, \theta)$ is called scattering amplitude and depends only to the relative energy of the colliding particles and the angle of scattering. The scattering amplitude is intimately connected with the differential cross section $d\sigma/d\Omega$, which gives us the total scattering cross section σ

$$\frac{d\sigma}{d\Omega} = |f(k, \theta)|^2 \quad \Rightarrow \quad \sigma = \int d\theta d\varphi \sin \theta |f(k, \theta)|^2 \quad (3.3)$$

Since the potential is spherically symmetric we can analyze the problem using the partial wave decomposition. The scattering state in terms of the Legendre polynomials $P_l(x)$ can be written as:

$$\psi_{\mathbf{k}}(\mathbf{r}) = \sum_{l=0}^{\infty} P_l(\cos \theta) \frac{R_{k,l}(r)}{r}. \quad (3.4)$$

With the help of this expansion the scattering problem reduces to a one-dimensional radial Schrödinger equation:

$$-\frac{1}{2M_r} \frac{d^2}{dr^2} R_{k,l}(r) + \left[U(r) + \frac{l(l+1)}{2M_r r^2} - \epsilon_k \right] R_{k,l}(r) = 0. \quad (3.5)$$

This equation can be solved outside the range of the potential, taking $r \gg R_e$, so that we can take the first terms of the spherical Hankel functions, which are the general solution of the above equation. This yields the following scattering wavefunction

$$\psi_{\mathbf{k}}(\mathbf{r}) = \sum_{l=0}^{\infty} \frac{A_l P_l(\cos \theta)}{k} \left[(-1)^{l+1} \frac{e^{-ikr}}{r} + e^{2i\delta_l(k)} \frac{e^{ikr}}{r} \right] \quad (3.6)$$

Thus we see that the sole effect of the interaction is a phase shift between the incident and the scattered wave. The scattering amplitude can be calculated by expanding Eq. (3.2) with partial waves

$$\psi_{\mathbf{k}}(\mathbf{r}) = \sum_{l=0}^{\infty} \frac{(2l+1)P_l(\cos \theta)}{2ki} \left[(-1)^{l+1} \frac{e^{-ikr}}{r} + e^{2i\delta_l(k)} \frac{e^{ikr}}{r} \right] + f(k, \theta) \frac{e^{ikr}}{r} \quad (3.7)$$

and comparing with Eq. (3.6) gives us

$$f(k, \theta) = \sum_{l=0}^{\infty} \frac{(2l+1)P_l(\cos \theta)}{2ki} [e^{2i\delta_l(k)} - 1]. \quad (3.8)$$

Integrating the Eq. (3.3) with the calculated scattering amplitude we get the total cross section

$$\sigma(k) = \sum_{l=0}^{\infty} \frac{4\pi(2l+1)}{k^2} \sin^2 \delta_l(k) \quad (3.9)$$

We are working in the ultracold regime as defined in the first section, therefore atoms are extremely slow $k \ll 1/R_e$. For small k , the phase shifts vary as $\delta_l(k) \propto k^{2l+1}$, therefore total cross section falls as $\sigma(k) \propto k^{4l}$. Thus therefore $l = 0$ wave is by far most dominant contribution to the total cross section. This can be also seen from

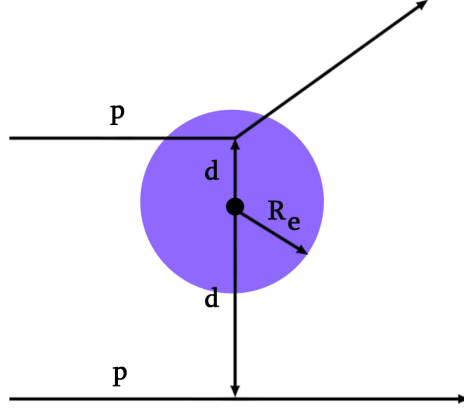


Figure 3.2: Scattering of a particle from a potential $U(r)$ with finite range R_e . The particle can see the potential only if $d < R_e$, which places a constraint on the angular momentum of the particle ($L = pd$) $L < pR_e$. Therefore only particles with angular momentum less than pR_e will be affected from the potential. In quantum mechanics angular momentum states are discrete, if momentum is sufficiently small like in cold atoms, than only particles at lowest s-wave state can see the potential.

Eq. (3.5), for finite angular momenta there is repulsive centrifugal $l(l+1)/(2M_r r^2)$ term near the real potential $U(r)$. This term constitutes a potential barrier which the incoming wave has to overcome in order to feel the short ranged potential. But for low momentum particle this is very low probability event. Particles with finite angular momentum, will reflect from this barrier and will not feel the potential. This argument has a simple classical counterpart, assume we have potential with finite range R_e (thus potential forms sphere with radius R_e in real space), and particle with classical momentum p is moving towards this potential. Assume d is the closest distance particle has from the center of the potential called impact parameter (see Fig. 3.2). In order for the particle to feel the potential this distance must be smaller than the range of the potential $d < R_e$. But this puts constraint on the angular momentum $L = pd$ which must be smaller than some cut-off $L < pR_e = L_c$. If the particle is slow, therefore it has low momentum and the range of the potential is small, than only the

particles with very low angular momentum will collide with the potential. In quantum mechanics angular momentum states are discrete, if momentum is sufficiently low like in cold atoms, than only particles at the lowest s-wave state can see the potential. Given this analysis we restrict ourselves to s-wave scattering, and all quantities become isotropic as a result of the symmetry of s-wave state and the potential. Than the scattering amplitude simplifies to

$$f(k) = \frac{e^{2i\delta_0} - 1}{2ik} = \frac{1}{k \cot \delta_0(k) - ik} \quad (3.10)$$

Since $k \ll 1/R_e$ we can expand $k \cot \delta_0(k) \approx -1/a_s + R_{\text{eff}}k^2/2 + \dots$ a_s is the s-wave scattering length which can be defined as

$$a_s = -\lim_{k \rightarrow 0} \frac{\tan[\delta_0(k)]}{k}. \quad (3.11)$$

The scattering length a_s acts as an effective hard-sphere diameter, it measures the interaction strength and determines the collision cross section at zero momentum limit. R_{eff} is characteristic length known as effective range of the potential. R_{eff} expresses how the potential affects the energy dependence of cross section and determines when $k \rightarrow 0$ limit is reached. For the Van der Waals potential R_{eff} is on the order of R_e [Flambaum et al., 1999], therefore in ultracold limit second term can also be neglected. If we substitute above expansion to Eq. (3.9), we determine the total cross section as

$$\sigma(k) = \frac{4\pi a_s^2}{1 + k^2 a_s^2} \quad (3.12)$$

We see that scattering length a_s is the most important parameter determining the collisional properties of the atoms. There are two interesting limits, the strongly interacting limit $ka_s \gg 1$ and the weakly interacting limit $ka_s \ll 1$. In the weakly interacting limit $f = -a_s$ and $\sigma = 4\pi a_s^2$, thus total cross section is that of solid sphere with radius a_s . In the strongly interacting limit, $f = -1/(ik)$ and $\sigma = 4\pi/k^2$, the

total cross section is independent of the scattering length. This regime is known as the unitary limit.

So far we discussed only the case of distinguishable particles, let us now discuss the case of indistinguishable particles. For identical bosons/fermions wavefunction $\psi_{\mathbf{k}}(\mathbf{r})$ must be symmetric/anti-symmetric under the particle exchange $\mathbf{r} \rightarrow -\mathbf{r}$. This corresponds to changing $r \rightarrow r$, $\theta \rightarrow \pi - \theta$ and $\phi \rightarrow \pi + \phi$, and symmetrizing/anti-symmetrizing the wave function:

$$\psi_{\mathbf{k}}(\mathbf{r}) = e^{i\mathbf{k}\mathbf{r}} \pm e^{i\mathbf{k}\mathbf{r}} + [f(k, \theta) \pm f(k, \pi - \theta)] \frac{e^{ikr}}{r} \quad (3.13)$$

Therefore cross section of s-wave collision for bosons and fermions in ultracold limit can be expressed as:

$$\sigma_{\text{bosons}} = 8\pi a_s, \quad \sigma_{\text{fermions}} = 0. \quad (3.14)$$

Thus identical fermions do not undergo s-wave scattering in ultracold limit, therefore one component Fermi gas can be very well approximated with the non-interacting Fermi gas. As we discussed in previous chapter, this is the main reason why we can not cool the one component Fermi gas with evaporative cooling. In general identical bosons do not scatter with odd l , while identical fermions do not scatter with even l .

3.2 Pseudo-potential

In previous section we demonstrated that for ultracold and dilute systems the properties of the gas can be quite accurately described by a single parameter, the s-wave scattering length a_s . The effect of interaction is independent of the details of the shape of the potential. Of course a_s depends on the potential. If we are just interested in the asymptotic phase shift it may be good idea to search for some alternative, mathematically simpler potential than e.g. the Van der Waals potential, which basically reproduces the same asymptotic behavior. Such a potential is called a

pseudo-potential [Huang and Yang, 1957]. This procedure is very similar to the image method used in electrostatics, where if we are interested in the long range behavior of spherically symmetric charge distribution we can model it with point charge at its center. Effectively, a point charge and a spherically symmetric charge distribution will generate the same electric field in long distance from the charge distribution, so it does not matter which one we use in our calculations. Similarly, in pseudo-potential approach we change the Van der Waals potential, with some model potential which reproduces the same a_s and therefore results in the same scattering amplitude. Since in the weakly interacting limit $f = -a_s$, we can connect the potential and a_s via the first order Born approximation [Pethick and Smith, 2008]

$$a_s = \frac{M_r}{2\pi} \int d\mathbf{r} U(\mathbf{r}). \quad (3.15)$$

From the above equality we can deduce that when $a_s > 0$ we have repulsive interaction and when $a_s < 0$ we have attractive interaction. Pseudo potential $U_{\text{eff}}(\mathbf{r})$ must satisfy the above equality, thus we have following equation

$$\int d\mathbf{r} U_{\text{eff}}(\mathbf{r}) = \frac{4\pi a_s}{M} \equiv g \quad (3.16)$$

where we used $M_r = M/2$. Obviously the simplest potential which can satisfy above equation is the so called contact interaction potential

$$U_{\text{eff}} = g\delta(\mathbf{r}) \quad (3.17)$$

where $\delta(\mathbf{r})$ is the Dirac-delta function. Thus, we use a "point interaction" to represent the spherically symmetric interaction, just as we can represent a spherical charge distribution with a point charge. While mathematically simple, the contact potential gives a bare constant g interaction in the momentum space. Therefore the potential will not fall off at large momenta leading to an ultra-violet divergence.

This is an unphysical behavior since any physical potential will fall off at large momenta. Fortunately this problem can be solved by adding a divergent integral which will cancel out the unphysical divergence. Thus when calculating physical quantities we can trade the bare interaction g with scattering length a_s via following relation [Ketterle and Zwierlein, 2008]

$$\frac{1}{g} = \frac{M}{4\pi a_s} - \int \frac{d^3k}{(2\pi)^3} \frac{M}{k^2}. \quad (3.18)$$

In this thesis we will model the pair interaction between the atoms with contact potential based on the arguments given in this section.

3.3 Tuning the Interaction Strength: Fano-Feshbach Resonance

A Fano-Feshbach is a scattering resonance which occurs when two scattering atoms couple to bound state during the scattering process. It was first investigated in 1930's by Fano [Fano, 1935] and later developed both in atomic physics by Fano [Fano, 1961] and in nuclear physics by Feshbach [Feshbach, 1958] independently. Fano-Feshbach resonance can be used to tune the scattering length. To understand the mechanism let us assume that we have two particles interacting via some potential $U(\mathbf{r})$ and have total energy E . Collision paths of scattered state like this are termed open channel. We also assume that there is another collision path which supports bound state with energy E_b . This state has larger continuum energy, therefore is not available to particles due to conservation of energy and therefore is termed as closed channel (see Fig. 3.3). However if the energy difference between the incident energy and the closed channel becomes small, they can couple when particles are scattered. This coupling alters the energy of the scattering state which can be calculated via the second order perturbation theory as [Ueda, 2010]

$$\Delta E = \frac{|\langle i | H_{\text{int}} | b \rangle|^2}{E - E_b} \quad (3.19)$$

where $|i\rangle$ is the incident state, $|b\rangle$ is the bound state, H_{int} is the interaction Hamiltonian representing the coupling of the incident and bound state. ΔE is the energy change due to Fano-Feshbach resonance. Since we are working in ultracold regime, energy of the incident state is very low and can be neglected

$$\Delta E = -\frac{|\langle i|H_{\text{int}}|b\rangle|^2}{E_b} \quad (3.20)$$

Due to their different spin configurations, the closed channel and the open channel can have different magnetic moments μ . Due to this difference in their magnetic moments, it is possible to tune their relative energy by applying a magnetic field. Therefore binding energy can be expressed as $E_b = \Delta\mu(B - B_0)$ under the influence of the magnetic field in terms of the magnetic moment difference between the open and closed channel. Here B_0 denotes the position of the Fano-Feshbach resonance. Substituting this to Eq. (3.20), we get

$$\Delta E = -\frac{|\langle i|H_{\text{int}}|b\rangle|^2}{\Delta\mu(B - B_0)} \quad (3.21)$$

As we saw in previous section the interaction between the atoms in the ultracold regime is related to the scattering length. Therefore we can deduce the dependence of the scattering length on the magnetic field from Eq. (3.21) as

$$a_s = a_{bg} \left(1 - \frac{\Delta B}{B - B_0} \right) \quad (3.22)$$

where a_{bg} is the background scattering length, ΔB is the width of the Feshbach resonance. Note that from Eq. (3.21) we can also see that ΔB is inversely proportional to $\Delta\mu$. From Eq. (3.22) we can see that by changing the external magnetic field we can tune the scattering length [Inouye et al., 1998, Courteille et al., 1998, Cornish et al., 2000], hence control the effective interaction between the atoms. Not only can we alter the strength of the interaction by several orders of magnitude but we can even change the sign of a_s going from attractive to repulsive interaction. This

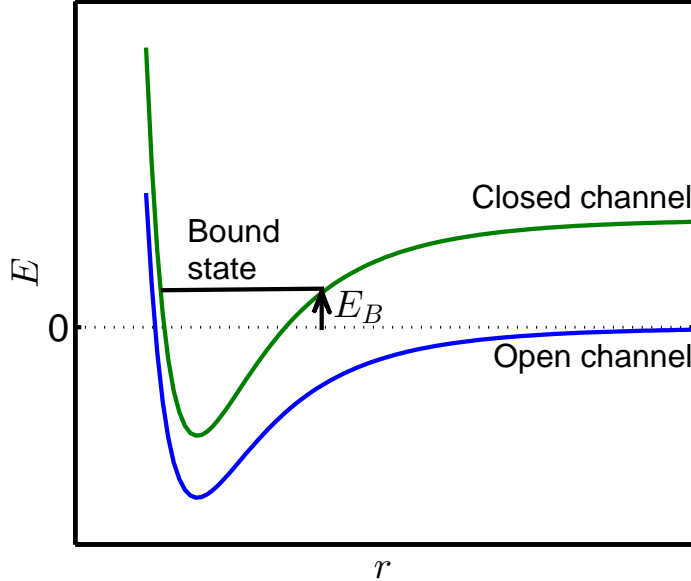


Figure 3.3: Schematic diagram showing two-channel model of Feshbach resonance. Closed channel supports bound state with energy E_b . As explained in the text relative distance between these two channels can be tuned via external magnetic field.

gives a very big advantage to ultracold atomic systems, since in no other system in physics we have such clear control over the interaction of the system. Let us note that besides the magnetically induced resonance studied in this section, there are other ways to induce resonance such as by optical means. For a comprehensive review of Feshbach resonances in ultracold atoms the reader may consult [Chin et al., 2010]

3.4 Scattering in 2D

Since in this thesis we will be mostly focused on 2D Fermi gas, it may be useful to analyze scattering in two dimensions. Reducing the dimension from 3D to 2D strongly changes the physics of the scattering process. We will repeat the same analysis we did for 3D Fermi gas. In this section we follow the presentation given in [Adhikari, 1986], (if interested in more details reader may consult that paper). We again start with assuming that two particles have equal mass M , and that we

have short ranged potential which has circular symmetry. We analyze the problem in center of mass reference frame and reduce the problem to single body Schrödinger equation with reduced mass $M_r = M/2$

$$\left[-\frac{\nabla^2}{2M_r} + U(\mathbf{r}) \right] \psi_{\mathbf{k}}(\mathbf{r}) = \epsilon_k \psi_{\mathbf{k}}(\mathbf{r}) \quad (3.23)$$

where $\epsilon_k = k^2/(2M_r)$ is the kinetic energy. We guess the solution in the asymptotic limit $|\mathbf{r}| \gg R_e$, where the potential can be taken as zero. In 2D this is superposition of an incident plane wave and a scattered circular wave

$$\psi_{\mathbf{k}}(\mathbf{r}) = e^{i\mathbf{k}\mathbf{r}} - f(k, \phi) \sqrt{\frac{i}{8\pi k r}} e^{ikr} \quad (3.24)$$

Here ϕ denotes the angle between the incident plane wave and the scattered wave and $f(k, \phi)$ is the scattering amplitude. The pre-factor $\sqrt{i/(8\pi k r)}$ accounts for the conservation of the probability density of the outgoing wave.

Differential cross section in 2D can be defined as:

$$\frac{d\sigma}{d\phi} = \frac{|f(k, \phi)|^2}{8\pi k} \quad (3.25)$$

By integrating the above equation we get the total cross section which depends only on k

$$\sigma(k) = \frac{1}{8\pi k} \int d\phi |f(k, \phi)|^2 \quad (3.26)$$

Since the potential has circular symmetry we use partial wave expansion in 2D

$$\psi_{\mathbf{k}}(\mathbf{r}) = \sum_{l=0}^{\infty} A_l \cos(l\phi) R_{k,l}(r) \quad (3.27)$$

with $A_l = 2 - \delta_{l,0}$, where $\delta_{l,0}$ is the Kronecker delta function. If we substitute this to the Schrödinger equation, the problem reduces to a one dimensional radial Schrödinger equation

$$-\frac{1}{2M_r r} \frac{d}{dr} \left(r \frac{dR_{k,l}(r)}{dr} \right) + \left[U(r) + \frac{l^2}{2M_r r^2} - \epsilon_k \right] R_{k,l}(r) = 0 \quad (3.28)$$

When $r \rightarrow \infty$, where we can ignore the potential and can take the first terms of Neumann and Bessel functions, the wave function becomes

$$\psi_{\mathbf{k}}(\mathbf{r}) = \sum_{l=0}^{\infty} \frac{B_l \cos(l\phi)}{2i\sqrt{k}} \left[(-i)^{l-1/2} e^{i\delta_l} \frac{e^{ikr}}{\sqrt{r}} - i^{l-1/2} e^{-i\delta_l} \frac{e^{-ikr}}{\sqrt{r}} \right]. \quad (3.29)$$

Here $e^{i\delta_l}$ represent the phase shift due to the collision. In order to determine the scattering amplitude, we also expand the Eq. (3.24) in partial waves

$$\psi_{\mathbf{k}}(\mathbf{r}) = \sum_{l=0}^{\infty} \frac{A_l i^l \cos(l\phi)}{i\sqrt{2\pi k}} \left[(-i)^{l-1/2} \frac{e^{ikr}}{\sqrt{r}} - i^{l-1/2} \frac{e^{-ikr}}{\sqrt{r}} \right] - f(k, \phi) \sqrt{\frac{i}{8\pi k}} \frac{e^{ikr}}{\sqrt{r}}. \quad (3.30)$$

By comparing Eq. (3.29) and Eq. (3.30) we determine the scattering amplitude

$$f(k, \phi) = \sum_{l=0}^{\infty} \frac{2A_l \cos(l\phi)}{i} (1 - e^{2i\delta_l}) \quad (3.31)$$

Integrating Eq. (3.26) we determine the total cross section

$$\sigma(k) = \sum_{l=0}^{\infty} \frac{4A_l \sin^2(\delta_l)}{k} \quad (3.32)$$

Since we are working in the ultracold limit, we are interested in the low energy scattering. Note that the repulsive potential barrier is still present in 2D as can be seen in Eq. (3.28). Therefore we can again restrict ourselves to the s-wave scattering. In this limit scattering amplitude can be expressed as

$$f(k) = \frac{2}{i} (1 - e^{2i\delta_0}) = \frac{4}{i - \cot \delta_0} \quad (3.33)$$

Similar to 3D case, in low energy limit we can expand the phase shift to get its relation with s-wave scattering length in two dimension $a_{s,2D}$

$$\cot \delta_0(k) \approx \frac{2}{\pi} \ln(ka_{s,2D}) + O(k^2). \quad (3.34)$$

Using the 2D scattering length we can define binding energy E_b

$$E_b = \frac{1}{Ma_{s,2D}^2} \quad (3.35)$$

Thus the 2D scattering amplitude in low energy takes the following simple form

$$f(k) = \frac{4\pi}{\ln\left(\frac{1}{ka_{s,2D}}\right)^2 + i\pi} = \frac{4\pi}{\ln\left(\frac{E_b}{\epsilon_k}\right) + i\pi} \quad (3.36)$$

Note that this result is considerably different than the 3D result. In the weakly interacting limit and low energies 3D scattering amplitude was independent of the energy and was simply $-a_s$. But in 2D scattering amplitude retains its logarithmic energy dependence even in this limit. Note that in $k \rightarrow 0$ limit the scattering amplitude goes to zero, not to $-a_s$ as in 3D and total cross section diverges.

As we discussed in the previous chapter, experimentally 2D Fermi gas can be realized in a trap by tight confinement in the z direction combined with weak harmonic trapping in x and y directions [Martinyanov et al., 2010]. Such a system is called a quasi-2D system. Such a system has the identical 2D scattering amplitude with the ideal 2D system. The E_b of the quasi-2D Fermi gas can be related to 3D scattering via following relation [Petrov et al., 2003, Randeria et al., 1990]

$$E_b = 0.915\omega_z e^{\sqrt{2\pi}a_0/a_s} \quad (3.37)$$

where ω_z is the trap frequency in z direction. Thus E_b can be tuned by changing a_s or ω_z and therefore can be controlled experimentally. Since it is the only parameter involved in the scattering amplitude and total cross section, in 2D we will represent interaction with E_b .

3.5 Two Body Bound States in 2D and 3D

In this section we will analyze the behavior of two particles under attractive interaction. Bosonic particles become superfluid due to occupation of single quantum state which leads to Bose-Einstein condensation. But fermions can not occupy single quantum state due to the Pauli exclusion principle, therefore non-interacting fermions can not become superfluid and do not undergo any phase transition at low temperatures. However if there is some form of attractive interaction, the situation changes fundamentally. Now, paired fermions can show bosonic behavior and become a superfluid. Therefore understanding the effect of attractive interaction and the mechanism of pairing for fermions plays a central role in understanding superfluidity.

We assume that we have two attractively interacting particles with mass M . We assume that particles interact via the attractive contact interaction $U(\mathbf{r}) = -g\delta(\mathbf{r})$, with $g > 0$. We will investigate the conditions for the emergence of a bound state in 2D and 3D. We start with writing the Schrödinger equation with reduced mass $M_r = M/2$ and relative coordinate \mathbf{r}

$$\left[-\frac{\nabla^2}{2M_r} + U(\mathbf{r})\right]\psi(\mathbf{r}) = -E_b\psi(\mathbf{r}) \quad (3.38)$$

with $E_b > 0$ denotes the energy of the bound pair. We transform the Schrödinger equation to Fourier space via the transformation $\psi(\mathbf{r}) = \sum_{\mathbf{k}} \psi_{\mathbf{k}} e^{i\mathbf{k}\mathbf{r}}$, we multiply both sides with $\int d\mathbf{r}$ and use the orthogonality condition $\int d\mathbf{r} e^{i(\mathbf{k}-\mathbf{k}')\mathbf{r}} = \delta_{\mathbf{k}\mathbf{k}'}$ to get

$$2\epsilon_{\mathbf{k}}\psi_{\mathbf{k}} + \frac{1}{V} \sum_{\mathbf{k}'} U_{\mathbf{k}'-\mathbf{k}}\psi_{\mathbf{k}'} = -E_b\psi_{\mathbf{k}} \quad (3.39)$$

where $\epsilon_{\mathbf{k}} = k^2/(2M)$ and $U_{\mathbf{k}'-\mathbf{k}} = \int d\mathbf{r} U(\mathbf{r}) e^{i\mathbf{r}(\mathbf{k}-\mathbf{k}')}$. If we substitute the contact interaction $U_{\mathbf{k}} = -g$ we obtain

$$\psi_{\mathbf{k}} = \frac{g}{2\epsilon_{\mathbf{k}} + E_b} \frac{1}{V} \sum_{\mathbf{k}'} \psi_{\mathbf{k}'}. \quad (3.40)$$

Summing both sides over \mathbf{k} , we get following simple expression

$$\frac{1}{g} = \frac{1}{V} \sum_{\mathbf{k}} \frac{1}{2\epsilon_k + E_b}. \quad (3.41)$$

Let us analyze this equation for the 3D case. First we change the above sum with \mathbf{k} integral. Since contact interaction leads to divergence we also choose some high enough cut-off k_c . Then we have following integral

$$\frac{1}{g} = \frac{1}{2\pi^2} \int_0^{k_c} dk \frac{k^2}{2\epsilon_k + E_b} = \frac{M}{2\pi^2} \left[k_c - \sqrt{E_b M} \arctan \left(\frac{k_c}{\sqrt{E_b M}} \right) \right]. \quad (3.42)$$

If we use $\arctan(1/x) \simeq \pi/2$, which is valid for small and positive x , given large k_c we have

$$\frac{1}{g} \simeq \frac{M}{2\pi^2} \left(k_c - \sqrt{E_b M} \frac{\pi}{2} \right). \quad (3.43)$$

Note that above equation can not be valid for all g and gives as following condition

$$\frac{Mk_c}{2\pi^2} - \frac{1}{g} > 0 \Rightarrow g > \frac{2\pi}{Mk_c}. \quad (3.44)$$

If above condition is not satisfied than bound state can not be formed. So in 3D attractive interaction is not sufficient for emergence of bound state in general. Interaction should be higher than some threshold value to bind the particles.

Let us now repeat the same analysis in 2D. We again change the sum with an integral in Eq. (3.41)

$$\frac{1}{g} = \frac{1}{2\pi} \int_0^{k_c} dk \frac{k}{2\epsilon_k + E_b} = \frac{M}{4\pi} \ln \left(1 + \frac{k_c}{ME_b} \right) \simeq -\frac{M}{4\pi} \ln \left(\frac{ME_b}{k_c} \right) \quad (3.45)$$

where we used $\ln(1 + 1/x) \simeq -\ln(x)$ for small x , given k_c is a big cut-off again so that this expansion is justified. Note that above equation can be satisfied for any g

no matter how small. If we rearrange above equation we get the relation between E_b and g as

$$E_b = \frac{k_c^2}{M} e^{\frac{-4\pi}{Mg}} = 2E_c e^{\frac{-2A}{Dg}} \quad (3.46)$$

where D denotes the density of states in 2D, and $E_c = k_c^2/(2M)$ cut-off energy. Thus we see that unlike 3D, in 2D we always have a bound state for arbitrary small attractive potential. This result can be also understood via difference of the density of states of 3D and 2D [Ketterle and Zwierlein, 2008]. If we change the sum in Eq. (3.41) with density of states integral with cut-off E_c we have

$$\frac{1}{g} = \frac{1}{V} \int_0^{E_c} d\epsilon \frac{D(\epsilon)}{2\epsilon_k + E_b}. \quad (3.47)$$

As $g \rightarrow 0$ left hand side of above equation diverges. If we are to have a bound state for arbitrarily weak interaction right hand side integral must diverge for $E_b \rightarrow 0$. For 1D gas $D(\epsilon) \propto 1/\sqrt{\epsilon}$, and above integral diverges as $1/\sqrt{\epsilon}$, so we can always find bound state in 1D. In 2D density of states is constant, hence above integral diverges logarithmically in the limit $E_b \rightarrow 0$, we again have a bound state for arbitrary weak attractive interaction. But in 3D $D(\epsilon) \propto \sqrt{\epsilon}$ and integral is convergent in this limit. Hence there is minimum threshold interaction which must be overcome in order to form a bound pair.

As we discussed in the previous section in 2D interaction strength between the pairs will be expressed with E_b . Therefore in order to get rid off the ultra-violet divergence due to contact potential in the gap equation we will exchange g in favor E_b in 2D, and for that purpose we will use bound state equation (3.41) which has the same divergence behavior and the results become cut-off independent for large enough cut-off.

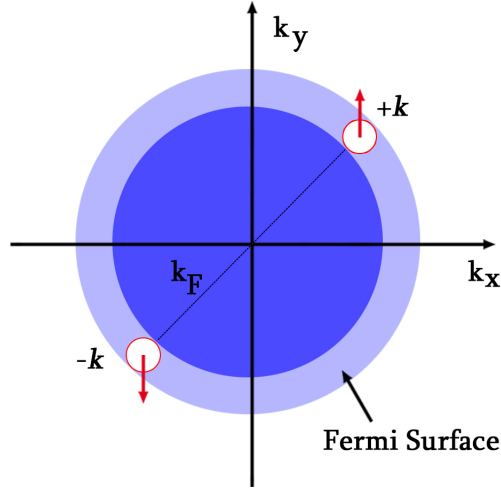


Figure 3.4: The Cooper problem. Two particles with opposite spin and momenta interact on the top of Fermi sea. The Fermi sea reduces the dimensionality of the system from 3D to 2D by blocking the low energy states. Since arbitrarily weak attractive interaction in 2D leads formation of bound pairs, these two particles form a Cooper pair.

3.6 The Cooper Problem

In this section we consider two weakly interacting fermions on top of a filled Fermi sphere in 3D (Fig. 3.4). This is known as the Cooper problem [Cooper, 1956]. The behavior of particles above the filled Fermi sphere is different than in vacuum. Pauli blocking makes the states below Fermi energy unavailable, therefore these weakly interacting particles are confined to a narrow shell above the Fermi surface. This effectively reduces the effective dimensionality to two, and we have effectively constant density of states. Thus based on the argument given in previous section that constant density of states leads to a bound state for arbitrary low attractive interaction, we expect the pair of fermions over the top of Fermi sea to form bound pairs for any attractive interaction no matter how small.

We again start our analysis with the Schrödinger equation of relative position \mathbf{r} in center of mass coordinates,

$$\left[-\frac{\nabla^2}{2M_r} + U(\mathbf{r}) \right] \psi_{\mathbf{k}}(\mathbf{r}) = E\psi_{\mathbf{k}}(\mathbf{r}) \quad (3.48)$$

where $E = 2E_F - E_b$ is the energy of the pair and E_b denotes the binding energy, we assume that particles have opposite spin and momentum. We again assume attractive contact interaction $U(\mathbf{r}) = -g\delta(\mathbf{r})$ which is relevant for our systems. Following the same procedure outlined in previous section we find an analogous expression of Eq. (3.41) for our case

$$\frac{1}{g} = \frac{1}{V} \sum_{\mathbf{k} > k_F} \frac{1}{2\epsilon_{\mathbf{k}} - E}. \quad (3.49)$$

In order to renormalize the the divergence due to contact interaction we use Eq. (3.18) and define $g_0 = 4\pi a_s/M$ for notational simplicity. If we also change the sum with an integral we get

$$-\frac{1}{g_0} = \frac{1}{2\pi^2} \int_{k_F}^{\infty} dk k^2 \left(\frac{1}{2\epsilon_k - E} - \frac{1}{2\epsilon_k} \right) = \frac{MK^2}{2\pi^2} \int_{k_F}^{\infty} dk \frac{1}{k^2 - K^2} \quad (3.50)$$

where $K = \sqrt{ME}$. If we integrate the above convergent integral we get

$$\frac{1}{g_0} = \frac{MK}{4\pi^2} \ln \left(\frac{k_F - K}{k_F + K} \right). \quad (3.51)$$

If assume that interaction is very weak, so that $E_b \ll E_F$ and expand the numerator and denominator of the fraction to first order in E_b/E_F we get $E_b = 8E_F e^{-4\pi/(MKg_0)}$. If we further insert $K \approx k_F$, we get following relation

$$E_b = 8E_F e^{-2/(D(E_F)g_0)} \quad (3.52)$$

where $D(E_F) = Mk_F/(2\pi^2)$ is the effective 2D density of states around the Fermi level. For any $g > 0$ above expression implies that $E_b > 0$, thus for any arbitrary

attractive interaction particles will form a bound state. This pair of particles is called a Cooper pair. Thus Fermi sea is unstable towards pair formation given a small attractive interaction creating the Fermi surface instability. The importance of Fermi sphere for pair formation is also visible in the above equation, if we take $E_F = 0$, which corresponds to having particles in vacuum instead of at the top of Fermi sphere, we get $E_b = 0$. Also we should note that as density of states increases E_b also increases.

It is interesting to calculate the mean square radius of the pair wave function, which relates to the size of the Cooper pair.

$$\langle r^2 \rangle = \frac{\int d\mathbf{r} r^2 |\psi(\mathbf{r})|^2}{\int d\mathbf{r} |\psi(\mathbf{r})|^2}. \quad (3.53)$$

We take the Fourier transform of the wavefunctions, so that the constraint $\mathbf{k} > k_F$ can be easily implemented

$$\langle r^2 \rangle = \frac{\sum_{k > k_F} |\nabla_{\mathbf{k}} \psi_{\mathbf{k}}|^2}{\sum_{k > k_F} |\psi_{\mathbf{k}}|^2} \quad (3.54)$$

and we used $\nabla_{\mathbf{k}} \psi_{\mathbf{k}} = -i \int d\mathbf{r} \mathbf{r} e^{-i\mathbf{k}\mathbf{r}} \psi(\mathbf{r})$. The momentum space wave functions can be expressed using Eq. (3.40) adapted for our problem (this corresponds interchanging E_b with $-E$). We change the sums with integrals

$$\langle r^2 \rangle = \frac{4 \int_{k_F}^{\infty} dk k^4 \left(\frac{k^2}{M} - E \right)^{-4}}{M^2 \int_{k_F}^{\infty} dk k^2 \left(\frac{k^2}{M} - E \right)^{-2}} \quad (3.55)$$

and use the assumption that interaction is weak $E_b \ll E_F$, we get the expression for the mean square radius of the pair wave function

$$\langle r^2 \rangle = \frac{4k_F^2}{3M^2 E_b^2}. \quad (3.56)$$

Using $\langle r^2 \rangle$ we define the coherence length $\xi = \sqrt{\langle r^2 \rangle}$ which gives the size of the Cooper pair. Let us compare the size of Cooper pairs with inter-particle distance

$$\frac{\xi}{d_n} = \xi n^{1/3} \sim \frac{E_F}{E_b} \ll 1 \quad (3.57)$$

where we related n to E_F using Eq. (2.40). Cooper pairs are very large compared to the inter-particle spacing, therefore Cooper pairs overlap in real space and can not be thought as localized bosons.

Lastly let us point out that in this section we assumed that center of mass momentum \mathbf{q} of the Cooper pair is zero. One can show that for small center of mass momentum the binding energy becomes

$$E_b(\mathbf{q}) = E_b - \frac{k_F |\mathbf{q}|}{2M}. \quad (3.58)$$

Thus binding energy of the pair is reduced by the center of mass motion of the pair, it can even be destroyed. Thus zero center of mass momentum pairing is generally preferred.

3.7 BCS-BEC Crossover in 3D

In previous section we demonstrated that if two fermions are placed near Fermi surface will form bound pairs no matter how small the interaction is. In real systems of course we have many fermions, hence the pairing should occur collectively and self consistently. In this section we discuss the BCS theory which involves such pairing, and initially was developed to explain superconductivity [Bardeen et al., 1957]. Since in previous section we demonstrated that zero center of mass momentum pairing is energetically preferred, we assume that all the pairs are formed from particles with opposite spin and momentum. We also assume that the particles interact via contact interaction $U(\mathbf{r}) = -g\delta(\mathbf{r})$. The Hamiltonian describing this system can be expressed as

$$H = \sum_{\mathbf{k}, \sigma} (\epsilon_{\mathbf{k}} - \mu) \hat{a}_{\mathbf{k}\sigma}^\dagger \hat{a}_{\mathbf{k}\sigma} - \frac{g}{V} \sum_{\mathbf{k}, \mathbf{k}'} \hat{a}_{\mathbf{k}\uparrow}^\dagger \hat{a}_{-\mathbf{k}\downarrow}^\dagger \hat{a}_{\mathbf{k}'\downarrow} \hat{a}_{-\mathbf{k}'\uparrow} \quad (3.59)$$

where $\epsilon_k = k^2/(2M)$ is the kinetic energy, $\hat{a}_{\mathbf{k}\sigma}^\dagger$ ($\hat{a}_{\mathbf{k}\sigma}$) is creation (annihilation) operator creating (annihilating) a fermion with pseudo-spin σ and momentum \mathbf{k} . μ is the chemical potential which fixes the average number of fermions to the desired value. We assume that the ground state of the above Hamiltonian is described by the so called BCS wave function [Bardeen et al., 1957, Leggett, 1980]

$$|\Psi_{\text{BCS}}\rangle = \prod_{\mathbf{k}} (u_{\mathbf{k}} + v_{\mathbf{k}} \hat{a}_{\mathbf{k}\uparrow}^\dagger \hat{a}_{-\mathbf{k}\downarrow}^\dagger) |0\rangle. \quad (3.60)$$

Here $|v_{\mathbf{k}}|^2$ represents the probability of the pair state $(\mathbf{k} \uparrow, -\mathbf{k} \downarrow)$ being occupied, and $|u_{\mathbf{k}}|^2$ denotes the probability of that state being empty. Therefore normalization of the wave function gives us following condition

$$1 = \langle \Psi_{\text{BCS}} | \Psi_{\text{BCS}} \rangle = \prod_{\mathbf{k}} (|u_{\mathbf{k}}|^2 + |v_{\mathbf{k}}|^2) \Rightarrow |u_{\mathbf{k}}|^2 + |v_{\mathbf{k}}|^2 = 1. \quad (3.61)$$

Note that the BCS wave function can also describe the non-interacting Fermi gas by setting $v_{\mathbf{k}} = \Theta(k_F - k)$. For $g > 0$, $v_{\mathbf{k}}$ can be determined by minimizing the expectation value of Eq. (3.59) over $|\Psi_{\text{BCS}}\rangle$. The expectation value of the Hamiltonian over BCS wavefunction can be determined as

$$\langle H \rangle = 2 \sum_{\mathbf{k}} (\epsilon_k - \mu) |v_{\mathbf{k}}|^2 - \frac{g}{V} \sum_{\mathbf{k}, \mathbf{k}'} v_{\mathbf{k}}^* u_{\mathbf{k}} v_{\mathbf{k}'} u_{\mathbf{k}'}. \quad (3.62)$$

For simplicity let us assume that $u_{\mathbf{k}}$ and $v_{\mathbf{k}}$ are real. If we minimize $\partial \langle H \rangle / \partial v_{\mathbf{k}}$ and apply the normalization condition $u_{\mathbf{k}}^2 + v_{\mathbf{k}}^2 = 1$ we get the following equation

$$2(\epsilon_k - \mu) u_{\mathbf{k}} v_{\mathbf{k}} = (u_{\mathbf{k}}^2 - v_{\mathbf{k}}^2) \Delta \quad (3.63)$$

where

$$\Delta \equiv \frac{g}{V} \sum_{\mathbf{k}} \langle \hat{a}_{\mathbf{k}\uparrow}^\dagger \hat{a}_{-\mathbf{k}\downarrow}^\dagger \rangle = \frac{g}{V} \sum_{\mathbf{k}} u_{\mathbf{k}} v_{\mathbf{k}}. \quad (3.64)$$

is called the order parameter of the superfluid state, it can be interpreted as energy required to break the pairs. We can further solve Eq. (3.63) to get

$$u_{\mathbf{k}}^2 = \frac{1}{2} \left[1 + \frac{(\epsilon_{\mathbf{k}} - \mu)}{E_{\mathbf{k}}} \right], \quad v_{\mathbf{k}}^2 = \frac{1}{2} \left[1 - \frac{(\epsilon_{\mathbf{k}} - \mu)}{E_{\mathbf{k}}} \right] \quad (3.65)$$

where as we will demonstrate below $E_{\mathbf{k}}$ is the excitation energy of the system and can be expressed as

$$E_{\mathbf{k}} = \sqrt{(\epsilon_{\mathbf{k}} - \mu)^2 + \Delta^2}. \quad (3.66)$$

If we divide both sides of Eq. (3.64) with $(\epsilon_{\mathbf{k}} - \mu)$ and sum over \mathbf{k} we get the so called gap equation

$$\frac{1}{g} = \frac{1}{V} \sum_{\mathbf{k}} \frac{1}{2E_{\mathbf{k}}}. \quad (3.67)$$

We again eliminate the ultra-violet divergence using Eq. (3.18), which gives us the final form of the gap equation

$$\frac{M}{4\pi a_s} = \frac{1}{V} \sum_{\mathbf{k}} \left(\frac{1}{2\epsilon_{\mathbf{k}}} - \frac{1}{2E_{\mathbf{k}}} \right). \quad (3.68)$$

In order to fully solve the problem we need to determine Δ and μ for a given a_s . Therefore we need one more equation, and this is the so called number equation which gives the total particle number

$$N = \sum_{\sigma, \mathbf{k}} \langle \hat{a}_{\mathbf{k}\sigma}^\dagger \hat{a}_{\mathbf{k}\sigma} \rangle = 2 \sum_{\mathbf{k}} v_{\mathbf{k}}^2 = \sum_{\mathbf{k}} \left[1 - \frac{(\epsilon_{\mathbf{k}} - \mu)}{E_{\mathbf{k}}} \right]. \quad (3.69)$$

In deriving the gap and the number equations we used a variational ansatz. Alternatively we can apply mean field approximation to the Hamiltonian given in Eq. (3.59). In the mean field approximation we assume that certain operator \hat{O} only weakly fluctuates around its nonzero expectation value so that we can write it as $\hat{O} = \langle \hat{O} \rangle + \delta\hat{O}$.

Under the mean field approximation the multiplication of two operators can be written as

$$\hat{O}_1 \hat{O}_2 \approx \hat{O}_1 \langle \hat{O}_2 \rangle + \hat{O}_2 \langle \hat{O}_1 \rangle - \langle \hat{O}_1 \rangle \langle \hat{O}_2 \rangle, \quad (3.70)$$

where we neglected the term $\delta \hat{O}_1 \delta \hat{O}_2$. If we choose $\hat{O}_1 = \hat{a}_{\mathbf{k}\uparrow}^\dagger \hat{a}_{-\mathbf{k}\downarrow}^\dagger$, $\hat{O}_2 = \hat{a}_{-\mathbf{k}'\downarrow} \hat{a}_{\mathbf{k}'\uparrow}$ and apply mean field approximation, by using the definition of Δ given in Eq. (3.64), Hamiltonian becomes

$$H^{\text{mf}} = \sum_{\mathbf{k}} \hat{\psi}_{\mathbf{k}}^\dagger \begin{pmatrix} \epsilon_k - \mu & \Delta \\ \Delta & -\epsilon_k + \mu \end{pmatrix} \hat{\psi}_{\mathbf{k}} + \sum_{\mathbf{k}} (\epsilon_k - \mu) + \frac{\Delta^2 V}{g} \quad (3.71)$$

where $\hat{\psi}_{\mathbf{k}}^\dagger = (\hat{a}_{\mathbf{k}\uparrow}^\dagger, \hat{a}_{-\mathbf{k}\downarrow}^\dagger)$. The above equation can be diagonalized via a Bogoliubov-Valatin transformation

$$\begin{pmatrix} \hat{\gamma}_{\mathbf{k}\uparrow} \\ \hat{\gamma}_{-\mathbf{k}\downarrow}^\dagger \end{pmatrix} = \begin{pmatrix} u_{\mathbf{k}} & -v_{\mathbf{k}} \\ v_{\mathbf{k}} & u_{\mathbf{k}} \end{pmatrix} \begin{pmatrix} \hat{a}_{\mathbf{k}\uparrow} \\ \hat{a}_{-\mathbf{k}\downarrow}^\dagger \end{pmatrix} \quad (3.72)$$

where $\hat{\gamma}_{\mathbf{k}\uparrow}^\dagger$ is the creation operator for quasi-particle such that the ground state of the superfluid is its vacuum, and satisfies the fermionic anticommutation relation $[\hat{\gamma}_{\mathbf{k}\uparrow}, \hat{\gamma}_{\mathbf{k}\uparrow}^\dagger]_+ = u_{\mathbf{k}}^2 + v_{\mathbf{k}}^2 = 1$. $u_{\mathbf{k}}$ and $v_{\mathbf{k}}$ are same with those we defined above. After this transformation Hamiltonian becomes diagonal

$$H^{\text{mf}} = \sum_{\mathbf{k}, \sigma} E_k \hat{\gamma}_{\mathbf{k}\sigma}^\dagger \hat{\gamma}_{\mathbf{k}\sigma} + \sum_{\mathbf{k}} (\epsilon_k - \mu - E_k) + \frac{\Delta^2 V}{g}. \quad (3.73)$$

From this equation we see that E_k is really the excitation energy of the system.

In general, number and gap equations need to be solved simultaneously in order to determine the Δ , μ and any physical quantity we are interested in. Let us investigate the two extreme limits. First let us investigate the weakly attractive limit $1/(k_F a_s) \rightarrow -\infty$ which is known as the BCS limit. In this limit since particles are weakly attractive

we expect the chemical potential to be very close to its non-interacting value $\mu \approx E_F$. Besides we expect that energy required to break the pairs is very small compared to the Fermi energy $\Delta \ll E_F$. If we change the sum in the gap equation Eq. (3.68) with density of states integral, and set $\mu = E_F$ it becomes

$$\frac{\pi}{2k_F a_s} = \int_0^\infty d\tilde{\epsilon} \sqrt{\tilde{\epsilon}} \left[\frac{1}{2\tilde{\epsilon}} - \frac{1}{2\sqrt{(\tilde{\epsilon}-1)^2 + (\Delta/E_F)^2}} \right] = \ln[e^2 \Delta / (8E_F)] \quad (3.74)$$

where $\tilde{\epsilon} = \epsilon_k / E_F$. If we rearrange this equation we get the order parameter in the BCS limit

$$\Delta = \frac{8}{e^2} E_F e^{-\pi/(2|a_s|k_F)} = \frac{8}{e^2} E_F e^{-1/[D(E_F g_0)]} \quad (3.75)$$

where similar to the single Cooper pair problem $D(E_F) = M k_F / (2\pi^2)$ is the effective 2D density of states around the Fermi level and $g_0 = 4\pi a_s / M$. Note that order parameter is larger than the binding energy of a single Cooper pair with a non-interacting Fermi sphere by a factor $e^{1/[D(E_F g_0)]}$. This is a direct result of collective pairing, but nevertheless still the gap is exponentially small compared to the Fermi energy, which signals that Cooper pairs are very fragile. Fermionic nature of this limit can be also seen from the momentum distribution $n_{\mathbf{k}} = \langle \hat{a}_{\mathbf{k}\sigma}^\dagger \hat{a}_{\mathbf{k}\sigma} \rangle = v_{\mathbf{k}}^2$ which can be expressed as

$$n_{\mathbf{k}} = \frac{1}{2} \left[1 - \frac{(\epsilon_k - \mu)}{\sqrt{(\epsilon_k - \mu)^2 + \Delta^2}} \right]. \quad (3.76)$$

If we substitute $\mu \approx E_F$ and take into account the inequality $E_F \ll \Delta$, the momentum distribution is almost the same with the non-interacting Fermi distribution $n_{\mathbf{k}} = \Theta(E_F - \epsilon_k)$, except in a very narrow region on the order of Δ around the Fermi energy $\epsilon_k = E_F$.

Let us now investigate the other limit $1/(k_F a_s) \rightarrow \infty$ known as the BEC limit. In this limit $\mu < 0$ and we assume that $|\mu| \gg \Delta$. We transform the sum in the number

equation to an integral, and expand the integrand as $1 - (\epsilon_k - \mu)/E_k \approx \Delta^2/2(\epsilon_k - \mu)^2$ using the $|\mu| \gg \Delta$ condition. The number integral can be evaluated analytically as

$$n \approx \frac{\Delta^2}{2\pi^2} \int_0^\infty dk \frac{k^2}{2[k^2/2M + |\mu|]^2} = \frac{M^{2/3} \Delta^2}{4\pi \sqrt{2|\mu|}}. \quad (3.77)$$

This equation can be rearranged to give us the following ratio

$$\frac{\Delta^2}{\mu^2} \approx \frac{4\sqrt{2}\pi n}{(M|\mu|)^{3/2}} \quad (3.78)$$

which self consistently confirms our assumption $|\mu| \gg \Delta$. Next we expand the integrand of the gap equation as $1/E_k \approx [|\mu| + k^2/(2M)]^{-1} - \Delta^2/[|\mu| + k^2/(2M)]^3$. After this expansion gap equation too can be solved analytically to yield

$$\frac{1}{a_s \sqrt{2M|\mu|}} \approx 1 + \frac{\Delta}{16\mu^2}. \quad (3.79)$$

If we solve Eq. (3.77) and Eq. (3.79) for μ and Δ we get

$$\Delta \approx \frac{4E_F}{\sqrt{3\pi k_F a_s}}, \quad (3.80)$$

$$\mu \approx -\frac{1}{2Ma_s^2} + \frac{\pi n a_s}{M}. \quad (3.81)$$

Using the chemical potential let us calculate the energy required to add two fermions with opposite spin to the system. This is simply twice the chemical potential

$$2\mu \approx -\frac{1}{Ma_s^2} + \frac{4\pi(2a_s)}{2M} \frac{n}{2}. \quad (3.82)$$

The first term is the the binding energy between the two fermions, the second term describes the mean-field term due to repulsive interaction of the molecule formed by

these fermions with other $n/2$ molecules. Thus chemical potential has exactly the value we would expect of repulsively interacting bosons. We started with fermions and ended up having bosons. Note that the effective scattering length describing the interaction between the bosons is $2a_s$. Let us also look at the momentum distribution given in Eq. (3.76) in the BEC limit. Note that in this limit the conditions $\mu < 0$ and $\Delta \ll |\mu|$ imply that n_k is monotonically decaying function with value smaller than one. Thus the fermionic nature of momentum distribution is lost.

Between these two limits gap and number equation can be solved self consistently to determine the order parameter and chemical potential. We present the numerically obtained μ and Δ in Fig. 3.5. It is seen that Δ , μ and any physical quantity is smoothly connected between BCS and BEC limits. If we tune the interaction between the fermions via Fano-Feshbach resonance we will observe a smooth crossover as opposed to a quantum phase transition where we would observe an abrupt change in the state of the system and some thermodynamic quantities diverge. In Fig. 3.6 we show the momentum distribution for different interaction strengths. In the weak interaction limit the characteristic Fermi distribution broadened with width Δ can be observed. As interaction increases the broadening becomes much more apparent and as we move to the BEC side the Fermi characteristic of the momentum distribution completely disappears.

It is interesting to analyze the excitation spectrum E_k . The excitation spectrum of the interacting Fermi gas acquires an energy gap as opposed to the non-interacting gas. For $\mu > 0$ the energy gap is equal to Δ and is located at finite momentum $k = \sqrt{2M\mu}$. But when $\mu \leq 0$, the energy gap is $\sqrt{\mu^2 + \Delta^2}$ and is located at $k = 0$ (See Fig. 3.7). The point at which the sign of chemical potential and therefore the nature of the excitation gap changes can be identified as a point where we pass from BCS to BEC side. The number and gap equations can be solved numerically at this point by substituting $\mu = 0$, to yield $1/(k_F a_s) \approx 0.553$ and $\Delta \approx 1.05E_F$. Note that at this point the order parameter is on the order of E_F which indicate strong pairing.

In this thesis we will be mainly interested in zero temperature properties of the

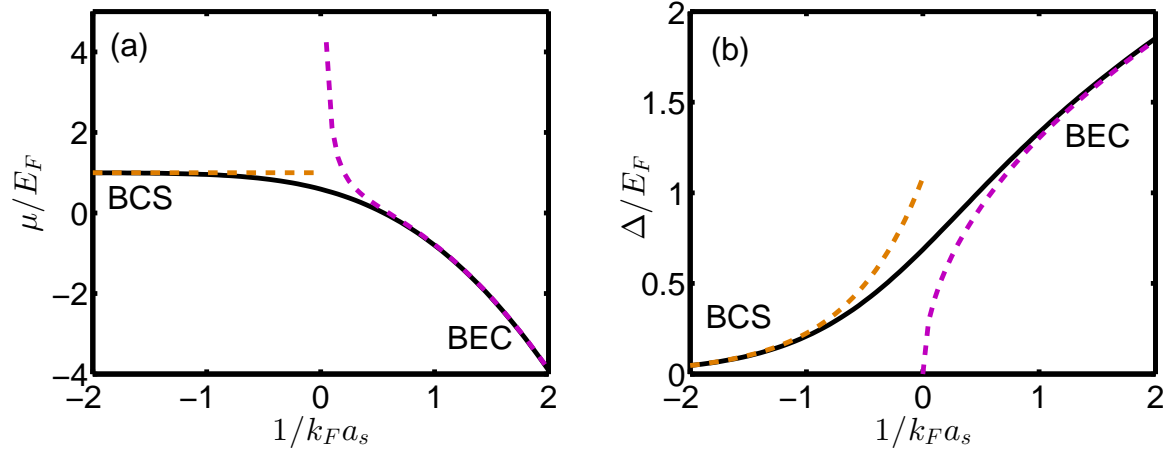


Figure 3.5: (a) Chemical potential μ and (b) order parameter Δ as a function scattering length $1/k_F a_s$ obtained from the self-consistent solution of the gap and number equations. Analytical expressions derived for the BCS and BEC limits are indicated with dashed lines, they agree very well with the numerical results. The transition from the BCS to the BEC side is smooth.

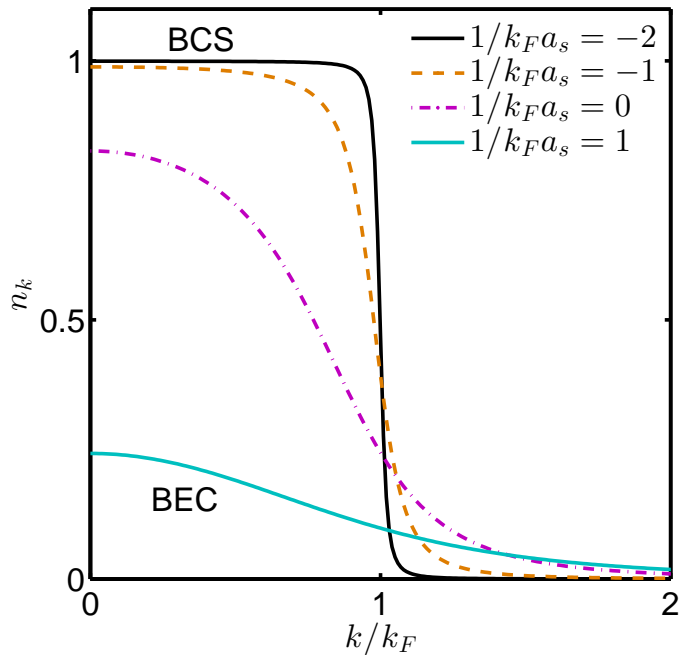


Figure 3.6: Momentum distribution n_k for different interaction strengths across the BCS-BEC crossover. In the BCS limit we observe a Fermi distribution broadened with width Δ , which clearly indicates fermionic character. On the other hand in the BEC limit we have occupation numbers much smaller than one, indicating absence of fermionic behavior.

Fermi gases. But for completeness let us briefly comment on the effect of the temperature T . Finite temperature leads to excitations on top of the superfluid ground state, and if high enough the excitations will eventually destroy the superfluidity. The critical temperature T_c for the destruction of superfluidity can be estimated from the gap equation at finite temperature. The finite temperature gap and number equations can be derived repeating the variational procedure given above using the finite temperature BCS wave function

$$|\Psi_{\text{BCS}}(T)\rangle = \prod_{\mathbf{k}} (u_{\mathbf{k}} \sqrt{1 - 2f_{\mathbf{k}}} + v_{\mathbf{k}} \sqrt{1 - 2f_{\mathbf{k}}} \hat{a}_{\mathbf{k}\uparrow}^\dagger \hat{a}_{-\mathbf{k}\downarrow}^\dagger + \sqrt{f_{\mathbf{k}}} \hat{a}_{\mathbf{k}\uparrow}^\dagger + \sqrt{f_{\mathbf{k}}} \hat{a}_{-\mathbf{k}\downarrow}^\dagger) |0\rangle. \quad (3.83)$$

where $u_{\mathbf{k}}^2(1 - 2f_{\mathbf{k}})$ and $v_{\mathbf{k}}^2(1 - 2f_{\mathbf{k}})$ are the probabilities of Cooper pairs not being occupied and occupied respectively, while $f_{\mathbf{k}}$ is the probability of broken pairs being occupied. Or alternatively we can substitute the inverse relation given in Eq. (4.33), which is

$$\hat{a}_{\mathbf{k}\uparrow} = u_{\mathbf{k}} \hat{\gamma}_{\mathbf{k}\uparrow} + v_{\mathbf{k}} \hat{\gamma}_{-\mathbf{k}\downarrow}^\dagger, \quad \hat{a}_{\mathbf{k}\downarrow} = u_{\mathbf{k}} \hat{\gamma}_{-\mathbf{k}\downarrow} - v_{\mathbf{k}} \hat{\gamma}_{-\mathbf{k}\uparrow}^\dagger, \quad (3.84)$$

to Eq. (3.64) and use the expectation values of the quasi-particles $\langle \hat{\gamma}_{\mathbf{k}\sigma}^\dagger \hat{\gamma}_{\mathbf{k}'\sigma'} \rangle = \delta_{\mathbf{k},\mathbf{k}'} \delta_{\sigma\sigma'} f(E_k)$, $\langle \hat{\gamma}_{\mathbf{k}\sigma} \hat{\gamma}_{\mathbf{k}'\sigma'}^\dagger \rangle = \delta_{\mathbf{k},\mathbf{k}'} \delta_{\sigma\sigma'} [1 - f(E_k)]$ and $\langle \hat{\gamma}_{\mathbf{k}\sigma} \hat{\gamma}_{\mathbf{k}'\sigma'} \rangle = \langle \hat{\gamma}_{\mathbf{k}\sigma}^\dagger \hat{\gamma}_{\mathbf{k}'\sigma'}^\dagger \rangle = 0$ to get the finite temperature gap equation. After renormalization the gap equation becomes

$$\frac{M}{4\pi a_s} = \frac{1}{V} \sum_{\mathbf{k}} \left(\frac{1}{2\epsilon_k} - \frac{1}{2E_k} \tanh \frac{\beta E_k}{2} \right) \quad (3.85)$$

where $\beta = 1/(k_B T)$ and $\tanh(\beta E_k/2) = [1 - 2f(E_k)]$. Similarly if we substitute quasi-particle expressions given in Eq. (3.84) to Eq. (3.69) we get the finite temperature number equation

$$N = \sum_{\mathbf{k}} \left[1 - \frac{(\epsilon_k - \mu)}{E_k} \tanh \frac{\beta E_k}{2} \right]. \quad (3.86)$$

In the BCS limit, in order to estimate the critical temperature for the emergence of superfluidity, we set $\Delta = 0$ and $\mu \approx E_F$ (which is not bad estimate for $\mu \gg k_B T$) and solve Eq. (3.85) for T . This gives as the following estimation for critical temperature

$$T_C \approx \frac{e^\gamma}{k_B \pi} \Delta_0 \quad (3.87)$$

where $\gamma = 0.57721$ is the Euler's constant, Δ_0 is the order parameter at $T = 0$. This estimation neglects the fact that the interacting particles are embedded in a many-body system that produces medium effects [Gor'kov and Melik-Barkhudarov, 1961]. If these effects are included then the critical temperature further reduces by a factor of $(4e)^{1/3} \approx 2.2$.

On the other hand if we solve the gap equation in the BEC limit by setting $\Delta = 0$ and $\mu \approx -1/(2Ma_s^2) = -E_b/2$, we get following temperature

$$T_C^* \approx \frac{E_b}{2k_B (\ln \frac{E_b}{E_F})^{3/2}}. \quad (3.88)$$

This is not the critical temperature for the superfluid transition, but temperature at which pairs start to form. Rather the transition temperature should be pretty close to the critical value of the non-interacting bose gas with mass $2M$ (mass of bosonic molecule) and density $n/2$ (since each boson is formed from two fermionic atom)

$$T_C \approx \frac{\pi}{Mk_B} \left(\frac{n}{2\zeta(3/2)} \right) \approx 0.21 E_F. \quad (3.89)$$

This result is a very good approximation for the weakly interacting Bose gas and can be improved by including the corrections due to the interactions.

The failure of the gap equation to supply the correct T_c is a direct result of the fact that the mechanism of superfluidity is different in the BCS and BEC limits. In the BCS limit, the interaction between the fermions is weak and T_c is determined by breaking of the Cooper pairs, or in other words disappearance of the energy the

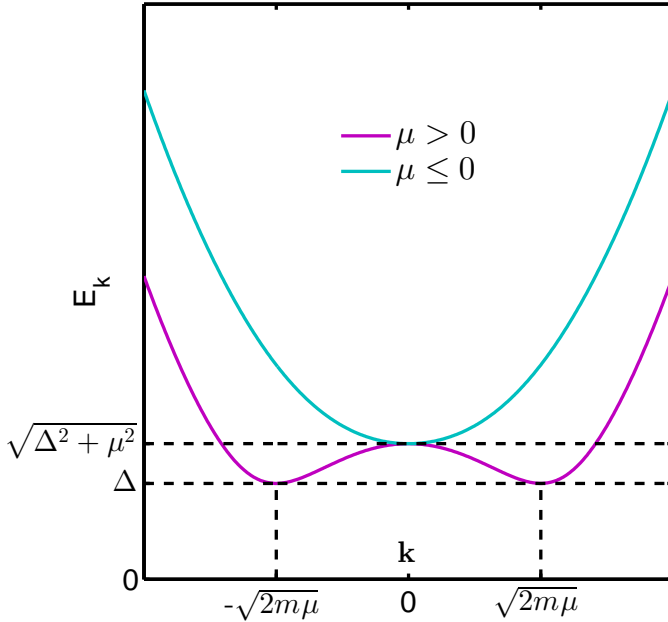


Figure 3.7: Schematic diagram of quasi-particle excitation spectrum on BCS ($\mu > 0$) and BEC ($\mu \leq 0$) sides. There is always a finite gap in the spectrum. Spectrum's behavior changes at $\mu = 0$, which can be identified as transition point from BCS to BEC side.

gap. Thus it is not surprising that the gap equation supplies the correct result. On the other hand in the BEC limit, interaction is strong and we have tightly bound molecules. Therefore pairs can not be broken easily and T_c is directly determined by the onset of Bose-Einstein condensation of the pairs.

The general value of the T_c which smoothly connects the two values can be calculated by incorporating the Gaussian fluctuations to our theory via Nozières and Schmitt-Rink scheme [Nozières and Schmitt-Rink, 1985].

3.8 BCS-BEC Crossover in 2D

After discussing the BCS-BEC crossover in 3D let us focus on the crossover in 2D. As we saw in Sec. 3.5, there is always bound state, no matter how small the attractive interaction is. Therefore the interaction strength in 2D can be controlled with E_b and we renormalize the gap with 2D bound state equation (3.41) [Randeria et al., 1990].

The gap and number equation in mean-field approximation can be derived following the same steps given in our 3D discussion, except the different renormalization, the gap and number equations turns out to have the same form

$$0 = \frac{1}{A} \sum_{\mathbf{k}} \left(\frac{1}{2E_k} - \frac{1}{2\epsilon_k + E_b} \right), \quad (3.90)$$

$$N = \sum_{\mathbf{k}} \left[1 - \frac{(\epsilon_k - \mu)}{E_k} \right]. \quad (3.91)$$

If we relate the particle number in the number equation with Fermi energy using the relation in Eq. (2.52), and change sums with 2D integrals, both the number and gap equation integrals can be performed analytically to yield the following simple equations

$$\sqrt{\mu^2 + \Delta^2} + \mu = 2E_F, \quad (3.92)$$

$$\sqrt{\mu^2 + \Delta^2} - \mu = E_b. \quad (3.93)$$

These equations can be easily solved to determine the order parameter and chemical potential analytically for any interaction strength as

$$\Delta = \sqrt{2E_F E_b}, \quad \mu = E_F - \frac{E_b}{2}. \quad (3.94)$$

We can also determine the pair size using the correlation $\xi^2 = \frac{\langle \psi_{\mathbf{k}} | r^2 | \psi_{\mathbf{k}} \rangle}{\langle \psi_{\mathbf{k}} | \psi_{\mathbf{k}} \rangle}$ analytically, where $\psi_{\mathbf{k}} = \langle \hat{a}_{\mathbf{k}\uparrow}^\dagger \hat{a}_{-\mathbf{k}\downarrow}^\dagger \rangle = u_{\mathbf{k}} v_{\mathbf{k}}$ is the momentum space pair wave function. If we integrate this equation we get the square of the size of the pair

$$\xi^2 = \frac{1}{4M\Delta} \left[\frac{\mu}{\Delta} + \frac{\mu^2 + 2\Delta^2}{\mu^2 + \Delta^2} \left(\frac{\pi}{2} + \arctan \frac{\mu}{\Delta} \right)^{-1} \right] \quad (3.95)$$

Having solved the gap and number equation let us briefly analyze the limits. In the weakly interacting BCS limit where $E_b \rightarrow 0$, we have $E_b \ll E_F$. Therefore Eq. (3.94) reduces to

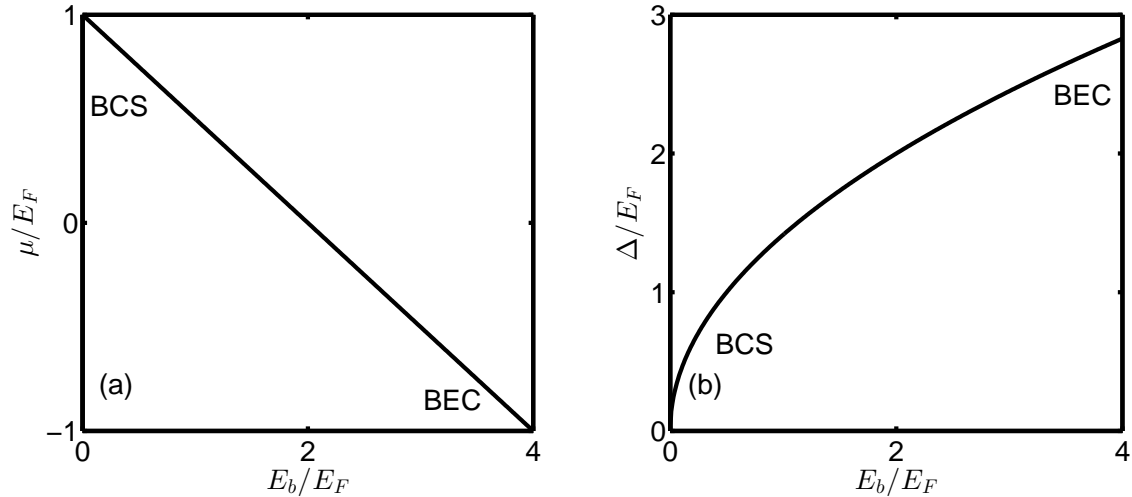


Figure 3.8: (a) Chemical potential μ and (b) order parameter versus Δ as a function of binding energy E_b obtained from self-consistent solution of the gap and number equations in two dimensions. They are analytic and given in the text.

$$\Delta = \sqrt{2E_F E_b}, \ll E_F \quad \mu \approx E_F. \quad (3.96)$$

Similar to 3D case, μ is very close to its non-interacting value and order parameter is exponentially small compared to the Fermi energy (see Eq. (3.46)), thus pairing is very weak. In this limit since $\mu \approx E_F \gg \Delta$, from Eq. (3.95) we get a very simple expression for the size of the pair $\xi = 2E_F/(k_F\Delta)$ which is larger than the inter-particle spacing $1/k_F$. Hence the pairs show Cooper pair characteristic, with large overlapping size.

In the BEC limit where we have $E_b \gg E_F$, the pairs are tightly bound molecules. In this limit

$$\Delta = \sqrt{2E_F E_b} > E_F, \quad \mu \approx -\frac{E_b}{2}. \quad (3.97)$$

Thus similar to 3D case, the chemical potential equals the binding energy per fermion. Pair size ξ is smaller. BCS and BEC limits are connected smoothly as we

can see from Eq. (3.94). The excitation energy has the same form in 2D and gap changes from Δ to $\sqrt{\mu^2 + \Delta^2}$ at $\mu = 0$. Thus the transition from BCS to BEC can again be identified as $\mu = 0$, which gives as the transition binding energy $E_b = 2E_F$.

At finite temperature the gap and number equations can be generalized using the same procedure outlined in the previous section, and they again have the same form as 3D case

$$0 = \frac{1}{A} \sum_{\mathbf{k}} \left(\frac{1}{2E_k} \tanh \frac{\beta E_k}{2} - \frac{1}{2\epsilon_k + E_b} \right), \quad (3.98)$$

$$N = \sum_{\mathbf{k}} \left[1 - \frac{(\epsilon_k - \mu)}{E_k} \tanh \frac{\beta E_k}{2} \right]. \quad (3.99)$$

Number equation can be integrated analytically also for $T \neq 0$ and becomes

$$2E_F = \sqrt{\mu^2 + \Delta^2} + \mu + 2Tk_B \ln \left(1 + e^{-\frac{\sqrt{\mu^2 + \Delta^2}}{Tk_B}} \right). \quad (3.100)$$

In the BCS limit, we can again set $\mu \approx E_F$, $\Delta = 0$ and solve the finite temperature gap equation to determine T_C for superfluidity which turns out to be [Levinsen and Parish, 2015]

$$T_C = \frac{e^\gamma}{k_B \pi} \Delta_0 = \frac{e^\gamma}{k_B \pi} \sqrt{2E_b E_F} = \frac{2e^\gamma}{\pi k_F a_{s,2D}} T_F \quad (3.101)$$

where we related E_b to $a_{s,2D}$ using the relation given in Eq. (3.35). Again if Gorkov-Melik-Barkhudarov correction which incorporates the particle-hole fluctuations around the Fermi surface is taken into account [Petrov et al., 2003], T_C reduces by factor e .

In the BEC limit again we can not use the gap equation to calculate T_C because the temperature of pairing does not coincide with the temperature of the emergence of superfluidity. Different than 3D case we do not have Bose-Einstein condensation in 2D at finite T [Mermin and Wagner, 1966, Hohenberg, 1967]. Rather we have a Berezinskii-Kosterlitz-Thouless (BKT) [Berezinskii, 1971, Kosterlitz and Thouless, 1973] transition from a normal Bose gas to a superfluid at the critical temperature

$$T_C = \frac{T_F}{2} \left\{ \ln \frac{C}{4\pi} + \ln [\ln(4\pi) - 2 \ln(k_F a_s, 2D)] \right\}^{-1} \quad (3.102)$$

where $C = 380 \pm 3$ is a constant [Prokof'ev et al., 2001].

3.9 BCS-BEC Crossover in a 2D Harmonic Trap

In the previous sections we discussed BCS-BEC crossover for homogeneous systems. However experiments are performed in trapping potentials which can be approximated with a harmonic potential. Therefore, it is necessary to extend the theory developed in the previous section to include the trapping potential. Since in this thesis we are interested in a 2D Fermi gas, we focus in two dimensional harmonically trapped Fermi gas. There are two main approaches to analyze a trapped Fermi gas, one is the semi-classical local density approximation, which we discussed for non-interacting Fermi gas in Sec. (2.6) and Sec. (2.7), and the other approach is the full quantum mechanical Bogoliubov-de Gennes theory. In this section we outline both approaches. We assume that our attractively interacting 2D Fermi gas is trapped in an isotropic harmonic trap $V(r) = M\omega^2 r^2/2$.

LDA amounts to treating the system at each r point as a uniform gas with local chemical potential

$$\mu(r) = \mu - \frac{M\omega^2 r^2}{2} \quad (3.103)$$

where μ is the global chemical potential, which enforces the total particle number N to the system. We also have local order parameter $\Delta(r)$ and local density $n(r)$ whose explicit r dependence needs to be determined from the gap and number equations. Since we treat the gas as homogeneous at each point r , the gap and number equations which we derived are still valid, but now they describe the local quantities. If we again integrate the number and gap equations, this time in terms of local variables, we get the following two equations

$$\sqrt{\mu(r)^2 + \Delta(r)^2} + \mu(r) = \frac{2\pi n(r)}{M}, \quad (3.104)$$

$$\sqrt{\mu(r)^2 + \Delta(r)^2} - \mu(r) = E_b. \quad (3.105)$$

If we solve the above equations for $\mu(r)$ and $\Delta(r)$ we get

$$\mu(r) = \frac{n(r)\pi}{M} - \frac{E_b}{2}, \quad (3.106)$$

$$\Delta(r) = \sqrt{\frac{2E_b n(r)\pi}{M}}. \quad (3.107)$$

From the first equation we get the density profile of the gas

$$n(r) = \frac{M}{\pi} \left(\mu + \frac{E_b}{2} - \frac{M\omega^2 r^2}{2} \right). \quad (3.108)$$

$n(r)$ is related to total particle number via $N = 2\pi \int r n(r) dr$, which can be used to determine the global chemical potential as

$$\mu = \omega\sqrt{N} - \frac{E_b}{2} = E_F - \frac{E_b}{2} \quad (3.109)$$

where E_F is Fermi energy of non-interacting 2D trapped Fermi gas as given in Eq. (2.57). Note that the global chemical potential is equal to the chemical potential of homogeneous system studied in previous section. If we substitute μ in Eq. (3.108), the local density becomes

$$n(r) = \frac{M}{\pi} \left(E_F - \frac{M\omega^2 r^2}{2} \right). \quad (3.110)$$

Note that the parabolic density profile of the interacting 2D Fermi gas is independent from E_b and is identical with the non-interacting one given in Eq. (2.59) under the mean-field approximation. Therefore the edge of the gas is again given by

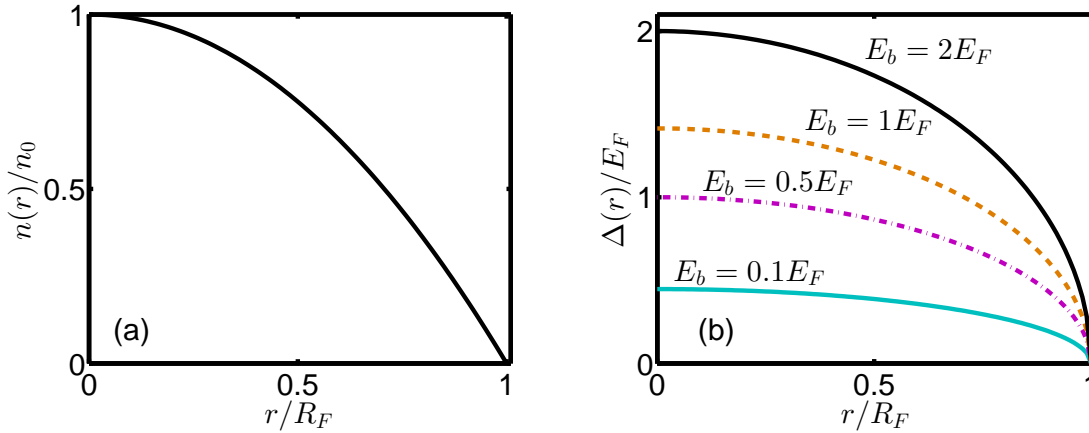


Figure 3.9: (a) Mean-field density profile under local density approximation of 2D Fermi gas for any E_b . The density profile is not effected by interaction.(b) Mean-field order parameter profile under local density approximation of a 2D Fermi gas for representative E_b values. Interaction enhances the pairing and the order parameter, and the system is superfluid as a whole at $T = 0$.

the Thomas-Fermi radius $R_O = R_F$. Thus increasing the E_b does not change the density profile of the gas. This is different than 3D case where, the gas contracts as interaction is increased.

If we insert $n(r)$ to Eq. (3.107), we get the order parameter profile of the gas, which unlike the density profile is not parabolic [He and Zhuang, 2008]

$$\Delta(r) = \sqrt{2E_b E_F} \sqrt{1 - \frac{r^2}{R_F^2}}. \quad (3.111)$$

Note that as expected the local order parameter increases by increasing the interaction E_b . Both $n(r)$ and $\Delta(r)$ vanish at R_F , thus the system is completely superfluid. Order parameter and density profiles are plotted in Fig. 3.9 for representative E_b values.

While LDA is a powerful approximation and provides very accurate result for $N \gg 1$, if we are interested in finite size effects we have to use the full quantum mechanical BDG approach. We start with the BCS hamiltonian in real space which

can be written as a sum of two terms

$$H = H_{\text{sho}} + H_{\text{int}}. \quad (3.112)$$

The simple harmonic oscillator part is given as

$$H_{\text{sho}} = \sum_{\sigma} \int d\mathbf{r} \hat{\psi}_{\sigma}^{\dagger}(\mathbf{r}) \left(-\frac{\nabla^2}{2M} + V(\mathbf{r}) - \mu \right) \hat{\psi}_{\sigma}(\mathbf{r}) \quad (3.113)$$

and the interacting part as

$$H_{\text{int}} = -g \int d\mathbf{r} \hat{\psi}_{\uparrow}^{\dagger}(\mathbf{r}) \hat{\psi}_{\downarrow}^{\dagger}(\mathbf{r}) \hat{\psi}_{\downarrow}(\mathbf{r}) \hat{\psi}_{\uparrow}(\mathbf{r}). \quad (3.114)$$

We again apply the mean-field approximation by introducing the order parameter $\Delta(\mathbf{r}) = g \langle \hat{\psi}_{\uparrow}(\mathbf{r}) \hat{\psi}_{\downarrow}(\mathbf{r}) \rangle$. The interaction term in the mean-field approximation becomes

$$H_{\text{int}}^{\text{mf}} = \int d\mathbf{r} \left(\Delta(\mathbf{r}) \hat{\psi}_{\uparrow}^{\dagger}(\mathbf{r}) \hat{\psi}_{\downarrow}^{\dagger}(\mathbf{r}) + \Delta^*(\mathbf{r}) \hat{\psi}_{\downarrow}(\mathbf{r}) \hat{\psi}_{\uparrow}(\mathbf{r}) + \frac{|\Delta(\mathbf{r})|^2}{g} \right) \quad (3.115)$$

so that our total Hamiltonian, in mean-field approximation becomes $H^{\text{mf}} = H_{\text{sho}} + H_{\text{int}}^{\text{mf}}$. Similar to the homogeneous case, we diagonalize the above Hamiltonian using the Bogoliubov-Valatin transformation given by [Gennes, 1999]

$$\begin{aligned} \hat{\psi}_{\uparrow}(\mathbf{r}) &= \sum_{\eta} \left[u_{\eta}(\mathbf{r}) \hat{\gamma}_{\eta\uparrow} - v_{\eta}^*(\mathbf{r}) \hat{\gamma}_{\eta\downarrow}^{\dagger} \right] \\ \hat{\psi}_{\downarrow}(\mathbf{r}) &= \sum_{\eta} \left[u_{\eta}(\mathbf{r}) \hat{\gamma}_{\eta\downarrow} + v_{\eta}^*(\mathbf{r}) \hat{\gamma}_{\eta\uparrow}^{\dagger} \right]. \end{aligned} \quad (3.116)$$

Here $\hat{\gamma}_{\eta\sigma}^{\dagger}$ and $\hat{\gamma}_{\eta\sigma}$ are the creation and annihilation operators of quasi-particles with quantum number η and spin σ , u_{η} and v_{η} are the Bogoliubov quasi-particle/quasi-hole amplitudes which display the amplitudes of quasi-particles or quasi-holes to the real space operators. Both $\hat{\psi}_{\sigma}^{\dagger}/\hat{\psi}_{\sigma}$ and $\hat{\gamma}_{\sigma,\eta}^{\dagger}/\hat{\gamma}_{\sigma,\eta}$ must comply with Fermi-Dirac statistics, hence must satisfy the anti-commutation relations. Therefore the amplitude functions must satisfy the completeness relations

$$\sum_{\eta} [u_{\eta}(\mathbf{r})u_{\eta}^*(\mathbf{r}') + v_{\eta}(\mathbf{r}')v_{\eta}^*(\mathbf{r})] = \delta(\mathbf{r} - \mathbf{r}') \quad (3.117)$$

$$\sum_{\eta} [u_{\eta}(\mathbf{r})u_{\eta}^*(\mathbf{r}') - v_{\eta}(\mathbf{r}')v_{\eta}^*(\mathbf{r})] = 0, \quad (3.118)$$

and we also have the orthogonality relations

$$\int d\mathbf{r} [u_{\eta}(\mathbf{r})u_{\nu}^*(\mathbf{r}') + v_{\eta}(\mathbf{r}')v_{\nu}^*(\mathbf{r})] = \delta_{\eta\nu} \quad (3.119)$$

$$\int d\mathbf{r} [u_{\eta}(\mathbf{r})u_{\nu}^*(\mathbf{r}') - v_{\eta}(\mathbf{r}')v_{\nu}^*(\mathbf{r})] = 0. \quad (3.120)$$

With these conditions, the Bogoliubov-Valatin transformation diagonalizes the mean-field Hamiltonian

$$H^{\text{mf}} = E_g + \sum_{\eta,\sigma} E_{\eta} \hat{\gamma}_{\sigma,\eta}^{\dagger} \hat{\gamma}_{\sigma,\eta}, \quad (3.121)$$

where E_g is the ground-state energy and E_{η} is the energy eigenvalue of the quasi-particle excitations. Using the anti-commutation relations between the operators and Eq. (3.121) we can show that

$$[H^{\text{mf}}, \hat{\gamma}_{\eta\sigma}]_{-} = -E_{\eta} \hat{\gamma}_{\eta\sigma}, \quad [H^{\text{mf}}, \hat{\gamma}_{\eta\sigma}^{\dagger}]_{-} = E_{\eta} \hat{\gamma}_{\eta\sigma}^{\dagger}. \quad (3.122)$$

Using Eq. (3.113) and Eq. (3.115) together with anti-commutation relations we also have

$$\begin{aligned} [H^{\text{mf}}, \hat{\psi}_{\uparrow}(\mathbf{r})]_{-} &= -[H_0 + V(\mathbf{r})] \hat{\psi}_{\uparrow}(\mathbf{r}) - \Delta(\mathbf{r}) \hat{\psi}_{\downarrow}^{\dagger}(\mathbf{r}), \\ [H^{\text{mf}}, \hat{\psi}_{\downarrow}(\mathbf{r})]_{-} &= -[H_0 + V(\mathbf{r})] \hat{\psi}_{\downarrow}(\mathbf{r}) + \Delta(\mathbf{r}) \hat{\psi}_{\uparrow}^{\dagger}(\mathbf{r}) \end{aligned} \quad (3.123)$$

where $H_0 = -\nabla^2/(2M) - \mu$. Using Eq. (3.116) and Eq. (3.122), we expand Eq. (3.123) in terms of $\hat{\gamma}_{\eta\sigma}$ operators. If we equate the coefficients of $\hat{\gamma}_{\eta\sigma}$ operators we get the following equations

$$\begin{aligned}
E_\eta u_\eta(\mathbf{r}) &= [H_0 + V(\mathbf{r})] u_\eta(\mathbf{r}) + \Delta(\mathbf{r}) v_\eta(\mathbf{r}), \\
E_\eta v_\eta(\mathbf{r}) &= -[H_0^* + V(\mathbf{r})] v_\eta(\mathbf{r}) + \Delta^*(\mathbf{r}) u_\eta(\mathbf{r}).
\end{aligned} \tag{3.124}$$

These are known as the Bogoliubov-de Gennes equations and they can be written in a matrix form as an eigenvalue equation

$$\begin{pmatrix} H_0 + V(\mathbf{r}) & \Delta(\mathbf{r}) \\ \Delta^*(\mathbf{r}) & -H_0^* - V(\mathbf{r}) \end{pmatrix} \begin{pmatrix} u_\eta(\mathbf{r}) \\ v_\eta(\mathbf{r}) \end{pmatrix} = E_\eta \begin{pmatrix} u_\eta(\mathbf{r}) \\ v_\eta(\mathbf{r}) \end{pmatrix} \tag{3.125}$$

The Bogoliubov-de Gennes equations must be solved self consistently with the order parameter equation

$$\Delta(\mathbf{r}) = g \langle \hat{\psi}_\uparrow(\mathbf{r}) \hat{\psi}_\downarrow(\mathbf{r}) \rangle = g \sum_\eta u_\eta(\mathbf{r}) v_\eta^*(\mathbf{r}) [1 - 2f(E_\eta)] \tag{3.126}$$

where we used the relations in Eq. (3.116) together with the averages of the fermionic quasi-particles

$$\begin{aligned}
\langle \hat{\gamma}_{\sigma,\eta}^\dagger \hat{\gamma}_{\sigma',\nu} \rangle &= \delta_{\eta\nu} \delta_{\sigma\sigma'} f(E_\eta), & \langle \hat{\gamma}_{\sigma,\eta} \hat{\gamma}_{\sigma',\nu}^\dagger \rangle &= \delta_{\eta\nu} \delta_{\sigma\sigma'} [1 - f(E_\eta)], \\
\langle \hat{\gamma}_{\sigma,\eta}^\dagger \hat{\gamma}_{\sigma',\nu}^\dagger \rangle &= \langle \hat{\gamma}_{\sigma,\eta} \hat{\gamma}_{\sigma',\nu} \rangle = 0.
\end{aligned} \tag{3.127}$$

Similarly we determine the local density, which is used to fix the chemical potential for the desired particle number,

$$n(\mathbf{r}) = \sum_\sigma \langle \hat{\psi}_\sigma^\dagger(\mathbf{r}) \hat{\psi}_\sigma(\mathbf{r}) \rangle = 2 \sum_\eta \{ |u_\eta(\mathbf{r})|^2 f(E_\eta) + |v_\eta(\mathbf{r})|^2 [1 - f(E_\eta)] \}. \tag{3.128}$$

The total particle number is given by $N = \int d\mathbf{r} n(\mathbf{r})$. These equations need to be solved self consistently. In numerical calculations, we again renormalized the gap equation. This is done by transforming the Eq. (3.41) into real space, which becomes

$$g = \frac{4\pi}{M \ln(1 + 2E_c/E_b)} \quad (3.129)$$

where E_c is the cut-off energy, which should be chosen high enough to ensure that the results are cut-off independent.

The BdG Hamiltonian has particle-hole symmetry. As a result of this symmetry BdG equations have the important property, if $(u_\eta, v_\eta)^T$ is solution with eigenvalue E_η , than $(-v_\eta^*, u_\eta)^T$ is also solution with eigenvalue $-E_\eta$. Therefore all the quasi-particle sums can be restricted to just positive energies.

In Fig. 3.10 we present a comparison of the density and order parameter trap profile for the representative $E_b = 0.5E_F$ value calculated with both LDA and BdG. LDA is in very good agreement with BdG calculation. Interactions destroy the Friedel oscillations, therefore we have perfect agreement at the center of the trap. LDA fails at the low density region at the edge as expected. Again as the particle number increases, the region at which LDA fails becomes small compared to the system size since small density region decreases.

3.10 Superfluidity

Superfluidity is a state of matter in which the matter behaves like a fluid with zero viscosity, therefore can flow without dissipating energy. Superfluidity was discovered in Helium-4 by Kapitza [Kapitza, 1938] and independently by Allen and Misener [Allen and Misener, 1938]. In the previous sections we claimed that Fermi gases with attractive interaction are superfluids, and Δ is the order parameter of the superfluid state. In this section we will try to provide arguments in support of these claims. Due to its relevance and simplicity we will constrain our analysis to the BCS limit.

Arguably the most basic criteria for superfluidity is due to Landau, which directly focuses on flow without dissipation [Landau, 1941]. Landau's criteria of superfluidity is based on the Galilean transformation of energy and momentum. Suppose we are

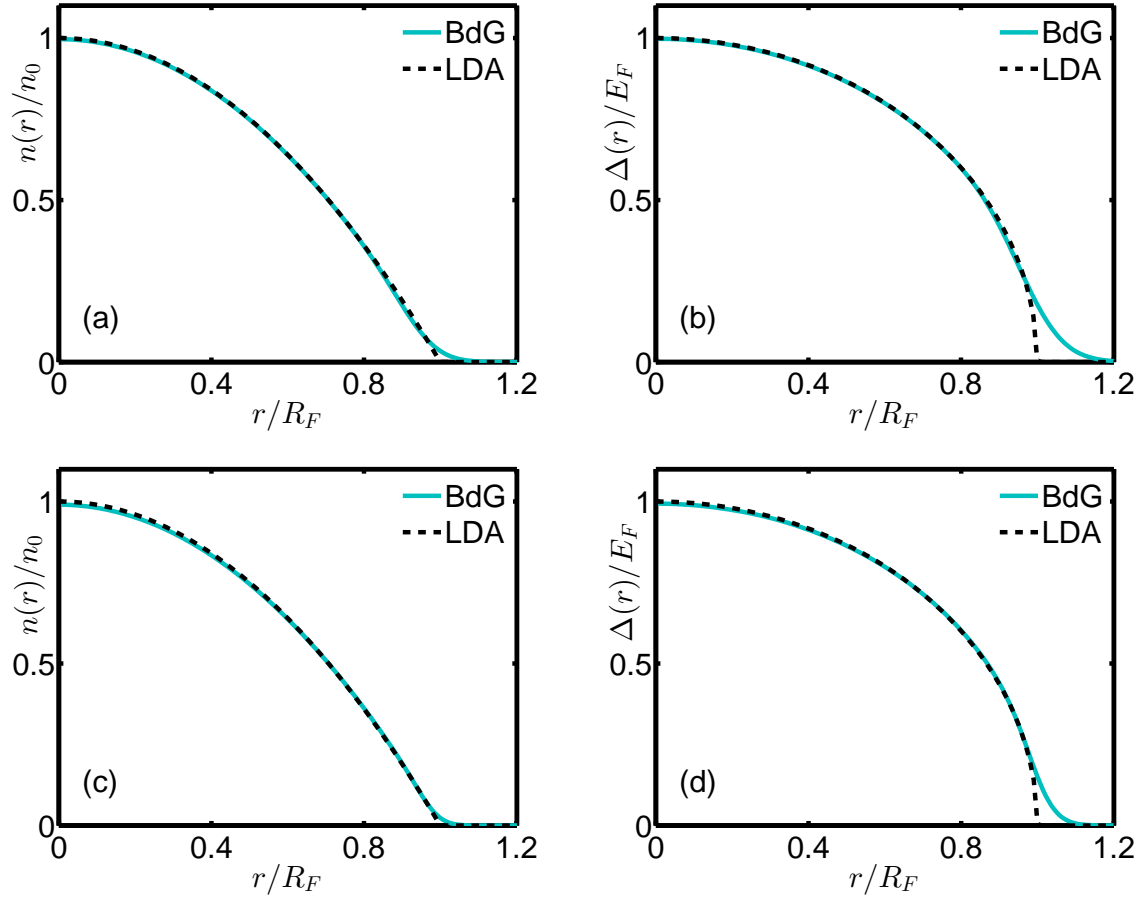


Figure 3.10: The trap profiles for a representative $E_b = 0.5E_F$. (a) $n(r)$ for $N = 100$, (b) $\Delta(r)$ for $N = 100$, (c) $n(r)$ for $N = 500$, (d) $\Delta(r)$ for $N = 500$. Even for $N = 100$ LDA is in very good agreement with BdG calculations. Interactions destroy the Friedel oscillations, therefore we have perfect agreement at the center of the trap. LDA fails at the low density region at the edge of the gas as expected. Note that by comparing $N = 100$ and $N = 500$, as the particle number increases the region at which LDA fails becomes small compared to the system size.

analyzing a fluid in some reference frame \mathfrak{R} , and in this frame fluid has energy E and momentum \mathbf{K} . If we want to express the energy and momentum of the fluid at some other reference frame \mathfrak{R}' , which is moving with velocity \mathbf{V} with respect to \mathfrak{R} , then the Galilean transformation gives us following relations

$$\mathbf{K}' = \mathbf{K} - M\mathbf{V}$$

$$E' = \frac{K'^2}{2M} = \frac{|\mathbf{K} - M\mathbf{V}|^2}{2M} = E - \mathbf{K} \cdot \mathbf{V} + \frac{MV^2}{2} \quad (3.130)$$

where E' and \mathbf{K}' are energy and momentum of the fluid in the moving frame \mathfrak{R}' respectively. M is the mass of the fluid. Galilean transformations fail and should be replaced by Lorentzian transformation for velocities close to speed of light. But since it is clear that $V \ll c$, where c denotes the speed of light, we can safely use it.

Now suppose that we have a fluid moving at some narrow tube with velocity \mathbf{v} in $T = 0$. Assume that all the particles are in the ground state. If the fluid has some viscosity it will lose kinetic energy due to friction. Such dissipation will lead to excitations in the system. Let us first analyze the system in the rest frame of the fluid, hence the tube is moving with velocity $-\mathbf{v}$. Assume that E_0 is the ground state energy of the fluid in this frame, and due to friction there is some elementary excitation with energy E_k and momentum \mathbf{k} . Using the Galilean transformation given in Eq. (3.130) with $\mathbf{V} = -\mathbf{v}$, we can write the momentum and the energy of the system at the rest frame of the tube using the quantities given in the rest frame of the fluid

$$\mathbf{K}' = \mathbf{k} + M\mathbf{v} \quad (3.131)$$

$$E' = E_0 + E_k + \mathbf{k} \cdot \mathbf{v} + \frac{Mv^2}{2} \quad (3.132)$$

Thus the change in the energy due to the elementary excitation is $\epsilon_k + \mathbf{k} \cdot \mathbf{v}$ in the rest frame of the tube. This excitation and therefore the energy dissipation can only occur if it is energetically favorable which gives the following condition

$$E_k - kv < 0 \Rightarrow v > \frac{E_k}{k} \quad (3.133)$$

If this condition is not satisfied than the liquid moves without friction. Thus it is called a superfluid. The minimum value of E_k/k is called the critical velocity v_c . The criterion for superfluidity can be expressed as

$$v < v_c = \min_k \left(\frac{E_k}{k} \right) \quad (3.134)$$

This condition is called the Landau criterion of superfluidity. Note that for the non-interacting Fermi gas with $E_k = k^2/(2M)$ above condition can not be satisfied since $v_c = 0$.

Let us now check whether the BCS state we discussed above satisfies the Landau criterion. For attractively interacting Fermi gas $E_k = \sqrt{(\epsilon_k - \mu)^2 + \Delta^2}$ as we discussed above in the BCS side of the crossover the minimum of the excitation is at $k = \sqrt{2M\mu}$ and its value at that point is Δ . If we set $\mu \approx E_F$, than

$$v_c = \min_k \left(\frac{E_k}{k} \right) = \frac{\Delta}{k_F} \quad (3.135)$$

Since $v_c \neq 0$, the attractive Fermi gas must be superfluid as long as $\Delta \neq 0$. Fermi gas will stay superfluid for any velocity $v < v_c$. For higher velocities Cooper pairs will be broken and system will no longer be in the superfluid phase.

We gave a local argument that an attractive Fermi gas is a SF. Let us now give an global argument to justify the claim that Δ is the order parameter of the SF and SF is really a different state of matter than a normal gas [Nicolai Nygaard, 2004].

When we have phase transitions, usually a system changes from high entropy disordered state to lower temperature and lower entropy state with more order. The temperature at which this transition occurs is known as the critical temperature T_c . The higher temperature state usually has more symmetry than the lower energy state,

thus the phase transitions therefore generally involve symmetry breaking. For example when a liquid transforms to a crystalline solid continuous translation symmetry is broken. This broken symmetry brings some order to the system, which can be measured by the so called order parameter. Thus, a non-zero order parameter can distinguish the ordered phase from the disordered one. Let's take ferromagnetic transition as an example. During this phase transition the direction of the magnetic moment of atoms change from random to aligned. The emergent order can be measured with the average magnetic moment, which is now nonzero and it is the order parameter of the system. In general we usually we have some operator \hat{O} whose thermal average $\langle \hat{O} \rangle$ is non-zero in the ordered phase, which is the order parameter of the system. This operator \hat{O} is not invariant under the full symmetry group G_s of the Hamiltonian of the system. This result is called symmetry breaking.

The symmetry group of Hamiltonian H can be defined as a group of transformations $U^\dagger H U$ which does not change the Hamiltonian. These transformations can be represented as $U = e^{-i\hat{T}\varepsilon}$, where \hat{T} is the generator of the symmetry operation and ε is the displacement of that transformation. For example for a spatial translation in x direction, can be represented by x component of the momentum operator, spatial displacement being the displacement of the transformation. The Hamiltonian necessarily commutes with the generators of its symmetry group, $[H, \hat{T}] = 0$. In order to have an order parameter, there must be some operator \hat{O} which is not invariant at least with one symmetry transformation, i.e.

$$U^\dagger \hat{O} U = e^{i\phi} \hat{O} \neq \hat{O}. \quad (3.136)$$

If we assume that $\hat{\rho}$ is the density matrix of our system, and use the cyclic property of the trace we have

$$\langle \hat{O} \rangle = \text{Tr}(\hat{\rho} \hat{O}) = \text{Tr}(\hat{\rho}' U^\dagger \hat{O} U) = \text{Tr}(\hat{\rho}' \hat{O}) e^{i\phi} \quad (3.137)$$

where $\hat{\rho}' = U^\dagger \hat{\rho} U$. If we require $\langle \hat{O} \rangle \neq 0$, than Eq. (3.137) implies that

$$\hat{\rho}' \neq \hat{\rho} \Rightarrow [\hat{\rho}, \hat{T}]_- \neq 0 \quad (3.138)$$

Thus the ordered phase does not have the full symmetry of the Hamiltonian, i.e. symmetry is broken in the phase transition and this is accompanied with non-zero order parameter $\langle \hat{O} \rangle$. In the case of ferromagnet, rotation symmetry of spin-degrees of freedom is broken, and magnetization emerges as non-zero order parameter of the system.

Let us now return to superfluidity. We already identified Δ as the order parameter. Let us now justify this claim. Since in the normal-superfluid phase transition, the superfluid state emerges in lower temperature, therefore we expect the superfluid to be the more ordered phase. Thus we expect that during the normal-superfluid phase transition some symmetry must be broken (note that not all phase transitions involve symmetry breaking). From the BCS wave-function Eq. (3.60) which does not have fixed number of particles one can guess that this symmetry breaking is associated with particle number. This symmetry which is broken during the normal-superfluid phase transition is known as a global U(1) symmetry and is associated with following transformation

$$U = e^{-i\hat{N}\phi} \quad (3.139)$$

where $\hat{N} = \sum_{\sigma} \int d\mathbf{r} \hat{\psi}_{\sigma}^{\dagger}(\mathbf{r}) \hat{\psi}_{\sigma}(\mathbf{r})$ is the total number operator. The general BCS Hamiltonian given in Eq. (3.112) can be easily shown to satisfy

$$[H, \hat{N}]_- = 0 \Rightarrow U^{\dagger} H U = H. \quad (3.140)$$

Therefore the general Hamiltonian has the global U(1) symmetry. Using the Baker-Hausdorff lemma together with $[\hat{N}, \hat{\psi}_{\sigma}^{\dagger}(\mathbf{r})]_- = \hat{\psi}_{\sigma}^{\dagger}(\mathbf{r})$ and $[\hat{N}, \hat{\psi}_{\sigma}(\mathbf{r})]_- = -\hat{\psi}_{\sigma}(\mathbf{r})$ we can show that

$$U^\dagger \hat{\psi}_\sigma^\dagger(\mathbf{r})U = \hat{\psi}_\sigma^\dagger e^{i\phi}, \quad U^\dagger \hat{\psi}_\sigma(\mathbf{r})U = \hat{\psi}_\sigma e^{-i\phi}. \quad (3.141)$$

Using these relations we can easily demonstrate that $\Delta(\mathbf{r}) = g\langle \hat{\psi}_\uparrow(\mathbf{r})\hat{\psi}_\downarrow(\mathbf{r}) \rangle = |\Delta(\mathbf{r})|e^{i\theta(\mathbf{r})}$ does not poses the global U(1) symmetry

$$g\langle U^\dagger \hat{\psi}_\uparrow(\mathbf{r})\hat{\psi}_\downarrow(\mathbf{r})U \rangle = g\langle \hat{\psi}_\uparrow(\mathbf{r})\hat{\psi}_\downarrow(\mathbf{r}) \rangle e^{-2i\phi} = |\Delta(\mathbf{r})|e^{i\theta(\mathbf{r})-2i\phi} \neq \Delta(\mathbf{r}) \quad (3.142)$$

where we inserted $UU^\dagger = I$ between the field operators. From this analysis we can conclude that when $\Delta(\mathbf{r}) \neq 0$ that global U(1) symmetry is broken and system is in superfluid state. Therefore in this thesis we will take $\Delta(\mathbf{r})$ as our order parameter, which will determine whether we have a normal gas or superfluid.

Chapter 4

TRAPPED 2D FERMI GAS WITH SPIN-ORBIT COUPLING

4.1 *Physical Origin of Spin-Orbit Coupling*

Spin-orbit coupling (SOC) is an interaction of a particle's spin with its motion. To explain how it may arise let us give very simple example which is depicted at Fig. 4.1(a). Let's assume that in the lab frame electron is moving on a plane in x direction, and a constant electric field is applied in z direction, say due to presence of some positive ions. Suppose we go to the rest frame of the electron, Lorentz transformations will imply that besides the electric field, electron in its rest frame will feel a magnetic field in y direction which is proportional to its velocity in the lab frame. This effective magnetic field which is proportional to the electron's velocity can couple with the magnetic moment of the electron, which is proportional to its spin. Hence the spin of the electron is coupled with its momentum. Origin of this effect can be easily understood by looking at the source of the electric field, i.e ions. In the rest frame of the electrons, the ions will be moving and therefore will create an magnetic field exactly the one deduced by the Lorentz transformation. Since the spin-orbit coupling is a result of Lorentz transformation we can suspect that it must be a relativistic effect. Indeed one can show that SOC appears in the Pauli equation, which includes the correction terms which come from the relativistic Dirac equation in its non-relativistic limit. We will demonstrate this following [Sakurai, 1967].

$$\begin{pmatrix} Mc^2 & c\mathbf{p} \cdot \vec{\sigma} \\ c\mathbf{p} \cdot \vec{\sigma} & -Mc^2 \end{pmatrix} \begin{pmatrix} \psi_1(\mathbf{r}) \\ \psi_2(\mathbf{r}) \end{pmatrix} = [E - V(\mathbf{r})] \begin{pmatrix} \psi_1(\mathbf{r}) \\ \psi_2(\mathbf{r}) \end{pmatrix}. \quad (4.1)$$

Here $\vec{\sigma} = (\sigma_x, \sigma_y, \sigma_z)$ is vector with Pauli matrices as its components, $V(\mathbf{r})$ is a

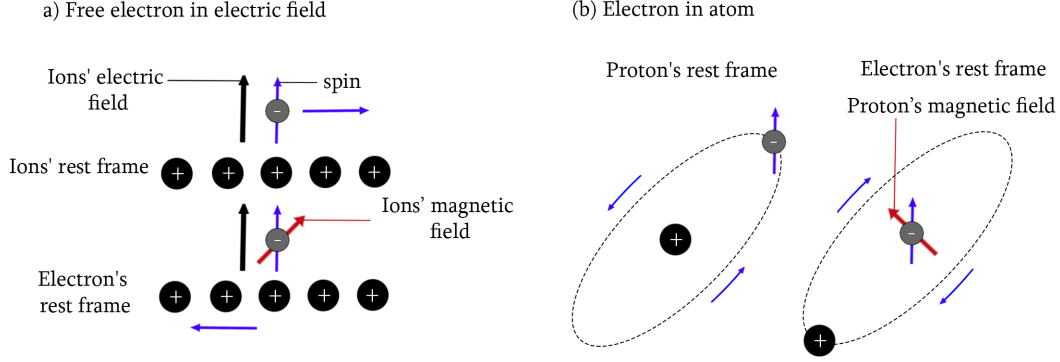


Figure 4.1: (a) Free electron moving in the presence of electric field due to ions. If we move to the rest frame of the electron, it will see apparent motion of the ions which will create magnetic field acting on the electron. This effective magnetic field which is proportional to the electron's velocity can couple with the magnetic moment of the electron, which is proportional to its spin. As a result of this spin of electron is coupled with its momentum. (b) In its rest frame electron will feel an effective magnetic field due to the apparent motion of the proton. This magnetic field which is proportional to the velocity of the electron in the proton's rest frame will couple to the electron's magnetic moment leading to coupling between its momentum and spin.

potential and ψ_1 and ψ_2 are large and small component of Dirac wave function. Dirac equations give us two coupled equations, which can be reduced to one

$$\left(\mathbf{p} \cdot \vec{\sigma} \frac{c^2}{E - V(\mathbf{r}) + Mc^2} \mathbf{p} \cdot \vec{\sigma} \right) \psi_1(\mathbf{r}) = (E - V(\mathbf{r}) - Mc^2) \psi_1(\mathbf{r}). \quad (4.2)$$

We are interested in the non-relativistic limit, thus we have $E = Mc^2 + \epsilon$ with $\epsilon \ll Mc^2$. We also assume that the potential is small compared to the rest mass energy of the particle $|V(\mathbf{r})| \ll Mc^2$. Then we can write

$$\frac{c^2}{E - V(\mathbf{r}) + Mc^2} \approx \frac{1}{2M} \left(1 - \frac{\epsilon - V(\mathbf{r})}{2Mc^2} \right). \quad (4.3)$$

The Dirac equation can be written as If we neglect second term in the left side of the above equation, the Dirac equation reduces to the Schrödinger equation. From Eq. (4.1) we see that in the first order large and small components of the Dirac wave function are related as

$$\psi_2(\mathbf{r}) \approx \frac{\mathbf{p} \cdot \vec{\sigma}}{2Mc} \psi_1(\mathbf{r}). \quad (4.4)$$

If insert this to the normalization condition we have

$$1 = \int d\mathbf{r} [\psi_1^\dagger(\mathbf{r})\psi_1(\mathbf{r}) + \psi_2^\dagger(\mathbf{r})\psi_2(\mathbf{r})] \approx \int d\mathbf{r} \psi_1^\dagger(\mathbf{r}) \left(1 + \frac{p^2}{4M^2c^2} \right) \psi_1(\mathbf{r}) \approx \int d\mathbf{r} \psi^\dagger(\mathbf{r})\psi(\mathbf{r}) \quad (4.5)$$

where we have $\psi(\mathbf{r}) = [1 + p^2/(8M^2C^2)]\psi_1(\mathbf{r})$. Substituting this to the Dirac equation together with the expansion given above we get the Pauli equation

$$\left(\frac{p^2}{2M} + V(\mathbf{r}) - \frac{p^4}{8M^3c^2} - \frac{1}{4M^2c^2} \vec{\sigma} \cdot \mathbf{p} \times \nabla V(\mathbf{r}) + \frac{1}{8M^2c^2} \nabla^2 V(\mathbf{r}) \right) \psi(\mathbf{r}) = \epsilon \psi(\mathbf{r}). \quad (4.6)$$

Note that in the classical limit $c \rightarrow \infty$ Pauli equation reduces to the Schrödinger equation. Third term in the above equation is an relativistic energy correction to the kinetic energy $\sqrt{(Mc^2)^2 + p^2c^2} - Mc^2 \approx p^2/(2M) - p^4/(8M^3c^2)$. The fifth term is an energy shift which is known as the Darwin term. Fourth term is the SOC term. Thus we see that SOC term arises in the Pauli equation, an equation which includes first order (in v/c) relativistic corrections to the Schrödinger equation. Pauli equation suggest that if we have a spatially variable potential $V(\mathbf{r})$ and either particle has small mass or is moving with high speed SOC term may become important.

The most famous example system where SOC term becomes important is an atom (see Fig. 4.1(b)). SOC causes shift in an electron's energy levels which leads to splitting of the spectral lines. Since the Coulomb potential has a central symmetry for an electron in an atom SOC term in Pauli equation becomes

$$H_{soc} = \frac{1}{4M^2c^2r} \frac{\partial V(r)}{\partial r} \mathbf{L} \cdot \vec{\sigma} \quad (4.7)$$

where $\mathbf{L} = \mathbf{r} \times \mathbf{p}$ is the angular momentum. SOC can play important role also for the protons and neutrons where potential results from the strong nuclear force, and leads to shift in their energy levels in the nucleus shell model.

Although usually, relativistic effects can be neglected in the solid state materials, SOC term in Pauli equation may become important in certain materials. For example in the materials known as the zinc blend structure materials where bulk inversion symmetry is broken SOC term reduces to cubic Dresselhaus SOC term [Dresselhaus, 1955, Krich and Halperin, 2007]

$$H_{soc,D} = \beta [k_x(k_y^2 - k_z^2)\sigma_x + k_y(k_z^2 - k_x^2)\sigma_y + k_z(k_x^2 - k_y^2)\sigma_z] \quad (4.8)$$

where β is the SOC strength. If an electron is confined to move in 2D plane, than the Dresselhaus SOC term reduces to

$$H_{soc,D} = \beta [-\langle k_z^2 \rangle (k_x\sigma_x - k_y\sigma_y) + (k_y^2 k_x\sigma_x - k_x^2 k_y\sigma_y)]. \quad (4.9)$$

Usually the cubic term is small compared to the linear term and is ignored leading to

$$H_{soc,D} = \gamma (k_x\sigma_x - k_y\sigma_y). \quad (4.10)$$

Another 2D electron system where the SOC become important is the materials which have structural inversion asymmetry. In this case Pauli equation predicts that we have linear SOC known as the Rashba SOC [Bychkov and Rashba, 1984]

$$H_{soc,R} = \alpha (k_x\sigma_y - k_y\sigma_x), \quad (4.11)$$

where α is the strength of the Rashba SOC. The Rashba spin-orbit coupling plays central role in many interesting phenomena such as quantum spin-Hall effect [Sinova et al., 2015, Qi and Zhang, 2011], topological superconductors and topological insulators [Hasan and Kane, 2010, Qi and Zhang, 2011].

We should note that the Rashba SOC in cold atom community is usually expressed in a different form than its original form given above. We can get the form used in the cold atom community by following procedure. We first rotate the pseudo-spins with the following unitary matrix

$$U = \begin{pmatrix} e^{-i\pi/8} & 0 \\ 0 & e^{i\pi/8} \end{pmatrix} \quad (4.12)$$

which when applied to Pauli matrices gives

$$U^\dagger \sigma_x U = \frac{\sigma_x - \sigma_y}{\sqrt{2}}, \quad U^\dagger \sigma_y U = \frac{\sigma_x + \sigma_y}{\sqrt{2}}. \quad (4.13)$$

Then we also rotate the momentum axis such that

$$\frac{k_x - k_y}{\sqrt{2}} \rightarrow k_x, \quad \frac{k_x + k_y}{\sqrt{2}} \rightarrow k_y. \quad (4.14)$$

As a result of these transformations Dresselhaus SOC remains unchanged, while Rashba SOC takes the following form, which following the convention of the cold atom community will be used in this thesis

$$H_{soc,R} = \alpha(k_x \sigma_x + k_y \sigma_y). \quad (4.15)$$

Since atoms in ultracold limit have very low velocity, their mass is very big compared to the electron mass, they are charge neutral and external electric fields are very weak we can not observe SOC naturally in cold atoms. If we want to study the effects of SOC on the ultracold atoms, we must engineer it artificially. In the next two section we discuss how this can be accomplished.

4.2 Artificial Gauge Fields, Berry Phase and the Adiabatic Principle

The types of SOC which we will analyze in this thesis is a form of static gauge field, i.e. SOC can be included to a kinetic energy part of Hamiltonian as $H = (\mathbf{p} - \mathbf{A})^2/(2M)$. Most basic type of gauge field is the electromagnetic vector potential \mathbf{A} , for which $\mathbf{A} = A/q$, where q is the charge of the particle. Magnetic field is related to the spatial variation of the vector potential via $\mathbf{B} = \nabla \times \mathbf{A}$, whereas electric field can be calculated from its temporal variation $\mathbf{E} = -\partial\mathbf{A}/\partial t$. SOC is type of non-Abelian gauge field. The non-Abelian gauge fields are gauge fields whose components do not commute $[A_x, A_y] \neq 0$.

Cold atoms are neutral, therefore can not be coupled with a magnetic field. But fortunately, it is possible to artificially create gauge fields which imitate the magnetic field or SOC. As we mentioned in the introduction there are two main methods to create the artificial gauge fields, one is to rotate the atoms and use the analogy between the magnetic component of the Lorentz force and the Coriolis fictitious force in the rotating frame. We will briefly discuss the analogy between these two forces in the next chapter. Another common approach is based on the adiabatic principle and phase associated with it. Usually using an atom-laser interaction an adiabatic potential is created. The geometric phase associated with this adiabatic potential creates an effective Hamiltonian with gauge field. Let us illustrate the basic principle behind this method. We follow [Dalibard et al., 2011], whom reader may consult for further information about the artificial gauge fields in neutral atoms.

Pancharatnam-Berry phase or simply the Berry phase is a phase which appears in the quantum mechanical systems described by two variables which evolve on different time scales [Berry, 1984]. In such systems we can apply the adiabatic principle first developed by Max Born and Vladimir Fock, which states that if the system starts at some eigenstate of the initial Hamiltonian of the fast changing variable, it will end in the corresponding eigenstate of the final Hamiltonian [Born and Fock, 1928]. For the laser-induced artificial gauge fields, the fast variable is the hyperfine state, which we take as the pseudo-spin of the system, while the slowly varying variable is the positions

of the atoms. Suppose that our system is described by following Hamiltonian

$$H = \left[\frac{-\nabla^2}{2M} + V(\mathbf{r}) \right] I + U(\mathbf{r}). \quad (4.16)$$

Here $U(\mathbf{r})$ is the general matrix which couples the internal states of the atoms, and is fast varying compared to the position of the atoms. Note that $U(\mathbf{r})$ does not explicitly dependent on time. I is the identity matrix. Assume that we diagonalize $U(\mathbf{r})$ and determine its eigenstates $|\chi_i(\mathbf{r})\rangle$, which are known as the dressed states. Next we expand the state vector of the atom using the eigenstates $|\chi_i(\mathbf{r})\rangle$

$$|\Psi(\mathbf{r}, t)\rangle = \sum_i \psi_i(\mathbf{r}, t) |\chi_i(\mathbf{r})\rangle. \quad (4.17)$$

Now assume that our state initially start at some state $|\chi_1(\mathbf{r})\rangle$ and assume that $|\chi_i(\mathbf{r})\rangle$ with $i \in \{2, 3, \dots, n\}$ are nearly degenerate eigenstates with our initial state. Assume that ϵ_i denotes the eigenvalue of $|\chi_i(\mathbf{r})\rangle$. Then assuming the validity of the adiabatic principle we can safely assume that our atom will be at some superposition of these states in its final form and therefore all the other states can be ignored. Therefore the expansion of the state vector in Eq. (4.17) simplifies to

$$|\Psi(\mathbf{r}, t)\rangle = \sum_i^n \psi_i(\mathbf{r}, t) |\chi_i(\mathbf{r})\rangle. \quad (4.18)$$

If we substitute this state vector to the time dependent Schrödinger equation describing the time evolution of the system we get

$$i \frac{\partial}{\partial t} \sum_i^n \psi_i(\mathbf{r}, t) |\chi_i(\mathbf{r})\rangle = \sum_i^n \left[\left(\frac{-\nabla^2}{2M} + V(\mathbf{r}) \right) I + U(\mathbf{r}) \right] \psi_i(\mathbf{r}, t) |\chi_i(\mathbf{r})\rangle \quad (4.19)$$

we act from left with the state $\langle \chi_j(\mathbf{r}) |$ to get

$$i \frac{\partial}{\partial t} \psi_j(\mathbf{r}, t) = [V(\mathbf{r}) + \epsilon_j] \psi_j(\mathbf{r}, t) - \frac{1}{2M} \sum_i^n \langle \chi_j(\mathbf{r}) | \nabla^2 [\psi_i(\mathbf{r}, t) |\chi_i(\mathbf{r})\rangle]. \quad (4.20)$$

Next we evaluate $\sum_i^n \langle \chi_j(\mathbf{r}) | \nabla^2 [\psi_i(\mathbf{r}, t) | \chi_i(\mathbf{r})] \rangle$

$$\begin{aligned}
& \sum_i^n \langle \chi_j(\mathbf{r}) | \nabla^2 [\psi_i(\mathbf{r}, t) | \chi_i(\mathbf{r})] \rangle = \\
& = \sum_i^n (\delta_{ji} \nabla^2 + 2 \langle \chi_j(\mathbf{r}) | \nabla | \chi_i(\mathbf{r}) \nabla \rangle) \psi_j(\mathbf{r}, t) + \sum_i^n \langle \chi_j(\mathbf{r}) | \nabla^2 | \chi_i(\mathbf{r}) \rangle \psi_i(\mathbf{r}, t) = \\
& = - \sum_{i,l}^n [-i \delta_{ji} \nabla - i \langle \chi_j(\mathbf{r}) | \nabla | \chi_i(\mathbf{r}) \rangle] \cdot [-i \delta_{il} \nabla - i \langle \chi_i(\mathbf{r}) | \nabla | \chi_l(\mathbf{r}) \rangle] \psi_l(\mathbf{r}, t) + \\
& + \sum_{i,l}^n \langle \chi_j(\mathbf{r}) | \nabla | \chi_i(\mathbf{r}) \rangle \langle \chi_i(\mathbf{r}) | \nabla | \chi_l(\mathbf{r}) \rangle \psi_l(\mathbf{r}, t) - \sum_i^n (\langle \chi_j(\mathbf{r}) | \nabla \rangle \cdot \langle \nabla | \chi_i(\mathbf{r}) \rangle) \psi_i(\mathbf{r}, t).
\end{aligned} \tag{4.21}$$

If we substitute this to the Schrödinger equation we get

$$i \frac{\partial}{\partial t} \Psi(\mathbf{r}, t) = \left[\frac{(\mathbf{p}\mathbf{I} - \mathbf{A})^2}{2M} + (V(\mathbf{r}) + \epsilon_j)\mathbf{I} + W(\mathbf{r}) \right] \Psi(\mathbf{r}, t) \tag{4.22}$$

where $\Psi(\mathbf{r}, t)$ is a vector with components $\psi_i(\mathbf{r}, t)$ and $\mathbf{p} = -i\nabla$ is the momentum. Effective vector potential \mathbf{A} is a 3-component vector matrix with components

$$\mathbf{A}_{ji} = \langle \chi_j(\mathbf{r}) | \nabla | \chi_i(\mathbf{r}) \rangle \tag{4.23}$$

and effective scalar potential $W(\mathbf{r})$ is matrix with components

$$W_{ji} = \frac{1}{2M} \left[(\langle \chi_j(\mathbf{r}) | \nabla \rangle \cdot \langle \nabla | \chi_i(\mathbf{r}) \rangle) - \sum_l^n \mathbf{A}_{il} \cdot \mathbf{A}_{lj} \right]. \tag{4.24}$$

We can clearly see that Eq. (4.22) is an effective Schrödinger equation with potential $V(\mathbf{r})\mathbf{I} + W(\mathbf{r})$ and a gauge field $\mathbf{A} = (\mathbf{A}_x, \mathbf{A}_y, \mathbf{A}_z)$. Note that if $n > 1$, \mathbf{A} is matrix and therefore we have non-Abelian gauge field, which SOC is a special case. Thus using the mechanism we discussed, it is possible to create a synthetic SOC.

4.3 Synthetic Spin Orbit Coupling in Cold Atomic Gases

Using the non-abelian generalization of Berry phase effect we described in previous section it is possible to create a synthetic SOC in cold atoms. In experiments, the adiabatic potential is generated by coupling the internal states of an atom with Raman laser beams. In 2009, Spielman's group in NIST realized the first synthetic gauge field, which was constant vector potential [Lin et al., 2009b]. In a follow up of this experiment Spielman's group by applying Zeeman field gradient, was able to make the vector potential position dependent, hence creating the first artificial magnetic field for the atoms [Lin et al., 2009a]. Later they achieved time dependent vector potential, which corresponds to artificial electric field [Lin et al., 2011a]. In 2011 these series of experiments of Spielman's group culminated with the creation of the first artificial SOC [Lin et al., 2011b].

Spielman's group used the so called NIST scheme. In the experiment two among the many hyperfine atomic states are chosen to represent spin as $|\uparrow\rangle$ and $|\downarrow\rangle$. In this scheme SOC is generated by two photon Raman transitions, which change the pseudo-spin of the atom. In this process two Raman lasers are used. These two counter-propagating lasers are used to couple these states via two photon Raman transition, the photon from first laser beam is absorbed and emitted to the second laser by stimulated re-emission. During this process $|\uparrow\rangle$ is flipped to $|\downarrow\rangle$ atom and it absorbs a momentum of $2k_0$, where k_0 is the recoil momentum of each photon inversely proportional to the wavelength of the laser beams. Since ultracold atoms have very small velocity, recoil momentum absorbed by the atom should be taken into account. Thus this momentum kick combined with the flipping of the spin, links the momentum of the atom with its spin, creating effective SOC.

In the NIST experiment the two hyperfine states were $|\uparrow\rangle = |F = 1, m_F = -1\rangle$ and $|\downarrow\rangle = |F = 1, m_F = 0\rangle$. Coupling matrix of the states is given as [Lin et al., 2011b]

$$U(\mathbf{r}, t) = \frac{\Omega}{2} e^{-i(\mathbf{k}\cdot\mathbf{r} - \omega t)} |\uparrow\rangle\langle\downarrow| + \text{H.C.} \quad (4.25)$$

here H.C. denotes the hermitian conjugate, $\Omega/2$ is the strength of Raman coupling. The two Raman lasers which are oriented along the $+\hat{x}$ and $-\hat{x}$ directions, have frequencies of ω_R and $\omega_R + \Delta\omega_R$ respectively. There is a bias Zeeman field along the \hat{y} direction with energy ω_z which leads to detuning from Raman resonance with $\delta = \Delta\omega_R - \omega_z$. The total Hamiltonian representing this system can be written as

$$H' = \begin{pmatrix} \frac{k^2}{2M} + \frac{\omega_z}{2} & \frac{\Omega}{2} e^{-i(2k_R x - \Delta\omega_R t)} \\ \frac{\Omega}{2} e^{-i(2k_R x - \Delta\omega_R t)} & \frac{k^2}{2M} + \frac{\omega_z}{2} \end{pmatrix} \quad (4.26)$$

time and space dependence of above Hamiltonian can be eliminated via a unitary transformation given as

$$U = \begin{pmatrix} e^{\frac{i}{2}(2k_R x - \Delta\omega_R t)} & 0 \\ 0 & e^{-\frac{i}{2}(2k_R x - \Delta\omega_R t)} \end{pmatrix} \quad (4.27)$$

which when applied to the Hamiltonian results in

$$H = U^\dagger H' U - iU^\dagger \frac{\partial}{\partial t} U = \begin{pmatrix} \frac{(k_x + k_R)^2}{2M} + \frac{k_y^2 + k_z^2}{2M} + \frac{\delta}{2} & \frac{\Omega}{2} \\ \frac{\Omega}{2} & \frac{(k_x - k_R)^2}{2M} + \frac{k_y^2 + k_z^2}{2M} - \frac{\delta}{2} \end{pmatrix}. \quad (4.28)$$

In terms of the Pauli matrices Hamiltonian can be expressed as

$$H = \frac{k_y^2 + k_z^2}{2M} + \frac{(k_x + k_R \sigma_z)}{2M} + \frac{\delta}{2} \sigma_z + \frac{\Omega}{2} \sigma_x. \quad (4.29)$$

If we rotate the spin along \hat{y} direction by $\pi/2$, which gives $\sigma_x \rightarrow \sigma_z$ and $\sigma_z \rightarrow -\sigma_x$, Hamiltonian takes more familiar form

$$H = \frac{k_y^2 + k_z^2}{2M} + \frac{(k_x - k_R \sigma_x)}{2M} - \frac{\delta}{2} \sigma_z + \frac{\Omega}{2} \sigma_x. \quad (4.30)$$

Note that second term corresponds to an equal combination of Rashba $\alpha(k_x \sigma_x + k_y \sigma_y)$ and Dresselhaus SOC $\gamma(k_x \sigma_x - k_y \sigma_y)$. Since SOC has effect only in single

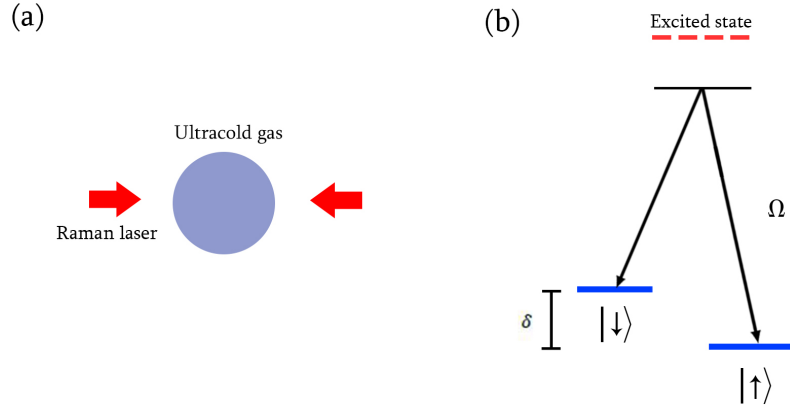


Figure 4.2: Schematic representation of the NIST scheme. (a) Two counter propagating Raman lasers couple together (b) a selected pair of atomic states labelled by $|\uparrow\rangle$ and $|\downarrow\rangle$ that represent the pseudo-spin of the atom. These lasers are arranged in a two-photon Raman configuration that uses an off-resonant intermediate state shown with black line in the figure and link atomic motion to the atoms pseudo-spin. $\Omega/2$ is strength of Raman coupling and δ is the two photon detuning.

direction, this is effectively a 1D SOC. This type of SOC is referred to as the equal Rashba-Dresselhaus (ERD) SOC or the NIST SOC.

After Spielman's group successfully realized the ERD SOC in bosonic rubidium-87, in 2012 two separate groups independently realized the ERD SOC in fermions, Jing Zhang's group using potassium-40 [Wang et al., 2012] and Zwerlein's MIT group using lithium-6 [Cheuk et al., 2012]. In the beginning of 2016 Wang's group realized ERD SOC for bosonic rubidium-87 [Luo et al., 2016], using gradient magnetic field and ground state of atoms, providing alternative scheme for realization of SOC besides the NIST Scheme described in this section. At the same time Jing Zhang's group realized the first two dimensional SOC on fermionic potassium-40 [Huang et al., 2016] using three Raman lasers and generalizing the NIST Scheme described above. The 2D SOC realized by Zhang's group has form of $\alpha_x k_x \sigma_x + \alpha_y k_y \sigma_y$. Given these experimental success in creating synthetic SOC, we can hope that soon pure Rashba SOC will be

realized in ultracold quantum gases. In this thesis due to its intriguing properties we will focus on Rashba SOC.

4.4 Single Particle Properties with Rashba Spin-Orbit Coupling in 2D

Since in this thesis we focus on 2D Fermi gas, let us analyze the single particle properties of Rashba SOC in 2D. In the absence of particle-particle interactions, Hamiltonian for Rashba SOC is given by

$$H = \sum_{\mathbf{k}} \hat{\psi}_{\mathbf{k}}^{\dagger} (\epsilon_{\mathbf{k}} \mathbf{I} + \alpha \vec{\sigma} \cdot \mathbf{k}) \hat{\psi}_{\mathbf{k}} \quad (4.31)$$

where $\epsilon_{\mathbf{k}} = k^2/(2M)$ is kinetic energy, and $\hat{\psi}_{\mathbf{k}}^{\dagger} = [\hat{a}_{\mathbf{k}\uparrow}^{\dagger}, \hat{a}_{\mathbf{k}\downarrow}^{\dagger}]$ denotes the fermionic operators collectively, $\alpha > 0$ denotes the SOC strength and $\vec{\sigma} = (\sigma_x, \sigma_y)$. Hamiltonian can be expressed in matrix form as

$$H = \sum_{\mathbf{k}} \begin{pmatrix} \hat{a}_{\mathbf{k}\uparrow}^{\dagger} & \hat{a}_{\mathbf{k}\downarrow}^{\dagger} \end{pmatrix} \begin{pmatrix} \frac{k^2}{2M} & \alpha(k_x - ik_y) \\ \alpha(k_x + ik_y) & \frac{k^2}{2M} \end{pmatrix} \begin{pmatrix} \hat{a}_{\mathbf{k}\uparrow} \\ \hat{a}_{\mathbf{k}\downarrow} \end{pmatrix}. \quad (4.32)$$

Above Hamiltonian can be diagonalized by a unitary transformation, which defines a new basis known as the helicity basis. Using the eigenvectors of above Hamiltonian we can derive following relation

$$\begin{pmatrix} \hat{a}_{\mathbf{k},+} \\ \hat{a}_{\mathbf{k},-} \end{pmatrix} = \frac{1}{\sqrt{2}} \begin{pmatrix} 1 & e^{-i\theta_{\mathbf{k}}} \\ e^{i\theta_{\mathbf{k}}} & -1 \end{pmatrix} \begin{pmatrix} \hat{a}_{\mathbf{k}\uparrow} \\ \hat{a}_{\mathbf{k}\downarrow} \end{pmatrix} \quad (4.33)$$

where $\theta_{\mathbf{k}} = \arctan(k_y/k_x)$ denotes the polar angle of the \mathbf{k} vector, therefore $e^{i\theta_{\mathbf{k}}} = (k_x + ik_y)/k$. Note that spin is no longer a good quantum number. $\hat{a}_{\mathbf{k},s}^{\dagger}(\hat{a}_{\mathbf{k},s})$ creates (annihilates) particle with helicity $s = \pm = \pm 1$. Helicity \pm denotes the spin direction is either paralel or anti-paralel to the in-plane momentum direction. After diagonalization $H = \sum_{\mathbf{k},s} \epsilon_{\mathbf{k}s} \hat{a}_{\mathbf{k},s}^{\dagger} \hat{a}_{\mathbf{k},s}$, we get the dispersion relation for each helicity

$$\varepsilon_{\mathbf{k}s} = \frac{k^2}{2M} + s\alpha k. \quad (4.34)$$

Note that the minimum of the spectrum of the lower energy – helicity branch is shifted to finite momenta, forming of a degenerate circle with radius $k = M\alpha$. Hamiltonian has a symmetry of simultaneous rotation of spin and momentum at $k_x - k_y$ plane. \mathbf{k} is still a good quantum number, but plane waves with finite \mathbf{k} does not poses this symmetry which necessarily leads to degeneracy in the minimum. Note that SOC breaks the inversion symmetry $\varepsilon_{-\mathbf{k}\uparrow} \neq \varepsilon_{\mathbf{k}\uparrow}$, but time reversal symmetry is still preserved. For illustration of the splitting of the dispersion relation for Rashba SOC see Fig. 4.3.

This change in dispersion relation effects the low energy DOS. Using the dispersion relation for s helicity particle we can calculate the DOS $D_s(\epsilon) = \sum_{\mathbf{k}} \delta(\epsilon - \varepsilon_{\mathbf{k},s})$ as

$$\begin{aligned} D_s(\epsilon > 0) &= \frac{MA}{2\pi} \left(1 - \frac{sM\alpha}{\sqrt{M^2\alpha^2 + 2M\epsilon}} \right), \\ D_s(\epsilon \leq 0) &= \frac{MA}{2\pi} \frac{(1-s)M\alpha}{\sqrt{M^2\alpha^2 + 2M\epsilon}} \Theta(M^2\alpha^2 + 2M\epsilon) \end{aligned} \quad (4.35)$$

We should note that as expected from the dispersion relation, for $\epsilon < 0$ we just have – helicity particles. The total density of states is given as

$$D(\epsilon > 0) = \frac{MA}{\pi} \quad (4.36)$$

$$D(\epsilon \leq 0) = \frac{MA}{\pi} \frac{M\alpha}{\sqrt{M^2\alpha^2 + 2M\epsilon}} \Theta(M^2\alpha^2 + 2M\epsilon) \quad (4.37)$$

Thus DOS is same as no SOC case for $\epsilon > 0$. On the other hand for $\epsilon < 0$ DOS increases and has similar behavior as 1D Fermi gas for which $D(\epsilon) \propto 1/\sqrt{\epsilon}$. This reduced dimensionality is direct result of the degenerate minimum of the dispersion, i.e. energy increases only along the perpendicular direction of the degenerate circle. As we will see increase in low energy DOS will have very interesting physical consequences.

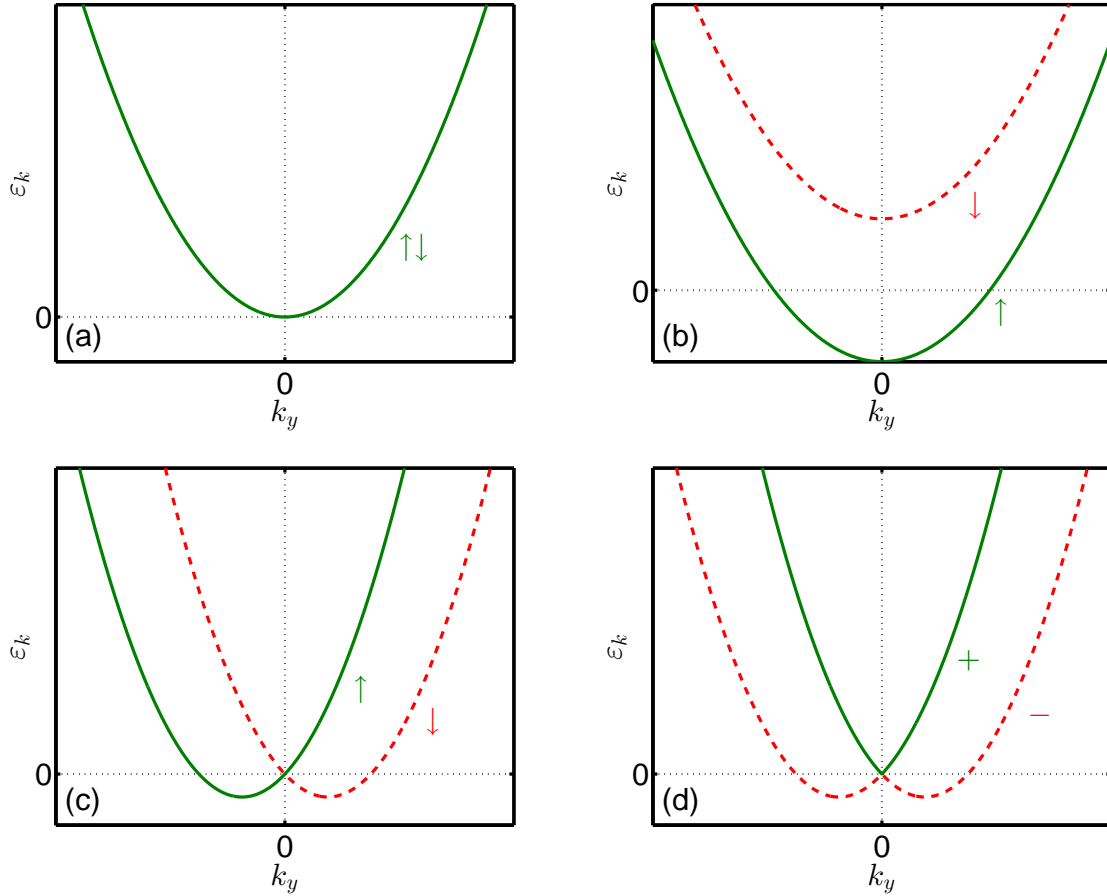


Figure 4.3: Illustration of the splitting of the spin degeneracy due to Rashba SOC. All the plots are shown for $k_x = 0$ without loss of generality since system has a symmetry of simultaneous rotation of spin and momentum at $k_x - k_y$ plane. (a) Dispersion relation of free Fermi gas, it is simple parabola. Both time reversal symmetry and inversion symmetry are present $\varepsilon_{-\mathbf{k}\uparrow} = \varepsilon_{\mathbf{k}\uparrow}$. We have spin degeneracy. (b) Dispersion relation of Fermi gas in the presence of Zeeman field. Zeeman field lifts the spin degeneracy and time reversal symmetry is broken. But inversion symmetry is still present. (c) Rashba SOC behaves like momentum dependent Zeeman field. Spin degeneracy is lifted (except at $\mathbf{k} = 0$) but time reversal symmetry is still present. Unlike standard Zeeman field, SOC breaks the inversion symmetry. (d) The positive and negative helicity bands of Rashba SOC.

Before finishing this section we should note that, SOC Hamiltonian can be interpreted as momentum dependent Zeeman field. As a result of this spin points to different direction for different momentum eigenstates (see Fig. 4.3).

4.5 Non-Interacting Homogeneous Fermi Gas with Rashba Spin-Orbit Coupling in 2D

In this section we again assume that we have two species atoms which we label with different pseudo-spin \uparrow and \downarrow . We assume that $T = 0$. Before analyzing the trapped Fermi gas with Rashba coupling in 2D, let us start with a brief analysis of the homogeneous Fermi gas. The curves describing the Fermi surface of s helicity particles can be calculated by setting $\varepsilon_{\mathbf{k}s} - \mu = 0$, and are given as

$$k_{1,2}^s = -s\alpha M \pm \sqrt{\alpha^2 M^2 + 2\mu M}. \quad (4.38)$$

Note that for $\alpha^2 M + 2\mu < 0$, $k_{1,2}^s$ are not real. Hence for chemical potentials which satisfy this condition no particle is present in the system. When $\mu > 0$, we have $k_1^s > 0$ and $k_2^s < 0$. Hence both positive and negative helicity particles' Fermi surface is a circle (see Fig. 6.1(a)). The radius of these circles are $k = k_1^s$, hence the Fermi surface of negative helicity particles is bigger than that of a positive helicity particles. On the other hand when $0 > \mu > -M\alpha^2/2$, the Fermi surface of positive helicity particles disappears. For negative helicity particles $k_{1,2}^- > 0$, thus Fermi surface is a ring with inner radius $k = k_2^-$ and outer radius $k = k_1^-$ (see Fig. 6.1(b)). Thus at $\mu = 0$ topology of the Fermi surface changes, ring shaped Fermi surface becomes circle for the negative helicity particles, while at that point the circular Fermi surface of positive helicity particles emerges. Such topological change in the Fermi surface is known as the Lifshitz transition. Hence in the non-interacting Fermi gas with SOC it is possible to observe the Lifshitz transition by changing the atomic density.

s helicity particle number for given α and μ can be calculated by integrating $N_s = \sum_{\mathbf{k}} \Theta(\mu - \varepsilon_{\mathbf{k}s})$. For the positive helicity particles we get

$$N_+ = \frac{A}{(2\pi)^2} \int_0^{k_1^+} dk 2\pi k \Theta(\mu) = \frac{MA}{2\pi} \left(M\alpha^2 + \mu - \alpha\sqrt{M^2\alpha^2 + 2M\mu} \right) \Theta(\mu). \quad (4.39)$$

Note that $N_+ \rightarrow 0$ as $\mu \rightarrow 0$. For the negative helicity particles

$$\begin{aligned} N_- &= \frac{A}{(2\pi)^2} \left(\int_0^{k_1^-} dk 2\pi k \Theta(\mu) + \int_{k_2^-}^{k_1^-} dk 2\pi k \Theta(-\mu) \Theta(\alpha^2 M + 2\mu) \right) \\ &= \frac{MA}{2\pi} \left(M\alpha^2 + \mu + \alpha\sqrt{M^2\alpha^2 + 2M\mu} \right) \Theta(\mu) \\ &\quad + \frac{MA}{\pi} \alpha\sqrt{M^2\alpha^2 + 2M\mu} \Theta(-\mu) \Theta(\alpha^2 M + 2\mu). \end{aligned} \quad (4.40)$$

By scaling the total number of particles with no SOC particle number $N = k_F^2/(2\pi)$ given in Eq. (2.52), chemical potential can be determined as $\mu = E_F - M\alpha^2$ for $\mu \geq 0$ and $\mu = E_F^2/(2M\alpha^2) - M\alpha^2/2$ for $\mu < 0$. Critical SOC strength for the Lifshitz transition can be determined from $\mu = 0$ as $\alpha = k_F/(\sqrt{2}M)$.

4.6 Trapped non-interacting Fermi gas with Rashba spin-orbit coupling in 2D

For the trapped Fermi gas, we again use LDA which permits us to apply the homogeneous case results for the inhomogeneous gas. Let us start with calculating the LDOS for harmonically trapped 2D Fermi gas with SOC. Dispersion relation under LDA can be written as

$$\epsilon_{\mathbf{k}s} = \frac{k^2}{2M} + s\alpha k + \frac{M\omega^2 r^2}{2}. \quad (4.41)$$

Therefore, LDOS expression can be deduced from Eq. (4.35), by changing ϵ with $\epsilon_r = \epsilon - M\omega^2 r^2/2$ which leads to

$$D_s(\epsilon, r) = \frac{MA}{2\pi} \left(1 - \frac{sM\alpha}{\sqrt{M^2\alpha^2 + 2M\epsilon_r}} \right) \quad \epsilon_r \geq 0$$

$$D_s(\epsilon, r) = \frac{MA}{2\pi} \frac{(1-s)M\alpha}{\sqrt{M^2\alpha^2 + 2M\epsilon_r}} \quad \epsilon_r < 0 \quad (4.42)$$

The main effect of the SOC for the trap profile is to increase the low energy ($\epsilon_r < 0$) LDOS so that it leads to an increased density at the center of the trap. Under LDA, the density relations given in Eq. (4.39) and Eq. (4.40) can be applied to the trapped Fermi gas by simply changing μ with local $\mu(r) = \mu - M\omega^2 r^2/2$. This gives the following density profile for the positive helicity particles.

$$n_+(r) = \frac{M}{2\pi} \left(M\alpha^2 + \mu_r - \alpha\sqrt{M^2\alpha^2 + 2M\mu_r} \right) \quad \mu(r) \geq 0. \quad (4.43)$$

In the trap region where $\mu(r) < 0$, there are no positive helicity particles. On the other hand the density profile of the negative helicity particles can be expressed as

$$n_-(r) = \frac{M}{2\pi} \left(M\alpha^2 + \mu_r + \alpha\sqrt{M^2\alpha^2 + 2M\mu_r} \right) \quad \mu(r) \geq 0 \quad (4.44)$$

$$n_-(r) = \frac{M}{\pi} \alpha\sqrt{M^2\alpha^2 + 2M\mu_r} \quad \mu(r) < 0. \quad (4.45)$$

By relating the particle number to the Fermi energy of the trapped 2D Fermi gas $E_F = \omega\sqrt{N}$, we can integrate above densities. When global $\mu = 0$, the positive helicity band becomes empty in the whole trap, i.e. we just have negative helicity particles. The critical SOC strength for which $\mu = 0$ can be determined as $\alpha_c = \sqrt[4]{6}E_F/k_F$. For $\alpha < \alpha_c$, trap separates into two regions, inner region [$\mu(r) \geq 0$] where we have both negative and positive helicity particles and an outer region [$\mu(r) < 0$] where we have just negative helicity particles (see Fig. 4.5). The global chemical potential can be determined by integrating the density as $\mu = -\alpha^2 M + \sqrt{\alpha^4 M^2/3 + E_F^2}$, which we can use to find the boundary between this two regions

$$r_c(\alpha) = \sqrt{\frac{-2\alpha^2}{\omega^2} + \sqrt{\frac{4\alpha^4}{3\omega^4} + R_F^4}}. \quad (4.46)$$

Where R_F is given by Eq. (2.60). For $r < r_c(\alpha)$ where we have both positive and negative helicity particles density has a parabolic shape, same as the no SOC case

$$n(r) = \frac{M}{\pi} \left(\sqrt{\frac{\alpha^2 k_F^2}{12} + E_F^2} - \frac{M\omega^2 r^2}{2} \right). \quad (4.47)$$

Note that as expected from the enhanced low energy LDOS, central density is higher than the no SOC case, and increases with increasing α . In the $\alpha \rightarrow 0$ limit above density reduces to that of a non-interacting 2D Fermi gas given in Eq. (2.59) as expected. On the outside region $r > r_c(\alpha)$ where we do not have positive helicity particles density profile differs from the no SOC parabolic density

$$n(r) = \frac{M^2 \alpha}{\pi} \sqrt{-\alpha^2 - \omega^2 r^2 + \sqrt{\frac{4\alpha^4}{3} + \frac{k_F^4}{M^4}}}. \quad (4.48)$$

From the density distribution we can determine the edge of the gas R_O^0 as

$$R_O^0 = \sqrt{\frac{-\alpha^2}{\omega^2} + \sqrt{\frac{4\alpha^4}{3\omega^4} + R_F^4}}. \quad (4.49)$$

Note that as $\alpha \rightarrow 0$, $R_O^0 \rightarrow R_F$ as expected. For increasing α , the edge of the gas moves towards the center as expected. As mentioned above for $\alpha > \alpha_c$, the whole trap is composed of negative helicity particles and the global chemical potential can be determined as $\mu = \left[-2\alpha^2 M + \left(6E_F^2 / \alpha \sqrt{2M} \right)^{2/3} \right] / 4$. In this parameter regime we have single density profile

$$n(r) = \frac{M^2 \alpha}{\pi} \sqrt{\left(\frac{3E_F^2}{2\alpha M^2} \right)^{2/3} - \omega^2 r^2}. \quad (4.50)$$

Again we can deduce from this density profile that central density increases monotonically with increasing α . The edge of the trap again can be determined analytically as

$$R_O^0 = R_F \left(\frac{3E_F}{4\alpha k_F} \right)^{1/3}. \quad (4.51)$$

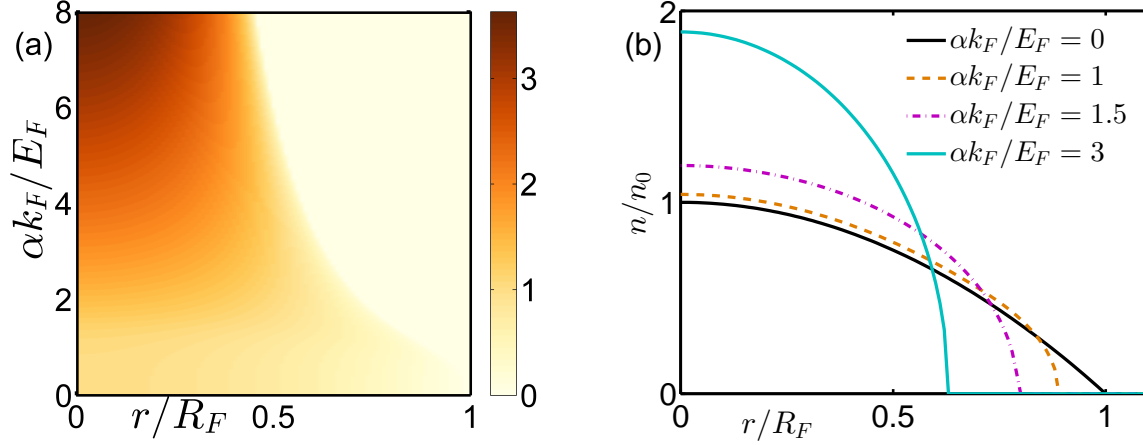


Figure 4.4: Density profile of the trapped Rashba coupled non-interacting Fermi gas. (a) Non-interacting density profile with changing SOC strength α . Central density monotonically increases and the gas shrinks. (b) Density at representative SOC values. We can clearly see that at the center of the trap we have a parabolic density profile, while at the edge where we have just negative helicity particles the density profile is non-parabolic.

In general as α increases the edge moves towards the center of the gas as the central density is increased as can be seen in Fig. 4.4(a) where we plot the density profile with changing α . In Fig. 4.4(b) we show density profile at some representative α values. Note that at the central region where we have both positive and negative helicity particles density is parabolic, on the other hand at the outer region of the trap where we have just negative helicity particles density is non-parabolic.

Similar to the no SOC case it is possible to relax the LDA and determine the density distribution exactly using the 2D harmonic oscillator basis. But unlike the no SOC case, Hamiltonian is no longer diagonal in 2D harmonic oscillator basis. The single particle Hamiltonian of the trapped 2D Fermi gas with SOC can be written in the real space as

$$H = \frac{\hat{p}^2}{2M} + \frac{1}{2}M\omega^2\hat{r}^2 + \alpha\hat{\mathbf{p}} \cdot \hat{\boldsymbol{\sigma}}. \quad (4.52)$$

The Rashba SOC term can be expressed by the spin and angular momentum raising lowering operators, $\hat{\sigma}_{\pm} = \hat{\sigma}_x \pm i\hat{\sigma}_y$ and $\hat{p}_{\pm} = \hat{p}_x \pm i\hat{p}_y$ respectively.

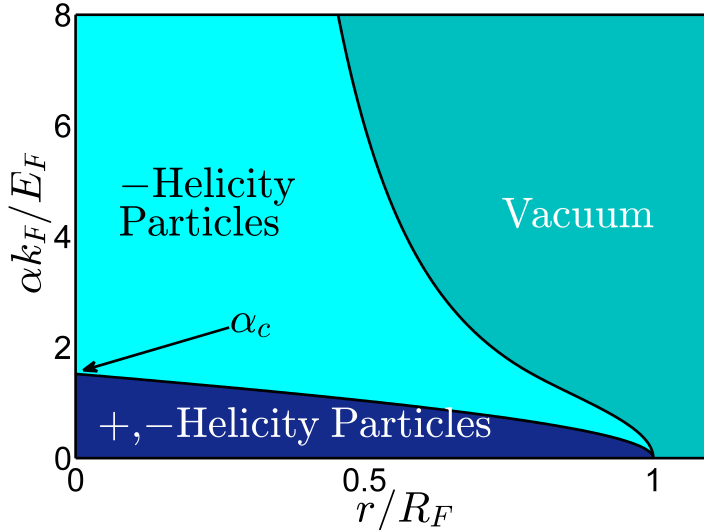


Figure 4.5: Distribution of + and - helicity particles in the trap for changing SOC strength α . For SOC strength $\alpha < \alpha_c = \sqrt[4]{6}E_F/k_F$ at the center of the trap we have both + and - helicity particles characterized by a parabolic density distribution and at the edge just - helicity particles characterized by a non-parabolic density distribution. Beyond α_c all the particles in the system are negative helicity particles.

$$\alpha \hat{\mathbf{p}} \cdot \hat{\boldsymbol{\sigma}} = \alpha(\hat{p}_x \hat{\sigma}_x + \hat{p}_y \hat{\sigma}_y) = \alpha \frac{1}{2} (\hat{p}_+ \hat{\sigma}_- + \hat{p}_- \hat{\sigma}_+). \quad (4.53)$$

Thus SOC either increases or decreases the angular momentum, depending on its spin state. Thus as we pointed above 2D harmonic oscillator states can not be an eigenstates of SOC operator. Note that while Rashba coupling does not preserve the individual spin or space rotational symmetry, the full rotational symmetry is still present. Thus the total Hamiltonian can be diagonalized simultaneously with the total angular momentum operator $J_z = L_z + S_z$. The effect of SOC term on the 2D harmonic oscillator basis can be deduced by writing the SOC operator in terms of the ladder operators associated with the left and right circular quanta defined in Eq. (2.66)

$$\alpha \hat{\mathbf{p}} \cdot \hat{\boldsymbol{\sigma}} = -\alpha i \frac{2}{a_0} \left[(\hat{b}_L^\dagger - \hat{b}_R) \hat{\sigma}_- + (\hat{b}_R^\dagger - \hat{b}_L) \hat{\sigma}_+ \right] \quad (4.54)$$

Thus the effect of Hamiltonian on the 2D harmonic oscillator states can be deduced as

$$\begin{aligned} H|n, l, \uparrow\rangle &= \omega(n+1)|n, l, \uparrow\rangle \\ &- \frac{2i\alpha}{a_0} \left(\sqrt{\frac{n+l}{2}} + 1 |n+1, l+1, \downarrow\rangle - \sqrt{\frac{n-l}{2}} |n-1, l+1, \downarrow\rangle \right) \end{aligned} \quad (4.55)$$

$$\begin{aligned} H|n, l, \downarrow\rangle &= \omega(n+1)|n, l, \downarrow\rangle \\ &- \frac{2i\alpha}{a_0} \left(\sqrt{\frac{n-l}{2}} + 1 |n+1, l-1, \uparrow\rangle - \sqrt{\frac{n+l}{2}} |n-1, l-1, \uparrow\rangle \right) \end{aligned} \quad (4.56)$$

From these expression we can deduce that Hamiltonian can be expressed in tri-diagonal form in 2D harmonic oscillator basis, and can be diagonalized numerically to get the eigenvectors and eigenvalues, which can be used to determine the exact density distribution. The details of this derivation are given in Sec. (6.2), for rotating spin-orbit coupled 2D Fermi gas. Taking $\Omega \rightarrow 0$ limit will yield the density expression desired for this section.

In Fig. 4.6 we compare the density profile obtained via the exact quantum mechanical calculations and LDA for different particle number and SOC strengths. At low particle numbers similar to the no SOC case, LDA fails to capture the Friedel oscillations and low density tail of the gas. For considerable particle numbers such as $N = 5000$, Friedel oscillations become invisible and the low density tail becomes very small compared to the system size. Thus at high particle limit LDA and exact QM calculations become indistinguishable for any SOC strength.

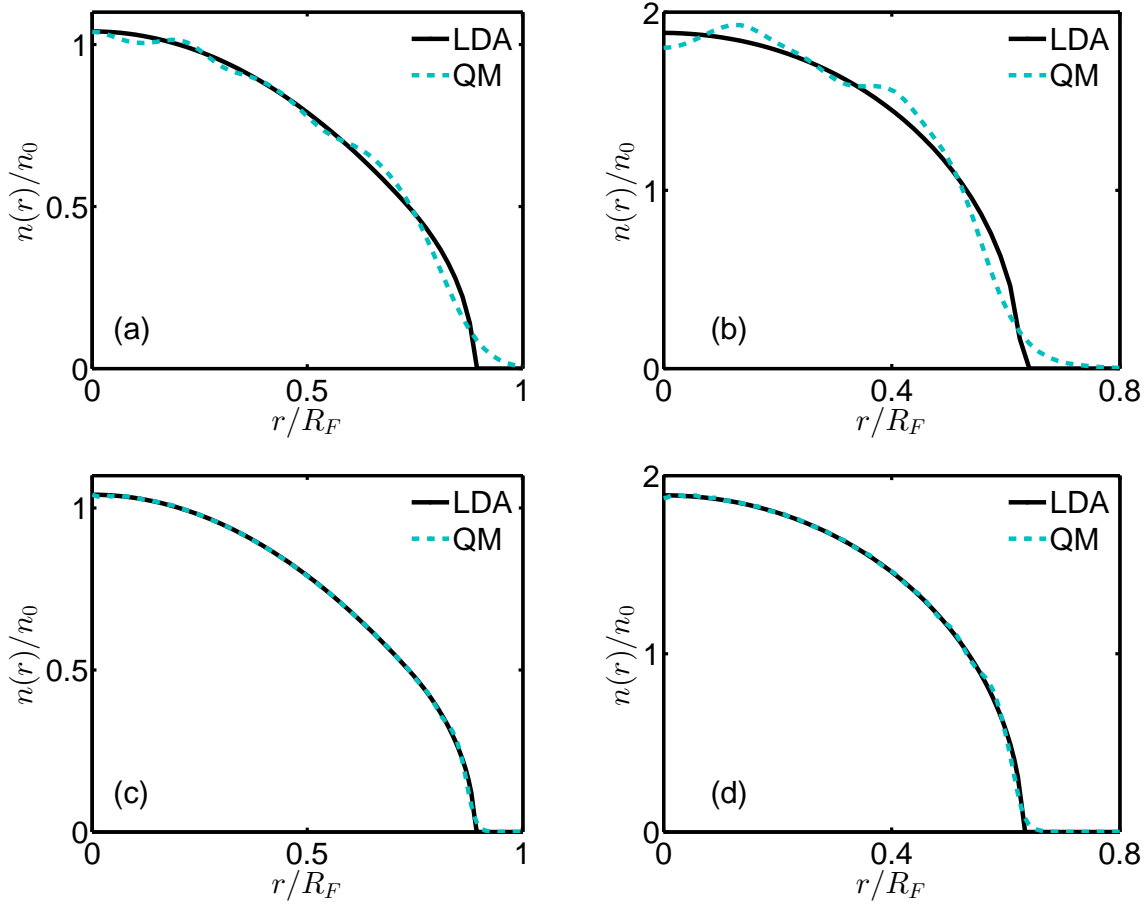


Figure 4.6: Density profile computed via the exact quantum mechanical calculations compared with the semi-classical LDA results for different particle numbers and SOC strengths: (a) $N = 100$, $\alpha = 1E_F/k_F < \alpha_c$ (b) $N = 100$, $\alpha = 3E_F/k_F > \alpha_c$ (c) $N = 5000$, $\alpha = 1E_F/k_F < \alpha_c$ (d) $N = 5000$, $\alpha = 3E_F/k_F > \alpha_c$. In low particle numbers such as $N = 100$ LDA fails to capture the Friedel oscillations and low density tail of the gas. For considerable particle numbers such as $N = 5000$, Friedel oscillations become invisible and the low density tail becomes very small compared to the system size. Thus at high particle limit LDA and exact QM calculations become practically indistinguishable for any SOC strength.

4.7 Trapped Interacting Fermi Gas with Rashba Spin-Orbit Coupling in 2D

In this section we investigate 2D interacting Fermi gas with SOC at $T = 0$. We again model the particle-particle interaction with the contact potential since we still work in the dilute limit. Contact interaction is still valid approximation in the presence of Rashba SOC if additional condition $\alpha R_e \ll 1$ is satisfied [Cui, 2012], where $\alpha > 0$ is the SOC strength. We will assume that this condition is satisfied. We again make the mean-field approximation. The total mean-field Hamiltonian describing the system can be written as a sum of three terms

$$H^{\text{mf}} = H_{\text{sho}} + H_{\text{soc}} + H_{\text{int}}^{\text{mf}} \quad (4.57)$$

where H_{sho} denotes the harmonic oscillator part of the Hamiltonian and is given in Eq. (3.113), $H_{\text{int}}^{\text{mf}}$ is the mean-field interaction term given in Eq. (3.115), with the order parameter defined again as $\Delta(\mathbf{r}) = g\langle\hat{\psi}_{\uparrow}(\mathbf{r})\hat{\psi}_{\downarrow}(\mathbf{r})\rangle$, and the SOC term H_{soc} is

$$H_{\text{soc}} = \alpha \sum_{\sigma\sigma'} \int d\mathbf{r} \hat{\psi}_{\sigma}^{\dagger}(\mathbf{r}) [\mathbf{p} \cdot \vec{\sigma}]_{\sigma\sigma'} \hat{\psi}_{\sigma'}(\mathbf{r}). \quad (4.58)$$

We again make the local density approximation, and define the local chemical potential as in Eq. (3.103). If we then transfer the field operators to the momentum space, our Hamiltonian becomes

$$H_{\mathbf{k}}^{\text{LDA}}(\mathbf{r}) = \frac{1}{2} \sum_{\mathbf{k}} \Psi_{\mathbf{k}}^{\dagger} H_{\mathbf{k}}^{\text{LDA}}(\mathbf{r}) \Psi_{\mathbf{k}} + C(\mathbf{r}) \quad (4.59)$$

where

$$H_{\mathbf{k}}^{\text{LDA}}(\mathbf{r}) = \begin{pmatrix} \xi_{\mathbf{k}}(\mathbf{r}) & S_{\mathbf{k}} & 0 & \Delta(\mathbf{r}) \\ S_{\mathbf{k}}^* & \xi_{\mathbf{k}}(\mathbf{r}) & -\Delta(\mathbf{r}) & 0 \\ 0 & -\Delta^*(\mathbf{r}) & -\xi_{\mathbf{k}}(\mathbf{r}) & S_{\mathbf{k}}^* \\ \Delta^*(\mathbf{r}) & 0 & S_{\mathbf{k}} & -\xi_{\mathbf{k}}(\mathbf{r}) \end{pmatrix}, \quad (4.60)$$

$\Psi_{\mathbf{k}}^\dagger = [a_{\mathbf{k}\uparrow}^\dagger, a_{\mathbf{k}\downarrow}^\dagger, a_{\mathbf{k}\uparrow}, a_{-\mathbf{k}\downarrow}]$ and $C(\mathbf{r}) = \sum_{\mathbf{k}}(\xi_{\mathbf{k}}(\mathbf{r}) + A|\Delta(\mathbf{r})|^2/g)$. Above, $\Delta(\mathbf{r}) = g/A \sum_{\mathbf{k}} \langle a_{\mathbf{k}\uparrow} a_{-\mathbf{k}\downarrow} \rangle$ is the local mean-field order parameter, $\xi_{\mathbf{k}}(\mathbf{r}) = \epsilon_{\mathbf{k}} - \mu(\mathbf{r})$, and $S_{\mathbf{k}} = \alpha(k_x - ik_y)$ is the SOC term. We should note that by transforming the above Hamiltonian to the helicity basis we can show that the pairing is between the opposite momentum states of the same helicity band, (s, \mathbf{k}) and $(s, -\mathbf{k})$.

If we diagonalize the above Hamiltonian we get the quasi-particle energies

$$E_{\mathbf{k}s}(\mathbf{r}) = \sqrt{(\xi_{\mathbf{k}}(\mathbf{r}) + s\alpha k)^2 + |\Delta(\mathbf{r})|^2} \quad (4.61)$$

where $s = \pm$ denotes the helicity of the particle. Note that similar to the non-interacting case, spectrum is split to positive and negative helicity bands. As expected in $\alpha \rightarrow 0$ we recover the standard BCS excitation energy. $E_{\mathbf{k}s}(\mathbf{r})$ is isotropic in $k_x - k_y$ plane, which is not surprising given that the Rashba SOC is isotropic in the momentum space.

The negative helicity band has lower energy than the positive helicity band. Similar to the no SOC case, the excitation energies are gapped. Let us analyze the behavior of the gap of the lower energy negative helicity excitation energy (see Fig. 4.7 for schematic representation). When $\mu(\mathbf{r}) > 0$, the excitation minimum is located at $k = M \left[\alpha + \sqrt{\alpha^2 + 2\mu(\mathbf{r})} \right]$. The energy gap is again equal to the order parameter $|\Delta(\mathbf{r})|$. As we move towards the edge of the trap, or increase the soc strength (as we will show μ decreases with increasing SOC) and the chemical potential becomes $\mu(\mathbf{r}) = 0$ second excitation minimum appears at $k = M \left[\alpha - \sqrt{\alpha^2 + 2\mu(\mathbf{r})} \right]$, the energy gap at this point again is $|\Delta(\mathbf{r})|$. As $\mu(\mathbf{r})$ further decrease and become $\mu(\mathbf{r}) = -M\alpha^2/2$ the two degenerate minima merge at $k = M\alpha$. For $\mu(\mathbf{r}) < -M\alpha^2$, minimum remains at $k = M\alpha$. In this regime excitation energy gap becomes $\sqrt{[\mu(\mathbf{r}) + M\alpha^2/2]^2 + |\Delta(\mathbf{r})|^2}$. Note that at $\mu(\mathbf{r}) = -M\alpha^2/2$, the excitation minimum changes character, and can be interpreted as the point at which we pass from the BCS to BEC side of the crossover. From this analysis we can see that in general SOC pushes the excitation minima to the higher momenta. Even in the BEC side, excitation energy remains at finite momentum. This result is also expected, since also in the non-interacting case, dispersion

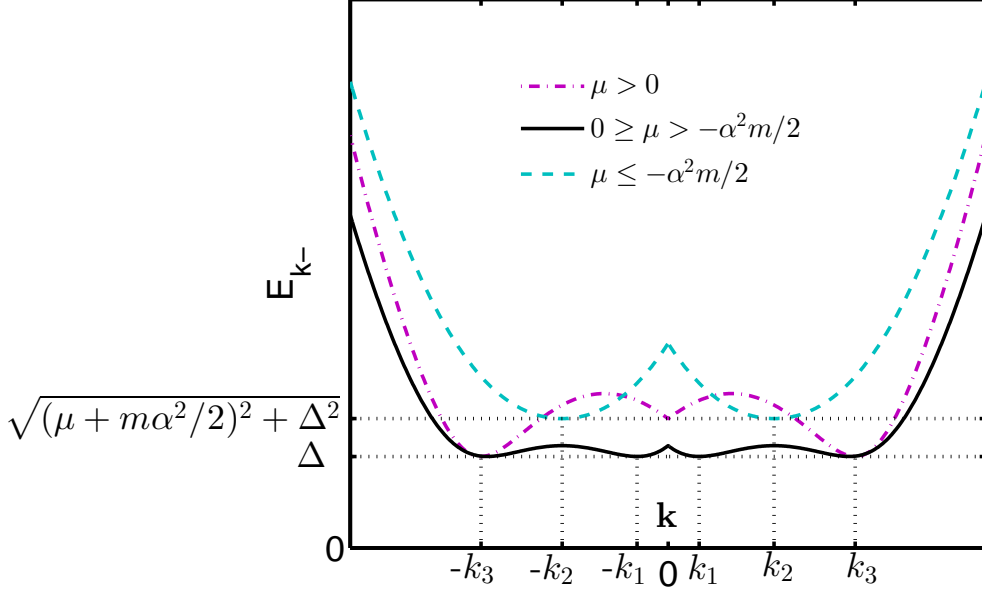


Figure 4.7: Schematic diagram of the quasi-particle excitation spectrum of the negative helicity particles for different μ values. The momentum values of the minima are $k_1 = M \left(\alpha - \sqrt{\alpha^2 + 2\mu} \right)$, $k_2 = M\alpha$ and $k_3 = M \left(\alpha + \sqrt{\alpha^2 + 2\mu} \right)$. SOC pushes the excitation minima to the higher momentum states and they remain so even in the extreme BEC limit.

minimum is pushed to the higher momenta by SOC.

The gap and number equations can be derived by the procedure given in Sec. 6.3, where the derivation is done for the rotating Rashba coupled Fermi gas. Simply taking $\Omega \rightarrow 0$ will give the gap and number equations for the case we consider in this section

$$\frac{1}{g} = \frac{1}{4A} \sum_{\mathbf{k}s} \frac{1}{E_{\mathbf{k}s}(\mathbf{r})} \tanh \frac{\beta E_{\mathbf{k}s}(\mathbf{r})}{2}, \quad (4.62)$$

$$n(\mathbf{r}) = \frac{1}{2A} \sum_{\mathbf{k}s} \left[1 - \frac{\xi_{\mathbf{r}\mathbf{k}} + s\alpha k}{E_{\mathbf{r}\mathbf{k}s}} \tanh \frac{\beta E_{\mathbf{k}s}(\mathbf{r})}{2} \right]. \quad (4.63)$$

These equations are to be solved locally within the trap and the total particle number is obtained by integrating the density, i.e., $N = \int d\mathbf{r}n(\mathbf{r})$. We renormalize the bare s-wave interaction g again using Eq. (3.41). Particle number is exchanged

in favor of the Fermi energy given by $E_F = \omega\sqrt{N}$. Since both the trap and Rashba SOC are isotropic we can deduce that local order parameter and local density is independent of the polar angle.

For small SOC, $M\alpha^2 \ll E_b + 2E_F$, the order parameter can be determined perturbatively [Chen et al., 2012] in the trap as

$$|\Delta(r)| \simeq \Delta_0 \sqrt{1 - r^2/R_F^2} \quad (4.64)$$

where $\Delta_0 = \sqrt{2E_F E_b} \sqrt{1 + 2M^2\alpha^4/3(E_b + 2E_F)^2}$. Since $M\alpha^2 \ll E_b + 2E_F$, the last term can be safely ignored and $\Delta_0 = \sqrt{2E_F E_b}$. Thus for small SOC compared to the Fermi energy or E_b , the order parameter profile remains unchanged compared to the no SOC case. This is also valid for the density profile which is also identical to its no SOC value. In this regime the global chemical potential is $\mu \simeq E_F - E_b/2 - M\alpha^2$. Thus, the effects of small SOC on density and pairing are negligible, however the non-zero angular momentum states of the lower helicity band become energetically more favorable.

As SOC becomes significant, $M\alpha^2 \sim E_b + 2E_F$, we can solve the gap and number equations self consistently. In Fig. 4.8 we show both the density and the order parameter profile of the trap with changing SOC strength obtained from the self-consistent numerical solutions of the number and gap equations. For small α trap profile remains almost unchanged as stated above. But when $M\alpha^2 \sim E_b + 2E_F$ similarly to the non-interacting case, the gas contracts towards the center of the trap ($R_O < R_F$) and $|\Delta(r)|$ starts to increase. This increase in the order parameter is expected since SOC increases low energy LDOS. This increase in $|\Delta(r)|$ and central density is monotonic with increasing α in this regime. Note that for greater E_b these effects on the trap profile become observable for larger values of α . This is illustrated in Fig. 4.9, where we plot the density and order parameter profile of the Fermi gas for $\alpha = 1.5E_F/k_F$ and various E_b values. As E_b increases gas expands, and eventually it becomes identical with the $\alpha = 0$ profile. As SOC enhances the pairing in general, the gas in the trap remains completely in the SF phase.

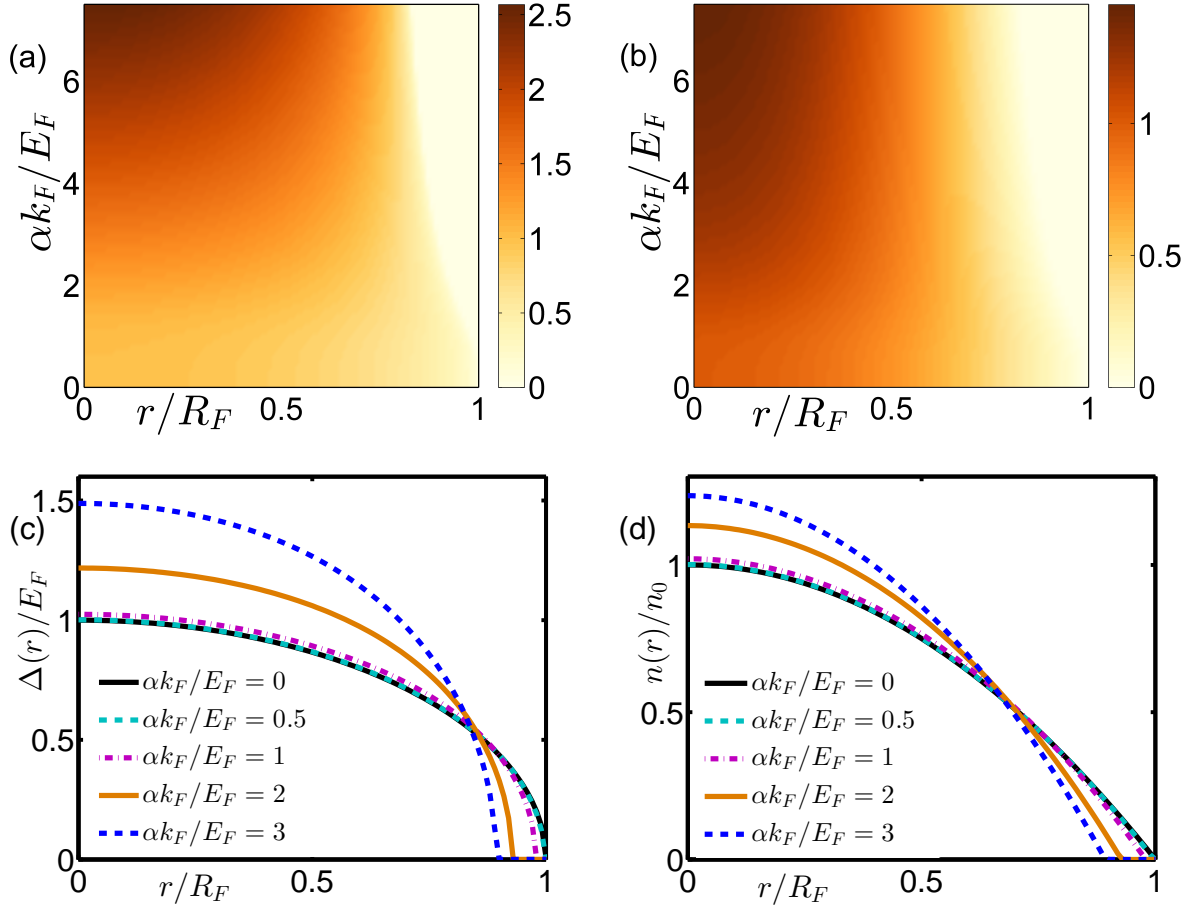


Figure 4.8: The trap profile of Rashba coupled interacting Fermi gas. In all the figures $E_b = 0.5E_F$. (a) The order parameter profile with changing SOC strength α . For small SOC $\alpha < 1E_F/k_F$, order parameter profile does not change, for higher values order parameter increases. (b) The density profile with changing SOC strength α . For small SOC $\alpha < 1E_F/k_F$, density profile does not change, on the other hand for higher SOC values central density increases and the gas shrinks. (c) Order parameter at representative SOC values. (d) Density at representative SOC values.

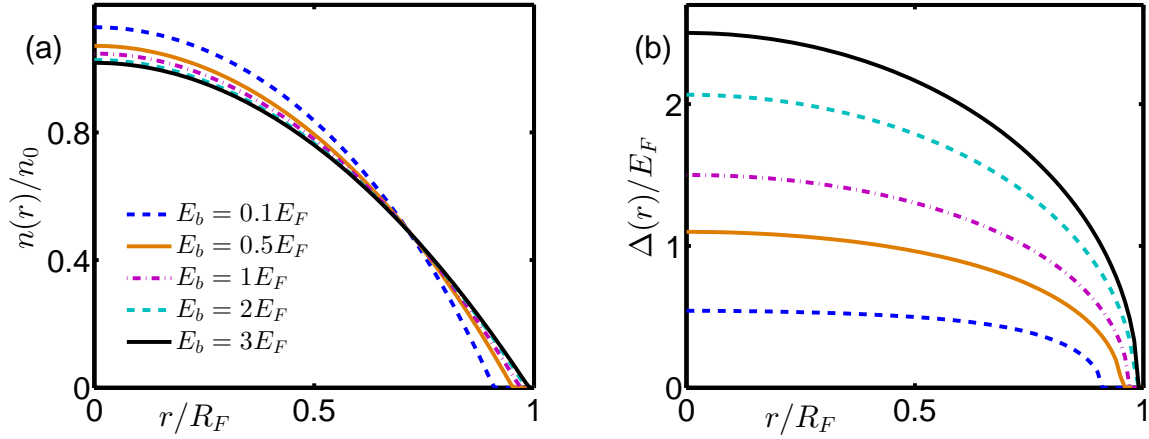


Figure 4.9: Trap profile for Rashba coupled Fermi gas for changing E_b . In all the curves $\alpha = 1.5E_F/k_F$. (a) Density profile for different E_b values. Note that as E_b increases density expands, and eventually it becomes identical with the $\alpha = 0$ profile. (b) Order parameter profile for different E_b values.

In order to check the validity of the LDA, we use the full quantum mechanical BdG equations. Given sufficiently large number of particles, BdG and LDA results agree with each other. The BdG equations used in these calculations can be deduced by taking $\Omega \rightarrow 0$ limit of the more general BdG equations derived in Sec. 6.5. In Fig. 4.10 we show representative trap profiles for representative $E_b = 0.5E_F$ and $\alpha = 2E_F/k_F$ calculated via both BdG and LDA for $N = 100$ and $N = 500$. Interactions destroy the Friedel oscillations, therefore we have perfect agreement at the center of the trap. LDA as expected just fails at the low density region at the edge of the gas. Note that by comparing $N = 100$ and $N = 500$, as the particle number increases the region at which LDA fails becomes small compared to the system size.

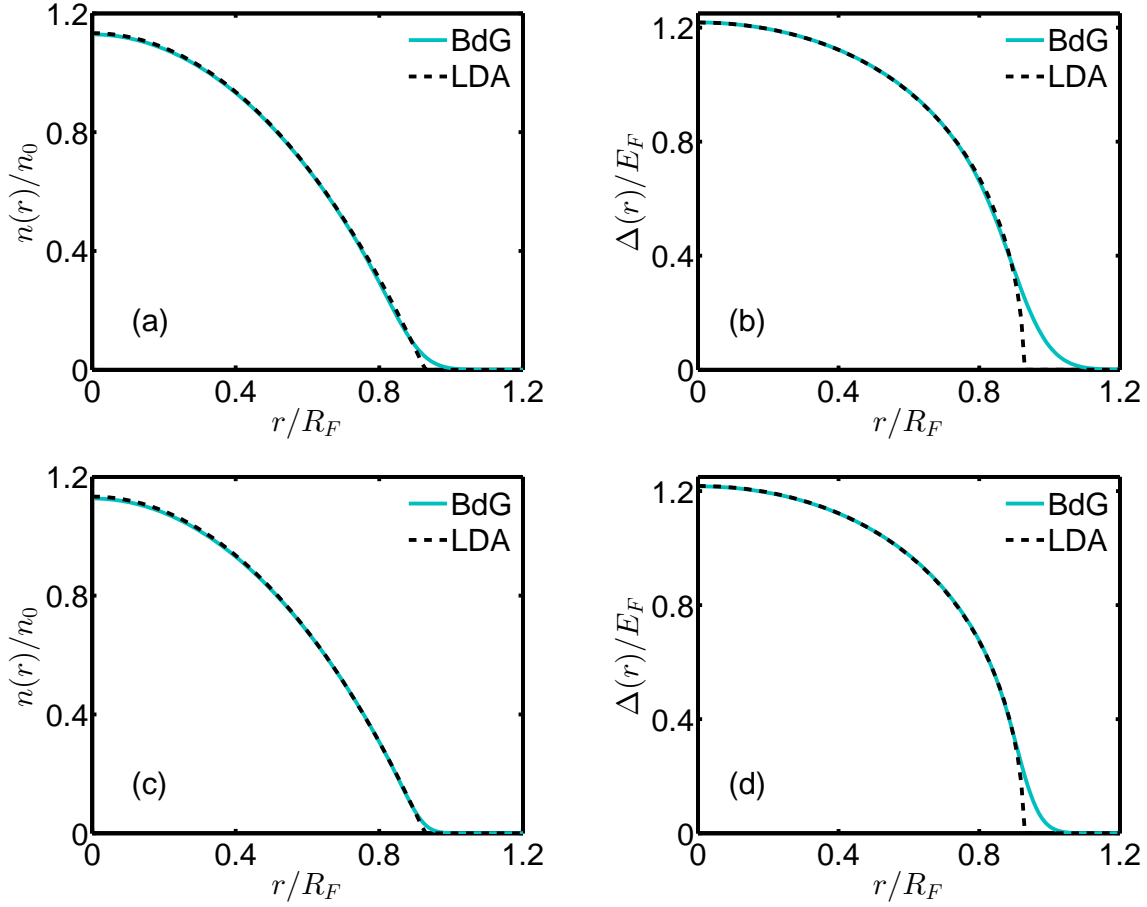


Figure 4.10: The trap profiles for representative $E_b = 0.5E_F$ and $\alpha = 2E_F/k_F$. (a) $n(r)$ for $N = 100$, (b) $\Delta(r)$ for $N = 100$, (c) $n(r)$ for $N = 500$, (d) $\Delta(r)$ for $N = 500$. Even for $N = 100$ LDA is in very good agreement with the BdG calculations. Interactions destroy the Friedel oscillations, therefore we have a perfect agreement at the center of the trap. LDA fails at the low density region at the edge of the trap as expected. Note that by comparing $N = 100$ and $N = 500$, as the particle number increases the region at which LDA fails becomes small compared to the system size.

Chapter 5

ROTATING 2D FERMI GAS

5.1 Motion in Rotating Frame of Reference

In this chapter we will study rotating 2D Fermi gas. We will analyze the problem in a rotating frame, where Hamiltonian is time independent. Therefore it will be useful to quickly remind the motion of particle in the rotating frame. We consider two frames of reference, first one is an inertial reference frame which we will refer to as the lab frame. The second reference frame is rotating with respect to the first one with angular velocity $\boldsymbol{\Omega}$. We will refer to this frame as the rotating frame. The coordinate axes of the lab frame can be labeled as \mathbf{e}_i where $i = \{1, 2, 3\}$. We assume that there is no relative motion between the frames except the rotation. Assume that \mathbf{e}'_i are the coordinates in the rotating frame. We use ' sign to denote physical quantities in the rotating frame. Using simple relations one can easily show that time derivative of the rotating frame coordinate axes are [Goldstein et al., 2007]

$$\frac{d\mathbf{e}'_i}{dt} = \boldsymbol{\Omega} \times \mathbf{e}'_i. \quad (5.1)$$

On the other hand time derivative of the lab frame coordinate axes are trivially zero. Assume that position of the particle is $\mathbf{r} = \mathbf{r}'$ in both frames. The position can be expanded as $\mathbf{r} = \sum_{i=1}^3 x_i \mathbf{e}_i = \sum_{i=1}^3 x'_i \mathbf{e}'_i$ using the coordinate axes of the lab and rotating frame respectively. Using above derivative we can easily prove that time derivative of any vector function $f(t) = \sum_{i=1}^3 f'_i(t) \mathbf{e}'_i$ can be written as

$$\frac{df}{dt} = \sum_{i=1}^3 \left(\frac{df'_i}{dt} \mathbf{e}'_i + f'_i \frac{d\mathbf{e}'_i}{dt} \right) = \left(\frac{df}{dt} \right)_r + \boldsymbol{\Omega} \times f(t) \quad (5.2)$$

where $[df/(dt)]_r$ is the rate of change of $f(t)$ in the rotating frame. Using this we can derive the basic kinematic relations. The velocity can be written as

$$\frac{d\mathbf{r}}{dt} = \left(\frac{d\mathbf{r}}{dt} \right)_r + \boldsymbol{\Omega} \times \mathbf{r} \Rightarrow \mathbf{v} = \mathbf{v}' + \boldsymbol{\Omega} \times \mathbf{r}. \quad (5.3)$$

If we take one more time derivative we get the acceleration in the laboratory frame

$$\mathbf{a} = \frac{d\mathbf{v}}{dt} = \left[\left(\frac{d}{dt} \right)_r + \boldsymbol{\Omega} \times \right] \left[\left(\frac{d\mathbf{r}}{dt} \right)_r + \boldsymbol{\Omega} \times \mathbf{r} \right]. \quad (5.4)$$

If we calculate right side of the equation and define $\mathbf{a}' = [d^2\mathbf{r}/(dt)]_r$ as the apparent acceleration in the rotating frame, we get

$$\mathbf{a}' = \mathbf{a} - \frac{d\boldsymbol{\Omega}}{dt} \times \mathbf{r} - \boldsymbol{\Omega} \times (\boldsymbol{\Omega} \times \mathbf{r}) - 2\boldsymbol{\Omega} \times \mathbf{v}'. \quad (5.5)$$

If we multiply both sides with the mass of the particle and use Newton's second law for the lab frame $\mathbf{F}_T = M\mathbf{a}$, where \mathbf{F}_T is the total physical force in the lab frame, we get Newton's second law in rotating frame as

$$M\mathbf{a}' = \mathbf{F}_T - M \frac{d\boldsymbol{\Omega}}{dt} \times \mathbf{r} - M\boldsymbol{\Omega} \times (\boldsymbol{\Omega} \times \mathbf{r}) - 2M\boldsymbol{\Omega} \times \mathbf{v}'. \quad (5.6)$$

This is Newton's second law analogous to the one written in the lab frame, except there are additional three terms which are called inertial or fictitious forces. Note that these forces do not arise from any physical interaction between two objects, they are direct result of the non-inertial nature of the rotating frame. The first term

$$F_E = -M \frac{d\boldsymbol{\Omega}}{dt} \times \mathbf{r} \quad (5.7)$$

is known as the Euler force. It is a tangential fictitious force that is felt in reaction to an angular acceleration. It is the force that pushes us back to our seat in merry-go-round when it starts to ride. In this thesis we will study Fermi gas under a uniform rotation, hence Euler force is zero. Second term in the equation of motion

$$F_{ce} = -M\boldsymbol{\Omega} \times (\boldsymbol{\Omega} \times \mathbf{r}) \quad (5.8)$$

is called the centrifugal force. It is fictitious force which acts radially outward from the axis of rotation. Assume that we tie a ball to a string and rotate it with a constant angular speed around us. Assume that we are in outer-space and only force acting the ball is the tension force. In the frame which rotates with same angular velocity as the ball, it will remain at rest. Therefore there must be some fictitious force which will balance the tension force. That force is the centrifugal force. The last term in the equation of motion

$$F_{Co} = -2M\boldsymbol{\Omega} \times \mathbf{v}' \quad (5.9)$$

is called the Coriolis force. As we can see from its expression it acts on the moving bodies. In a reference frame which rotates in the clockwise direction, the Coriolis force acts to the left of the motion of the object. On the other hand for rotation in anti-clockwise direction it acts to the right. An object which moves in straight line in lab frame, will appear to have spiral trajectory in rotating frame. This spiral trajectory is result of the Coriolis force. Arguably Coriolis is the most important fictitious force. It plays central role in meteorology and oceanography, because it causes moving objects on the surface of the Earth to be deflected to the right in the Northern Hemisphere and to the left in the Southern Hemisphere, since Earth's reference frame is also a rotating frame.

We should note that there is clear mathematical analogy between the Coriolis force and the magnetic component of the Lorentz force,

$$F_L = q\mathbf{v} \times \mathbf{B} \quad (5.10)$$

where q is the charge of the particle and \mathbf{B} is the magnetic field. If we analyze the expressions of the two forces we can clearly see $2M$ acts as the charge q and $\boldsymbol{\Omega}$ acts as

an \mathbf{B} . This mathematical analogy (some physicist think that is not just an analogy and there is deep physical connection between the two forces see [Royer, 2011].) as we will see in next sections makes it possible to study the effect of magnetic field in neutral particles using rotation.

Before we finish this section let us briefly discuss how we can do statistical mechanics in the rotating frame. For detailed discussion see [Landau and Lifshitz, 1980, Leggett, 2006]. Suppose we have a system which is confined to a trap potential $V(\mathbf{r}_i)$ which is not necessarily symmetric and particles interact via some central symmetric potential $U(r_{ij})$ ($r_{ij} = |\mathbf{r}_i - \mathbf{r}_j|$) in the lab frame. The Hamiltonian of the system is given as

$$H(\mathbf{r}_i, p_i) = \sum_i \left[\frac{p_i^2}{2M} + V(\mathbf{r}_i) \right] + \frac{1}{2} \sum_{i,j} U(r_{ij}). \quad (5.11)$$

When we rotate the system with angular velocity Ω let say along the \hat{z} direction, the confining potential becomes time dependent $V(\mathbf{r}_i, t) = V[\mathbf{r}'_i(t)]$, with $\mathbf{r}'_i(t) = (x_i \cos \Omega t + y_i \sin \Omega t, -x_i \sin \Omega t + y_i \cos \Omega t, z_i)$. Thus in general our Hamiltonian is time dependent in the lab frame. On the other hand given that the interaction potential is symmetric as in the case of cold atoms, than the system is time independent in the rotating frame which rotates with the equal angular velocity with the system. Hence using the standard procedure of canonical transformation by first writing the Lagrangian and than the deriving the Hamiltonian from it, system can be described in the rotating frame via

$$H_{\text{eff}} = H(\mathbf{r}'_i, p'_i) - \boldsymbol{\Omega} \cdot \mathbf{r}' \times \mathbf{p}'. \quad (5.12)$$

Note that this Hamiltonian is time independent, assuming that system is in thermal equilibrium with a heat bath rotating with the system, standard equilibrium thermodynamics can be applied. In special times $t = 2\pi n/\Omega$ where n is integer, the coordinates and momenta of the lab and rotating frame will coincide. Therefore at

these special times we can replace the coordinates and momenta in above Hamiltonian with that of lab frame

$$H_{\text{eff}} = H(\mathbf{r}_i, p_i) - \boldsymbol{\Omega} \cdot \mathbf{r} \times \mathbf{p} = H(\mathbf{r}_i, p_i) - \boldsymbol{\Omega} L_z(\mathbf{r}, \mathbf{p}) \quad (5.13)$$

where $L_z(\mathbf{r}, \mathbf{p})$ is the z -projection of the angular momentum operator. In general, we know that system is stationary in the rotating frame and therefore distribution will remain stationary. As a result of this in any general time t , the anisotropy of the distribution will rotate with angular momentum $\boldsymbol{\Omega}$ around \hat{z} axis viewed from the lab frame. If the trapping potential is isotropic as in the case we will consider in this and next chapter, the distributions will also be isotropic. As a result, the above effective Hamiltonian written in terms of the lab frame coordinates and momenta will be valid at all times. In this special case the distribution is stationary also in the lab frame. We will use this effective Hamiltonian to describe the effect of rotation in the rest of the thesis.

5.2 Rotating Non-interacting 2D Fermi Gas: Local Density Approximation

In this section we study two species harmonically trapped non-interacting Fermi gas at $T = 0$, rotating with angular velocity $\boldsymbol{\Omega} > 0$. We assume again that trap is isotropic. The Hamiltonian describing the system can be written in two parts

$$H = H_{\text{sho}} + H_{\text{rot}} \quad (5.14)$$

where H_{sho} again denotes the harmonic oscillator part of the Hamiltonian given in Eq. (3.113) and H_{rot} denotes the rotation term of the Hamiltonian in the rotating frame

$$H_{\text{rot}} = \sum_{\sigma} \int d\mathbf{r} \hat{\psi}_{\sigma}^{\dagger}(\mathbf{r}) [-\boldsymbol{\Omega} L_z(\mathbf{r}, \mathbf{p})] \hat{\psi}_{\sigma}(\mathbf{r}) \quad (5.15)$$

where $L_z(\mathbf{r}, \mathbf{p})$ is the z -projection of the angular momentum operator $L(\mathbf{r}) = \mathbf{r} \times \mathbf{p}$. As we will show below rotation frequency is limited by trap frequency $\Omega < \omega$. We transfer the Hamiltonian to the momentum basis using Eq. (2.38) and make the local density approximation. For rotating Fermi gas under LDA, besides local chemical potential we also have the effective local rotation term $\Omega L_{\mathbf{k}}(\mathbf{r}) = \mathbf{v}(\mathbf{r}) \cdot \mathbf{k}$, where $\mathbf{v}(\mathbf{r}) = \Omega \hat{z} \times \mathbf{r}$. LDA Hamiltonian in momentum basis can be written as

$$H^{\text{LDA}}(\mathbf{r}) = \sum_{\mathbf{k}, \sigma} [\epsilon_{\mathbf{k}} - \mu(\mathbf{r}) - \Omega L_{\mathbf{k}}(\mathbf{r})] \hat{a}_{\mathbf{k}\sigma}^\dagger \hat{a}_{\mathbf{k}\sigma}. \quad (5.16)$$

Hamiltonian is already diagonal, therefore the dispersion relation can be deduced as

$$\epsilon_{\mathbf{k}}(\mathbf{r}) = \frac{k^2}{2M} - r\Omega k \sin(\theta_{\mathbf{k}} - \theta_{\mathbf{r}}) - \mu(r) \quad (5.17)$$

where $\theta_{\mathbf{k}}$ is the polar angle in \mathbf{k} -space and $\theta_{\mathbf{r}}$ is the polar angle in \mathbf{r} -space. Since the trap is rotationally symmetric and we are interested in the rotationally symmetric solutions, without loss of generality, we take $\theta_{\mathbf{r}} = 0$ corresponding to the positive x -direction in real space. From above expression we see that rotation breaks the rotation and inversion symmetry of the dispersion relation in \mathbf{k} -space. This asymmetry results in a tilt of the excitation spectrum. As a result, the minimum of the paraboloid shifts from the center to finite $k = r\Omega M$ and the Fermi surface is a circle centered around this finite momentum [see Fig. 6.1(c)].

LDOS can be calculated from Eq. (2.62) as

$$D(\epsilon, r) = \frac{MA}{\pi} \Theta \left[\epsilon + \frac{(\Omega^2 - \omega^2)Mr^2}{2} \right] \quad (5.18)$$

thus LDOS is constant in the non-zero region and has parabolic shape similar to LDOS of the non-rotating 2D Fermi gas. Rotation decreases the curvature of the parabolic LDOS. From this LDOS profile we can deduce that 2D Fermi gas will

retain its parabolic density profile under rotation and gas will expand as the rotation is increased. In order to demonstrate this let us compute the density distribution either via $n(r) = \sum_{\mathbf{k}} \Theta[-\varepsilon_{\mathbf{k}}(r)]/A$, or by counting the local states up to the local chemical potential $\mu(r)$, i.e. to integrate

$$\begin{aligned} n(r) &= 2 \int_0^{\mu(r)} D(\varepsilon, r)/A d\varepsilon = 2 \int_0^{\mu(r)} \frac{M}{\pi} \Theta \left[\varepsilon + \frac{(\Omega^2 - \omega^2)Mr^2}{2} \right] d\varepsilon \\ &= 2 \int_{\frac{(\Omega^2 - \omega^2)Mr^2}{2}}^{\mu(r)} \frac{M}{\pi} d\varepsilon = \frac{M^2}{\pi} \left[\frac{2\mu}{M} - (\omega^2 - \Omega^2)r^2 \right]. \end{aligned} \quad (5.19)$$

If we integrate above expression over all the trap, relating density to Fermi energy of the non-interacting 2D Fermi gas we get the global chemical potential as

$$\mu = E_F \sqrt{1 - \frac{\Omega^2}{\omega^2}}. \quad (5.20)$$

Note that at $\mu \rightarrow E_F$ as $\Omega \rightarrow 0$. Rotation reduces the chemical potential, as expected from LDOS profile given above, but it is always positive. Thus the density profile of the non-interacting 2D Fermi gas is given as

$$n(r) = \frac{M}{\pi} \left[2E_F \sqrt{1 - \frac{\Omega^2}{\omega^2}} - (\omega^2 - \Omega^2)Mr^2 \right]. \quad (5.21)$$

As we correctly predicted from LDOS, trap profile is an inverted parabola with a decreasing curvature for increased Ω . We can deduce the edge of the trap from the density distribution, i.e. $n(R_O^0) = 0$,

$$R_O^0 = \frac{R_F}{(1 - \frac{\Omega^2}{\omega^2})^{1/4}}. \quad (5.22)$$

As expected, gas expands with increasing Ω due to the centrifugal effects. Note that at $\Omega = \omega$ trap can not supply the necessary centripetal acceleration and particles escape from the trap.

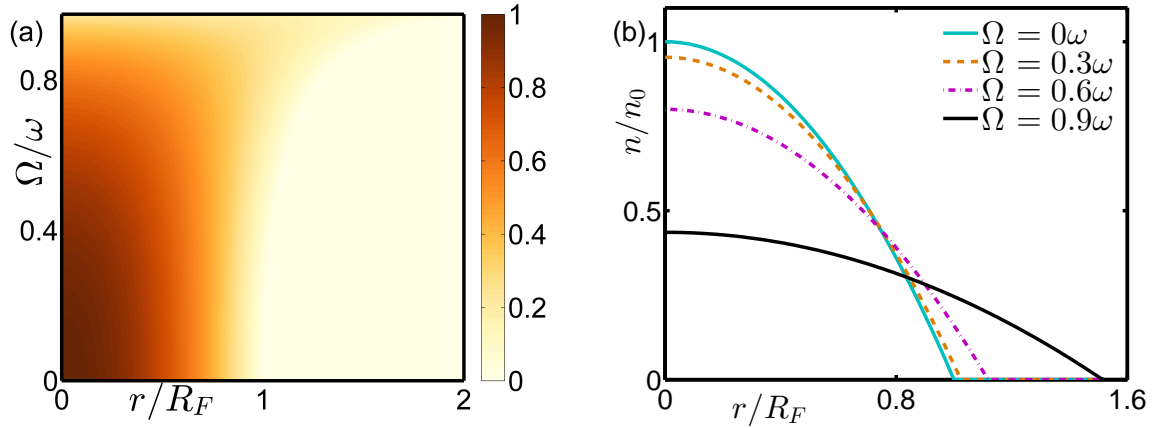


Figure 5.1: The density profile of the rotating non-interacting Fermi gas. (a) Density profile with changing rotation frequency Ω . The central density monotonically decreases and gas expands due to the centrifugal effects. (b) Density at representative Ω values. Density retains its parabolic shape under LDA.

Normal Fermi gas rotates rigidly like any classical object. The angular current associated with the rigid body rotation can be written as

$$J_{\theta}(r) = Mr\Omega n(r). \quad (5.23)$$

There are several methods for rotating the quantum gases experimentally. One common method is to pump an angular momentum to the gas before it is trapped by an isotropic trap which will preserve the angular momentum [Abo-Shaeer et al., 2001, Haljan et al., 2001]. Alternatively one can create a rotating anisotropic trap, which will lead to rotating system [Rosenbusch et al., 2002].

5.3 Rotating Non-interacting 2D Fermi Gas: Exact Quantum Mechanical Approach

In this section we will determine the density distribution of the rotating 2D Fermi gas exactly using the 2D harmonic oscillator basis. It turns out that single particle Hamiltonian describing the states of the rotating harmonically trapped 2D Fermi gas is still diagonal in this basis. This is so because 2D harmonic oscillator states are

eigenstates of the angular momentum operator, as we demonstrated in Eq. (2.69). Using Eq. (2.68) and Eq. (2.69), single particle Hamiltonian can be written as

$$H = \frac{\hat{p}^2}{2M} + \frac{1}{2}M\omega^2\hat{r}^2 - \Omega(\hat{x}\hat{p}_y - \hat{y}\hat{p}_x) = \omega(\hat{n}_L + \hat{n}_R + 1) - \Omega(\hat{n}_L - \hat{n}_R). \quad (5.24)$$

If we apply the Hamiltonian to the eigenstate $|n, l\rangle$, we get the energy eigenvalue of the state

$$\epsilon_{N_L, N_R} = N_L\omega_- + N_R\omega_+ + \omega \quad (5.25)$$

where $\omega_{\pm} = \omega \pm \Omega$ or in terms of the quantum numbers n and l

$$\epsilon_{n,l} = \omega(n+1) - \Omega l. \quad (5.26)$$

Thus rotation breaks the degeneracy between the states with same quantum number n . Since eigenstates of the Hamiltonian are known exactly, the density profile for the rotating 2D non-interacting Fermi gas can be obtained by summing over the single particle states up to the chemical potential μ . This yields the following density expression

$$n(r) = 2 \sum'_{n,l} [R_n^{l|}(r)]^2 \Theta(\mu - \epsilon_{n,l}). \quad (5.27)$$

where 2 indicates the degeneracy due the two pseudo-spins, and ' indicates that for given n , l takes value from the set $\{-n, -n+2, -n+4, \dots, n-2, n\}$. In Fig. 5.2 we compare a density of representative Fermi gas rotating with $\Omega = 0.75\omega$ for different particle numbers. Again for low particle number, LDA fails to capture Friedel oscillations as well as the low density tail of the gas. This difference becomes negligible at high particle numbers such as $N = 2500$.

There is a very interesting limit, where LDA fails to capture the physics and we need to relay to the exact calculations. This is the so called rapid rotation limit where $\Omega \rightarrow \omega$ [Ho and Ciobanu, 2000]. In order to understand the significance of this limit,

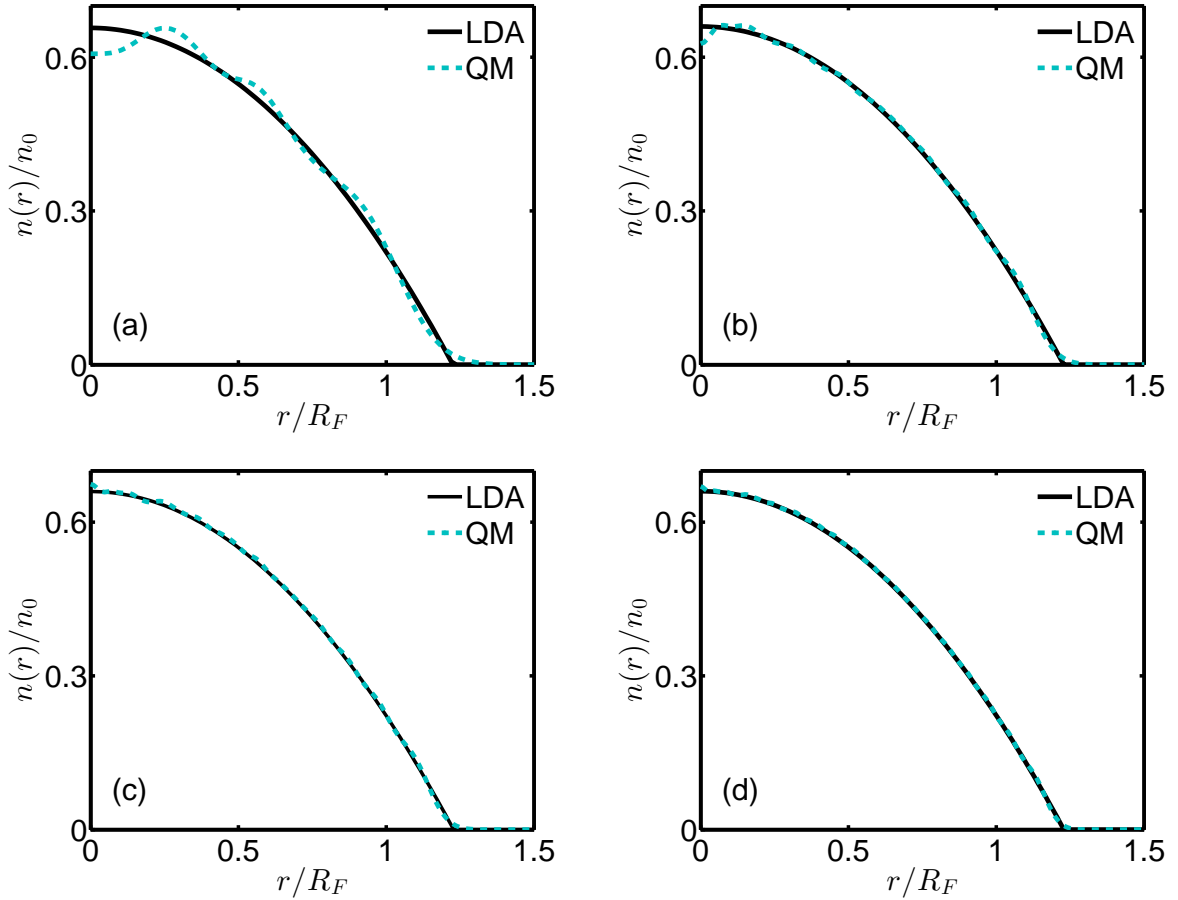


Figure 5.2: Density profile computed via the exact quantum mechanical calculations compared to the semi-classical LDA results for representative $\Omega = 0.75\omega$ and different particle numbers: (a) $N = 100$, (b) $N = 500$, (c) $N = 1000$, (d) $N = 2500$. In low particle numbers such as $N = 100$ LDA fails to capture Friedel oscillations at the center of the trap and low density tail of the gas. For considerable particle numbers such as $N = 2500$, Friedel oscillations become invisible and low density tail becomes very small compared to the system size. Thus at high particle limit LDA and exact QM calculations become indistinguishable both for all Ω except the fast rotation limit $\Omega \rightarrow \omega$. See text for details.

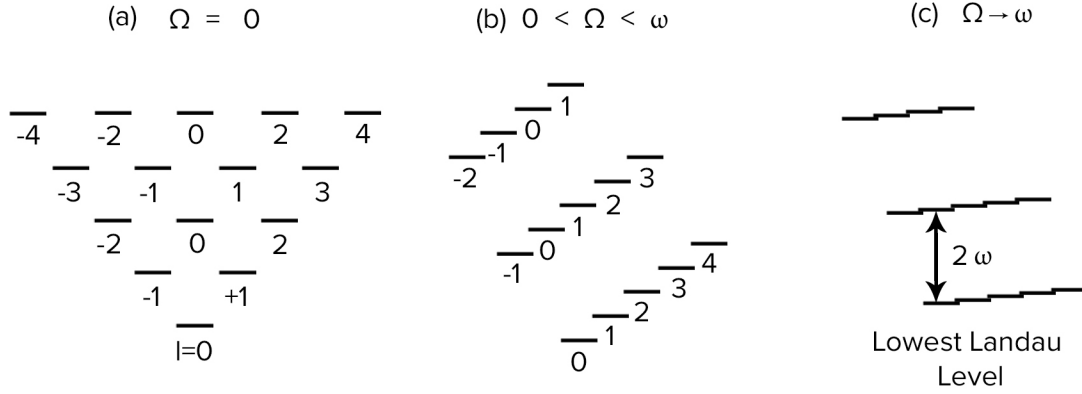


Figure 5.3: Schematic representation of the energy levels for (a) $\Omega = 0$, (b) $0 < \Omega < \omega$, (c) $\Omega \rightarrow \omega$. Numbers denote the angular momentum quantum number l . We can clearly see the emergence of Landau level structure with energy gap 2ω in $\Omega \rightarrow \omega$ limit.

let us rewrite the single particle Hamiltonian of the rotating 2D non-interacting Fermi gas in more suggestive way.

$$\begin{aligned}
 H &= \frac{\hat{p}^2}{2M} + \frac{1}{2}M\omega^2\hat{r}^2 - \Omega L_z(\mathbf{r}) \\
 &= \frac{1}{2M}(\hat{p} - M\boldsymbol{\Omega} \times \hat{\mathbf{r}})^2 + \frac{1}{2}M(\omega^2 - \Omega^2)\hat{r}^2.
 \end{aligned} \tag{5.28}$$

Note that the first term is very similar to the kinetic energy term of a charge q particle moving in a uniform magnetic field \mathbf{B} , which can be related to the rotation frequency as $\mathbf{B} = 2M\boldsymbol{\Omega}/q$. Thus this analogy can be used to simulate the effects of a uniform magnetic field on the charged particle in a neutral atomic gas. Hence rotating non-interacting Fermi gas can be used to study the physics of the quantum Hall effect [Ho and Ciobanu, 2000]. This is expected since, Coriolis pseudo-force is analogous to the magnetic component of the Lorentz force as we discussed above. Of

course second term is absent in the magnetic field Hamiltonian and therefore weakens the analogy. But if rotation is very rapid, and $\Omega \rightarrow \omega$ the second term becomes negligible and we have one to one correspondence between the two Hamiltonians. Hence we expect appearance of Landau level structure in this rapid rotation limit. This structure can be seen from the dispersion relation which in this limit becomes

$$\epsilon_{n_L, l} = \omega(2n_L + 1) + \omega_- l \approx \omega(2n_L + 1) \quad (5.29)$$

where $n_L = N_R$ denotes the Landau level index. Note that the energy levels with same n_L are almost degenerate, and energy levels with different n_L are separated by an energy gap 2ω . This results in single particle energy levels grouped into almost degenerate energy bands (See Fig. 5.3). Thus clearly Landau level structure is emerging, and N_R denotes the Landau Level index n_L . The first three Landau levels in the trap are shown for $\Omega = 0.99\omega$ by the (purple) dots in Fig. 6.9 as a function of angular momentum. These levels are still two-fold degenerate because of the spin of the particles.

Each filled Landau level results in homogeneous density and this leads to zigzag shaped density profiles in the trap, reflecting the number of the filled Landau levels. Such staircase profiles with one, two and three filled Landau level are exemplified by (purple) dotted lines in Fig. 6.10(a)-(c), respectively. Between each step there are oscillations. These oscillations is directly related to the index of Landau level. When passing from n th Landau level to $n+1$ th Landau level n oscillations appear. Maximum number of particles in each band can be estimated for given chemical potential from the dispersion relation as

$$N_{n_L} = 2\text{Int} \left(\frac{\mu - n_L(\omega + \Omega) + \omega}{(\omega - \Omega)} \right) \quad (5.30)$$

where Int is function which gives the, smaller integer neighbor of its input. Landau level structure in the density is finite size effect and become less visible as we go towards the thermodynamic limit. Hence it can not be captured by LDA, which provides the thermodynamic limit picture of the system. We note that rapid rotation

limit is accessible experimentally and was first time reached in 2004 in JILA, where $\Omega \approx 0.993\omega$ rotational speed was achieved [Schweikhard et al., 2004].

5.4 Rotating Superfluids: Hess-Fairbank Effect and Vortices

Superconductivity is a superfluidity of a charged particles. For detailed discussion of superconductivity and its relation to superfluidity see [Annett, 2004]. Superconductivity is usually defined through the Meissner effect. The Meissner effect is the spontaneous expulsion of a magnetic field lines from the interior of the superconductor which occurs after transition from normal metal to superconductivity (assuming magnetic field is weak) [Meissner and Ochsenfeld, 1933]. Given that the Meissner effect is the defining characteristic of superconductivity, natural question to ask is whether there is an analogous effect in the superfluids. As we discussed in the previous sections, Coriolis force is analogous to the magnetic part of the Lorentz force, therefore rotation can be expected to lead to an analogous effect to the Meissner effect. It turns out that this expectation is correct and there is a similar effect known as the Hess-Fairbank effect [Hess and Fairbank, 1967]. Analogous to superconductors, superfluids "expel" the angular momentum of its container. To understand this effect let us assume that we have a liquid in hollow cylinder container with inner radius $R - d/2$ and outer radius $R + d/2$ such that $R \gg d$, and assume that container is very close but not perfect cylinder [Leggett, 2006]. If the liquid is normal liquid like water and we rotate the container with an angular frequency Ω after some time water will start to rotate rigidly with the same angular frequency Ω . Unless we stop the container water will continue to rotate rigidly and carry angular momentum $L = I\Omega$, where the moment of inertial is $I = NMR^2$. Suppose now we put some fluid which becomes superfluid at low temperatures such as He4. Suppose the temperature of the system is $T > T_c$, where T_c is the critical temperature of the normal to superfluid transition of the fluid. Suppose we rotate the container with low rotation $\Omega < \Omega_1 = 1/(2MR^2)$ (in analogy to weak magnetic field). Similar to water, after some time fluid will start to rotate rigidly with the same angular velocity of the container. Suppose we slowly lower

the temperature while container still rotates with constant angular velocity. After temperature falls below T_c something interesting happens, slowly fluid comes out of equilibrium from its container. The fluid rotates with non-classical moment of inertia $I < NMR^2$, whose value is smaller from the classical moment of inertia by fraction of n_N/n , where n_N is the density of normal fluid and n is the total density. As we come closer to $T = 0$ fluid's rotation slows down and at $T = 0$ it completely stops. Thus when system becomes completely superfluid, angular momentum is completely "expelled" from the fluid. Hess-Fairbank effect, i.e. emergence of non-classical moment of inertia is one of the phenomenological definitions of superfluidity complementary to the ones given in Sec. 3.10)

The non-rotational character of superfluid can be demonstrated by calculating the vorticity of the superfluid. Vorticity is a pseudo-vector field which measures the tendency of something to rotate. It is defined as the curl of the flow velocity

$$\vec{\omega} = \nabla \times \mathbf{v}. \quad (5.31)$$

For rigid body rotation like in the non-interacting Fermi gas flow velocity is given as

$$\mathbf{v} = \boldsymbol{\Omega} \times \mathbf{r} \quad (5.32)$$

which yields a uniform vorticity

$$\vec{\omega} = \nabla \times \boldsymbol{\Omega} \times \mathbf{r} = 2\boldsymbol{\Omega}. \quad (5.33)$$

The flow velocity of the superfluid \mathbf{v}_s is given by the gradient of the phase of the order parameter $\Delta(\mathbf{r}) = |\Delta(\mathbf{r})|e^{i\theta(\mathbf{r})}$ as

$$\mathbf{v}_s = \frac{1}{2M} \nabla \theta(\mathbf{r}) \quad (5.34)$$

where $2M$ is the mass of the Cooper pairs. From this relation it is clear why superfluid has non-rotational character, its vorticity vanishes

$$\vec{\omega} = \frac{1}{2M} \nabla \times \nabla \theta(\mathbf{r}) = 0. \quad (5.35)$$

Another useful concept is the circulation Γ , which is the line integral around a closed curve of the flow velocity and can be related to the vorticity via the Stokes theorem. The circulation of simply connected geometry is trivially zero

$$\Gamma = \int \nabla \times \mathbf{v}_s \cdot d\mathbf{a} = \oint \mathbf{v}_s \cdot d\mathbf{l} = 0. \quad (5.36)$$

Thus under normal conditions superfluids can not carry any angular momentum due to their irrotationality. But if the phase $\theta(\mathbf{r})$ has singularity than irrotationality condition can be satisfied even though system carries angular momentum. Even in the presence of singularity order parameter, which is the wave function of boson in BEC limit must be single valued. Hence the change in the phase around some closed contour must be integer multiple of 2π

$$\Delta\theta = \oint \nabla\theta(\mathbf{r}) \cdot d\mathbf{l} = 2\pi m \quad (5.37)$$

where m is some integer. This leads to circulation

$$\Gamma = \oint \mathbf{v} \cdot d\mathbf{l} = \frac{1}{2M} \oint \nabla\theta(\mathbf{r}) \cdot d\mathbf{l} = \frac{2\pi m}{2M}. \quad (5.38)$$

The vorticity of this system is given by

$$\vec{\omega} = \frac{2\pi m}{2M} \delta^2(r) \hat{z}. \quad (5.39)$$

This result is known as the Onsager-Feynman quantization condition [Onsager, 1949, Feynman, 1955]. Note that circulation is quantized, which implies that this is a macroscopic quantum phenomenon. The singularity is known as the vortex. The superfluid systems can carry angular momentum via vortices. Vortices may appear in normal fluids, but they are meta-stable, if there is finite viscosity system will start to rotate like rigid body eventually. On the other hand quantized vortices

are direct and unique signature of the superfluidity and they can persist for arbitrary long times. These vortices are analogous to the vortices which appear in the type II superconductors, where beyond certain critical magnetic field B_{c1} the applied magnetic field starts to penetrate the sample via vortices. Analogously for appearance of vortices in the superfluids system must be rotated with angular velocity $\Omega > \Omega_1$. The first quantized vortices were observed on superfluid Helium-4 in 1958 by Vinen [Hall and Vinen, 1956]. Later vortices were observed in both bosonic and fermionic ultracold quantum gases [Abo-Shaeer et al., 2001, Zwierlein et al., 2005].

We should note that if superfluid density is constant with time $\partial n_s / \partial t = 0$, continuity equation implies that $\nabla \cdot \mathbf{J}_s = 0$, where \mathbf{J}_s is the superfluid current. This in turn implies that $\nabla \cdot \mathbf{v} = 0$, which together with irrotationality condition $\nabla \times \mathbf{v} = 0$ resemble the Maxwell equations for magnetic field in the vacuum. The analog of vortex line in this picture is wire carrying the electrical current penetrating the surface, which will modify the corresponding Maxwell equation. From analogy between the two systems we can conclude that vortices with an opposite circulation attract, while vortices with same circulation repel each other. As a result of the attraction we can only have stable vortices with same circulation which will arrange themselves in the hexagonal lattices as a result of the repulsion. We should also note that vortices with angular momentum higher than $n > 1$ will disintegrate to $n = 1$ vortices, since energy of such vortex is higher than its decayed counterpart.

Vortex can not appear directly inside the superfluid, rather they enter from the surface where the order parameter is zero.

5.5 2D Interacting Fermi Gas Under Adiabatic Rotation

As we saw in the previous section an essential signature of the superfluid phase is the appearance of vortices beyond certain angular velocity when the system is rotated. The vortex cores consist of rotating normal gas with quantized angular momenta. The rotation breaks the time-reversal symmetry and eventually leads to the destruction of the superfluid phase. However, if the rotation is introduced adiabatically without

exciting vortices, Cooper pairs in a Fermi system may be broken due to the Coriolis effects and a normal component carrying angular momentum may be created (For schematic representation of the possible responses of the superfluid to the rotation see Fig. 5.4). Adiabaticity requires that the rotation is introduced slowly to the system. In particular the rate of change of rotation frequency should be much smaller than the quasiparticle excitation frequency for vortex creation.

This possibility was previously considered for a 3D Fermi gas at unitarity using the energy densities obtained from Monte Carlo simulations together with local-density approximation [Bausmerth et al., 2008a, Bausmerth et al., 2008b]. It was shown that adiabatic rotation gives rise to a phase separation between the non-rotating superfluid (SF) at the center and a rigidly-rotating normal (N) gas at the edge. This result also follows from the microscopic BCS theory using both the local-density approximation [Urban and Schuck, 2008] and the Bogoliubov-de Gennes approaches [Iskin and Tiesinga, 2009]. These studies also showed that besides SF and N phase, there is also a partially-rotating gapless superfluid phase (gSF) separating them. Later studies based on BdG approach showed that pair-breaking scenario can be energetically preferred over vortex formation even in the absence of the adiabaticity assumption [Warringa and Sedrakian, 2011, Warringa, 2012].

In this section we will study the effect of adiabatic rotation on interacting 2D Fermi gas using the BCS theory [Doko et al., 2016]. The pair breaking mechanism can be understood via the Coriolis force in the rotating frame. As we discussed in the previous sections, superfluidity emerges due to formation of the Cooper pairs with momentum in opposite direction and spin, i.e. $(\mathbf{k}, \uparrow; -\mathbf{k}, \downarrow)$. As we demonstrated the Coriolis force is proportional to the velocity of the particle, therefore particles forming the Cooper pair will feel force in opposite directions. If the force is strong enough Coriolis force will break the Cooper pairs and hence destroy the superfluidity.

We again analyze the system both under mean-field and LDA. The Hamiltonian in momentum basis can be written as sum of non-interacting terms given in Eq. (5.16) and mean-field term. Gap and number equations, as well as the excitation energy

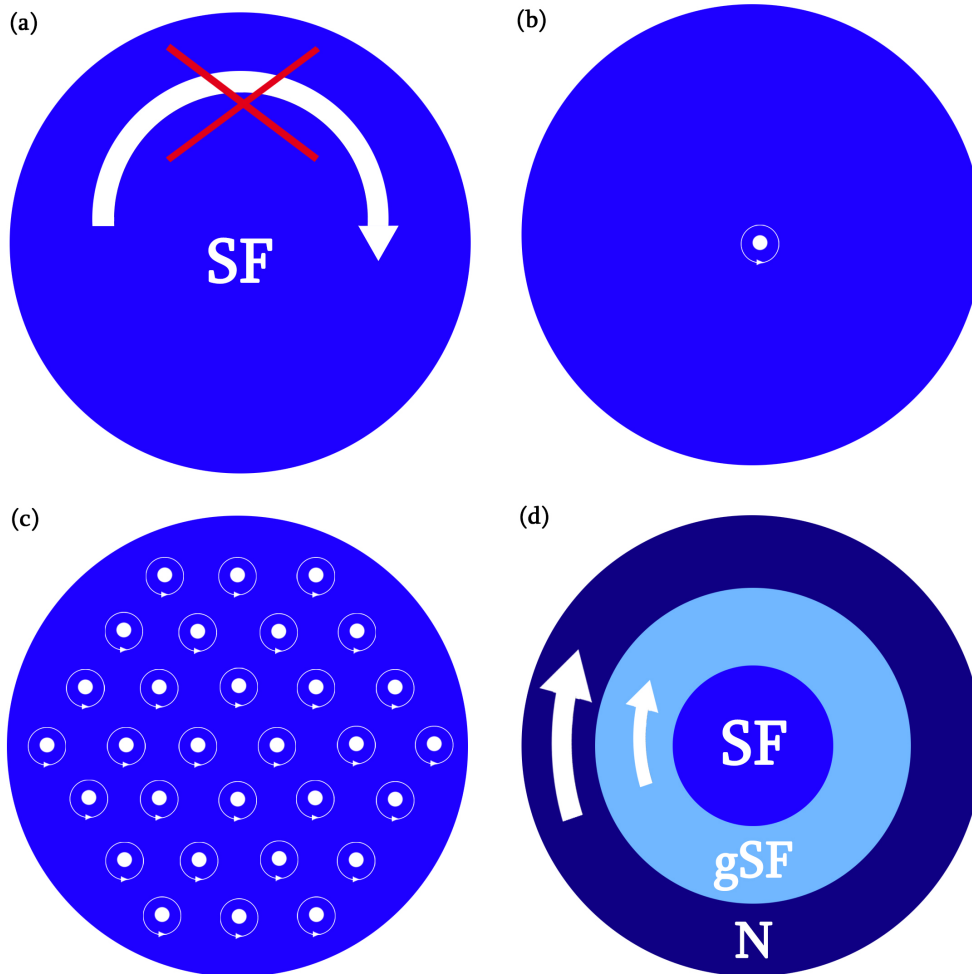


Figure 5.4: Schematic representation of the possible responses of the superfluid to the rotation. (a) Hess-Fairbank effect. At low rotations $\Omega < \Omega_1 = 1/(2MR^2)$, superfluid is irrotational and "expels" the angular momentum. (b) Vortex. At higher rotational frequencies $\Omega > \Omega_1$ superfluid can carry angular momentum with the help of singularities known as the vortex. (c) Vortex lattice. Angular momentum carried via vortices is quantized and at even higher rotation frequencies hexagonal vortex array with same circulation emerges. (d) Superfluid-Normal phase separation. If rotation is introduced adiabatically so that vortices does not emerge, Coriolis force may break the Cooper pairs at the edge of the trap, creating gappless superfluid which can rotate non-rigidly and normal fluid which rotates rigidly, surrounding the non-rotating superfluid core respectively.

can be derived by the procedure given in Sec. 6.3, where the derivation is done for rotating Rashba coupled Fermi gas. Simply taking $\alpha \rightarrow 0$ will give the gap and number equations for the case we consider in this section. The excitation energy is given as

$$E_{\mathbf{k}}(\mathbf{r}) = \sqrt{[\epsilon_k - \mu(r)]^2 + |\Delta(r)|^2} - \Omega L_{\mathbf{k}}(\mathbf{r}) \quad (5.40)$$

where again $\epsilon_k = k^2/(2M)$ is the kinetic energy, $\mu(r)$ is the local chemical potential given in Eq. (3.103) and the rotation term $\Omega L_{\mathbf{k}}(\mathbf{r}) = r\Omega k \sin(\theta_{\mathbf{k}} - \theta_{\mathbf{r}})$. The number and gap equations are given as

$$n(\mathbf{r}) = \frac{1}{A} \sum_{\mathbf{k}} \left(1 - \frac{\epsilon_k - \mu(r)}{[\epsilon_k - \mu(r)]^2 + |\Delta(r)|^2} \{1 - 2f[E_{\mathbf{k}}(\mathbf{r})]\} \right), \quad (5.41)$$

$$\frac{1}{g} = \frac{1}{2A} \sum_{\mathbf{k}} \frac{1 - 2f[E_{\mathbf{k}}(\mathbf{r})]}{\sqrt{[\epsilon_k - \mu(r)]^2 + |\Delta(r)|^2}}. \quad (5.42)$$

Rotation enters the gap and number equation via Fermi function, which at $T = 0$ reduces to a step function. Therefore note that if $E_{\mathbf{k}}(\mathbf{r}) > 0$ for all \mathbf{k} values both number and gap equation are unaffected by the rotation, hence system remains completely superfluid. We have Hess-Fairbank effect, system does not carry any current. However if we have fast enough rotation, the Cooper pairs start to break and emerging normal gas starts to carry current. The pair breaking mechanism can be analyzed by looking at the excitation spectra. When the gas is not rotating, $\Omega = 0$, the quasi-particle $E_{\mathbf{k}}(\mathbf{r})$ and quasi-hole

$$E'_{\mathbf{k}}(\mathbf{r}) = -\sqrt{[\epsilon_k - \mu(r)]^2 + |\Delta(r)|^2} - \Omega L_{\mathbf{k}}(\mathbf{r}) \quad (5.43)$$

excitation energies are symmetric. This is the ideal situation for pair formation with zero center of mass momentum. On the other hand when $\Omega \neq 0$, rotation breaks the symmetry between the time-reversed pairing states $(\mathbf{k}, \uparrow; -\mathbf{k}, \downarrow)$ and the excitation energies become dependent on the direction of momentum. This asymmetry can

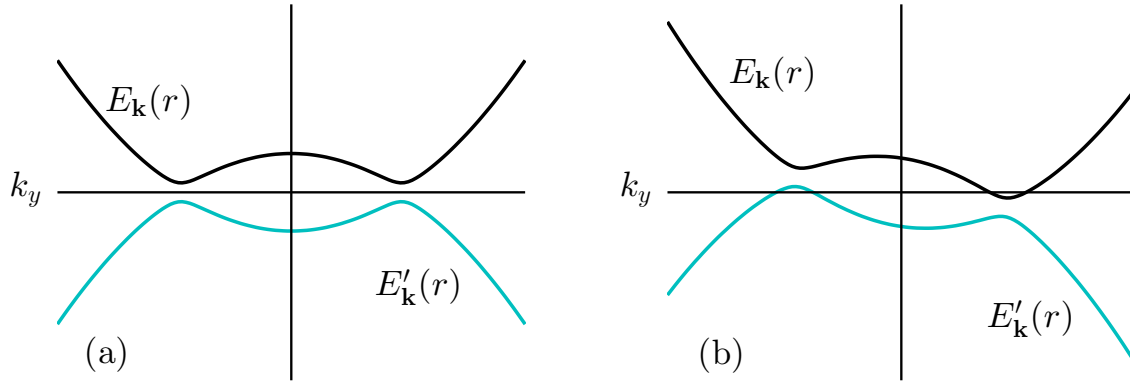


Figure 5.5: Schematic diagrams showing the excitation spectrum $E_{\mathbf{k}}(r)$ with $\Omega \neq 0$ for (a) a gapped superfluid at $r = 0$, (b) a gapless superfluid at $r > 0$. The regions with negative quasi-particle energy result in the pair breaking effect.

eventually lead to negative quasi-particle energies and broken pairs in the ground state. The $E_{\mathbf{k}}(\mathbf{r}) < 0$ and $-E'_{-\mathbf{k}}(\mathbf{r}) > 0$ regions between the gapless boundaries in \mathbf{k} -space, which due to the particle-hole symmetry appear at \mathbf{k} and $-\mathbf{k}$ respectively, are occupied not by pairs but by single particles. We can find these intervals $k_1 < k < k_2$ by setting $E_{\mathbf{k}}(\mathbf{r}) = 0$, which gives

$$k_{1,2}^2 = 2M (\mu(r) + M\Omega^2 r^2) \pm 2M\sqrt{A(r)} \quad (5.44)$$

with $A(r) = 2M\Omega^2 r^2 (\mu(r) + M\Omega^2 r^2/2) - |\Delta(r)|^2$. Hence the condition for the emergence of \mathbf{r} -space regions with gapless excitations is $A(r) \geq 0$. We assumed in this computation that $\theta_{\mathbf{r}} = 0$ without loss of generality because system has an azimuthal symmetry in the real space.

We should note that having gapless excitations does not imply complete destruction of the superfluidity in that region. As we mentioned above we have three possible phases:

1. The Superfluid(SF) phase: This is a gapped superfluid phase characterized by a non-zero order parameter $\Delta(r) > 0$ and a gapped excitation spectrum $E_{\mathbf{k}}(\mathbf{r}) > 0$

for all \mathbf{k} . Alternatively this phase can be characterized by zero mass current density $\mathbf{J}(\mathbf{r}) = 0$ for $\Omega > 0$ showing Hess-Fairbank effect.

2. The Gapless-Superfluid (gSF) phase: This phase is characterized by a non-zero order parameter $\Delta(r) > 0$ and a gapless excitation spectrum $E_{\mathbf{k}}(\mathbf{r}) < 0$ for some \mathbf{k} . Alternatively this phase can be characterized by a non-zero mass current density in azimuthal direction $J_{\theta}(r) \neq 0$ which differs from the rigid body current $J_{\theta}(r) < Mr\Omega n(r)$.

3. The Normal(N) phase: This phase is characterized by a zero order parameter $\Delta(r) = 0$. This phase is trivially gapless and carries rigid body current in azimuthal direction $J_{\theta}(r) = Mr\Omega n(r)$.

The mass current density can be calculated from

$$\mathbf{J}(\mathbf{r}) = \frac{2}{A} \sum_{\mathbf{k}} \mathbf{k} n_{\mathbf{k}}(\mathbf{r}) = \frac{2}{A} \sum_{\mathbf{k}} \mathbf{k} \left(1 - \frac{\epsilon_{\mathbf{k}} - \mu(r)}{[\epsilon_{\mathbf{k}} - \mu(r)]^2 + |\Delta(r)|^2} \{1 - 2f[E_{\mathbf{k}}(\mathbf{r})]\} \right). \quad (5.45)$$

In above equation $n_{\mathbf{k}}(\mathbf{r})$ is the summand of the number equation and 2 counts the spin degeneracy. Note that for $E_{\mathbf{k}}(\mathbf{r}) > 0$ for all \mathbf{k} , summand of above expression is same for both \mathbf{k} and $-\mathbf{k}$ and therefore for gapped superfluid case trivially $\mathbf{J}(\mathbf{r}) = 0$. But if $E_{\mathbf{k}}(\mathbf{r}) < 0$ for some \mathbf{k} , the symmetry between \mathbf{k} and $-\mathbf{k}$ is broken due to different Fermi function values, and we have $\mathbf{J}(\mathbf{r}) \neq 0$. For $\Delta(r) = 0$ above expression can be calculated analytically to yield rigid body rotation current expression.

When there is no pair breaking (either sufficiently strong interactions or slow rotation); μ , $n(r)$ and $|\Delta(r)|$ are not affected by rotation. The whole gas is in the SF phase and the edge is located at $R_O = R_F$. At the critical rotation frequency Ω_c for the onset of pair breaking, the gapless excitations appear at the edge of the gas, i.e. $A(R_F) = 0$. At the same time, the radius of the normal gas having the same chemical potential coincides with the Thomas-Fermi radius at Ω_c , i.e. $R_O^0 = R_F$. This indicates the phase transition from the SF phase to the N phase at the edge. Hence the occurrence of the gSF and N phases start at the edge of the gas and the

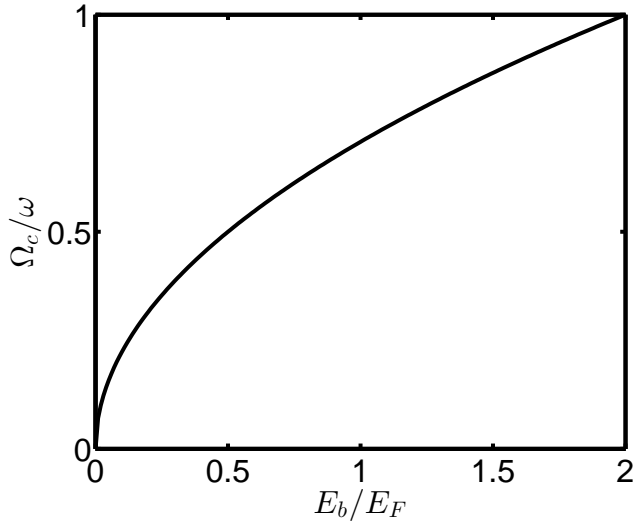


Figure 5.6: Critical rotation frequency for the onset of pair breaking as a function of binding energy E_b . Since rotation frequency is limited by the trap frequency, $\Omega \leq \omega$, it follows that pair breaking cannot occur in the trapped gas for $E_b > 2E_F$.

SF boundary moves toward the center of the trap as Ω further increases. In 2D, as opposed to the 3D case, one can analytically obtain the critical rotation frequency for onset of pair breaking [Doko et al., 2016]

$$\Omega_c = \omega \sqrt{\frac{E_b}{2E_F}}. \quad (5.46)$$

This expression can be obtained from $A(R_F) = 0$, using Eq. (3.94) and is plotted in Fig. 5.6. Since rotation frequency is limited by the trap frequency, $\Omega \leq \omega$, it follows that pair breaking cannot occur in the trapped gas for $E_b > 2E_F$. Incidentally, the point $E_b = 2E_F$ above which no pair breaking is possible, corresponds to the point where μ changes sign. This is consistent with the 3D results where it is known that when $\mu < 0$ there is no pair breaking [Urban and Schuck, 2008].

Beyond Ω_c pair breaking occurs and the trap profile consists of three regions. At the center of the trap there is a SF followed by a gSF region and an unpaired N phase at the outer edge. For $\Omega > \Omega_c$, the SF region monotonically shrinks with increasing Ω , but survives in the limit $\Omega \rightarrow \omega$ since the center is never directly affected by the

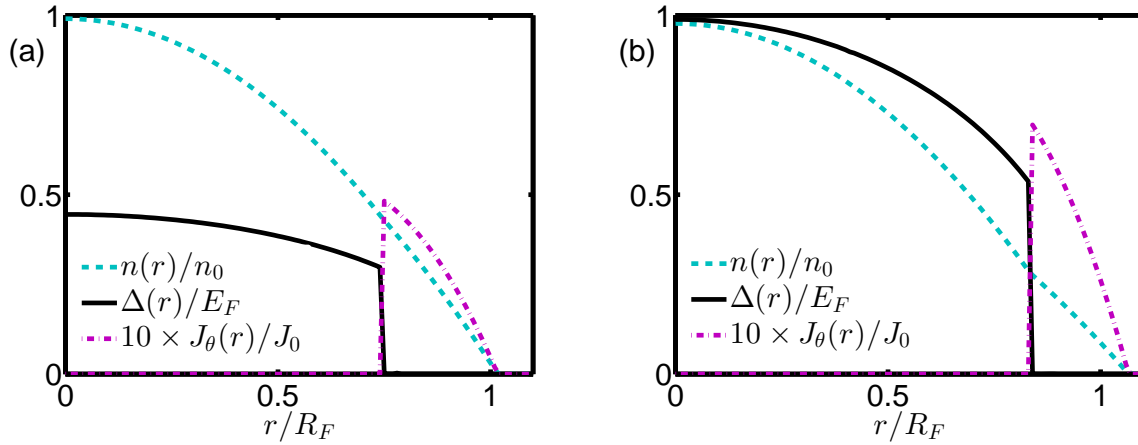


Figure 5.7: Trap profile of an adiabatically rotating interacting Fermi gas with $\Omega > \Omega_c$. We present density, order parameter and mass current density for representative (a) $E_b = 0.1E_F$ ($\Omega_c = 0.2236\omega$), $\Omega = 0.3\omega$ and (b) $E_b = 0.5E_F$ ($\Omega_c = 0.5\omega$), $\Omega = 0.6\omega$. gSF region is very small but still visible between the SF and N phase.

rotation. The ring of N phase expands both inwards and outwards as Ω increases. For fast rotations, the density may form a kink at the SF-N interface, a feature which is also similar to the 3D results [Urban and Schuck, 2008]. This kink is a direct result from the fact that curvature of the superfluid density is not effected by the rotation, whereas the curvature of the N phase density increases with increasing Ω . In Fig. 5.7 we plot trap profile of an adiabatically rotating interacting Fermi gas with $\Omega > \Omega_c$ for representative $E_b = 0.1E_F$ ($\Omega_c = 0.2236\omega$), $\Omega = 0.3\omega$ and $E_b = 0.5E_F$ ($\Omega_c = 0.5\omega$), $\Omega = 0.6\omega$. We clearly see that at the center we have SF ($J_\theta(r) = 0$) and at the edge of the trap we have N phase ($\Delta(r) = 0$). gSF phase is present but occupies very small region and is hardly visible. SF-N phase transition in the trap can be also detected from the kink at the density.

Again in order to check validity of the LDA, we use the full quantum mechanical BdG equations. The BdG equations used in these calculations can be deduced by taking $\alpha \rightarrow 0$ limit of the more general BdG equations derived in Sec. 6.5. In Fig. 5.8 we compare density and order parameter profiles computed via both LDA and BdG calculations. LDA provides a reasonable approximation to BdG calculations. Ro-

tation breaks the Cooper pairs and leads to emergence of normal phase, as a result of this Friedel oscillations are resurrected at the edge of the trap. This results in a detectable difference between LDA and BdG in the outer regions of the trap for low particle numbers such as $N = 100$. LDA also fails at the region where $\Delta(r)$ falls sharply as expected, but this failure also becomes less prominent as particle number increases.

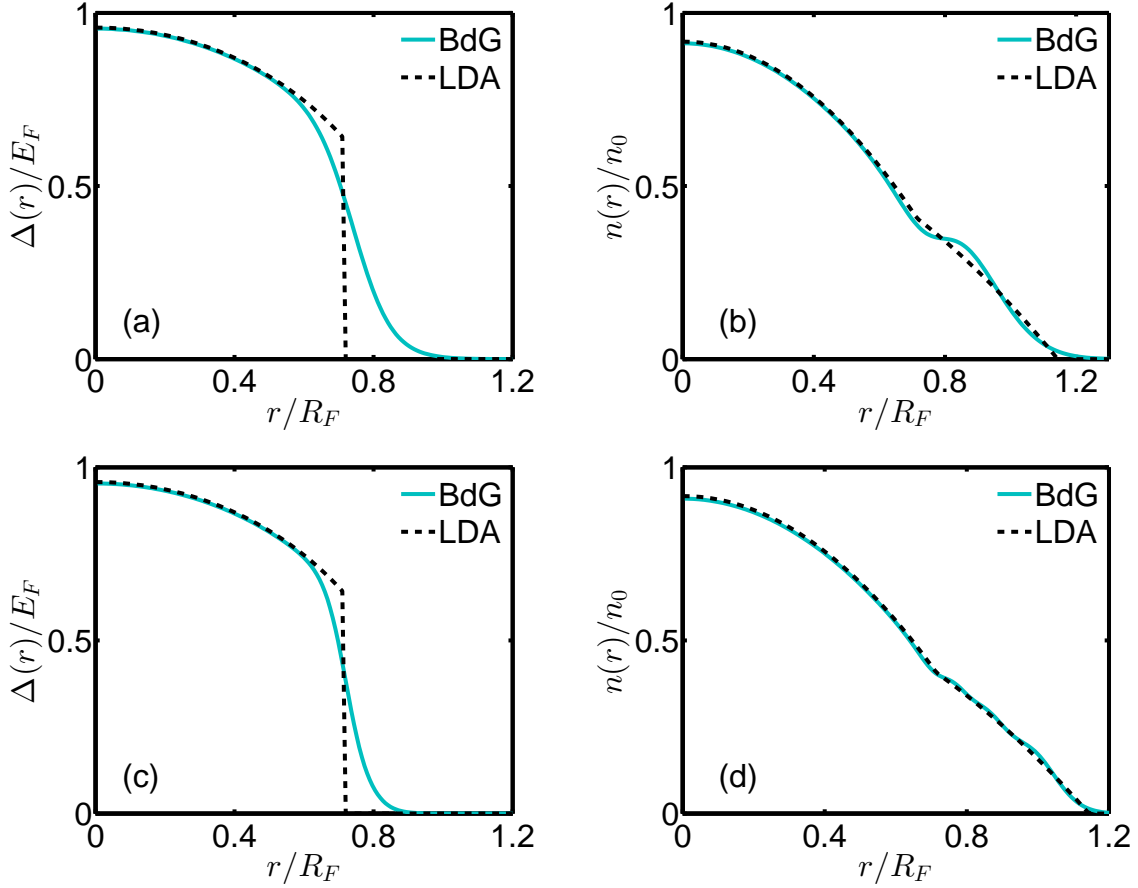


Figure 5.8: The trap profiles for representative $E_b = 0.5E_F$ and $\Omega = 0.7\omega$. (a) $n(r)$ for $N = 100$, (b) $\Delta(r)$ for $N = 100$, (c) $n(r)$ for $N = 500$, (d) $\Delta(r)$ for $N = 500$. LDA provides reasonable approximation to BdG calculations. Rotation breaks the Cooper pairs and leads to the emergence of a normal phase. As a result of this Friedel oscillations are resurrected at the edge of the trap. This results in a considerable amount of difference between LDA and BdG in the outer regions of the trap for low particle numbers such as $N = 100$. We should note that the sharp decrease in $\Delta(r)$ is not present in BdG where $\Delta(r)$ decreases continuously.

Chapter 6

ROTATING RASHBA COUPLED 2D FERMI GAS

6.1 Rotating Non-Interacting 2D Fermi Gas with Rashba SOC: Local Density Approximation

In this section we analyze the behavior of the non-interacting Fermi gas confined by the harmonic trap in the presence of Rashba SOC and rotation using LDA. But before we present the theoretical analysis let us briefly discuss experimental realizability of the systems we discuss in this chapter. In previous chapter we demonstrated that Hamiltonian describing the system with rotating trap can be made time independent by describing the system in the rotating frame. But in the presence of SOC, this approach may not work in straightforward way. As discussed in Sec. 4.3 SOC is created with a pair of Raman lasers which in the rotating frame will not be stationary but will rotate with the frame's angular velocity with respect to the lab frame. The time dependence created from these lasers can not be eliminated in general with any unitary transformation, rendering tools of equilibrium statistical mechanics inapplicable. Fortunately there are two ways to solve this problem. First lasers can be rotated with the rotating frame so that they are stationary in the rotating frame. Or synthetic SOC can be combined with synthetic Abelian magnetic field which imitates rotation [Radić et al., 2011]. For example the NIST scheme implemented in the recent experiments yields time independent Hamiltonian if lasers are rotated with the same frequency as the trap. On the other hand rotating Rashba coupled Fermi gas, which is our focus in this section can be realized with the so called tripod scheme [Ruseckas et al., 2005, Stanescu et al., 2007], where three degenerate ground states couple with an excited state. Interestingly in the tripod scheme, if we rotate just the trap and leave the lasers stationary, if the SOC is Rashba type

and an effective Zeeman splitting is zero, i.e. $\delta_0 = 0$ the non-interacting part of the Hamiltonian becomes time independent [Radić et al., 2011]

$$H = \left[\frac{\mathbf{p}^2}{2M} + w(\mathbf{r}) - \Omega L_z(\mathbf{r}, \mathbf{p}) \right] \mathbf{I} - \alpha (\mathbf{p}_x \sigma_y + \mathbf{p}_y \sigma_z) - \frac{\Omega \sigma_x}{2} \quad (6.1)$$

where $w(\mathbf{r})$ is the spin-independent part of the Hamiltonian. Alternatively, again by just rotating the trap in so called 4-level-scheme [Campbell et al., 2011] and choosing the parameters so that we have Rashba type SOC, the non-interacting part of the Hamiltonian becomes time independent [Radić et al., 2011]

$$H = \left[\frac{\mathbf{k}^2}{2M} + V(\mathbf{r}) - \Omega L_z(\mathbf{r}, \mathbf{k}) \right] \mathbf{I} + \alpha (\mathbf{k}_y \sigma_x - \mathbf{k}_x \sigma_y) + \left(\frac{\Delta_z}{2} - \frac{\Omega}{2} \right) \sigma_z \quad (6.2)$$

where Δ_z is the effective Zeeman field. Thus we have at least two schemes for crating non-interacting rotating Fermi gas with Rashba SOC, which does not even rely on rotating the lasers, besides rotating the set up on the experimentally realized NIST scheme. Alternatively spatially-dependent detuning can be used to generate effective rotation. Thus while there are many technical challenges which needs to be overcome, rotating Fermi gas with Rashba SOC in principle can be realized. Motivated with this analysis we first study the non-interacting Fermi gas with SOC under LDA. The Hamiltonian of non-interacting Fermi gas with SOC can be written as a sum of three terms:

$$H_{\text{ni}} = H_{\text{sho}} + H_{\text{rot}} + H_{\text{soc}} \quad (6.3)$$

where H_{sho} is the simple harmonic oscillator term given in Eq. (3.113), H_{rot} is the rotation term in the rotating frame given in Eq. (5.15) and lastly H_{soc} is the SOC term expressed in Eq. (4.58). We again make LDA and transform our Hamiltonian to momentum basis using standard relation, $\psi_\sigma(\mathbf{r}) = (1/\sqrt{A}) \sum_{\mathbf{k}} e^{i\mathbf{k}\cdot\mathbf{r}} a_{\mathbf{k}\sigma}$,

$$H_{\text{ni}}^{\text{LDA}} = \sum_{\mathbf{k}} \begin{pmatrix} \hat{a}_{\mathbf{k}\uparrow}^\dagger & \hat{a}_{\mathbf{k}\downarrow}^\dagger \end{pmatrix} \begin{pmatrix} \frac{k^2}{2M} - \mu(\mathbf{r}) - \Omega L_{\mathbf{k}}(\mathbf{r}) & \alpha(k_x - ik_y) \\ \alpha(k_x + ik_y) & \frac{k^2}{2M} - \mu(\mathbf{r}) - \Omega L_{\mathbf{k}}(\mathbf{r}) \end{pmatrix} \begin{pmatrix} \hat{a}_{\mathbf{k}\uparrow} \\ \hat{a}_{\mathbf{k}\downarrow} \end{pmatrix}.$$

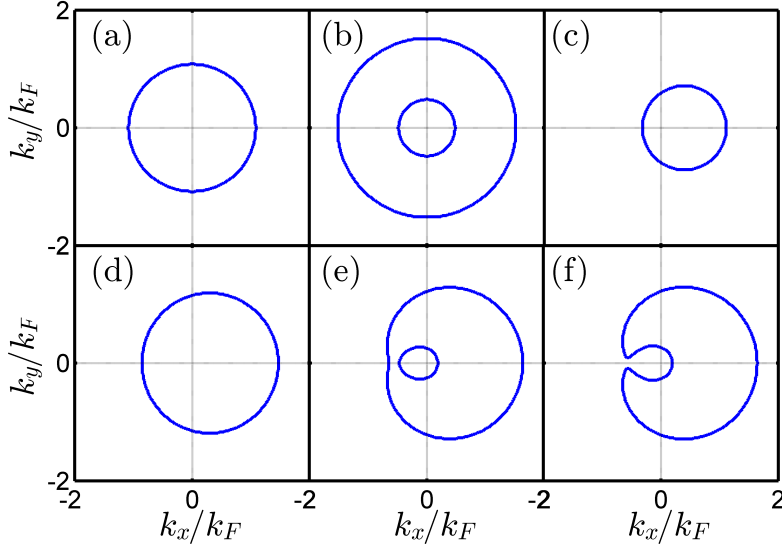


Figure 6.1: Illustration of negative helicity Fermi surfaces: $(\Omega/\omega, \alpha k_F/E_F) = (0, 0.5)$ in (a), $(0, 2)$ in (b), $(0.8, 0)$ in (c), $(0.35, 1)$ in (d), $(0.35, 1.47)$ in (e), $(0.35, 1.49)$ in (f), respectively. See text for discussion.

(6.4)

Above Hamiltonian can be easily diagonalized to yield the dispersion relation for a s helicity particle

$$\varepsilon_{\mathbf{k}s}(\mathbf{r}) = \frac{k^2}{2M} + s\alpha k - r\Omega k \sin(\theta_{\mathbf{k}} - \theta_{\mathbf{r}}) - \mu(r). \quad (6.5)$$

Since the trap is rotationally symmetric without loss of generality, we take $\theta_{\mathbf{r}} = 0$ corresponding to the positive x -direction in the real space. Note that the negative helicity dispersion minima is tilted by rotation, breaking the degeneracy in the lowest energy state resulting from SOC. Within LDA the tilting effect is proportional to k , hence the effect can be enhanced by SOC.

The curves describing the Fermi surface of s helicity particles can be calculated by setting $\varepsilon_{\mathbf{k}s}(\mathbf{r}) = 0$, and is given as

$$k_{1,2}^s = M(\Omega r \sin \theta_{\mathbf{k}} - s\alpha) \pm \sqrt{M^2(\Omega r \sin \theta_{\mathbf{k}} - s\alpha)^2 + 2M\mu(r)}. \quad (6.6)$$

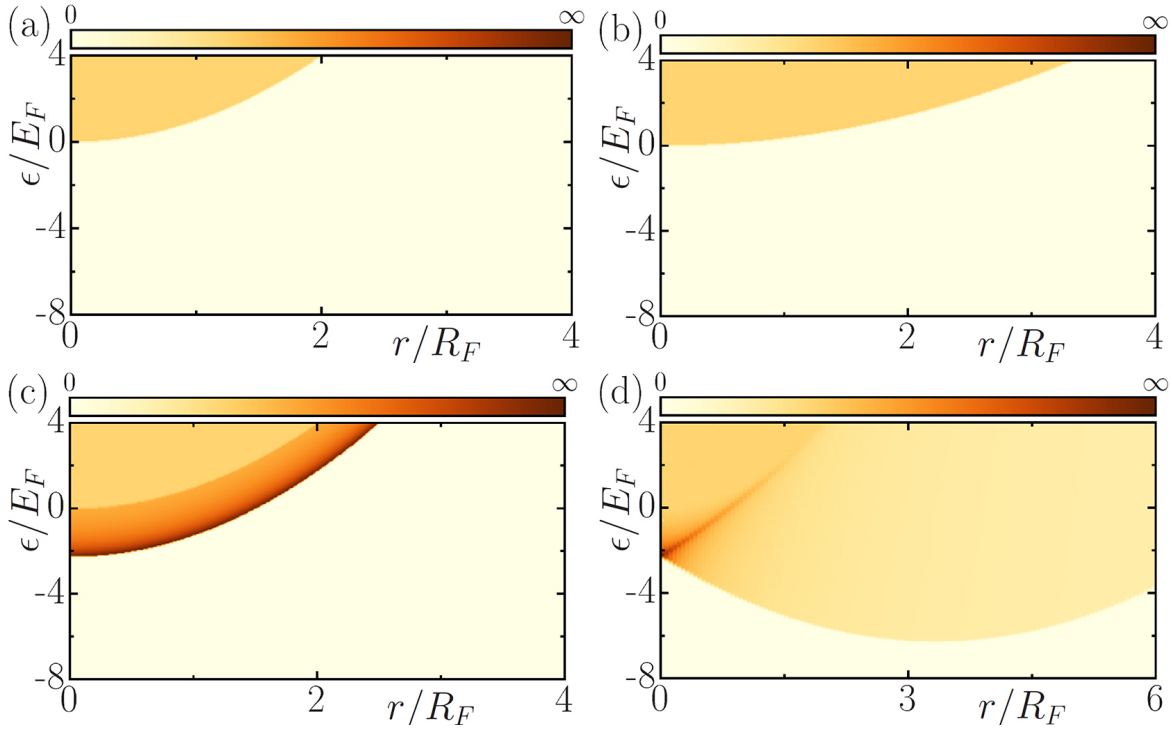


Figure 6.2: Local energy density of states in the trap for increasing values of Ω and α . Within LDA for a gas without SOC (a) ($\Omega = 0, \alpha = 0$) and (b) ($\Omega = 0.4\omega, \alpha = 0$) LDOS displays standard constant behavior for the energy DOS in 2D except the outward extension due to rotation. SOC enhances LDOS for lowest energies as in (c) ($\Omega = 0, \alpha = 3E_F/k_F$). For the most general case (d) ($\Omega = 0.8\omega, \alpha = 3E_F/k_F$), rotation pushes the minimum of LDOS away from the center and removes the divergence for $r \neq 0$ as discussed in the main text in detail.

This new excitation spectrum gives rise to three topologically distinct Fermi surfaces for negative and one for positive helicity particles. For $\mu(r) > 0$, the Fermi surface of negative helicity particles is a circle around some finite k (see Fig. 6.1(d)). For $\mu(r) < 0$ and $(\sqrt{-2\mu(r)/M} - \alpha)/(2r\Omega) \leq -1$, the Fermi surface is a deformed ring centered around $\mathbf{k} = 0$ (see Fig. 6.1(e)). For $\mu(r) < 0$ and $|\left(\sqrt{-2\mu(r)/M} - \alpha\right)/(r\Omega)| \leq 1$, negative helicity particles form a crescent shaped Fermi surface (see Fig. 6.1(f)). On the other hand the positive helicity Fermi surface is a deformed circle centered at some finite k . Unlike the non-rotating case, positive helicity particles exist even when $\mu_r \leq 0$ as long as $(\sqrt{-4\mu(r)} + \alpha)/(2r\Omega) \leq 1$.

The position of the lowest energy state in the trap can be obtained by minimizing

the lower energy branch $\varepsilon_{k-}(\mathbf{r})$ with respect to both \mathbf{k} and r . Whereas for $\alpha = 0$ or $\Omega = 0$ the lowest energy state is located at the center of the trap, in the general case it has momentum $k = \alpha M \omega^2 / (\omega^2 - \Omega^2)$ in the opposite flow direction ($\theta_k = \pi/2$) and is located at the radial distance

$$r = \frac{\alpha \Omega}{\omega^2 - \Omega^2}. \quad (6.7)$$

Thus lowest energy state moves to higher radial distances when either α or Ω is increased and it can be only at finite r if they both are present.

In this most general case LDOS $D(r, \epsilon) = \sum_{\mathbf{k}, s} \delta[\epsilon - \varepsilon_{\mathbf{k}s}(\mathbf{r})]$ can not be calculated analytically, but we can calculate it numerically using the following representation of Dirac delta function

$$\delta(x) \approx \frac{\varsigma}{\pi(x^2 + \varsigma^2)} \quad (6.8)$$

with $\varsigma = 10^{-3}$. In Fig. 6.2(d) we show an example LDOS profile. The higher angular momentum states, which are localized at higher radial distances, have lowest energy. Therefore the energy at finite angular momentum is lower than the non-rotating SOC level at the center of the trap. For high enough Ω and α , all the particles leave the center giving rise to a ring shaped density profile discussed below and requires the presence of both SOC and rotation simultaneously. Since as we discussed above for $\alpha = 0$ or $\Omega = 0$ lowest energy state is at the center of the trap and therefore we always have particle in the center of the trap. Rotation removes the 1D character and the divergence of LDOS with SOC for $r \neq 0$ because it breaks the degeneracy of the negative helicity dispersion minima.

Since we do not know the LDOS analytically, we can not obtain an expression for density distribution in the trap. Nevertheless we can obtain the central density analytically since the rotation term is zero there. Thus the density is same as that given in Sec. (4.6)

$$n(0) = \frac{M}{\pi}(\alpha^2 M + \mu) \quad (6.9)$$

for $\mu \geq 0$ and

$$n(0) = \frac{\alpha M^2}{\pi} \sqrt{\alpha^2 + \frac{2\mu}{M}} \quad (6.10)$$

for $\mu < 0$. This result is important because we can identify the critical condition

$$\alpha^2 + \frac{2\mu}{M} \leq 0 \quad (6.11)$$

for which the trap center is empty due to the above mentioned effect.

The points where the local density vanishes and thus the local Fermi surfaces disappear define the inner and outer radii forming the edges of the gas. The presence of the Fermi surface implies real $k_{1,2}^s$, thus we can find the edge(s) from the vanishing of the square root in Eq. (6.6) as the solutions to $M^2(\Omega r - s\alpha)^2 + 2M\mu(r) = 0$ so that

$$R_{I,O}^0 = R_F \frac{\omega\Omega\alpha \pm \omega\sqrt{\alpha^2\omega^2 + 2\mu(\omega^2 - \Omega^2)}/M}{k_F(\omega^2 - \Omega^2)/M}. \quad (6.12)$$

The inner radius appears $R_I^0 \geq 0$ only when $\alpha^2 + 2\mu/M \leq 0$ and the gas forms an annulus.

The density distribution can be calculated by integrating numerically

$$n(r) = \frac{1}{A} \sum_{\mathbf{k},s} \Theta[-\varepsilon_{\mathbf{k}s}(r)]. \quad (6.13)$$

We should note that we again relate the particle number to Fermi energy of trapped 2D Fermi gas $E_F = \omega\sqrt{N}$. In Fig. 6.3, we show the density profiles for different values of Ω and α . For $\Omega = 0.15\omega$ shown in Fig. 6.3(a) we plot the density in the whole trap as a function of α . Fig. 6.3(c) shows the trap profile at representative values of α corresponding to horizontal cuts from the surface plot in Fig. 6.3(a). The density at the center of the trap increases with SOC due to increasing low energy density of states we discussed in Ch.4. However, SOC energetically favors some finite angular momentum states as well. As α is increased, the latter effect causes the gas to expand, while the density at the center also increases as result of the former effect.

This competition results in a sharp decrease of density as we move away from the center. Further increasing α approaching the critical value of $\alpha = \sqrt{-2\mu/M}$, the latter effect completely dominates and the center density starts to decrease as the gas continues to expand. As we get very close to this critical value, the density develops a second local maximum. When we reach the critical value, the density at the center of the trap depletes. The radius R_I^0 of the empty core region in the center of the trap grows linearly with α once it forms. For faster rotation $\Omega = 0.5\omega$ shown in Fig. 6.3(b) even for a small α the latter effect mentioned above is dominant and the gas expands immediately as α is increased. The center density decreases, however this can happen non-monotonically by first decreasing than increasing and as we get close to critical value decreasing again. Note that depletion of the center takes place at lower critical α for faster rotating traps, which is expected from Eq. (6.7) since at faster rotation minimum energy states move to higher r .

The same expansion effect can also be observed as Ω is increased at fixed α as shown in Fig. 6.4. In contrast to changing α , increasing rotation results in monotonic expansion and decrease of density at the center of the trap, which is more pronounced for large values of α . [Compare Fig. 6.4(a) and Fig. 6.4(b)]. The edges of the gas show a nonlinear behavior as a function of Ω . The lower panel of Fig. 6.4 similarly shows the radial density of representative values of Ω corresponding to various different distributions.

The critical rotation frequency Ω_c^0 for the emergence of the annulus can be calculated by self consistent solution of Eq. (6.13) together with the condition $\alpha^2 + 2\mu/M = 0$ and is plotted in Fig. 6.5. In the $\alpha \rightarrow 0$ limit, there is no ring formation but the confinement disappears when $\Omega = \Omega_c^0 \rightarrow \omega$. However any finite α eventually leads to an annulus for some $\Omega < \omega$. Ω_c^0 monotonically decreases for increasing α as seen in Fig. 6.5.

Since the experiments are done in finite temperatures, it is an interesting question whether this ring shaped annulus persist in experimentally accessible finite T . The finite temperature density profile can be obtained by integrating

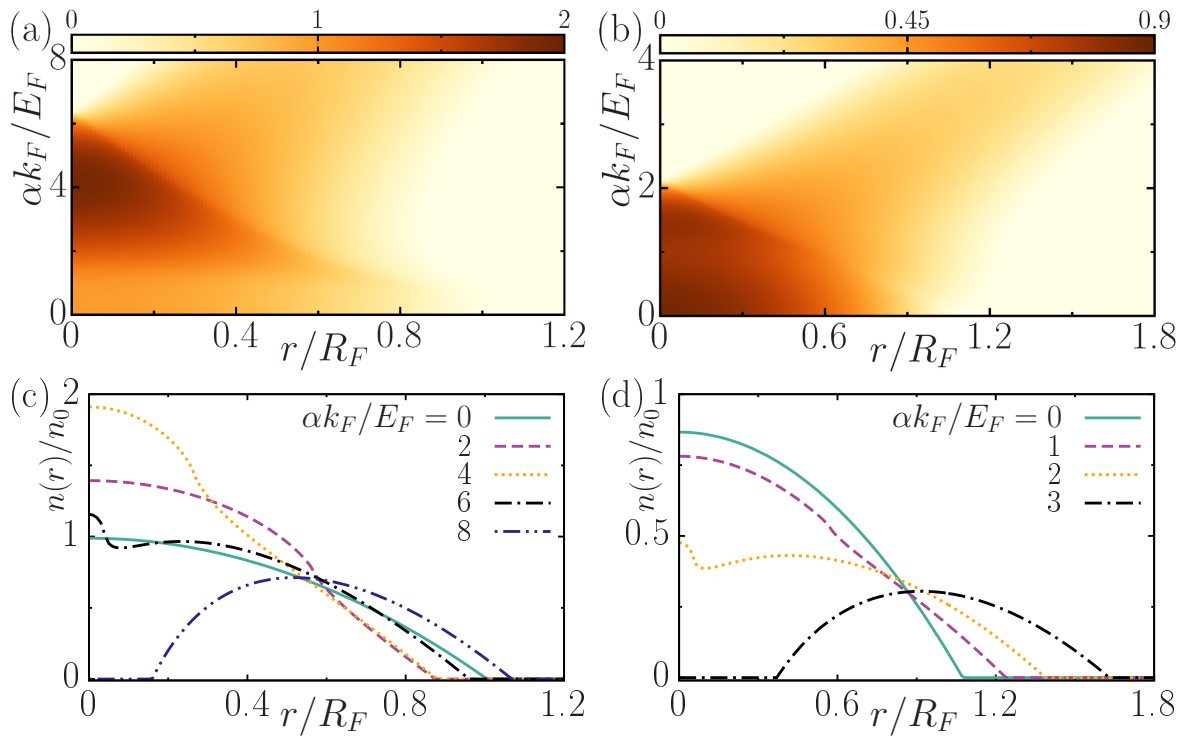


Figure 6.3: Non-interacting density profiles in the trap with changing SOC strength α for (a) $\Omega = 0.15\omega$ and (b) $\Omega = 0.5\omega$. The density at representative SOC values from (a) and (b) are plotted in (c) and (d), respectively. The rotating gas takes up a ring-shaped form as α is increased.

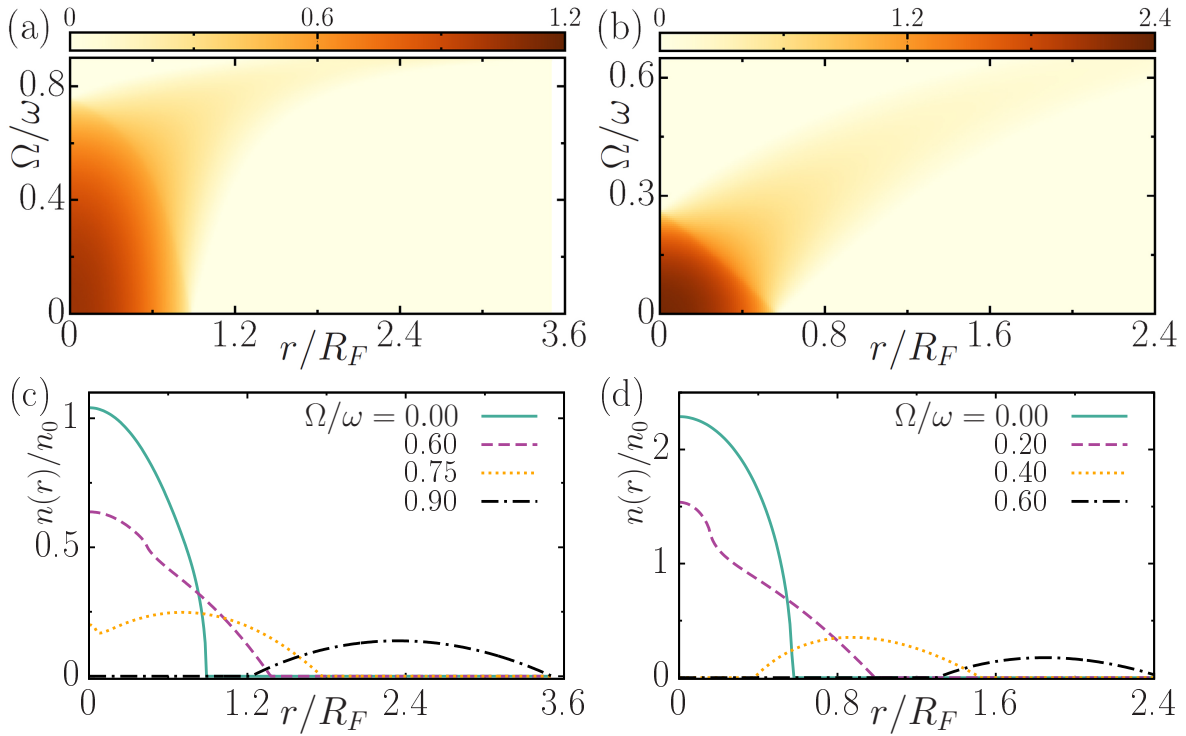


Figure 6.4: Non-interacting density profiles in the trap with changing Ω for (a) $\alpha = 1k_F/E_F$ and (b) $\alpha = 4k_F/E_F$. The density at representative Ω values from (a) and (b) are plotted in (c) and (d), respectively. The SOC gas takes up a ring-shaped form as Ω is increased.

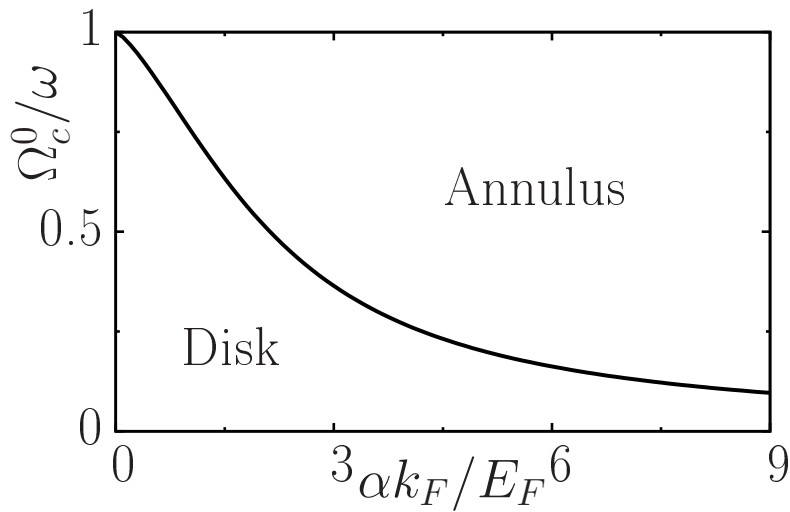


Figure 6.5: The critical rotation frequency Ω_c^0 for the depletion of the center as a function of SOC strength α , at which the disk-shaped density of the non-interacting gas transforms into a ring. An annulus forms at $\Omega < \omega$ for any finite α . The $\alpha \rightarrow 0$ limit of Ω_c^0 gives the trap frequency ω indicating the necessity of SOC for this effect.

$$n(\mathbf{r}) = \frac{1}{A} \sum_{\mathbf{k},s} f[\varepsilon_{\mathbf{k}s}(\mathbf{r})]. \quad (6.14)$$

Fig.6.6 shows the effects of temperature T on the density profiles at the simultaneous presence of α and Ω . The temperature broadening effect is most significant for the ring shaped density distributions, which eventually recover a disk profile at some high enough temperature. However the ring shaped annulus can persist at higher temperatures by increasing α and/or Ω , reaching the order of Fermi temperature $T_F = E_F/k_B$, therefore making experimental observation possible. We also note that before the high temperature Gaussian density profile is recovered, we observe a flat density distribution, the width of which can be on the order of R_F , at the intermediate temperature region.

Another interesting quantity to compute is the local spin polarization defined as

$$P_i(\mathbf{r}) = \frac{1}{A} \sum_{\sigma\sigma'} \frac{\langle \hat{a}_{\mathbf{k}\sigma}^\dagger \sigma^i_{\sigma\sigma'} \hat{a}_{\mathbf{k}\sigma'} \rangle}{n(\mathbf{r})} \quad (6.15)$$

where i denotes the components. The components of the local polarization vector can be calculated via

$$P_x(\mathbf{r}) + iP_y(\mathbf{r}) = \frac{2}{A} \sum_{\mathbf{k}} \frac{\langle \hat{a}_{\mathbf{k}\uparrow}^\dagger \hat{a}_{\mathbf{k}\downarrow} \rangle}{n(\mathbf{r})}. \quad (6.16)$$

As we discussed, while the presence of α creates helicity bands with definite spin orientation with respect to momentum direction, the rotation favors momenta parallel to the rotational flow. These two facts combined also lead to finite local polarization of spin in angular direction

$$P_\theta(\mathbf{r}) = -\sin(\theta_{\mathbf{r}})P_x(\mathbf{r}) + \cos(\theta_{\mathbf{r}})P_y(\mathbf{r}). \quad (6.17)$$

Such spin polarization is absent in $\Omega = 0$ limit since opposite momentum states contribute equally with opposite spin polarizations, whereas in $\alpha = 0$ limit the decoupled spins again average to zero polarization. Therefore the effect relies on $\Omega > 0$

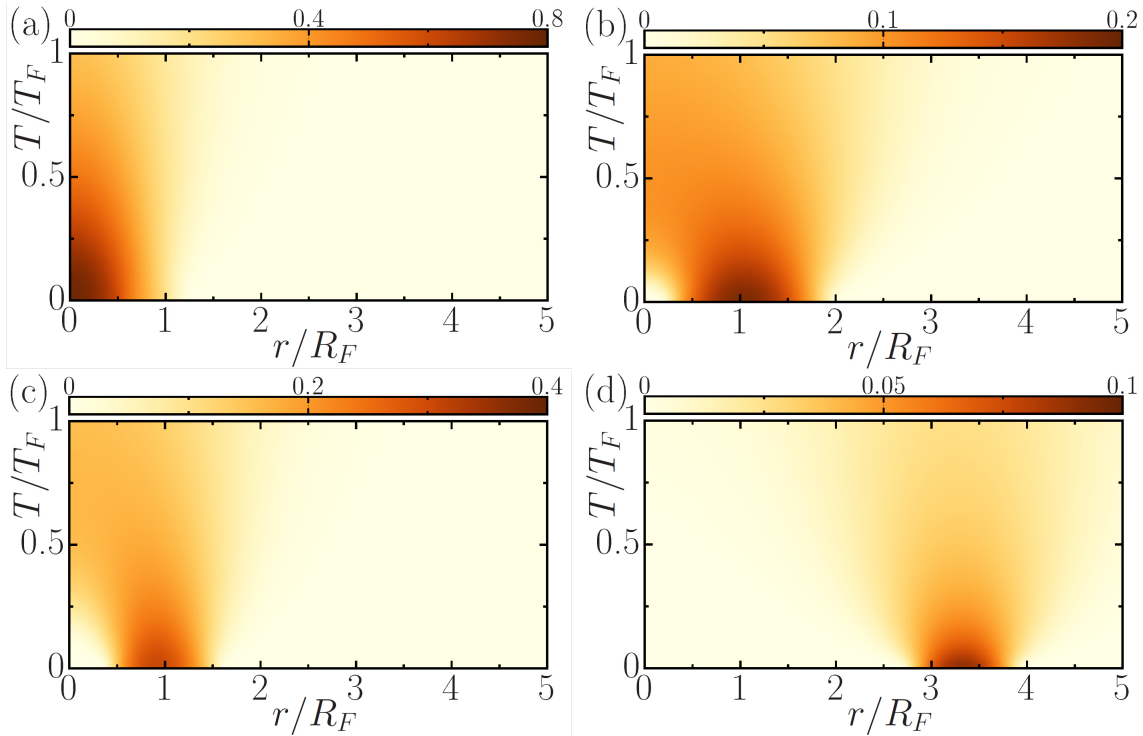


Figure 6.6: Finite temperature non-interacting density profiles for $\Omega > 0$ and $\alpha > 0$. Increasing either Ω or α from (a) ($\Omega = 0.5\omega, \alpha = 1E_F/k_F$), the disk profile transform into a ring for (b) ($\Omega = 0.8\omega, \alpha = 1E_F/k_F$) and (c) ($\Omega = 0.5\omega, \alpha = 3E_F/k_F$), where the depletion of the central density is visible for low T . Increasing either Ω or α further, the effect persists for higher temperatures as in (d) ($\Omega = 0.8\omega, \alpha = 3E_F/k_F$).

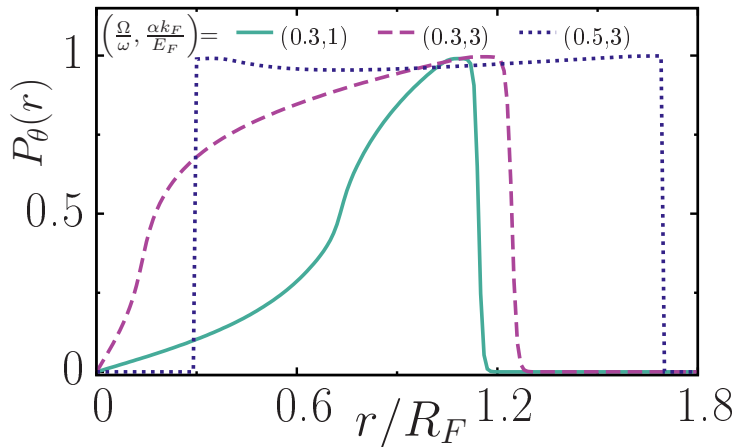


Figure 6.7: The polarization in angular direction for $\alpha > 0$ and $\Omega > 0$, increases monotonically starting from zero at the center and becoming unity at the edge. When the gas takes up a ring shape, it becomes almost fully polarized.

and $\alpha > 0$ similar to the ring formation phenomenon. The spin polarization in this non-trivial case is shown in Fig. 6.7 for increasing values of α and Ω . The polarization starts from zero at the center which is not effected from the rotation and reaches unity at the edge where only the negative helicity lowest energy non-degenerate state with spin anti-parallel to the angular direction is occupied. For increasing α and Ω spin polarization in between the edge and the center increases monotonically because of the disappearance of the positive helicity band and increasing asymmetry in the dispersion. For a ring shaped density profile, full polarization similarly appears at the inner and outer edges with polarization approaching almost unity in between as seen for the $\Omega = 0.5\omega$, $\alpha = 3E_F/k_F$ curve in Fig. 6.7.

6.2 Rotating Non-Interacting 2D Fermi Gas with Rashba SOC: Exact Quantum Mechanical Approach

In this section we will compute the density distribution of rotating 2D Fermi gas with SOC exactly using the 2D harmonic oscillator basis to check the validity of LDA. We use the real space Hamiltonian in Eq. (6.3) without making any approximation

$$H_{\text{ni}} = \int d\mathbf{r} \hat{\psi}^\dagger(\mathbf{r}) \left[\frac{\hat{p}^2}{2M} + \frac{1}{2}M\omega^2 \hat{r}^2 + \alpha \hat{p} \cdot \hat{\sigma} - \Omega \hat{L}_z - \mu \right] \hat{\psi}(\mathbf{r}), \quad (6.18)$$

where $\hat{\psi}^\dagger(\mathbf{r}) = (\hat{\psi}_\uparrow^\dagger(\mathbf{r}), \hat{\psi}_\downarrow^\dagger(\mathbf{r}))$ denotes the particle creation operators. We make use of the rotational symmetry of the system, and expand the field operators in terms of the angular momentum basis of the 2D harmonic oscillator as

$$\hat{\psi}_\sigma(\mathbf{r}) = \sum_{n,l} R_n^{|l|}(r) e^{il\theta} \hat{c}_{n,l,\sigma}, \quad (6.19)$$

where $\hat{c}_{n,l,\sigma}$ annihilates a spin σ particle in the $|n, l\rangle$ state that is given by the normalized real-space wave function given in Eq. (2.72). Using the relations given in Sec. (4.6) and Sec. (5.3) Hamiltonian can be written in this basis as

where $f [E_m^{(j)}] = \langle \hat{C}_{j,m}^\dagger \hat{C}_{j,m} \rangle$. Here the density $n_{\sigma,m}^{(j)}(r)$ for the m^{th} energy eigenstate with total angular momentum j are given by

$$n_{\uparrow,m}^{(j)}(r) = \left| \sum_{k=0}^{n_c/2} u_{l+2k,\uparrow,m}^{(j)} R_{l+2k}^{|l|}(r) \right|^2, \quad n_{\downarrow,m}^{(j)}(r) = \left| \sum_{k=0}^{n_c/2} u_{l+1+2k,\downarrow,m}^{(j)} R_{l+2k}^{|l+1|}(r) \right|^2, \quad (6.28)$$

for $j > 0$ ($l \geq 0$) and

$$n_{\uparrow,m}^{(j)}(r) = \left| \sum_{k=0}^{n_c/2} u_{-l+2k,\uparrow,m}^{(j)} R_{l+2k}^{|l|}(r) \right|^2, \quad n_{\downarrow,m}^{(j)}(r) = \left| \sum_{k=0}^{n_c/2} u_{-l-1+2k,\downarrow,m}^{(j)} R_{l+2k}^{|l+1|}(r) \right|^2, \quad (6.29)$$

for $j < 0$ ($l < 0$) and $n_c = (|l|_{\text{max}} - |l|)/2$ is the cut-off which can be related to cut-off energy $E_c = \omega(|l|_{\text{max}} + 1) \gg E_F$. We make sure that cut-off is high enough so that results are cut-off independent. Note that the density is independent of the angle θ .

Another useful expression is the mass current density. Since the presence of SOC mixes \uparrow and \downarrow spins, the mass current density should be identified from the continuity equation

$$\partial_t \rho(\mathbf{r}) + \nabla \cdot \mathbf{J}(\mathbf{r}) = 0 \quad (6.30)$$

where $\rho(\mathbf{r}) = Mn(\mathbf{r})$ is the mass density. This yields

$$\begin{aligned} J_\theta(r) &= \sum_{\sigma} \Im \langle \hat{\psi}_{\sigma}^\dagger(r) \frac{\partial}{r \partial \theta} \hat{\psi}_{\sigma}(r) \rangle + 2M\alpha |\langle \hat{\psi}_{\uparrow}^\dagger(r) \hat{\psi}_{\downarrow}(r) \rangle| \\ &= M \sum_j \sum_m J_{\theta,m}^{(j)}(r) f [E_m^{(j)}], \end{aligned} \quad (6.31)$$

where \Im denotes the imaginary part. The angular component of the mass current density $J_{\theta,m}^{(j)}(r)$ for the m^{th} energy eigenstate with total angular momentum j are given by

$$\begin{aligned} J_{\theta,m}^{(j)}(r) &= \frac{l}{r} n_{\uparrow,m}^{(j)}(r) + \frac{l+1}{r} n_{\downarrow,m}^{(j)}(r) \\ &+ 2\alpha \left| \left[\sum_{k=0}^{n_c/2} u_{l+2k,\uparrow,m}^{(j)} R_{l+2k}^{|l|}(r) e^{il\theta} \right]^* \left[\sum_{k=0}^{n_c/2} u_{l+1+2k,\downarrow,m}^{(j)} R_{l+2k}^{|l+1|}(r) e^{i(l+1)\theta} \right] \right|, \end{aligned} \quad (6.32)$$

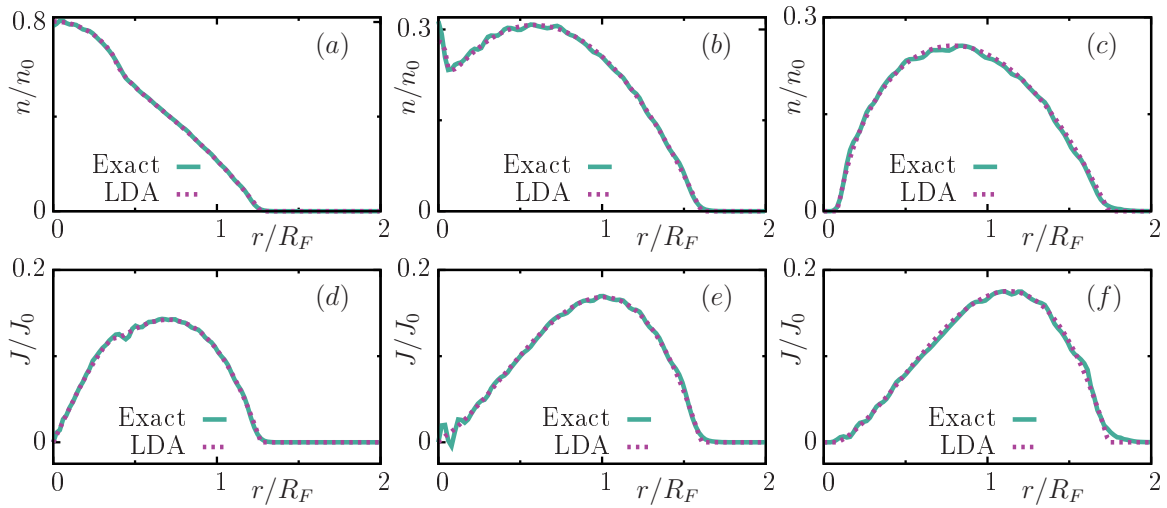


Figure 6.8: Exact solutions for the (a)-(c) number density, and (d)-(f) mass-current density are compared with those of semi-classical LDA approach, where $\Omega/\omega = 0.5$ in (a) and (d), 0.68 in (b) and (e), and 0.7 in (c) and (f). We also set $N = 800$ and $\alpha = 1.33E_F/k_F$ in all figures. The overall results are in excellent agreement with each other up to minor deviations due to finite-size effects.

for $j > 0$ ($l \geq 0$) and

$$\begin{aligned}
 J_{\theta,m}^{(j)}(r) = & \frac{l}{r}n_{\uparrow,m}^{(j)}(r) + \frac{l+1}{r}n_{\downarrow,m}^{(j)}(r) \\
 & + 2\alpha \left| \left[\sum_{k=0}^{n_c/2} u_{-l+2k\uparrow,m}^{(j)} R_{l+2k}^{|l|}(r) e^{il\theta} \right]^* \left[\sum_{k=0}^{n_c/2} u_{-l-1+2k\downarrow,m}^{(j)} R_{l+2k}^{|l+1|}(r) e^{i(l+1)\theta} \right] \right|,
 \end{aligned} \tag{6.33}$$

for $j < 0$ ($l < 0$). In Fig. 6.8, we present the number density and mass-current density profiles in the trap that are obtained from the exact calculation given above and the LDA approach described in the text, showing an excellent agreement between the two. The total number of particles is $N = 2\pi \int dr r n(r) = 800$. The finite size effects such as Friedel oscillations vanish in the thermodynamic limit when $N \rightarrow \infty$. The LDA expression for mass-current density is the rigid body rotation value $J_{\theta}(r) = r\Omega n(r)$.

As we demonstrated in previous section LDA developed in this thesis fails to capture the physics of rapidly rotating limit $\Omega \rightarrow \omega$, where we have Landau level structure which leads to ziggurat shaped density profile. Let us now discuss the effect of SOC on the density profile in rapid rotating limit using the exact quantum

mechanical calculations developed in this section.

The introduction of SOC breaks the spin degeneracy within each Landau level resulting in two helicity branches. In the perturbative regime when $\alpha \ll 2a_0\omega$, where $a_0 = 1/\sqrt{m\omega}$ is the harmonic oscillator length, the helicity $s = \pm$ energies can be approximated by

$$\varepsilon_{n_L, l, s} = \omega(2n_L + 1) + \omega_- l + \omega_-/2 \left[1 + s\sqrt{1 + \alpha^2(n_L + l + 1)/(a_0\omega_-)^2} \right] \quad (6.34)$$

and are shown with lines along with numerical values indicated by (green) crosses in Fig. 6.9(a). The helicity branches display avoided level crossings for larger angular momenta as in Fig. 6.9(b) and negative helicity branches develop a minimum for $\alpha \gtrsim a_0\omega_-$ at finite angular momentum located near $l_{\min} = \alpha^2/(4a_0\omega_-)^2$ as can be seen in Fig. 6.9(c). The energy gap between same helicity branches remains approximately 2ω in this perturbative regime.

Therefore the effect of small SOC on the density in the Landau regime is to double the number of quantized steps initially and then to eventually lead to a ring shaped profile as SOC is increased to $\alpha \gtrsim a_0\omega_-$ which is demonstrated for the lowest Landau level in Fig. 6.10(a) by the (green) dashed and solid (blue) lines, respectively. The density of the ring is exactly half of that of the lowest Landau level without SOC. With more than one Landau level filled the energy level structure may lead to dips in between two plateaus as in Fig. 6.10(b) or a ziggurat ring shown in Fig. 6.10(c).

6.3 Rashba Coupled 2D Interacting Fermi Gas Under Adiabatic Rotation: Local Density Approximation

In this section we turn our attention to the 2D interacting Fermi gas with SOC. We assume that system is rotated adiabatically so that no vortices are excited. We will investigate the effect of SOC on the pair breaking effect of the rotation. Naive expectation based on our observation in Ch. 4. that SOC enhances the order parameter, i.e. pairing may be that SOC will resist the pair breaking effect of rotation. But

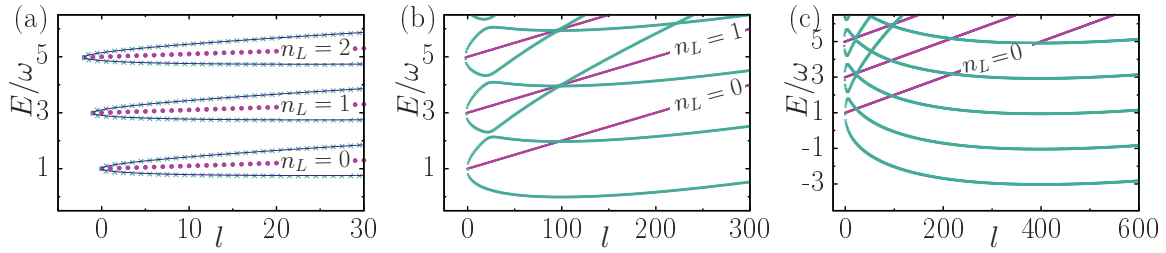


Figure 6.9: Energy levels as a function of angular momentum for a rapidly-rotating Fermi gas with Rashba coupling in the Landau regime when $\Omega = 0.99\omega$. Here, $\alpha = 0$ limit is shown in purple dots for the first three Landau levels as a reference. (a) $\alpha = 0.2\sqrt{\omega/M}$: Rashba coupling splits each of the Landau levels into two helicity branches with a widening energy gap in between as a function of angular momentum. (b) $\alpha = 0.4\sqrt{\omega/M}$: the helicity branches display avoided level crossings. (c) $\alpha = 0.8\sqrt{\omega/M}$: all of the negative-helicity branches not only occupy lowest energies but they also develop minimum at finite angular momentum. All of these couplings are in the perturbative $\alpha \ll 2a_0\omega$ regime.

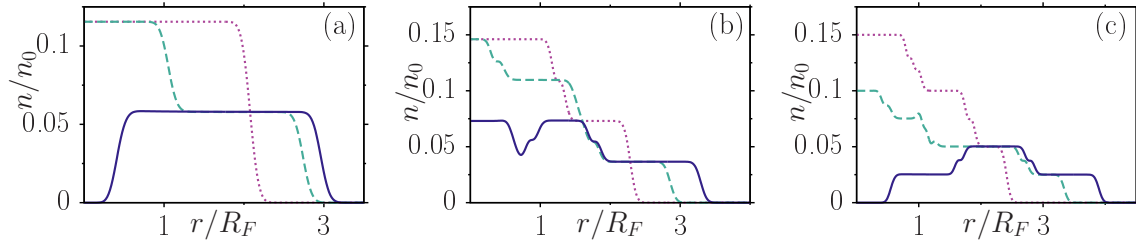


Figure 6.10: Radial-density profiles at $T = 0$ in the Landau regime when $\Omega = 0.99\omega$. The (purple) dotted, (green) dashed and solid (blue) lines correspond, respectively, to higher Rashba couplings where $\alpha = 0, 0.2, 0.4\sqrt{\omega/M}$ in (a) with $N = 750$ in the lowest-Landau level, $\alpha = 0, 0.2, 0.4\sqrt{\omega/M}$ in (b) with $N = 900$ in the first two Landau levels, and $\alpha = 0, 0.4, 0.8\sqrt{\omega/M}$ in (c) with $N = 1600$ in the first three Landau levels. These intriguing profiles directly reflect the corresponding energy-level structures shown in Fig. 6.9, where the higher the angular momentum of the single-particle state the further away its localization distance from the trap center.

as we will demonstrate below this expectation is not quite right, and there are more than one mechanisms involved. We will again analyze the system in the mean-field approximation, and derive the gap and number equations using LDA. The mean-field Hamiltonian describing the system can be written as

$$H^{\text{mf}} = H_{\text{ni}} + H_{\text{int}}^{\text{mf}} \quad (6.35)$$

where H_{ni} is the non-interacting Hamiltonian introduced in the previous sections and $H_{\text{int}}^{\text{mf}}$ is the mean-field interaction term given in given in Eq. (3.115), with order parameter defined again as $\Delta(\mathbf{r}) = g\langle\hat{\psi}_{\uparrow}(\mathbf{r})\hat{\psi}_{\downarrow}(\mathbf{r})\rangle$. We make LDA and define the local chemical potential $\mu(\mathbf{r}) = \mu - V(\mathbf{r})$ and the effective local rotation term $\Omega L_{\mathbf{k}}(\mathbf{r}) = \mathbf{v}(\mathbf{r}) \cdot \mathbf{k}$, where $\mathbf{v}(\mathbf{r}) = \Omega \hat{\mathbf{z}} \times \mathbf{r}$. We go to the momentum basis where the local Hamiltonian density $H^{\text{LDA}}(\mathbf{r})$ can be written as

$$H^{\text{LDA}}(\mathbf{r}) = \frac{1}{2} \sum_{\mathbf{k}} \hat{\Psi}_{\mathbf{k}}^{\dagger} H_{\mathbf{k}}^{\text{LDA}}(\mathbf{r}) \hat{\Psi}_{\mathbf{k}} + C(\mathbf{r}) \quad (6.36)$$

with

$$H_{\mathbf{k}}^{\text{LDA}}(\mathbf{r}) = \begin{pmatrix} \xi_{\mathbf{k}}(\mathbf{r}) & S_{\mathbf{k}} & 0 & \Delta(\mathbf{r}) \\ S_{\mathbf{k}}^* & \xi_{\mathbf{k}}(\mathbf{r}) & -\Delta(\mathbf{r}) & 0 \\ 0 & -\Delta^*(\mathbf{r}) & -\xi_{\mathbf{k}}(\mathbf{r}) & S_{\mathbf{k}}^* \\ \Delta^*(\mathbf{r}) & 0 & S_{\mathbf{k}} & -\xi_{\mathbf{k}}(\mathbf{r}) \end{pmatrix} - \Omega L_{\mathbf{k}}(\mathbf{r}), \quad (6.37)$$

$\hat{\Psi}_{\mathbf{k}}^{\dagger} = [\hat{a}_{\mathbf{k}\uparrow}^{\dagger}, \hat{a}_{\mathbf{k}\downarrow}^{\dagger}, \hat{a}_{\mathbf{k}\uparrow}, \hat{a}_{-\mathbf{k}\downarrow}]$ and $C(\mathbf{r}) = \sum_{\mathbf{k}} [\xi_{\mathbf{k}}(\mathbf{r}) + \Omega L_{\mathbf{k}}(\mathbf{r})] + A|\Delta(\mathbf{r})|^2/g$. Above, $\Delta(\mathbf{r}) = (g/A) \sum_{\mathbf{k}} \langle \hat{a}_{\mathbf{k}\uparrow} \hat{a}_{-\mathbf{k}\downarrow} \rangle$ is the local mean-field order parameter $\xi_{\mathbf{k}}(\mathbf{r}) = \epsilon_{\mathbf{k}} - \mu(r)$ with $\epsilon_{\mathbf{k}} = k^2/(2M)$, and $S_{\mathbf{k}} = \alpha(k_x - ik_y)$ is the SOC term. We can diagonalize the local Hamiltonian analytically and get

$$H^{\text{LDA}}(\mathbf{r}) = \sum_{\mathbf{k}s} \left[E_{\mathbf{k}s}(\mathbf{r}) \gamma_{\mathbf{k}s}^{\dagger} \gamma_{\mathbf{k}s} - \frac{E_{\mathbf{k}s}(\mathbf{r})}{2} \right] + C(\mathbf{r}), \quad (6.38)$$

where $\gamma_{\mathbf{k}s}^{\dagger}$ ($\gamma_{\mathbf{k}s}$) denotes the quasi-particle creation (annihilation) operator with momentum \mathbf{k} and helicity $s = \pm$. The quasi-particle excitation energies are

$$E_{\mathbf{k}s}(\mathbf{r}) = \sqrt{[\xi_{\mathbf{k}}(\mathbf{r}) + s\alpha k]^2 + |\Delta(\mathbf{r})|^2} - \Omega L_{\mathbf{k}}(\mathbf{r}). \quad (6.39)$$

We can calculate the thermodynamic potential $G(\mathbf{r}) = -(1/\beta)\text{Tr}[\ln e^{-\beta H^{\text{LDA}}(\mathbf{r})}]$ as

$$G(\mathbf{r}) = \sum_{\mathbf{k}\sigma} \left\{ \frac{1}{2\beta} \ln(1 - f[E_{\mathbf{k}\sigma}(\mathbf{r})]) - \frac{E_{\mathbf{k}\sigma}(\mathbf{r})}{2} \right\} + C(\mathbf{r}) \quad (6.40)$$

and get the gap and the number equations by minimizing the thermodynamic potential, $\partial G(\mathbf{r})/\partial|\Delta(\mathbf{r})| = 0$ and $n(\mathbf{r}) = -(1/A)\partial G(\mathbf{r})/\partial\mu(\mathbf{r})$, as

$$\frac{1}{g} = \frac{1}{4A} \sum_{\mathbf{k}\sigma} \frac{1 - 2f[E_{\mathbf{k}\sigma}(\mathbf{r})]}{\sqrt{[\xi_{\mathbf{k}}(\mathbf{r}) + s\alpha k]^2 + |\Delta(\mathbf{r})|^2}}, \quad (6.41)$$

$$n(\mathbf{r}) = \frac{1}{2A} \sum_{\mathbf{k}\sigma} \left\{ 1 - \frac{\xi_{\mathbf{k}}(\mathbf{r}) + s\alpha k}{\sqrt{[\xi_{\mathbf{k}}(\mathbf{r}) + s\alpha k]^2 + |\Delta(\mathbf{r})|^2}} (1 - 2f[E_{\mathbf{k}\sigma}(\mathbf{r})]) \right\}, \quad (6.42)$$

respectively. These equations are to be solved locally within the trap and the total particle number is obtained by integrating the density, i.e., $N = \int d\mathbf{r}n(\mathbf{r})$. We renormalize the bare s-wave interaction g using the binding energy as before. In order to differentiate the gSF and SF phase, it may be useful to calculate the mass current density $\mathbf{J}(\mathbf{r}) = [J_x(\mathbf{r}), J_y(\mathbf{r})]$. To do so we transfer the expression given in Eq. (6.31) to momentum basis which yields

$$[J_x(\mathbf{r}), J_y(\mathbf{r})] = \frac{1}{A} \sum_{\mathbf{k}\sigma} (k_x, k_y) n_{\mathbf{k}\sigma}(\mathbf{r}) + [P_x(\mathbf{r}), P_y(\mathbf{r})] M\alpha n(\mathbf{r}), \quad (6.43)$$

Above, $n_{\mathbf{k}\sigma}(\mathbf{r}) = \langle \hat{a}_{\mathbf{k}\sigma}^\dagger \hat{a}_{\mathbf{k}\sigma} \rangle$ is the spin momentum distribution, the local density $n(\mathbf{r}) = \sum_{\mathbf{k}\sigma} n_{\mathbf{k}\sigma}(\mathbf{r})/A$ is explicitly given by the summand of Eq. (6.42) and the components of the local polarization vector can be calculated via $P_x(\mathbf{r}) + iP_y(\mathbf{r}) = \frac{2}{A} \sum_{\mathbf{k}} \langle \hat{a}_{\mathbf{k}\uparrow}^\dagger \hat{a}_{\mathbf{k}\downarrow} \rangle / n(\mathbf{r})$.

In the following section we consider the zero temperature ground states and study the simultaneous effects of SOC and rotation on trap profiles and superfluidity.

6.4 Phase Diagram and Trap Profiles

The simultaneous presence of SOC and rotation has interesting consequences for the interacting gas similar to the non-interacting case. Whereas rotation always has a pair

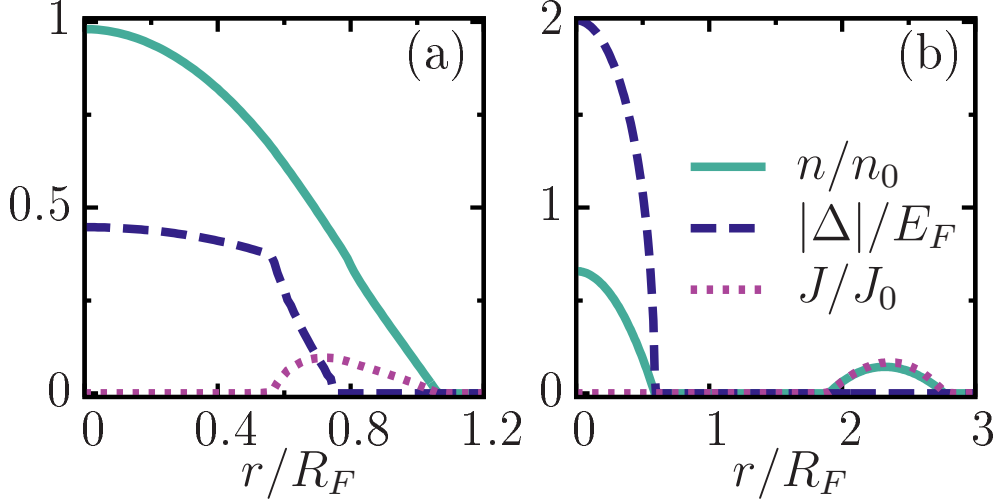


Figure 6.11: Typical profiles showing (a) a partially-rotating gSF region, and (b) a vacuum separating the non-rotating SF pairs from the rigidly-rotating N particles. Here, $E_b = 0.1E_F$, $\alpha = 0.8E_F/k_F$ and $\Omega = 0.3\omega$ in (a), and $E_b = 1E_F$, $\alpha = 7E_F/k_F$ and $\Omega = 0.5\omega$ in (b), where $n_0 = k_F^2/(2\pi)$ and $J_0 = Mn_0\omega R_F$.

breaking effect, depending on interaction and relative strengths of the parameters, SOC can either enhance pairing or pair breaking.

Similar to no SOC case, SF is robust and not affected by rotation for $\Omega < \Omega_c$, so that the trap profile and other physical quantities remain the same as in the non-rotating case, which we can use to determine Ω_c . The critical value Ω_c is the smallest Ω satisfying the inequality

$$R_O^0(\alpha, \Omega = \Omega_c) \geq R_O(\alpha, \Omega = 0). \quad (6.44)$$

When the equality is satisfied, the N phase appears at the edge of the cloud separated from the SF phase by the gSF layer as in no SOC case we studied in previous section. Whereas in the case of an inequality, the N phase appears at a larger radius disconnected from the SF phase. The appearance of a normal ring is reminiscent of the same ring formation phenomenon for the non-interacting case. For $\Omega > \Omega_c$, the former profile is realized for $\alpha^2 + 2\mu/M > 0$ with the non-rotating SF phase [$|\Delta(r)| \neq 0$ and $J_\theta(r) = 0$] at the center of the trap, a N component at the

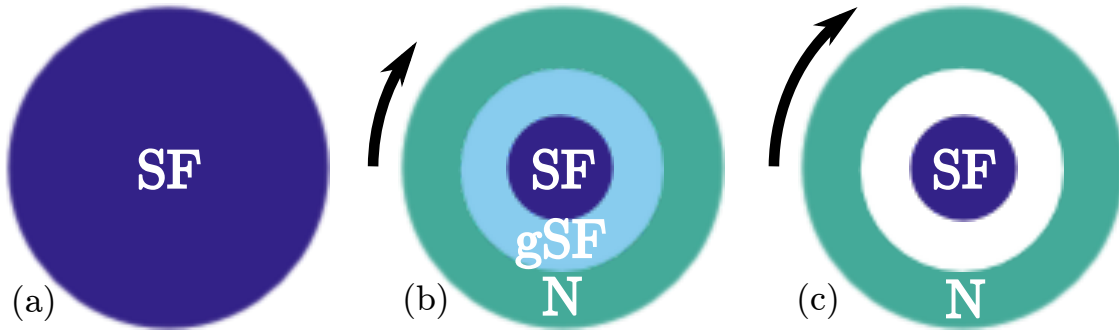


Figure 6.12: (a) In the absence of rotation the whole gas is superfluid (SF). (b) High enough rotation can through pair breaking induce an intermediate gSF phase separating SF from the normal (N) gas. (c) N phase can appear disconnected from the SF as a ring for higher rotation in the presence of spin-orbit coupling.

edge of the trap [$|\Delta(r)| = 0$ and $J_\theta(r) \neq 0$] and a gSF [$|\Delta(r)| \neq 0$ and $J_\theta(r) \neq 0$] in between. The N gas rotates rigidly as a whole, i.e. $J_\theta(r) = Mn(r)\Omega r$, and gSF phase rotates only partially as in $\alpha = 0$ case.

In Fig. 6.11(a), an example of such a trap profile is shown. On the other hand, under more extreme cases (provided that $\alpha^2 + 2\mu/M < 0$) it is possible to observe the latter trap profile where N is separated from SF core by vacuum. An example of this interesting scenario is shown in Fig. 6.11(b) where a rigid $J_\theta(r)$ overlaps with the N phase and there is no gSF region. Both trap profiles are generated by self consistent solution of gap and number equation derived in previous section. In Fig. 6.12 we show schematic representation of the possible phase profiles of adiabatically rotating Fermi gas with SOC.

We start with analyzing the effect of SOC on the Ω_c . We calculate Ω_c using Eq. (6.44), $R_O^0(\alpha, \Omega = \Omega_c)$ is given in Eq. (6.12), and $R_O(\alpha, \Omega = 0)$ is determined by solving the gap and number equation self-consistently to determine the edge of the gas.

In contrast to the $\alpha = 0$ case, finite α eventually leads to pair breaking and appearance of the N phase at some Ω_c for all E_b as shown as a function of α for different E_b in Fig. 6.13(a). The critical value for pair breaking at fixed α increases

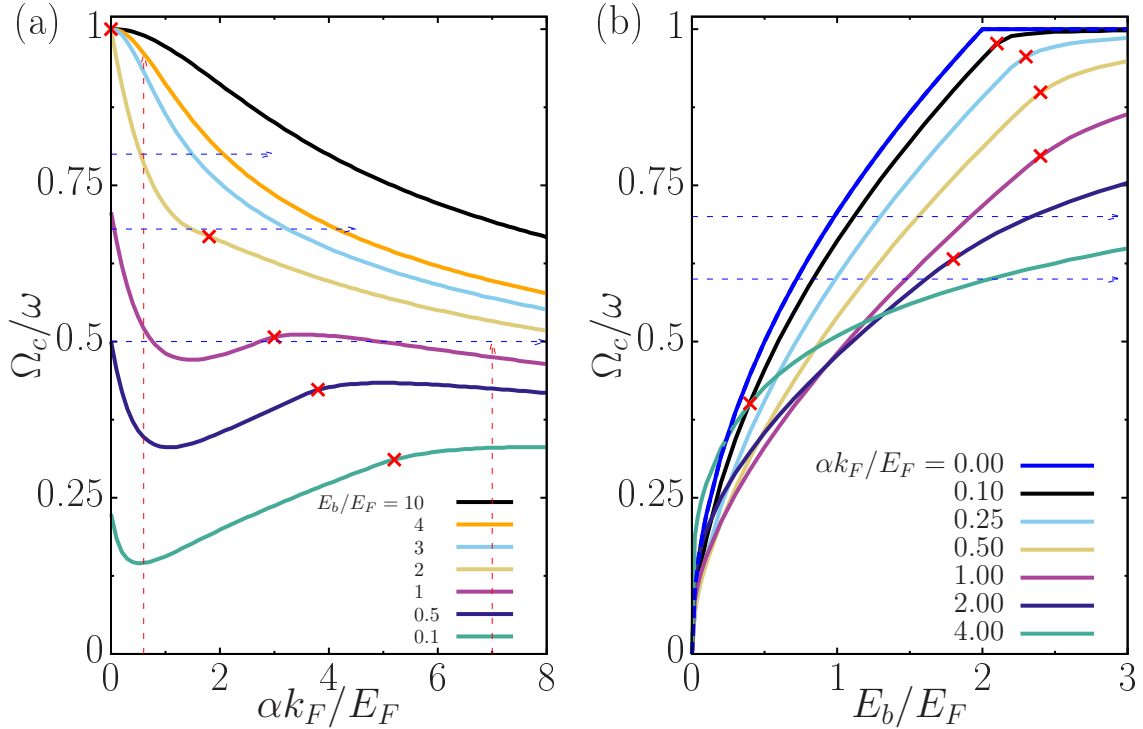


Figure 6.13: The critical rotation frequency for pair breaking and the appearance of a normal phase for (a) different interaction strengths characterized by binding energy E_b as function of SOC strength α and (b) fixed values of α as a function of E_b . The “x” indicate the point beyond which the normal phase emerges disconnected from the superfluid separated by vacuum as the relevant curve is crossed. The details of the structures of the curves are discussed in the text. The phase profiles in the trap along the horizontal (blue) arrows in (a) are shown in Fig. 6.16 as a function of α and the phase profiles along the vertical (red) arrows in (a) are shown in Fig. 6.17 as a function of Ω in horizontal and vertical panels, respectively. Similarly the phase profiles along the horizontal lines in (b) are shown in Fig. 6.18.

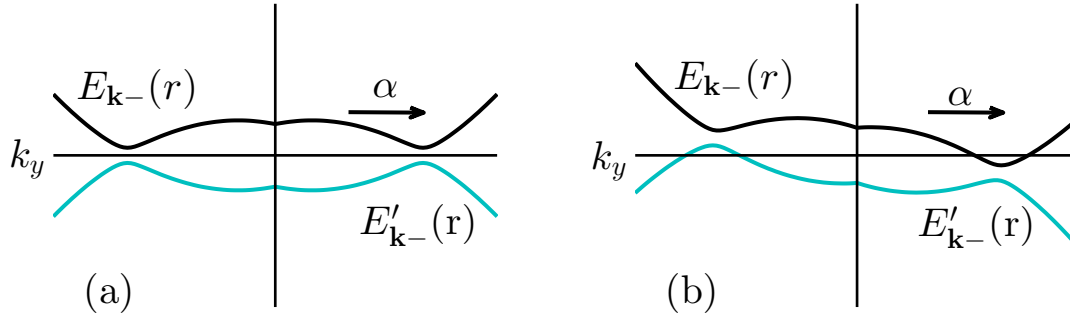


Figure 6.14: Schematic diagrams showing the excitation spectrum of negative helicity particles $E_{\mathbf{k}-}(r)$ with $\Omega \neq 0$ and $\alpha \neq 0$ for (a) a gapped superfluid at $r = 0$, (b) a gapless superfluid at $r > 0$. The regions with negative quasi-particle energy result in the pair breaking effect. Finite α shifts excitation minimum to higher momenta, which can make pair breaking easier.

with increasing E_b as expected intuitively. For large $E_b \gtrsim 2E_F$, we find that there is also a threshold value $\alpha > 0$ required for pair breaking. Increasing α from zero, $\Omega_c = \omega$ until large enough α (depending on E_b) after which point the $\Omega_c(\alpha)$ decreases monotonically as pair breaking starts at smaller Ω for larger α (top three curves in the figure). In this strong interaction regime the N phase always appears disconnected from the SF core for $\Omega > \Omega_c$. However, the structure of $\Omega_c(\alpha)$ curves for $E_b \lesssim 2E_F$ (bottom three curves in the figure) show a different behavior. Ω_c decreases as α is increased from zero and develops a minimum. This form is a result of the multiple effects of SOC discussed in Sec. (4.7). For small α , the dominant effect comes from the simultaneous action of SOC and rotation making pair breaking easier. This is directly related to shifting of the excitation minima to higher momentum states (see Fig. 6.14) some of which are more susceptible to rotation. As α becomes significant for given E_b , it has two further effects. It enhances $|\Delta(r)|$ and decreases the gas radius both of which make pair breaking more difficult. Therefore when these effects dominate, Ω_c starts to increase with α which explains the minimum in the shape of $\Omega_c(\alpha)$ curve. The minimum moves to higher values of α for stronger interactions because the latter effects of SOC become significant only at relatively greater values of α . Before this

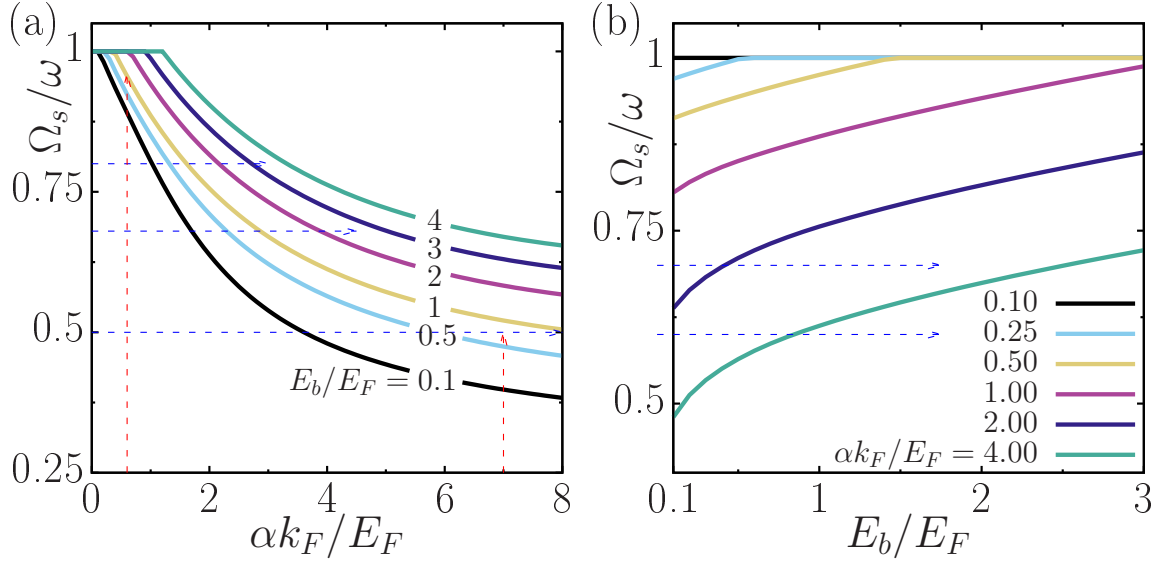


Figure 6.15: The rotation frequency Ω_s for complete destruction of the superfluid phase for (a) various interaction strengths characterized by the binding energy E_b as function of SOC strength α and (b) fixed α values as a function of E_b . The horizontal part at $\Omega = \omega$ of each curve indicates the persistence of the superfluid for all rotation frequencies up to a threshold value of α for the corresponding E_b or vice versa. The complete disappearance of SF in 2D requires the simultaneous presence of SOC and rotation and is accompanied by the depletion of the central density. The trap profiles along the dashed arrows are as given in Fig. 6.13.

minimum, we can estimate Ω_c by neglecting the effect of SOC on the radius of the trap, i.e., taking $R_O \approx R_F$, and inserting μ given in Sec. (4.7) for small SOC into the dispersion relation. The rotation for which the dispersion relation becomes zero at the edge of the gas then gives the critical rotation

$$\Omega_c \approx \frac{\omega}{2} \left(\sqrt{\frac{2\alpha^2 k_F^2}{E_F^2} + \frac{2E_b}{E_F}} - \frac{\alpha k_F}{E_F} \right). \quad (6.45)$$

This agrees very well with the numerical data given in Fig. 6.13(a) in the small α regime (not plotted). For even greater values of α , the N phase is favored under rotation and appears at larger distances from the center. This changes the mechanism of suppressing the SF phase by directly favoring previously unoccupied unpaired states and alters the behavior of $\Omega_c(\alpha)$ curve. Beyond the points marked by “x”s in Fig. 6.13,

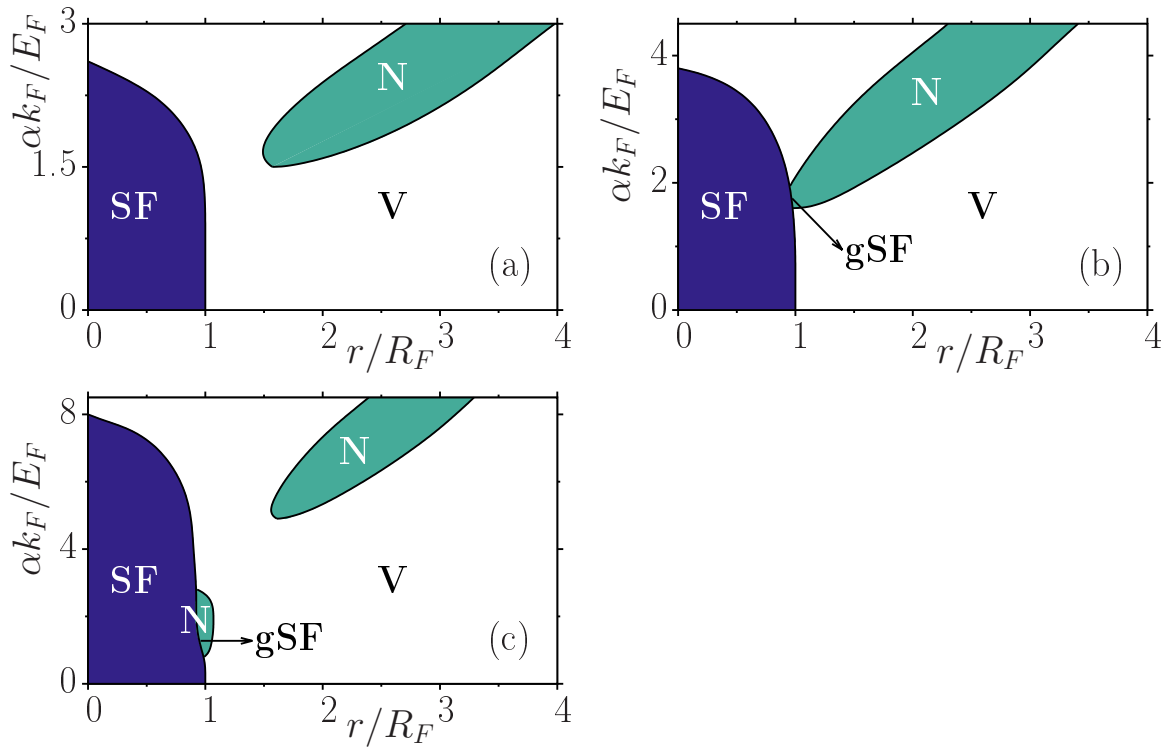


Figure 6.16: Radial phase profile in the trap with changing SOC: SF-Superfluid (dark blue), N-Normal phase (green) and V-Vacuum (white). (a) $E_b = 3E_F$ $\Omega = 0.8\omega$, (b) $E_b = 2E_F$ $\Omega = 0.68\omega$, (c) $E_b = 1E_F$ $\Omega = 0.5\omega$. The three panels show the different possibilities of the appearance of the normal phase as a function of the SOC strength α .

the curve goes through a maximum after which it eventually decreases with increasing α . For parameters in this region, the N phase appears disconnected from the SF phase. This point occurs at smaller values of α as the interaction increases which can also be seen by the condition given above and the fact that μ decreases with increasing E_b . Therefore, for $E_b \gtrsim 2.5E_F$, the “x” occurs at $(\alpha = 0, \Omega = \omega)$.

We plot $\Omega_c(E_b)$ for different α values in Fig. 6.13(b), where Ω_c increases monotonically with E_b until it saturates at $\Omega_c = \omega$. For small and large E_b , α plays opposite roles as seen from the crossing of $\Omega_c(E_b)$ curves and the reversing order of the curves. The points indicated by “x” again mark the interaction strength beyond which N phase appears as a separated annulus. The presence of gSF therefore requires increasing Ω from zero on the left of the relevant “x” mark and happens up to $E_b \lesssim 2.5E_F$.

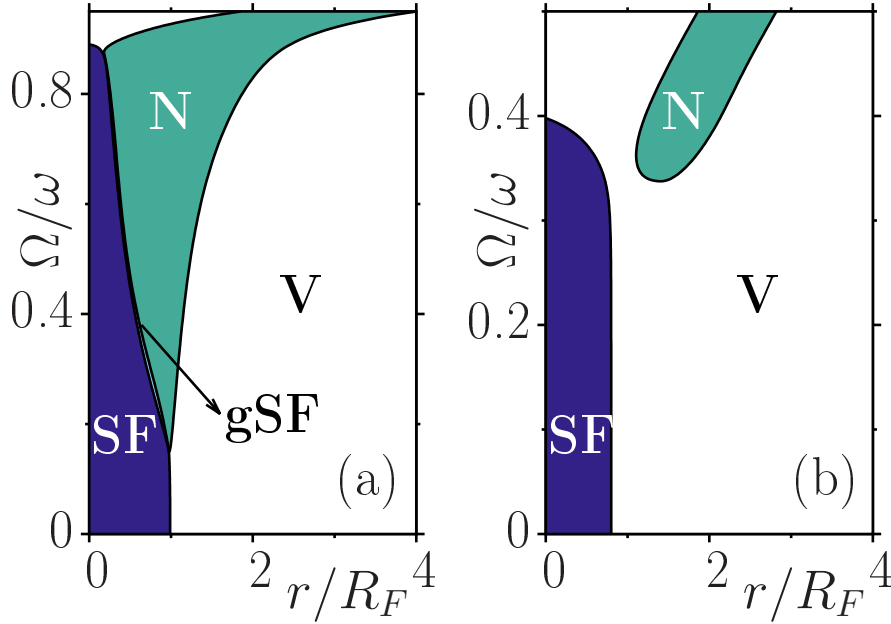


Figure 6.17: Radial phase profile in the trap with changing Ω : SF-Superfluid (dark blue), gSF-gapless superfluid (light blue), N-Normal phase (green) and V-Vacuum (white). (a) $E_b = 0.1E_F$, $\alpha = 0.6E_F/k_F$, (b) $E_b = 0.1E_F$, $\alpha = 7E_F/k_F$. The two panels show the different possibilities of the appearance of the normal phase as a function of the rotation frequency Ω .

The disconnected appearance of the normal annulus between $E_b \sim 2 - 2.5E_F$ actually happens twice as a function of α where after the first appearance the ring merges with the SF core and separates again as α is increased further. This is not shown in Fig. 6.13(a) but is the reason for the behavior of “x” marks in Fig. 6.13(b) for $E_b \sim 2 - 2.5E_F$ curves.

The simultaneous presence of SOC and rotation can lead to complete destruction of the SF phase within our model. The disappearance of SF also means the depletion of the density at the center of the trap because the center of the trap is not rotating. We use this reasoning to estimate the frequency Ω_s for which SF is completely destroyed by solving the gap and number equations with vanishing density $n(r=0)$ and vanishing $|\Delta(\mathbf{r}=0)|$ at the center of the trap. One can obtain μ for vanishing $|\Delta(\mathbf{r}=0)|$ from the gap equation and then use the number equation for a N gas to

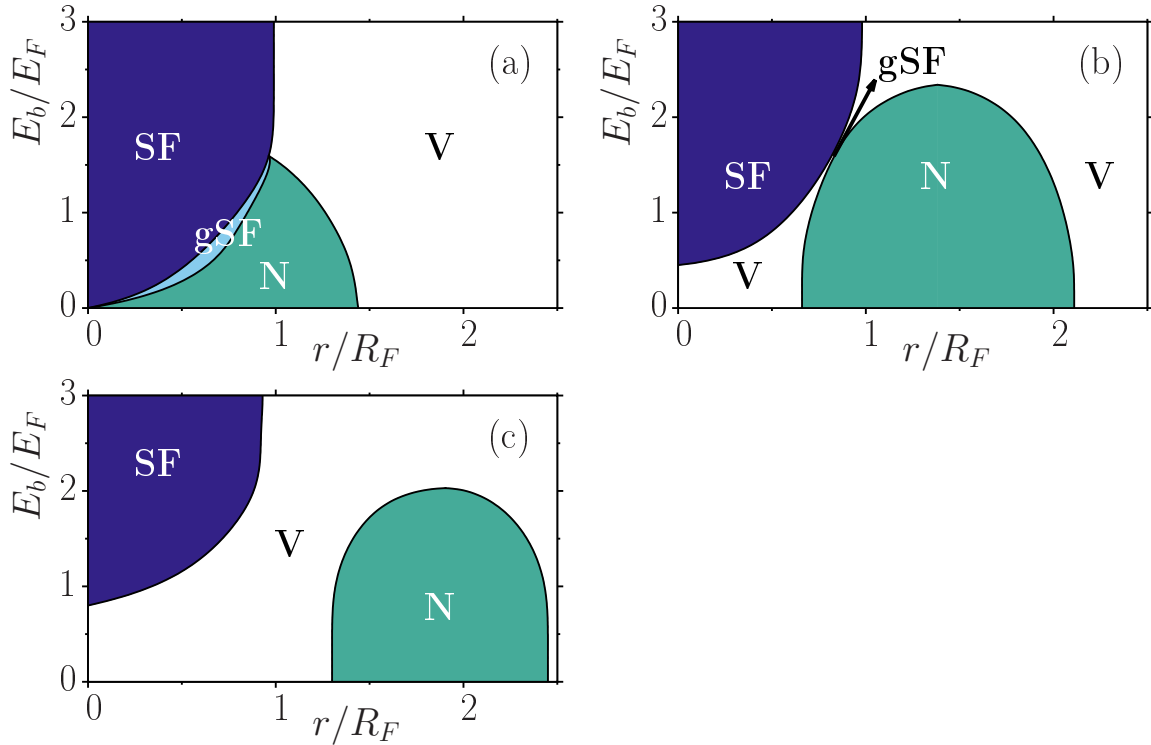


Figure 6.18: Radial phase profile in the trap with changing interaction: SF-Superfluid (dark blue), gSF-gapless superfluid (light blue), N-Normal phase (green) and V-Vacuum (white). (a) $\alpha = 0.5E_F/k_F$, $\Omega = 0.7\omega$, (b) $\alpha = 2E_F/k_F$, $\Omega = 0.7\omega$, (c) $\alpha = 4E_F/k_F$, $\Omega = 0.6\omega$. The three panels show the different possibilities of the appearance of the SF phase as a function of the interaction strength E_b .

solve for Ω_s .

In Fig. 6.15(a) we present Ω_s as a function of α for different E_b . For greater E_b , Ω_s curves move up towards higher frequencies as complete destruction of the SF phase is expected to take place at higher Ω . SF persists for finite α up to a threshold value which translates to the horizontal part at $\Omega = \omega$ of the $\Omega_s(\alpha)$ curve. This threshold value is higher for higher E_b , beyond which $\Omega_s(\alpha)$ starts to decrease monotonically. Fig. 6.15(b) shows $\Omega_s(E_b)$ for fixed α values when the interaction strength is increased at fixed SOC. Each curve now saturates again at $\Omega_s = \omega$ when E_b is strong enough to hold up pairs together until the rotation frequency equals the trap frequency.

Next we analyze all possible phase diagrams using $\Omega_c(\alpha)$ in Fig. 6.13(a) and $\Omega_s(\alpha)$ in Fig. 6.15(a). In order to demonstrate this, we check the phase profiles along the

horizontal (blue) arrows as a function of α in Fig. 6.16 where different phases in the trap are shown. The three panels show the different possibilities for the appearance and disappearance of gSF/N phases obtained from the self-consistent solution of the gap and number equations as a function of α and r .

Fig. 6.16(c) shows the profile along the bottom horizontal (blue) arrow in Fig. 6.13(a) and gives an example of the appearance of the N phase at the edge of the cloud at fixed $\Omega = 0.5\omega$ and $E_b = E_F$ as α is increased from zero. (The N and SF boundary has a very thin layer of gSF which is not visible on this scale.) This α value agrees with the first intersection of the $\Omega = 0.5\omega$ horizontal line with $\Omega_c(\alpha)$ curve in Fig. 6.13(a). As α is increased further at this E_b and Ω , we see the N phase region first widening and then contracting. The disappearance of the N phase due to the discussed interplay of different SOC effects takes places at the α value which corresponds to the second intersection point of the $\Omega = 0.5\omega$ horizontal line with $\Omega_c(\alpha)$. Finally, at very large α values, the N phase is favored at large r separated from the SF core forming an annulus of increasing width as SF is suppressed for greater α values (beyond the third intersection point in Fig. 6.13(a)). The point of complete destruction of SF happens at $\alpha \approx 8E_F/k_F$, which can also be read by following the bottom dashed (blue) horizontal arrow at $\Omega = 0.5\omega$ to the end of the plotted x -axis, i.e. to its intersection with $E_b/E_F = 1$ curve in Fig. 6.15(a). Fig. 6.16(b) shows the phase profile at $E_b = 2E_F$ and $\Omega = 0.68\omega$ where the N phase region shows up at the SF edge, separates from it and moves outward as the width of its annular shape increases with increasing α . The α value at which the N phase appears corresponds to the single intersection point of the $\Omega = 0.68\omega$ line along the middle horizontal (blue) arrow with the $\Omega_c(\alpha)$ curve in Fig. 6.13(a). For even stronger interactions, the SF disappears only through the appearance of the N phase at large α and Ω as can be seen in Fig. 6.16(a) with $E_b = 3E_F$ and $\Omega = 0.8\omega$ (to be compared with the top horizontal (blue) arrow in Fig. 6.13(a)).

We perform a similar analysis also for fixed α and E_b when Ω is increased from zero. The two possible trap profiles are demonstrated in Fig. 6.17, where different

phases in the trap are shown as a function of Ω . For small $\alpha < 2E_F/k_F$ and $E_b < 2E_F$, Fig. 6.17(a) shows how the gSF and N phases appear first at the edge of the cloud at $\Omega = \Omega_c$ and following left dashed (red) vertical arrow in Fig. 6.13(a) the N phase disconnects simultaneously with the disappearance of the gSF phase as Ω is increased. For large enough α or large enough interaction, the appearance of a disconnected N phase starts immediately at Ω_c as can be seen in Fig. 6.17(b), i.e. when right dashed (red) vertical arrow crosses the Ω_c curve to the right of the corresponding “x” mark.

Finally, in Fig. 6.18 we show all possible phase profiles in the trap as a function of the interaction strength for representative values of Ω and α . For small α or Ω , SF emerges in the center as E_b increases with gSF in between the SF core and the N ring as in Fig. 6.18(a). The interaction value for SF to emerge can be read from Fig. 6.15(b) by following the horizontal line at given Ω and the curve for given α . Similarly, the point of complete disappearance of N ($E_b \sim 1.6E_F$) can be read from Fig. 6.13(b) by looking at the intersection of the top horizontal (blue) arrow at $\Omega = 0.7\omega$ level with the $\alpha = 0.5E_F/k_F$ curve. For large values of E_b only the SF phase is present. In Fig. 6.18(b),(c) with larger values of α and Ω such that (α, Ω) is above the $\Omega_c^0(\alpha)$ in Fig. 6.5 and the non-interacting gas forms a ring, increasing E_b makes SF core appear disconnected from N. Further increase of E_b results in the whole gas becoming SF.

An important result of the simultaneous presence of SOC and rotation is that the gSF phase can occupy a much larger region in the trap as shown in Fig. 6.19. This is possible for weak E_b and intermediate α values ($E_b = 0.1E_F$ and $\alpha \sim E_F/k_F$ in Fig. 6.19(a) where the gSF phase shows itself as an annulus in the middle of the gas. An example of such a trap profile is shown in Fig. 6.19(b) where the order parameter and the mass current are plotted. In next section we will show that trap region occupied by gSF phase is slightly larger under BdG calculations. The ultimate fate of this phase is determined by both its local stability as well as its robustness against a coexistence of N and SF phases.

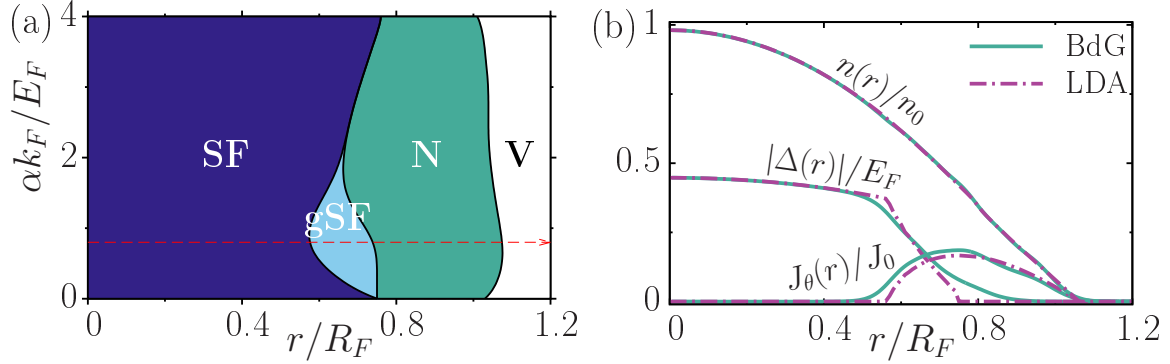


Figure 6.19: (a) Radial phase profile in the trap as a function of SOC for weak interaction $E_b = 0.1E_F$ and rotation $\Omega = 0.3\omega$: SF-Superfluid (dark blue), gSF-gapless superfluid (light blue), N-Normal phase (green) and V-Vacuum (white). The interplay of SOC and rotation effects may allow for an increased gSF region. (b) Sample gSF trap profile along the dashed (red) arrow in (a) showing the order parameter and current comparing LDA (dot-dashed) and BdG (solid lines) with $N = 500$ results for $\alpha = 0.8E_F/k_F$.

6.5 Rashba Coupled 2D Interacting Fermi Gas Under Adiabatic Rotation: Bogoliubov de-Gennes Approach

In this section we develop a full quantum mechanical BdG approach to check the validity of the results we presented in the previous section using LDA. We again start with mean-field Hamiltonian given in Eq. (6.35). We diagonalize H^{mf} via a generalized Bogoliubov-Valatin transformation, which gives the BdG eigenvalue equation

$$H^{\text{BdG}}(\mathbf{r})\Psi_\eta(\mathbf{r}) = E_\eta\Psi_\eta(\mathbf{r}) \quad (6.46)$$

where the BdG Hamiltonian can be written as

$$H^{\text{BdG}}(\mathbf{r}) = \begin{pmatrix} K(\mathbf{r}) & S(\mathbf{r}) & 0 & \Delta(\mathbf{r}) \\ S^\dagger(\mathbf{r}) & K(\mathbf{r}) & -\Delta(\mathbf{r}) & 0 \\ 0 & -\Delta^*(\mathbf{r}) & -K(\mathbf{r}) & -S^\dagger(\mathbf{r}) \\ \Delta^*(\mathbf{r}) & 0 & -S(\mathbf{r}) & -K(\mathbf{r}) \end{pmatrix} - \Omega L_z(\mathbf{r}) \quad (6.47)$$

with $K(\mathbf{r}) = -\nabla^2/(2M) + V(r) - \mu$, $L_z(\mathbf{r}) = x\partial_y - y\partial_x$ and and and and and and and and $S(\mathbf{r}) = \alpha(\partial_x - i\partial_y)$. The eigenfunctions are formed by a four component Nambu spinor $\Psi_\eta(\mathbf{r}) = [u_{\uparrow\eta}(\mathbf{r}), u_{\downarrow\eta}(\mathbf{r}), v_{\uparrow\eta}(\mathbf{r}), v_{\downarrow\eta}(\mathbf{r})]^T$. The associated quasi-particles have energy $E_\eta > 0$ and creation/annihilation operators $\hat{\gamma}_\eta^\dagger/\hat{\gamma}_\eta$ so that

$$H^{\text{mf}} = E_{\text{gs}} + \sum_{\eta} E_{\eta} \hat{\gamma}_{\eta}^{\dagger} \hat{\gamma}_{\eta} \quad (6.48)$$

with E_{gs} being the ground state energy of the system. The inverse transformations

$$\hat{\psi}_{\sigma}(\mathbf{r}) = \sum_{\eta} [u_{\sigma\eta}(\mathbf{r}) \hat{\gamma}_{\eta} + v_{\sigma\eta}^*(\mathbf{r}) \hat{\gamma}_{\eta}^{\dagger}] \quad (6.49)$$

can be used to determine the self-consistency equations. By inserting this relations to the definition $\Delta(\mathbf{r}) = g \langle \hat{\psi}_{\uparrow}(\mathbf{r}) \hat{\psi}_{\downarrow}(\mathbf{r}) \rangle$ we get the gap equation

$$\Delta(\mathbf{r}) = g \sum_{\eta} [u_{\uparrow\eta}(\mathbf{r}) v_{\downarrow\eta}^*(\mathbf{r}) f(-E_{\eta}) + u_{\downarrow\eta}(\mathbf{r}) v_{\uparrow\eta}^*(\mathbf{r}) f(E_{\eta})]. \quad (6.50)$$

Similarly we can calculate the local density $n(\mathbf{r}) = \sum_{\sigma} \langle \hat{\psi}_{\sigma}^{\dagger}(\mathbf{r}) \hat{\psi}_{\sigma}(\mathbf{r}) \rangle$ given by

$$n(\mathbf{r}) = \sum_{\eta\sigma} [|u_{\sigma\eta}(\mathbf{r})|^2 f(E_{\eta}) + |v_{\sigma\eta}(\mathbf{r})|^2 f(-E_{\eta})]. \quad (6.51)$$

The total particle number is again obtained by integrating the density $N = \int d\mathbf{r} n(\mathbf{r})$. In order to classify different superfluid phases we also calculate the mass current density $\mathbf{J}(r)$. The non-zero angular component of the current density can be computed using Eq. (6.31)

$$J_{\theta}(r) = \sum_{\sigma} J_{\theta\sigma}(r) + 2M\alpha J_{\theta\uparrow\downarrow}(r) \quad (6.52)$$

with

$$\begin{aligned}
J_{\theta\sigma}(r) &= \sum_{\eta\sigma} \left[u_{\sigma\eta}^*(\mathbf{r}) \frac{\partial}{r\partial\theta} u_{\sigma\eta}(\mathbf{r}) f(E_\eta) + v_{\sigma\eta}(\mathbf{r}) \frac{\partial}{r\partial\theta} v_{\sigma\eta}^*(\mathbf{r}) f(-E_\eta) \right], \\
J_{\theta\uparrow\downarrow}(r) &= \sum_{\eta} \left[|u_{\uparrow\eta}^*(\mathbf{r}) u_{\downarrow\eta}(\mathbf{r})| f(E_\eta) + |v_{\uparrow\eta}(\mathbf{r}) v_{\downarrow\eta}^*(\mathbf{r})| f(-E_\eta) \right]. \quad (6.53)
\end{aligned}$$

In order to make use of the rotational symmetry we further expand the eigenvectors in 2D harmonic oscillator basis. Using the conservation of total angular momentum around the rotation axis we first decompose BdG eigenvectors into $(|l| + 1/2)$ ($|l| \geq 0$) sectors. Then by defining $u_{\uparrow\eta}(\mathbf{r}) = u_{\uparrow\mathbf{m}}^l(\mathbf{r})$, $u_{\downarrow\eta}(\mathbf{r}) = u_{\downarrow\mathbf{m}}^{l+1}(\mathbf{r})$, $u_{\uparrow\eta}(\mathbf{r}) = u_{\uparrow\mathbf{m}}^l(\mathbf{r})$ and $v_{\uparrow\eta}(\mathbf{r}) = v_{\uparrow\mathbf{m}}^{l+1}(\mathbf{r})$ we expand the functions in terms of the angular momentum basis of the 2D harmonic oscillator as

$$u_{\uparrow\mathbf{m}}^l(\mathbf{r}) = \sum_n u_{n\uparrow\mathbf{m}}^l R_n^{|l|}(r) e^{il\theta}, \quad u_{\downarrow\mathbf{m}}^{l+1}(\mathbf{r}) = \sum_n u_{n+1\downarrow\mathbf{m}}^{l+1} R_{n+1}^{|l+1|}(r) e^{i(l+1)\theta} \quad (6.54)$$

$$v_{\downarrow\mathbf{m}}^l(\mathbf{r}) = \sum_n v_{n\downarrow\mathbf{m}}^l R_n^{|l|}(r) e^{il\theta}, \quad v_{\uparrow\mathbf{m}}^{l+1}(\mathbf{r}) = \sum_n v_{n+1\uparrow\mathbf{m}}^{l+1} R_{n+1}^{|l+1|}(r) e^{i(l+1)\theta} \quad (6.55)$$

Using the orthogonality of the basis we can obtain the following eigenvalue equation for each $(|l| + 1/2)$ sector:

$$\sum_{n'} \begin{pmatrix} K_{nn'}^l & S_{n,n'+1}^{-,l+1} & 0 & \Delta_{nn'}^{l'} \\ S_{n+1,n'}^{+,l} & K_{n+1,n'+1}^{l+1} & -\Delta_{n+1,n'+1}^{l+1} & 0 \\ 0 & -(\Delta_{n+1,n'+1}^{l+1})^* & -K_{n+1,n'+1}^{-l-1} & -S_{n+1,n'}^{+,-l} \\ (\Delta_{nn'}^l)^* & 0 & -S_{n,n'+1}^{-,-l-1} & -K_{nn'}^{-l'} \end{pmatrix} \begin{pmatrix} u_{n'\uparrow\mathbf{m}}^l \\ u_{n'+1\downarrow\mathbf{m}}^{l+1} \\ v_{n'+1\uparrow\mathbf{m}}^{l+1} \\ v_{n'\downarrow\mathbf{m}}^l \end{pmatrix} = E_{\mathbf{m}}^l \begin{pmatrix} u_{n'\uparrow\mathbf{m}}^l \\ u_{n'+1\downarrow\mathbf{m}}^{l+1} \\ v_{n'+1\uparrow\mathbf{m}}^{l+1} \\ v_{n'\downarrow\mathbf{m}}^l \end{pmatrix} \quad (6.56)$$

with

$$K_{nn'}^l = \langle nl | K(\mathbf{r}) - \Omega L_z(\mathbf{r}) | n'l \rangle = [\omega(n+1) - \mu - \Omega l] \delta_{nn'} \quad (6.57)$$

$$\Delta_{nn'}^l = \langle nl | \Delta(r) | n'l \rangle = 2\pi \int_0^\infty r dr \Delta(r) R_n^{l|}(r) R_{n'}^{l|}(r) \quad (6.58)$$

$$\begin{aligned} S_{nn'}^{-,l} &= \alpha i / (2a_0) \langle nl - 1 | S_{\mathbf{r}} | n'l \rangle = \alpha i / (2a_0) \left[\int d\mathbf{r} R_{rn}^{l|-1} e^{-i(l-1)\theta} S_{\mathbf{r}} R_{rn'}^{l|} e^{il\theta} \right] \\ &= \alpha i / (2a_0) [\sqrt{(n'+l)/2} \delta_{n,n'-1} - \sqrt{(n'-l)/2+1} \delta_{n,n'+1}] = -S_{n'n}^{+,l-1} \end{aligned} \quad (6.59)$$

where we have assumed a rotationally symmetric solution $\Delta(r)$. The gap, number and current expressions can be written as

$$\begin{aligned} \Delta(r) &= g \sum_{lm} \left(\sum_n u_{n\uparrow m}^l R_n^{l|}(r) \sum_{n'} v_{n'\downarrow m}^{*l} R_{n'}^{l|}(r) f(-E_m^l) \right. \\ &\quad \left. + \sum_n u_{n+1\downarrow m}^{l+1} R_{n+1}^{l+1|}(r) \sum_{n'} v_{n'+1\uparrow m}^{*l+1} R_{n'+1}^{l+1|}(r) f(E_m^l) \right) \end{aligned} \quad (6.60)$$

$$\begin{aligned} n(r) &= \sum_{lm} \left[\left(\left| \sum_n u_{n\uparrow m}^l R_n^{l|}(r) \right|^2 + \left| \sum_n u_{n+1\downarrow m}^{l+1} R_{n+1}^{l+1|}(r) \right|^2 \right) f(E_m^l) \right. \\ &\quad \left. + \left(\left| \sum_n v_{n+1\uparrow m}^{l+1} R_{n+1}^{l+1|}(r) \right|^2 + \left| \sum_n v_{n\downarrow m}^l R_n^{l|}(r) \right|^2 \right) f(-E_m^l) \right] \end{aligned} \quad (6.61)$$

$$\begin{aligned} J_\theta(r) &= \sum_{lm} \left\{ \left[\frac{l}{r} \left| \sum_n u_{n\uparrow m}^l R_n^{l|}(r) \right|^2 + \frac{l+1}{r} \left| \sum_n u_{n+1\downarrow m}^{l+1} R_{n+1}^{l+1|}(r) \right|^2 \right] f(E_m^l) \right. \\ &\quad \left. - \left[\frac{l+1}{r} \left| \sum_n v_{n+1\uparrow m}^{l+1} R_{n+1}^{l+1|}(r) \right|^2 + \frac{l}{r} \left| \sum_n v_{n\downarrow m}^l R_n^{l|}(r) \right|^2 \right] f(-E_m^l) \right. \\ &\quad \left. + 2M\alpha \left[\left| \sum_n (u_{n\uparrow m}^l)^* R_n^{l|}(r) \sum_{n'} u_{n'+1\downarrow m}^{l+1} R_{n'+1}^{l+1|}(r) \right| f(E_m^l) \right. \right. \\ &\quad \left. \left. + \left| \sum_n (v_{n\downarrow m}^l)^* R_n^{l|}(r) \sum_{n'} v_{n'+1\uparrow m}^{l+1} R_{n'+1}^{l+1|}(r) \right| f(-E_m^l) \right] \right\}. \end{aligned} \quad (6.62)$$

The above sums are performed for $E_m^l < E_c$ and E_c is chosen sufficiently large so that the results become cut-off independent. Note that E_c is used also in renormalization equation given in Eq. (3.129), which we use to interchange g with E_b .

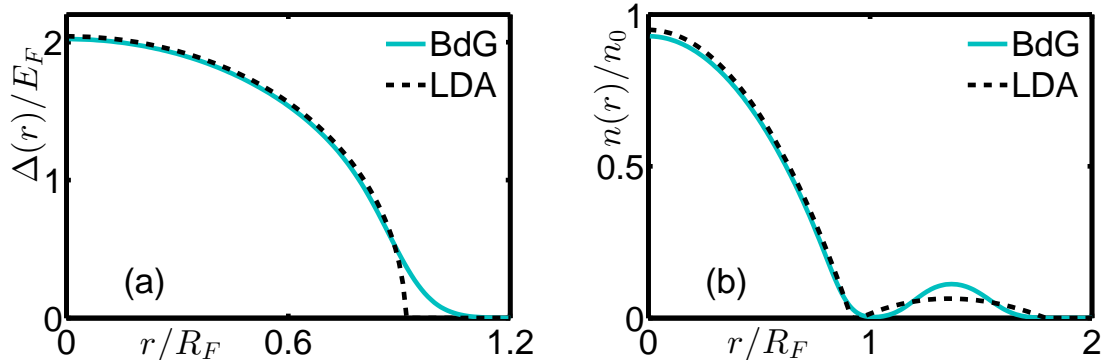


Figure 6.20: The trap profiles for representative $E_b = 2E_F$, $\alpha = 2E_F/k_F$ and $\Omega = 0.7\omega$ for $N = 100$. (a) $\Delta(r)$, (b) $n(r)$. LDA is in very good agreement with BdG calculations even for $N = 100$. Cut-off used in BdG calculation is $E_c \sim 60E_F$.

Similar to the non-interacting case we find that within the mean-field approximation, LDA provides a very good approximation to the full quantum mechanical BdG calculations. The comparison between LDA and BdG results is shown in Fig. 6.20 and Fig. 6.19. The difference between the two calculations becomes visible only in regions where quantities change rapidly and LDA is expected to fail. As a result, $\Delta(r)$ survives in larger radius in BdG approach. As a result of this gSF is wider in BdG approach compared to LDA. This expected difference means that gSF in the phase diagrams presented in previous section may occupy a slightly larger region in the trap and the parameter space.

Chapter 7

CONCLUSION AND OUTLOOK

In this section we summarize our findings on the spin-orbit coupled 2D Fermi gas in a rotating harmonic trap and point out relevant directions for future research.

First, we analyzed the combined effects of spin-orbit coupling and rotation on the ground state of the non-interacting system under local density approximation (LDA) using the the local density of states and obtained parameter regimes for the formation of the characteristic ring shaped density profile. It is important to emphasize that neither rotation nor SOC alone can deplete the central density to zero no matter how fast the rotation or large SOC is, and the formation of such an intriguing annulus requires both of them simultaneously. The analysis yields analytic and semi-analytic results for the density and the inner and outer radii of the gas cloud. In this way, we determined the critical rotation frequency for the depletion of the central density as a function of SOC. We benchmark our semi-classical LDA results with those of exact quantum-mechanical treatment and found an excellent agreement between the two for all relevant parameter regimes.

An interesting extension of our study would be the effects of anisotropy regarding both the trapping potential in real space and SOC in momentum space. The anisotropy is expected to deform the ring shaped density profile and in extreme limits split the ring into parts. We note that although finite temperature smears out the edges of the ring shaped density and a Gaussian profile emerges at high temperatures, the effect remains visible up to temperatures $\sim T_F$ with comparable SOC values.

We have found that the rotation induced particle current polarizes the system along the flow via SOC. In the presence of an imbalance of between different pseudo-spin types, which is the analog of a perpendicular Zeeman field, SOC and rotation

can further affect the spin polarization creating non-trivial spin textures.

Another important limit of this model is that of extremely rapid rotation which gives rise to Landau levels in the absence of SOC and interactions. It is known that semi-classical approach will fail in this limit, thus we resorted to the full quantum mechanical formalism and studied how the Landau levels are modified as SOC is introduced to the system. Our model predicts a ring shaped density starting from smaller and smaller SOC as $\Omega \rightarrow \omega$. However, the eventual ring shaped gas has constant density in this limit, which equals the density at half filling in the no SOC case. Furthermore, the splitting of Landau levels for different total angular momentum sectors allows for various staircase like disk and ring density distributions with equal height up and down steps inbetween the initial Landau level picture and the final ring of constant density formed by half of the lowest Landau level finite angular momentum states.

Secondly, we studied the interacting system under the BCS mean-field approximation. Assuming that rotation is introduced adiabatically and no vortices are excited, we studied the superfluid phase and its robustness. Interestingly, the presence of SOC can either facilitate or resist the pair breaking effects of rotation. We calculated the critical frequency for the onset of pair breaking, identifying different mechanisms for it, and discussed the consequences. In particular, we find that SOC works in favor of pairing for weak interactions, whereas it helps pair breaking for strong interactions in a rotating gas. Unlike the no SOC case, it is possible to break pairs for any interaction strength given sufficiently high rotation and/or SOC. We showed that the cooperation of rotation and SOC allows for the possibility of creating either an isolated annulus of rigidly rotating normal particles that is disconnected from the central core of non-rotating superfluid pairs or an intermediate gapless superfluid phase which is characterized by the coexistence of superfluid pairs and normal particles. Although similar effects of separation between the SF and N phases are known for the case with excess unpaired particles in a non-rotating imbalanced gas, in that case the combined effect of rotation and SOC is expected to result in more interesting profiles

with different successive rings in density.

The appearance of the gSF and the N phase is accompanied by a non-zero current. The system acquires only partial mass current as opposed to a rigidly rotating gas. For sufficiently fast rotation or high SOC strength, gSF and SF components eventually and successively disappear leaving the characteristic annulus of the rigidly rotating normal phase behind. Hence in the presence of SOC, superfluidity can be completely destroyed. We calculated the minimum rotation frequency for complete disappearance of the SF phase as a function of SOC and interaction strengths. The critical frequency curves that we obtain can be used to predict all possible phase profiles in the trap.

We presented extensive phase diagrams and corresponding trap profiles for various values of SOC, rotation frequency and interaction strength demonstrating all possible scenarios of pair breaking and complete destruction of the superfluid phase as a function of these three parameters. We discussed in detail how these phase diagrams can also be predicted from the critical rotation frequency curves for the onset of pair-breaking and complete destruction of SF. We hope that the phase diagrams will be helpful in exploring different parameter regimes for future experiments. For example, it may be possible to observe a gSF phase for weak interactions in an appreciable region within the trap. In the absence of SOC, this phase is present only as a sliver in the radial trap profile. Furthermore the effects of rotation on the topologically non-trivial phases of the imbalanced gas have so far not been investigated.

We compared the LDA results with those of the BdG approach finding excellent agreement in all cases including the most general case considered in this paper. As expected, for finite number of particles LDA findings deviate from BdG results in regions of low density and rapidly changing order parameter. However, this small difference becomes negligible as the number of particles in the system increases. The BdG formalism can easily be extended to calculate the critical rotation frequency for vortex formation and its stability which will be subject of a future study. This will be important to judge our no vortex assumption in the case of non-adiabatic rotation. In 3D without SOC, pair breaking with no vortices can indeed be pre-

ferred [Warringa and Sedrakian, 2011, Warringa, 2012].

We hope that, given the ongoing push towards simulating Rashba-coupled Fermi gases by many groups worldwide, our compelling results may soon be realized once the technical experimental difficulties are cleared out of the way.

BIBLIOGRAPHY

- [Abo-Shaeer et al., 2001] Abo-Shaeer, J. R., Raman, C., Vogels, J. M., and Ketterle, W. (2001). Observation of vortex lattices in Bose-Einstein condensates. *Science*, 292(5516):476–479.
- [Abrikosov, 1957] Abrikosov, A. A. (1957). The magnetic properties of superconducting alloys. *Journal Of Physics And Chemistry Of Solids*, 2(3):199–208.
- [Adhikari, 1986] Adhikari, S. K. (1986). Quantum scattering in two dimensions. *American Journal of Physics*, 54(1986):362.
- [Allen and Misener, 1938] Allen, J. F. and Misener, a. D. (1938). Flow of Liquid Helium II. *Nature*, 141:75–75.
- [Ambrosetti et al., 2014] Ambrosetti, A., Lombardi, G., Salasnich, L., Silvestrelli, P. L., and Toigo, F. (2014). Polarization of a quasi-two-dimensional repulsive Fermi gas with Rashba spin-orbit coupling: A variational study. *Physical Review A*, 90(4):043614.
- [Anderson et al., 1995] Anderson, M. H., Ensher, J. R., Matthews, M. R., Wieman, C. E., and Cornell, E. A. (1995). Observation of Bose-Einstein Condensation in a Dilute Atomic Vapor. *Science*, 269(5221):198–201.
- [Annett, 2004] Annett, J. F. (2004). Superconductivity, Superfluids and Condensates. *Oxford Master Series*, (May):140.
- [Ashcroft and Mermin, 1976] Ashcroft, N. W. and Mermin, N. D. (1976). *Solid State Physics*, volume 2.

- [Bardeen et al., 1957] Bardeen, J., Cooper, L. N., and Schrieffer, J. R. (1957). Theory of Superconductivity. *Physical Review*, 108(5):1175–1204.
- [Bausmerth et al., 2008a] Bausmerth, I., Recati, A., and Stringari, S. (2008a). Destroying superfluidity by rotating a Fermi gas at unitarity. *Physical review letters*, 100(7):070401.
- [Bausmerth et al., 2008b] Bausmerth, I., Recati, A., and Stringari, S. (2008b). Unitary polarized Fermi gas under adiabatic rotation. *Physical Review A*, 78(6):063603.
- [Berezinskii, 1971] Berezinskii, V. L. (1971). Destruction of long-range order in one-dimensional and two-dimensional systems having a continuous symmetry group I. classical systems. *Sov. Phys. JETP*, 32(3):493.
- [Berry, 1984] Berry, M. V. (1984). Quantal Phase Factors Accompanying Adiabatic Changes. *Proceedings of the Royal Society of London A: Mathematical, Physical and Engineering Sciences*, 392(1802):45–57.
- [Bloch et al., 2008] Bloch, I., Dalibard, J., and Zwirger, W. (2008). Many-body physics with ultracold gases. *Reviews of Modern Physics*, 80(3):885–964.
- [Boettcher et al., 2012] Boettcher, I., Pawłowski, J. M., and Diehl, S. (2012). Ultracold atoms and the Functional Renormalization Group. *Nuclear Physics B - Proceedings Supplements*, 228:63–135.
- [Born and Fock, 1928] Born, M. and Fock, V. (1928). Beweis des Adiabatenatzes. *Zeitschrift für Physik*, 51(3-4):165–180.
- [Bose, 1924] Bose, S. N. (1924). Planck's Law and Light Quantum Hypothesis. *Zeitschrift für Physik*, 26(Received):1–4.

- [Bradley et al., 1997] Bradley, C. C., Sackett, C. A., and Hulet, R. G. (1997). Bose-Einstein Condensation of Lithium: Observation of Limited Condensate Number. *Physical Review Letters*, 78(6):985–989.
- [Bychkov and Rashba, 1984] Bychkov, Y. A. and Rashba, E. I. (1984). Properties of a 2D electron gas with lifted spectral degeneracy. *JETP Letters*, 39:78–81.
- [Campbell et al., 2011] Campbell, D. L., Juzelinas, G., and Spielman, I. B. (2011). Realistic Rashba and Dresselhaus spin-orbit coupling for neutral atoms. *Physical Review A*, 84(2):025602.
- [Cao et al., 2014] Cao, Y., Zou, S.-H., Liu, X.-J., Yi, S., Long, G.-L., and Hu, H. (2014). Gapless topological Fulde-Ferrell superfluidity in spin-orbit coupled Fermi gases. *Physical review letters*, 113(11):115302.
- [Chen et al., 2012] Chen, G., Gong, M., and Zhang, C. (2012). BCS-BEC crossover in spin-orbit-coupled two-dimensional Fermi gases. *Physical Review A*, 85(1):013601.
- [Cheuk et al., 2012] Cheuk, L. W., Sommer, A. T., Hadzibabic, Z., Yefsah, T., Bakr, W. S., and Zwierlein, M. W. (2012). Spin-injection spectroscopy of a spin-orbit coupled Fermi gas. *Physical Review Letters*, 109(9).
- [Chin et al., 2010] Chin, C., Grimm, R., Julienne, P., and Tiesinga, E. (2010). Feshbach resonances in ultracold gases. *Reviews of Modern Physics*, 82(2):1225–1286.
- [Cohen-Tannoudji et al., 1977] Cohen-Tannoudji, C., Diu, B., and Laloë, F. (1977). Quantum Mechanics Vol. I.
- [Cooper, 1956] Cooper, L. N. (1956). Bound Electron Pairs in a Degenerate Fermi Gas. *Physical Review*, 104(4):1189–1190.

- [Cornish et al., 2000] Cornish, S., Claussen, N., Roberts, J., Cornell, E., and Wieman, C. (2000). Stable ^{85}Rb bose-einstein condensates with widely tunable interactions. *Physical review letters*, 85(9):1795–8.
- [Courteille et al., 1998] Courteille, P., Freeland, R. S., Heinzen, D. J., van Abeelen, F. A., and Verhaar, B. J. (1998). Observation of a Feshbach Resonance in Cold Atom Scattering. *Physical Review Letters*, 81(1):69–72.
- [Cui, 2012] Cui, X. (2012). Mixed-partial-wave scattering with spin-orbit coupling and validity of pseudopotentials. *Physical Review A*, 85(2):022705.
- [Dalibard, 1999] Dalibard, J. (1999). Collisional dynamics of ultra-cold atomic gases. *Proceedings of the International School of Physics- . . .*, pages 1–29.
- [Dalibard et al., 2011] Dalibard, J., Gerbier, F., Juzelinas, G., and Öhberg, P. (2011). Colloquium : Artificial gauge potentials for neutral atoms. *Reviews of Modern Physics*, 83(4):1523–1543.
- [Davis et al., 1995] Davis, K., Mewes, M., Andrews, M., van Druten, N., Durfee, D., Kurn, D., and Ketterle, W. (1995). Bose-Einstein Condensation in a Gas of Sodium Atoms. *Physical Review Letters*, 75(22):3969–3973.
- [DeMarco, 1999] DeMarco, B. (1999). Onset of Fermi Degeneracy in a Trapped Atomic Gas. *Science*, 285(5434):1703–1706.
- [Doko et al., 2012] Doko, E., Suba, A. L., and Iskin, M. (2012). Counterflow of spontaneous mass currents in trapped spin-orbit-coupled Fermi gases. *Physical Review A*, 85(5):053634.
- [Doko et al., 2016] Doko, E., Suba, A. L., and Iskin, M. (2016). Rotating a Rashba-coupled Fermi gas in two dimensions. *Physical Review A*, 93(3):033640.

- [Dresselhaus, 1955] Dresselhaus, G. (1955). Spin-Orbit Coupling Effects in Zinc Blende Structures. *Physical Review*, 100(2):580–586.
- [Dyke et al., 2011] Dyke, P., Kuhnle, E. D., Whitlock, S., Hu, H., Mark, M., Hoinka, S., Lingham, M., Hannaford, P., and Vale, C. J. (2011). Crossover from 2D to 3D in a weakly interacting Fermi gas. *Physical review letters*, 106(10):105304.
- [Eagles, 1969] Eagles, D. M. (1969). Possible pairing without superconductivity at low carrier concentrations in bulk and thin-film superconducting semiconductors. *Physical Review*, 186(2):456–463.
- [Einstein, 1925] Einstein, A. (1925). Quantentheorie des einatomigen idealen Gases. *Sitzungsberichte der Preussischen Akademie der Wissenschaften*, 1(3).
- [Fano, 1935] Fano, U. (1935). Sullo spettro di assorbimento dei gas nobili presso il limite dello spettro d’arco. *Il Nuovo Cimento*, 12(3):154–161.
- [Fano, 1961] Fano, U. (1961). Effects of configuration interaction on intensities and phase shifts. *Physical Review*, 124(6):1866–1878.
- [Feld et al., 2011] Feld, M., Fröhlich, B., Vogt, E., Koschorreck, M., and Köhl, M. (2011). Observation of a pairing pseudogap in a two-dimensional Fermi gas. *Nature*, 480(7375):75–78.
- [Feshbach, 1958] Feshbach, H. (1958). Unified theory of nuclear reactions. *Annals of Physics*, 5(4):357–390.
- [Fetter, 2009] Fetter, A. L. (2009). Rotating trapped Bose-Einstein condensates. *Reviews of Modern Physics*, 81(2):647–691.
- [Feynman, 1955] Feynman, R. P. (1955). Progress in Low Temperature Physics Vol. 1. chapter 2. North-Holland.

- [Feynman, 1982] Feynman, R. P. (1982). Simulating physics with computers. *International Journal of Theoretical Physics*, 21(6-7):467–488.
- [Feynman, 1986] Feynman, R. P. (1986). Quantum mechanical computers. *Foundations of Physics*, 16(6):507–531.
- [Fierz, 1939] Fierz, M. (1939). Über die relativistische Theorie kräftefreier Teilchen mit beliebigem Spin. *Helvetica Physica Acta*, 12(1):3–37.
- [Flambaum et al., 1999] Flambaum, V. V., Gribakin, G. F., and Harabati, C. (1999). Analytical calculation of cold-atom scattering. *Physical Review A*, 59(3):1998–2005.
- [Friedel, 1958] Friedel, J. (1958). Metallic alloys. *Nuovo Cimento*, 7(2):287–311.
- [Fröhlich et al., 2011] Fröhlich, B., Feld, M., Vogt, E., Koschorreck, M., Zwerger, W., and Köhl, M. (2011). Radio-frequency spectroscopy of a strongly interacting two-dimensional Fermi gas. *Physical review letters*, 106(10):105301.
- [Gennes, 1999] Gennes, P. D. (1999). *Superconductivity of Metals and Alloys*. Westview Press.
- [Goldstein et al., 2007] Goldstein, H., Poole, C., and Safko, J. (2007). *Classical Mechanics*.
- [Gong et al., 2012] Gong, M., Chen, G., Jia, S., and Zhang, C. (2012). Searching for Majorana fermions in 2D spin-orbit coupled Fermi superfluids at finite temperature. *Physical review letters*, 109(10):105302.
- [Gor'kov and Melik-Barkhudarov, 1961] Gor'kov, L. P. and Melik-Barkhudarov, T. K. (1961). Contribution to the theory of superfluidity in an imperfect Fermi gas. *JETP*, 13(5):1018.

- [Greiner et al., 2002] Greiner, M., Mendel, O., Esslinger, T., Hänsch, T. W., and Bloch, I. (2002). Quantum phase transition from a superfluid to a Mott insulator in a gas of ultracold atoms. *Nature*, 415(6867):39–44.
- [Greiner et al., 2003] Greiner, M., Regal, C. a., and Jin, D. S. (2003). Emergence of a molecular BoseEinstein condensate from a Fermi gas. *Nature*, 426(6966):537–540.
- [Haljan et al., 2001] Haljan, P. C., Coddington, I., Engels, P., and Cornell, E. A. (2001). Driving Bose-Einstein-condensate vorticity with a rotating normal cloud. *Physical review letters*, 87(21):210403.
- [Hall and Vinen, 1956] Hall, H. E. and Vinen, W. F. (1956). The Rotation of Liquid Helium II. II. The Theory of Mutual Friction in Uniformly Rotating Helium II. *Proceedings of the Royal Society A: Mathematical, Physical and Engineering Sciences*, 238(1213):215–234.
- [Hasan and Kane, 2010] Hasan, M. Z. and Kane, C. L. (2010). Topological Insulators. *Rev. Mod. Phys.*, 82:3045.
- [He and Huang, 2012] He, L. and Huang, X.-G. (2012). BCS-BEC crossover in 2D Fermi gases with Rashba spin-orbit coupling. *Physical review letters*, 108(14):145302.
- [He and Zhuang, 2008] He, L. and Zhuang, P. (2008). Phase diagram of a cold polarized Fermi gas in two dimensions. *Physical Review A*, 78(3):033613.
- [Hess and Fairbank, 1967] Hess, G. B. and Fairbank, W. M. (1967). Measurements of Angular Momentum in Superfluid Helium. *Physical Review Letters*, 19(5):216–218.
- [Ho and Ciobanu, 2000] Ho, T. and Ciobanu, C. (2000). Rapidly rotating fermi gases. *Physical review letters*, 85(22):4648–51.

- [Hohenberg, 1967] Hohenberg, P. C. (1967). Existence of Long-Range Order in One and Two Dimensions. *Physical Review*, 158(2):383–386.
- [Huang and Yang, 1957] Huang, K. and Yang, C. N. (1957). Quantum-mechanical many-body problem with hard-sphere interaction. *Physical Review*, 105(3):767–775.
- [Huang et al., 2016] Huang, L., Meng, Z., Wang, P., Peng, P., Zhang, S.-L., Chen, L., Li, D., Zhou, Q., and Zhang, J. (2016). Experimental realization of two-dimensional synthetic spinorbit coupling in ultracold Fermi gases. *Nature Physics*, 12:540–544.
- [Inouye et al., 1998] Inouye, S., Andrews, M. R., Stenger, J., Miesner, H.-J., Stamper-Kurn, D. M., and Ketterle, W. (1998). Observation of Feshbach resonances in a Bose-Einstein condensate. *Nature*, 392(6672):151–154.
- [Iskin and Subasi, 2011] Iskin, M. and Subasi, A. L. (2011). Stability of spin-orbit coupled Fermi gases with population imbalance. *Physical review letters*, 107(5):050402.
- [Iskin and Tiesinga, 2009] Iskin, M. and Tiesinga, E. (2009). Rotation-induced superfluid-normal phase separation in trapped Fermi gases. *Physical Review A*, 79(5):053621.
- [Jervis and Thywissen, 2014] Jervis, D. and Thywissen, J. (2014). Making an ultracold gas. *arXiv preprint arXiv:1401.7659*, page 28.
- [Jiang et al., 2011] Jiang, L., Liu, X.-J., Hu, H., and Pu, H. (2011). Rashba spin-orbit-coupled atomic Fermi gases. *Physical Review A*, 84(6):063618.
- [Jochim et al., 2003] Jochim, S., Bartenstein, M., Altmeyer, A., Hendl, G., Riedl, S., Chin, C., Denschlag, J. H., and Grimm, R. (2003). Bose-Einstein Condensation of Molecules. *Science*, 302(5653):2101–2103.

- [Kapitza, 1938] Kapitza, P. (1938). Viscosity of Liquid Helium below the λ -Point.
- [Ketterle and Zwierlein, 2008] Ketterle, W. and Zwierlein, M. W. (2008). Making, probing and understanding ultracold Fermi gases. *Rivista del Nuovo Cimento*, 31(5-6):247–422.
- [Kosterlitz and Thouless, 1973] Kosterlitz, J. M. and Thouless, D. J. (1973). Ordering, metastability and phase transitions in two-dimensional systems. *Journal of Physics C: Solid State Physics*, 6(7):1181–1203.
- [Krich and Halperin, 2007] Krich, J. J. and Halperin, B. I. (2007). Cubic Dresselhaus spin-orbit coupling in 2D electron quantum dots. *Physical review letters*, 98(22):226802.
- [Landau, 1941] Landau, L. D. (1941). The theory of superfluidity of helium II. *J. Phys (USSR)*, 5(71).
- [Landau and Lifshitz, 1980] Landau, L. D. and Lifshitz, E. M. (1980). *Statistical Physics, Part 1*. Butterworth-Heinemann.
- [Leggett, 1980] Leggett, A. (1980). Cooper pairing in spin-polarized Fermi systems. *Le Journal de Physique Colloques*, 41:C7–19.
- [Leggett, 2006] Leggett, A. J. (2006). *Quantum Liquids: Bose Condensation and Cooper Pairing in Condensed-Matter Systems*. Oxford University Press.
- [Levinsen and Parish, 2015] Levinsen, J. and Parish, M. M. (2015). Strongly interacting two-dimensional Fermi gases. *Annual Review of Cold Atoms and Molecules*, 3(1):71.
- [Liao et al., 2012] Liao, R., Yu, Y.-X., and Liu, W.-M. (2012). Tuning the tricritical point with spin-orbit coupling in polarized fermionic condensates. *Physical review letters*, 108(8):080406.

- [Lin et al., 2011a] Lin, Y. J., Compton, R. L., Jimenez-Garcia, K., Phillips, W. D., Porto, J. V., and Spielman, I. B. (2011a). A synthetic electric force acting on neutral atoms. *Nature Physics*, 7(7):531–534.
- [Lin et al., 2009a] Lin, Y.-J., Compton, R. L., Jiménez-García, K., Porto, J. V., and Spielman, I. B. (2009a). Synthetic magnetic fields for ultracold neutral atoms. *Nature*, 462(7273):628–32.
- [Lin et al., 2009b] Lin, Y. J., Compton, R. L., Perry, A. R., Phillips, W. D., Porto, J. V., and Spielman, I. B. (2009b). Bose-Einstein condensate in a uniform light-induced vector potential. *Physical Review Letters*, 102(13).
- [Lin et al., 2011b] Lin, Y. J., Jimenez-Garcia, K., and Spielman, I. B. (2011b). Spin-orbit-coupled Bose-Einstein condensates. *Nature*, 471(7336):83–U99.
- [Luo et al., 2016] Luo, X., Wu, L., Chen, J., Guan, Q., Gao, K., Xu, Z.-F., You, L., and Wang, R. (2016). Tunable atomic spin-orbit coupling synthesized with a modulating gradient magnetic field. *Scientific Reports*, 6:18983.
- [Martianov et al., 2010] Martiyanov, K., Makhlov, V., and Turlapov, A. (2010). Observation of a two-dimensional fermi gas of atoms. *Physical Review Letters*, 105(3).
- [Meissner and Ochsenfeld, 1933] Meissner, W. and Ochsenfeld, R. (1933). Ein neuer Effekt bei Eintritt der Supraleitfähigkeit. *Naturwissenschaften*, 21(44):787–788.
- [Mermin and Wagner, 1966] Mermin, N. D. and Wagner, H. (1966). Absence of Ferromagnetism or Antiferromagnetism in One- or Two-Dimensional Isotropic Heisenberg Models. *Physical Review Letters*, 17(22):1133–1136.
- [Nicolai Nygaard, 2004] Nicolai Nygaard (2004). *Superfluidity in a Degenerate Atomic Fermi Gas*. Phd. thesis, University of Maryland at College Park.

- [Nozières and Schmitt-Rink, 1985] Nozières, P. and Schmitt-Rink, S. (1985). Bose condensation in an attractive fermion gas: From weak to strong coupling superconductivity. *Journal of Low Temperature Physics*, 59(3-4):195–211.
- [Onsager, 1949] Onsager, L. (1949). Statistical hydrodynamics. *Il Nuovo Cimento Series 9*, 6(2 Supplement):279–287.
- [Pauli, 1940] Pauli, W. (1940). The connection between spin and statistics. *Physical Review*, 58(8):716–722.
- [Pethick and Smith, 2008] Pethick, C. and Smith, H. (2008). *Bose-Einstein condensation in Dilute gases*. Cambridge University Press.
- [Petrov et al., 2003] Petrov, D. S., Baranov, M. A., and Shlyapnikov, G. V. (2003). Superfluid transition in quasi-two-dimensional Fermi gases. *Physical Review A*, 67(3):031601.
- [Prokof'ev et al., 2001] Prokof'ev, N., Ruebenacker, O., and Svistunov, B. (2001). Critical point of a weakly interacting two-dimensional Bose gas. *Physical review letters*, 87(27 Pt 1):270402.
- [Qi and Zhang, 2011] Qi, X.-L. and Zhang, S.-C. (2011). Topological insulators and superconductors. *Reviews of Modern Physics*, 83(4):1057–1110.
- [Radić et al., 2011] Radić, J., Sedrakyan, T. A., Spielman, I. B., and Galitski, V. (2011). Vortices in spin-orbit-coupled Bose-Einstein condensates. *Physical Review A*, 84(6):063604.
- [Randeria et al., 1990] Randeria, M., Duan, J.-M., and Shieh, L.-Y. (1990). Superconductivity in a two-dimensional Fermi gas: Evolution from Cooper pairing to Bose condensation. *Physical Review B*, 41(1):327–343.

- [Regal et al., 2004] Regal, C. A., Greiner, M., and Jin, D. S. (2004). Observation of resonance condensation of fermionic atom pairs. *Physical review letters*, 92(4):040403.
- [Ries et al., 2015] Ries, M. G., Wenz, A. N., Zürn, G., Bayha, L., Boettcher, I., Kedar, D., Murthy, P. A., Neidig, M., Lompe, T., and Jochim, S. (2015). Observation of Pair Condensation in the Quasi-2D BEC-BCS Crossover. *Physical review letters*, 114(23):230401.
- [Rosenbusch et al., 2002] Rosenbusch, P., Petrov, D. S., Sinha, S., Chevy, F., Bretin, V., Castin, Y., Shlyapnikov, G., and Dalibard, J. (2002). Critical rotation of a harmonically trapped Bose gas. *Physical review letters*, 88(25 Pt 1):250403.
- [Royer, 2011] Royer, A. (2011). Why is the magnetic force similar to a Coriolis force?
- [Ruseckas et al., 2005] Ruseckas, J., Juzelinis, G., Ohberg, P., and Fleischhauer, M. (2005). Non-Abelian gauge potentials for ultracold atoms with degenerate dark states. *Physical review letters*, 95(1):010404.
- [Sakurai, 1967] Sakurai, J. J. (1967). *Advanced Quantum Mechanics*. Pearson.
- [Schreck et al., 2001] Schreck, F., Khaykovich, L., Corwin, K. L., Ferrari, G., Bourdel, T., Cubizolles, J., and Salomon, C. (2001). Quasipure Bose-Einstein condensate immersed in a Fermi sea. *Physical review letters*, 87(8):080403.
- [Schweikhard et al., 2004] Schweikhard, V., Coddington, I., Engels, P., Mogendorff, V. P., and Cornell, E. A. (2004). Rapidly rotating Bose-Einstein condensates in and near the lowest Landau level. *Physical review letters*, 92(4):040404.
- [Seo et al., 2012] Seo, K., Han, L., and Sá de Melo, C. A. R. (2012). Emergence of Majorana and Dirac particles in ultracold fermions via tunable interactions, spin-orbit effects, and Zeeman fields. *Physical review letters*, 109(10):105303.

- [Silvera and Walraven, 1980] Silvera, I. F. and Walraven, J. T. M. (1980). Stabilization of Atomic Hydrogen at Low Temperature. *Physical Review Letters*, 44(3):164–168.
- [Sinova et al., 2015] Sinova, J., Valenzuela, S. O., Wunderlich, J., Back, C., and Jungwirth, T. (2015). Spin Hall effects. *Reviews of Modern Physics*, 87(4):1213–1260.
- [Sommer et al., 2012] Sommer, A. T., Cheuk, L. W., Ku, M. J. H., Bakr, W. S., and Zwierlein, M. W. (2012). Evolution of fermion pairing from three to two dimensions. *Physical review letters*, 108(4):045302.
- [Sommerfeld, 1928] Sommerfeld, A. (1928). Zur Elektronentheorie der Metalle auf Grund der Fermischen Statistik - I. Teil: Allgemeines, Strömungs- und Austrittsvorgänge. *Zeitschrift für Physik*, 47(1-2):1–32.
- [Stanescu et al., 2007] Stanescu, T. D., Zhang, C., and Galitski, V. (2007). Nonequilibrium spin dynamics in a trapped fermi gas with effective spin-orbit interactions. *Physical review letters*, 99(11):110403.
- [Stone and Anduaga, 2008] Stone, M. and Anduaga, I. (2008). Mass flows and angular momentum density for $px + ipy$ paired fermions in a harmonic trap. *Annals of Physics*, 323(1):2–16.
- [Takei et al., 2012] Takei, S., Lin, C.-H., Anderson, B. M., and Galitski, V. (2012). Low-density molecular gas of tightly bound Rashba-Dresselhaus fermions. *Physical Review A*, 85(2):023626.
- [Truscott et al., 2001] Truscott, a. G., Strecker, K. E., McAlexander, W. I., Partridge, G. B., and Hulet, R. G. (2001). Observation of Fermi pressure in a gas of trapped atoms. *Science (New York, N.Y.)*, 291(5513):2570–2572.
- [Ueda, 2010] Ueda, M. (2010). *Fundamentals and New Frontiers of Bose-Einstein condensation*. World Scientific.

- [Urban and Schuck, 2008] Urban, M. and Schuck, P. (2008). Pair breaking in rotating Fermi gases. *Physical Review A*, 78(1):011601.
- [Vyasankere et al., 2011] Vyasankere, J. P., Zhang, S., and Shenoy, V. B. (2011). BCS-BEC crossover induced by a synthetic non-Abelian gauge field. *Physical Review B*, 84(1):014512.
- [Wang et al., 2012] Wang, P., Yu, Z. Q., Fu, Z., Miao, J., Huang, L., Chai, S., Zhai, H., and Zhang, J. (2012). Spin-orbit coupled degenerate Fermi gases. *Physical Review Letters*, 109(9).
- [Warringa, 2012] Warringa, H. J. (2012). Location of the vortex phase in the phase diagram of a rotating two-component Fermi gas. *Physical Review A*, 86(4):043615.
- [Warringa and Sedrakian, 2011] Warringa, H. J. and Sedrakian, A. (2011). Vortex formation in a rotating two-component Fermi gas. *Physical Review A*, 84(2):023609.
- [Yang and Wan, 2012] Yang, X. and Wan, S. (2012). Phase diagram of a uniform two-dimensional Fermi gas with spin-orbit coupling. *Physical Review A*, 85(2):023633.
- [Yi and Guo, 2011] Yi, W. and Guo, G.-C. (2011). Phase separation in a polarized Fermi gas with spin-orbit coupling. *Physical Review A*, 84(3):031608.
- [Yu and Zhai, 2011] Yu, Z.-Q. and Zhai, H. (2011). Spin-orbit coupled Fermi gases across a Feshbach resonance. *Physical review letters*, 107(19):195305.
- [Zhang and Yi, 2013] Zhang, W. and Yi, W. (2013). Topological Fulde-Ferrell-Larkin-Ovchinnikov states in spin-orbit-coupled Fermi gases. *Nature communications*, 4:2711.
- [Zhou and Zhang, 2012] Zhou, K. and Zhang, Z. (2012). Opposite effect of spin-orbit coupling on condensation and superfluidity. *Physical review letters*, 108(2):025301.

- [Žutić and Das Sarma, 2004] Žutić, I. and Das Sarma, S. (2004). Spintronics: Fundamentals and applications. *Reviews of Modern Physics*, 76(2):323–410.
- [Zwierlein et al., 2005] Zwierlein, M. W., Abo-Shaeer, J. R., Schirotzek, A., Schunck, C. H., and Ketterle, W. (2005). Vortices and superfluidity in a strongly interacting Fermi gas. *Nature*, 435(7045):1047–1051.
- [Zwierlein et al., 2003] Zwierlein, M. W., Stan, C. A., Schunck, C. H., Raupach, S. M. F., Gupta, S., Hadzibabic, Z., and Ketterle, W. (2003). Observation of Bose-Einstein condensation of molecules. *Physical review letters*, 91(25):250401.